THE UNIVERSITY *of* EDINBURGH

Fire risk associated with photovoltaic installations on flat roof constructions

Experimental analysis of fire spread in semi-enclosures

Jens Steemann Kristensen

Doctor of Philosophy

THE UNIVERSITY OF EDINBURGH

2022

To those who donated their hearts

Abstract

An increase of photovoltaic (PV) installations facilitated by a significant cost reduction give rise to the utilization of commercial flat roof constructions, as unexploited surfaces elevated above ground level are ideal for building applied PV (BAPV) systems. However, an increased number of fires related to the PV systems have been reported; thus, it is essential to understand the fire-related risk.

The thesis aims to provide an improved understanding of the fire-related risk associated with BAPV systems on commercial flat roof constructions. In addition to the main focus on the fire dynamics of the system consisting of the PV module, the roof construction, and the initial fire between the two surfaces, supplementary studies are conducted to understand the frequency of PV-related fires. As such, the objectives of the thesis are i) to quantify the frequency and origin of PV-related fires. ii) To design and build a novel experimental set-up to enable measurement of relevant parameters, to iii) quantify the consequences of the semi-enclosure's geometry and facilitate analysis with a basis in fundamental flame spread theory. iv) To detach the geometry from the material parameters in the system of fire dynamics to enable, v) the selection of relevant parameters facilitating flame spread. Based on the outcome of those objectives, the final objective is vi) to discuss, suggest and examine possible mitigation solutions.

A fault tree analysis of all available data on PV-related fires estimated an annual frequency of 28.9 fires per gigawatt. However, in 49% of the analysed fires, the initial source of ignition was unknown or not related to the PV system. As such, it was concluded that the risk associated with BAPV systems was not only related to the inherent likelihood of the direct current PV system acting as an ignition source. The modification of the roof construction also changed the fire dynamic scenario and thus the consequences of an ignition.

The existence of a critical gap height was defined for one-dimensional flame spread on thermally thin polymethyl methacrylate (PMMA) in a semi-enclosure below a horizontal non-combustible stainless-steel board. If the gap height was above the critical gap height, a constant flame spread rate (FSR) occurred after ignition. In contrast, an enhancing heat feedback loop caused an increase of the FSR, which accelerated rapidly when the flame deflected below the horizontal barrier if the gap height was below the critical gap height. The relationship between the location of the flame front, the temperature of the PMMA, and heat flux towards the fuel ahead of the flame front corresponded well with the fundamental flame spread theories by F.A. Williams and J. Quintiere.

The importance of the critical gap height was evident when the PMMA was replaced with a PVC-based roofing membrane compliant with EN 13501-5 (B_{ROOF}(t4)), where it defined the difference between flame spread and no flame spread outside the domain of the ignition source. If the flame front detached from the ignition source, it propagated below all of the PV module, which corresponded with results from published large scale experiments and genuine PV-related fires.

To quantify the severity of fires in a semi-enclosure, experiments were conducted with half a square meter of roofing membrane below a PV module, which caused a peak heat release rate of 90 kW and a maximum heat flux of more than 20 kW/m^2 at a distance of 15 cm from the flame front. Similar to previous large-scale experiments, the fire did not propagate outside the semi-enclosure.

Tree feasible mitigation solutions were discussed: i) increase of gap height, ii) increase of distance between PV arrays, and iii) protection against downward flame spread. For experimental examination of the final case, the use of both 60 mm polyisocyanurate (PIR) insulation or 50 mm mineral wool insulation provided sufficient protection of a subjacent layer of flame retarded expanded polystyrene (EPS), as the EPS was not ignited, although sections melted in the majority of the experiments.

Altogether the thesis provides a new perspective on the fire-related risk associated with the novel introduction of the PV technology into the built environment. It provides an increased understanding of flame spread in semi-enclosures and evaluates potential mitigation solutions. Besides the direct outcome of the thesis, it will form a basis for further exploration of the topic.

Lay Summary

The global capacity of solar photovoltaic (PV) systems has increased exponential over the last decade and represents a technology where energy emitted from the sun can be transformed into electricity. The technology is ideal for utilising elevated roof constructions, especially commercial flat roofs on warehouses and production facilities.

However, PV systems in the built environment have been linked to fires. Partly because the technology increase the probability of ignition and partly because building applied PV (BAPV) systems can facilitate flame spread along the roof.

The thesis focus on BAPV systems on sizeable flat roof constructions, identical to the type of installation seen on many warehouses such as IKEA or Walmart. BAPV systems are, as the name implies, a method where PV systems are installed on existing roof constructions. Hence, a semi-enclosure is formed between the roof construction and the PV modules, where the geometry of the semi-enclosure depends on the inclination of the modules and the gap height defined as the vertical distance between the roof and the lowest edge of the PV module.

Initially, a global annual frequency of 28.9 fires per gigawatt installed capacity was estimated based on all publicly available data sets. 51% of the fires were caused by identified components of the PV system, whereas the remaining 49% were caused by unidentified components or external ignition sources, and thus it could be concluded that a fire related to the PV system is not necessarily caused by the system. Consequently, in the remaining part of the thesis, three experimental campaigns were conducted to study how the material and geometric parameters affect flame spread within the semi-enclosure.

The geometric and material complexity of the semi-enclosure were increased gradually through the experiments, after which it became possible to determine how crucial the individual parameters were for the consequences of an initial fire.

Through simple flame spread studies with the reference material polymethyl methacrylate (PMMA) below a horizontal surface, the existence of a critical gap height was identified. From the experiments, it was seen that a gap height reduction of a few centimetres made the difference between a slow and constant flame spread rate and an enhancing flame spread rate which transitioned into a rapidly accelerating flame front.

The gap height remained a crucial parameter when the PMMA was replaced with a roof construction mock-up compliant with regulations in Europe (EN 13501-5 (B_{ROOF}(t4))), as a gap height reduction of 1 cm defined the difference between *no flame spread* and *flame spread*. The critical gap height increased when the PV module was inclined, as a larger amount of

heat was transferred from the flame towards the upper layer of the roof construction mock-up consisting of a polyvinyl chloride (PVC) roofing membrane with flame retardants. In addition, it was concluded that the polymer backsheet membrane of the PV modules had little to no effect on whether the fire propagated or not.

Based on those findings, it was concluded that the geometry of the semi-enclosure generated by the introduction of the BAPV system as a physical object could change the behaviour of a roof construction, which was initially designed to prevent flame spread. As such, introducing a BAPV system can lead to a breach of basic fire safety engineering principles, namely the concept of no flame spread along with the building envelope, which is established to prevent flame spread from one fire compartment to another.

In addition to the horizontal flame spread studies, two types of insulation materials were examined to prevent downward flame spread within the roof, which is a worst-case scenario that could lead to burn down of the property. The two types of insulation, 50 mm of mineral wool or 60 mm of polyisocyanurate (PIR) insulation, were installed on top of an existing roof construction insulated with expanded polystyrene (EPS) below a roofing membrane. No matter the upper layer of insulation, parts of the EPS melted but were never ignited. Thus both products were able to prevent downward flame spread.

To summarise, the findings in the thesis conclude that the current test methods and regulations in most European countries do not consider the consequences of the semi-enclosure generated when a BAPV system is introduced to a flat roof. Thus, it can be concluded that the current test methods are inadequate if the previous level of fire safety is anticipated.

Acknowledgements

What a journey it has been. A journey which I have only been able to complete thanks to an incredible support from everyone around me. A journey I could continue thanks to the hospitality of my alma mater. And a journey I could not have finished without the selfless decisions made by people I will never meet but always take with me. I try to appreciate those privileges every day.

First of all, thanks to Grunde Jomaas, my supervisor, my mentor, and after many years also a person I consider a good friend. Our conversations have been endless without delimitation. Still, you managed to make me a better engineer, and I am sure our relationship will continue prospectively. Thanks for your constant support, trust in my abilities, and harsh but constructive criticism!

Without the economic support from the three project sponsors, I had never received the chance of being able to continue the work I initiated during my master thesis at the Technical University of Denmark. In addition, your support allowed me to take care of my health when needed. Thanks to Tom Pedersen, my contact person from Ingka Services AB (formerly IKEA Services AB). Thanks to Roy Weghorst from Kingspan Holdings (Irl) Limited. Thanks to the full team from ROCKWOOL International A/S, especially my current contact person Susanne Dyrbøl and former contact person Fanny Guay.

When I was a BSc student, I swore that I would never be a PhD student. Never. As an MSc student, I spend countless hours in the fire laboratory at the Technical University of Denmark. Senior MSc students such as Ulises Rojas-Alva and Andrea Lucherni became my lab buddies, and the PhD students Rolff Leisted and Laurens van Gelderen showed me that curiosity and passion were crucial parts of their job. Thanks to all of you for inspiring me!

Being a PhD student at the University of Edinburgh was never on my radar. It was out of my league. An exchange to Ghent University and cooperation with Bart Merci on my first scientific paper made me change my mind. I was indeed a student, and I had a lot to learn, but I felt accepted and I felt that I was part of the community. Thanks for including me, and thanks for the recommendation.

My time in Edinburgh was fantastic, but too short! During my 15 months in the Scottish capital, I met like-minded people from all over the world. The inspiring, smart and passionated PhD students in the John Muir building turned out to be relatively normal human beings who rarely said no to a pint at the pub. Thanks to all of you for a good and memorable time. A special

thanks to Mohamed Beshir, Zak Campbell-Lochrie, Carlos *"Does it matter?"* Walker-Ravena, Simón Santamaria, Martina Manes, Cia-Lung (Farian) Wu, Georgios Kanellopoulos, Vasileios Koutsomarkos, Chris Bateman, Tim Aspinall, Norlizan Wahid, Xu Dai, Ian Pope (University of Queensland), and Ulises Rojas-Alva (again!) for the company, friendship and great discussions.

Besides my supervisor, the academics in Edinburgh were busy people. To be honest, I wish I had more conversations with them as I felt challenged and inspired the few times I had the opportunity. Thanks to Rory Hadden for being my secondary supervisor and Angus Law, Stephen Welch, and Ricky Carvel for questioning me during my annual reviews. Especially the first annual review with Angus was harsh. His criticism was spot on, but it took me months to appreciate. In hindsight, it formed the basis of what became the experimental cornerstone of the thesis.

When I left Edinburgh for health reasons, the Department of Civil Engineering (now: DTU Construct) at the Technical University of Denmark (DTU) demonstrated a level of hospitality that I will never forget! I was treated like a local PhD student. I had their privileges, but not the burdens of being a Danish PhD student. Everyone accepted my status as a *"permanent exchange student"*, and no one ever questioned why I used most of my time in Denmark. Thanks to Niels-Jørgen Aagaard and Jan Karlshøj for your roles as my local Head of Department and Head of Section. Thanks for your hospitality and for including me as "one of your own". A special thanks to everyone from the Section for Design and Processes, to Line Leth Christiansen and Annette Frøhling for their willingness to answer all of my administrative questions, to the technicians for their patience and assistance, and to Troels Kristensen for his compassion and shoulder to cry on when I realised, that I could not finish the PhD project without a solid interruption and a heart transplant.

I felt that the University of Edinburgh skipped its usual level of bureaucracy when I got sick. I appreciate that and I will always appreciate the work that my supervisor Grunde Jomaas did to lift every university-related burden from my shoulders during my sick leave.

Thanks to the fantastic team at the National Hospital of Denmark (Rigshospitalet) ward 2153.

Thanks to my parents, Henriette and Philip, and to my sister, Kristine, for taking care of me when I was sick and for your endless support when I struggled with the project. Without you, I would never have made it!

Finally, I would like to express my gratitude to the two donors and their families. Within days of each other, I received the ultimate gift from both of you, and regardless of the circumstances, I appreciate them just the same. I keep you in my mind, and I will do my best to honour you.

Tak for alt!

Declaration

The dissertation is the result of my own work and includes nothing, which is the outcome of work done in collaboration except where specifically indicated in the text. Unless stated differently, no part of the dissertation has been previously submitted to any university or institution for any degree, diploma, or qualification. The project was sponsored by Ingka Services AB (formerly IKEA Services AB), Kingspan ltd., and ROCKWOOL A/S. The three stakeholders did not have any influence on any part of the scientific work, design of experimental setups, analysis of data, publication of results, or the final dissertation.

Signature: _____

Jens Steemann Kristensen

Publications and works related to the thesis

Four journal papers were published during the PhD project, and I also collaborated with three MSc and MEng students for their thesis research. These works are listed as the seven first entries in the reference list. The experimental work of the paper *Experimental Study of the Fire Behaviour on Flat Roof Constructions with Multiple Photovoltaic (PV) Panels* [1], was conducted as part of my MSc thesis project at the Technical University of Denmark (DTU) [2]. The paper was written during the initial part of the PhD project but is not considered part of the PhD, and thus the paper is solely used as a reference.

The frequency analysis presented in Chapter 2 is based on the paper *Fault tree analysis of fires on rooftops with photovoltaic systems* [3] written in co-operation with mainly Nur Aliah Fatin Mohd Nizam Ong from Putra University in Malaysia. As the Malaysian team wrote the initial manuscript, it was accepted that Mohd Nizam Ong became the first author. However, significant contributions, including changed calculation methods, change of manuscript focus, and equal written contributions to the final version of the paper, justify the inclusion of the paper within the project. My contribution was acknowledged by making me last author of the paper.

The three MSc and MEng thesis students from the International Master of Science in Fire Safety Engineering (IMFSE) and the University of Edinburgh (UoE) worked on initial versions of the three experimental set-ups: set-up A, set-up B, and set-up C. I supervised the laboratory work and subsequent analysis conducted by the students on a day-to-day basis.

The thesis projects of Farah Binte Mohd Faudzi (IMFSE) [4] and Benjamin Jacobs (UoE) [5] was based on data from the initial versions of respectively set-up A and set-up B. Their data was analysed and used to optimise the two experimental set-ups, and subsequently, new experimental series were conducted for the PhD project and resulted in two papers co-authored with the thesis students and my PhD supervisor, Grunde Jomaas.

The paper *Experimental study of flame spread underneath photovoltaic (PV) modules* [6] is based on the experimental set-up A described in Section 3.4 and the results presented in Section 4.3.

The paper *Experimental Study of the Fire Dynamics in a Semi-enclosure Formed by Photovoltaic (PV) Installations on Flat Roof Constructions* [7] is based on the experimental set-up B described in Section 3.5 and the results presented in Section 4.4.

Finally, the experimental set-up C presented in Section 3.5 as well as the results in Section 4.4 is based on the experiments conducted together with IMFSE thesis student Mingcian Hong who used the same raw data for his MSc thesis [8]. I have carried out further analysis and placed the work in the context of the other results presented herein.

Contents

Abstract v

Lay Summary vii

Acknowledgements ix

Declaration xi

Publications and works related to the thesis xiii

Figures and Tables xix

1 Introduction 1

1.1 Background . . . 1
1.1.1 The photovoltaic technology . . . 2
1.1.2 Application methods . . . 3
1.2 Building applied photovoltaic installations . . . 5
1.3 Fires related to the photovoltaic system . . . 6
1.4 Previous work on PV fire risk . . . 8
1.4.1 Standards . . . 8
1.4.2 Current research . . . 16
1.5 Flame spread . . . 24
1.5.1 Thermal thickness and heat transfer model . . . 24
1.5.2 Material factors . . . 27
1.5.3 Geometric parameters . . . 28
1.5.4 Environmental factors . . . 29
1.5.5 Reference materials . . . 30
1.6 Flame spread below the BAPV module . . . 31
1.6.1 Horizontal cavity or semi-enclosure? . . . 31
1.6.2 Flame spread between two vertical surfaces . . . 31
1.6.3 Flame spread between two horizontal surfaces . . . 32
1.7 Problem identification . . . 35
1.7.1 Frequency and cause of ignition . . . 35
1.7.2 Influence of BAPV module . . . 35
1.8 Thesis aim . . . 38
1.9 Objectives . . . 38

2 Frequency and fault analysis **41**
2.1 Analysis methods . . . 41
2.2 Frequency of PV-related fires . . . 42
2.2.1 Available data and method . . . 42
2.2.2 Results . . . 44
2.3 Fault tree analysis . . . 47
2.3.1 Available data and method . . . 47
2.3.2 Results . . . 51
2.4 Uncertainties . . . 52
2.5 Preliminary conclusion based on frequency analysis . . . 52

3 Experimental designs and methods **55**
3.1 Chapter overview and organization . . . 55
3.1.1 Set-up A: Flame spread on PMMA in horizontal semi-enclosures . . . 55
3.1.2 Set-up B: Flame spread on roof construction mock-up in semi-enclosure 57
3.1.3 Set-up C: Medium-scale experiments with adjacent roof . . . 57
3.2 Panels . . . 58
3.2.1 Black-body stainless-steel board . . . 58
3.2.2 Photovoltaic modules . . . 60
3.3 Panel Rig . . . 61
3.3.1 Location of camera . . . 62
3.3.2 Adjustment and definition of gap height . . . 62
3.4 Set-up A: Flame spread on PMMA in horizontal semi-enclosures . . . 64
3.4.1 Design concept . . . 64
3.4.2 The aluminium support . . . 65
3.4.3 Instrumentation . . . 65
3.4.4 Polymethyl methacrylate (PMMA) samples . . . 67
3.4.5 Experimental matrix . . . 67
3.4.6 Ignition of the PMMA . . . 68
3.5 Set-up B: Flame spread on roof construction mock-up in semi-enclosure . . . 69
3.5.1 Design concept . . . 69
3.5.2 Ignition source . . . 70
3.5.3 The aluminium support and instrumentation . . . 72
3.5.4 Roof constructions and materials . . . 73
3.5.5 Experimental matrix . . . 76
3.6 Set-up C: Medium-scale experiments with adjacent roof . . . 77
3.6.1 Design concept . . . 78
3.6.2 Location of the PV module . . . 79
3.6.3 Source of ignition . . . 79

3.6.4 Maximum size and type of roofing membrane . . . 81
3.6.5 Instrumentation . . . 82
3.6.6 Experimental matrix . . . 82

4 Results and analysis 85
4.1 Chapter overview and organization . . . 85
4.2 Recording and analysis of one-dimensional flame spread . . . 86
4.2.1 Location of the camera and video output . . . 87
4.2.2 Transformation from video frames to binary matrix . . . 89
4.2.3 Analysis of binary matrix . . . 90
4.3 Set-up A: Flame spread on PMMA in horizontal semi-enclosures . . . 95
4.3.1 Baseline experiments . . . 95
4.3.2 Flame spread below horizontal panels . . . 105
4.3.3 Conclusion based on experimental campaign . . . 113
4.4 Set-up B: Flame spread on roof construction mock-up in semi-enclosure . . . 115
4.4.1 Visual observations . . . 115
4.4.2 Flame spread length (FSL) . . . 117
4.4.3 Flame spread rate (FSR) . . . 121
4.4.4 Exposure . . . 125
4.4.5 Maximum temperature in insulation materials . . . 129
4.4.6 Conclusion based on experimental campaign . . . 133
4.5 Set-up C: Medium-scale experiments with adjacent roof . . . 136
4.5.1 Visual observations . . . 136
4.5.2 Heat release rate below PV modules . . . 138
4.5.3 Heat flux outside semi-enclosure . . . 143
4.5.4 Heat flux inside semi-enclosure . . . 144
4.5.5 Conclusion based on experimental campaign . . . 146

5 Flame spread between two surfaces 149
5.1 Orientation of the fuel . . . 149
5.2 Influence of horizontal barrier . . . 150
5.2.1 Gap height to horizontal surface . . . 150
5.2.2 Geometry of horizontal barrier . . . 151
5.2.3 Inclination of barrier above horizontal surface . . . 151
5.3 Influence of fuel properties . . . 152
5.3.1 Material parameters of fuel . . . 152
5.3.2 Fuel geometry . . . 152
5.4 Flame spread between surfaces with non-horizontal orientation . . . 152

6 Conclusion 155

6.1 Frequency analysis . . . 155
6.2 Experimental work . . . 156
6.3 Recommendations and further work . . . 158
6.3.1 Quantification of frequency . . . 158
6.3.2 Acceptance of building applied PV systems as part of the building . . . 159
6.3.3 Development of standard test method for roofing products . . . 159
6.3.4 Compartmentalisation of roof . . . 160
6.3.5 Repetition and improvement of experiments . . . 160
6.3.6 Computational Fluid Dynamics modelling . . . 161

Bibliography **163**

A Additional figures of experimental set-up **181**
A.1 Laboratory jacks . . . 181
A.2 Set-up A - additional figures . . . 181
A.3 Time dependent raw data for Figure 4.10 . . . 183

B Material data sheets **185**
B.1 Calcium silicate board . . . 186
B.2 PIR insulation . . . 188
B.3 Mineral wool . . . 191
B.4 Polymethyl methacrylate (PMMA) . . . 197
B.5 Roofing membrane . . . 200
B.5.1 Critical heat flux for both membranes . . . 200
B.5.2 Heat of combustion . . . 201
B.6 Black paint . . . 208

Figures and Tables

Figures

1.1 Development of the PV market share. 3
1.2 Application methods of the photovoltaic technology. 4
1.3 Simplified schematic overview of typical PV-system. 6
1.4 Video frame from drone video of the PV-related fire. 7
1.5 Sketch of roof construction and PV module. 13
1.6 Conceptual sketch of the experimental set-up. 21
1.7 Model by Tang et al. compared to data from Ju et al. and Kristensen et al. 22
1.8 Measured heat flux and calculated view factor below module with an inclination of 10°. 23
1.9 Thermal model for surface flame spread. (from: *Fundamentals of Fire phenomena, Chapter 8, J. Quintiere [9]*) 26
1.10 Upward flame spread on thermally thick PMMA 28
1.11 East-west orientated BAPV system on flat roof construction. From: [10]. 31
1.12 Simple heat transfer models of flame spread on thin fuel and the effect of a horizontal barrier above thermally thin fuel. 33
1.13 Continuation of figure 1.12. Reduction of the vertical distance H_2 and thus deflection of the flame below the horizontal barrier. (from: Kristensen, Faudzi and Jomaas [6]) 34
1.14 Sketched ignition process of roof construction. 36
1.15 Sketched ignition process of roof construction below BAPV module. 37

2.1 Annual PV-related fires per GW installed capacity. 44
2.2 Qualitative fault tree diagram with a PV-related fire as the top event. 49

3.1 Paint damages at the stainless-steel board. 59
3.2 Soot buildup below the stainless-steel board. 60
3.3 The panel rig, the test wagon, and the lower surface from set-up A. 62
3.4 Top view of the experimental set-up A. 65
3.5 Image from an experiment in progress. 66
3.6 Flame front after ignition of a PMMA sample with a sample width of 400 mm. . . 68
3.7 Sketch of the roof construction mock-up. 70
3.8 Top view of the mock-up roof construction before ignition of the wood crib. 71
3.9 Side view of the roof mock-up during preparation. 73
3.10 Visual overview of the medium-scale experimental set-up. 80
3.11 Bauder roofing membrane installed on the calcium silicate board. 82

4.1 Flame spread along the roof construction mock-up. 87
4.2 Similar experiments with different camera locations and exposure settings. 88
4.3 Video frame from experiment B25. 89
4.4 Relevant steps of the video processing in MATLAB for experiment B25. 91
4.5 Example of the manual selection process. 93
4.6 Example of an idealised binary plot based on the non-smoothed data points defining the flame front and the burnout edge. 94
4.7 Set-up A: Baseline experiment with flame spread on PMMA with a width of 30 cm and no panel. 95
4.8 Flame front location as a function of time for the baseline experiments conducted without any horizontal barrier. 96
4.9 Moss loss rate for the baseline experiments normalised for the three sample widths as a function of flame front location. 98
4.10 Measured heat flux and temperature plotted as a function of distance to the approaching flame front for baseline experiment. 99
4.11 Set-up A: Flame spread on PMMA with a width of 30 cm and a gap distance of 15 cm between the stainless-steel board and the PMMA surface. 106
4.12 Location of the flame front plotted against time for flame spread on PMMA samples in horizontal semi-enclosures with gap heights between 22 cm and 15 cm. 107
4.13 Relative flame spread rate compared to the average flame spread rate for the baseline experiments. 109
4.14 Experiment conducted with PV module, sample width of 30 cm, and a gap height of 17 cm. 110
4.15 Normalised mass loss rate (MLR) as a function of gap height. 111
4.16 Heat flux near the location of the heat flux gauge. 111
4.17 Top view of flame spread on roofing membrane from left to right with a gap height of 12 cm between the roofing membrane and a horizontal panel. 116
4.18 Flame spread on roof construction mock-up with mineral wool below the roofing membrane, a gap height of 8 cm, and an inclination of 10°. 117
4.19 The backside of the PV module and top view of the roof construction mock-up. . 118
4.20 Flame spread length as a function of gap height, panel type, and insulation material. 119
4.21 Flame front location as a function of time for experiments with horizontal and inclined PV modules. 122
4.22 Flame spread rate as a function of gap height, panel type, or insulation material. 123
4.23 Post experiment Sectional view along the centre-line for an experiment conducted with PIR insulation. 125
4.24 Location of the flame front, burn out zone, and width of pyrolysis zone as a function of time. 127
4.25 Exposure plotted against gap height, panel type, or insulation material. 128

4.26 Maximum temperature below the horizontal panels plotted against Exposure, depth, panel type, and insulation material. 130
4.27 A sectional view of the mineral wool after an experiment conducted with a gap height of 11 cm to a horizontal PV module. 131
4.28 Side view of an experiment conducted with mineral wool and a gap height of 10 cm to a horizontal PV module. 132
4.29 Maximum temperature below the inclined PV modules plotted against Exposure, depth, inclination, PV module, insulation material. 133
4.30 Flame spread in semi-enclosure between a sheet of roofing membrane with a side length of 70 cm and a new PV module. 137
4.31 Smouldering wood crib and location of flame spread on roofing membrane with a side length of 45 cm. 138
4.32 Heat release rate as a function of time, PV module condition, and extraction flow. 139
4.33 Area affected by flame spread and corresponding peak heat release rate for experiments conducted with a roofing membrane side length of 45 cm. 140
4.34 Heat release rate as a function of time, PV module condition, displacement of the wood crib from the lower edge of the PV module, and extraction flow. 142
4.35 Heat fluxes measured outside the semi-enclosure with a distance of 16 cm to the PV module for experiments with a squared roofing membrane side length of 45 cm. 144
4.36 Heat fluxes measured outside the semi-enclosure with a distance of 16 cm to the PV module for experiments with a squared roofing membrane side length of 70 cm. 145
4.37 Filtered heat fluxes measured inside the semi-enclosure. 146

A.1 Side and top view of laboratory jack. 181
A.2 Detailed images of the aluminium support and installation of the heat flux gauge. 182
A.3 Installation process of thermocouples and quartz disc used for protection of heat flux gauge. 183
A.4 Raw data from experiment A8. The data is the basis for the flame front dependent plot of PMMA temperature and heat flux in figure 4.10. 183

B.1 Time to piloted ignition as a function of heat flux measured in the cone calorimeter. 200

Tables

1.1 Events and component failures causing ignition which can result in fires related to the photovoltaic system. . . . 17
1.2 Factors affecting flame spread over solid fuels. . . . 25

2.1 Overview of data-sets on PV-related fires. . . . 43
2.2 Input data and calculation of the overall number of PV-related fires per gigawatt (GW) capacity. . . . 46
2.3 Overview of event types. . . . 48
2.4 Qualitative Fault Tree Diagram for PV-related fires. . . . 50
2.5 Annual frequency of PV-related fires caused by the seven major events. . . . 50

3.1 Overview of variables and data collected for the three experimental set-ups. . . . 56
3.2 Overview of PV module brands used for the three experimental campaigns. . . . 60
3.3 Experimental matrix of experiments conducted with different sample widths and gap heights. . . . 67
3.4 Overview of the layers in the roof mock-up. . . . 73
3.5 Thermal properties of the mineral wool (MW), PIR insulation (PIR), expanded polystyrene (EPS), and calcium silicate board (CSB). . . . 75
3.6 Experimental matrix for the experiments conducted with the roof construction mock-up. . . . 77
3.7 Parameters of the two used PVC-based roofing membranes. . . . 81
3.8 Experimental matrix of the 12 medium-scale experiments. . . . 83

4.1 Data types extracted from the three experimental set-ups. . . . 85
4.2 Average flame spread rate in mm/s for the baseline experiments. . . . 97
4.3 Calculated cumulative net radiative heat transfer towards the PMMA. . . . 102
4.4 The energy necessary to obtain the average flame spread rates. . . . 104

B.1 Heat of combustion for the Bauder Thermofol U15 FR roofing membrane 201

.

Chapter 1

Introduction

> *We know what must be done. Keeping the 1.5 ℃ goal within reach means reducing emissions globally by 45 per cent by 2030.*
>
> António Guterres, *COP26*, 2021 [11]

1.1 Background

Another year, another United Nations (UN) Climate Conference and a concerning speech from the UN Secretary-General António Guterres, where it was stated that even if the National Determined Contributions are fully implemented, emissions will still increase by 2030, and the World will remain on a catastrophic temperature rise track well above 2℃ [11]. Neither the impact nor the Global political negotiations are the topic of the PhD dissertation, nor is it the reason for the climate change. But the potential consequences of climate change are a driver for the development and implementation of new technologies with the purpose of ensuring the well being of the global population.

With a global population growth projected to exceed 9 billion by 2050, the pressures on natural resources, energy supply and food are expected to increase, and the global Gross domestic product (GDP) will probably quadruple compared to the level of 2012 [12]. Without any actions, the Organisation for Economic Co-operation and Development (OECD) expected that such a growth of the global economy would entail an 80% increase in energy demand, with an energy mix similar to 2012 [12]. That will lead to a 50% rise of global greenhouse gas emissions and, consequently, a projection of a 3℃ to 6℃ temperature increase compared to pre-industrial levels [12]. The effects of the climate changes are vast and already present, with rising sea levels and more extreme weather phenomena as the most frequently mentioned consequences. In the 2019 European Green Deal by the European Commission, it was stated that *"A power sector must be developed that is based largely on renewable sources, complemented by the rapid phasing out of coal and decarbonising gas"* [13]. Wind-, hydro-, and photovoltaic power production are three primary renewable energy sources [14] of which both modern

wind turbines and hydroelectric power production require significant infrastructure, whereas the photovoltaic technology can be applied on every scale. The potential of renewable energy is highlighted by IKEA (Ingka Group), who, in 2022, had 935.000 PV modules installed on their warehouses which, in combination with ten solar parks and 547 wind turbines, had an annual production equivalent to the electricity consumption of more than one million European households [15].

As a consequence of the political sanctions against Russia due to their invasion of Ukraine, the European Union launched the REPowerEU plan in May 2022. The program aims to enable rapid acceleration of PV systems in the built environment by doubling the current capacity of 320 GW before 2025 and almost 600 GW by 2030 [16]. The European Commission plan to accelerate the implementation by limiting the length of the permission process for PV installation to three months, adopting provisions to ensure that all new buildings are "solar ready", and making rooftop solar energy compulsory for all new public and commercial buildings by 2025, and all existing public and commercial buildings by 2027 if the roof have a useful floor area above 250 m^2. In addition, solar PV should be installed on all new residential buildings by 2029 [16].

1.1.1 The photovoltaic technology

Historical

From a historical point of view, the photovoltaic (PV) effect, discovered by Becquerel in 1839 [17], is a way to generate electric energy from the radiative energy of the sun. Despite the early discovery of the technology, it did not leave the laboratories before 1958 [18], where six PV cells powered the transmitter of the Vanguard 1 satellite until 1964 [19]. The oil crisis in the seventies caused public and governmental interest in an alternative to fossil fuels, including PV technology. However, it was deemed that system price needed to be reduced by three magnitudes before the technology was comparable with fossil fuels [18] and remained a niche product.
Facilitated by significant cost reductions, the global cumulative capacity increased significantly from the early 2010s (figure 1.1a) and repeatedly exceeded the most optimistic projections by the International Energy Agency (IEA) [17, 20]. As of 2019, Haegel et al. stated “that we are entering an era in which PV already is or will soon become cost-competitive with conventional electricity generation in many parts of the world” [21].

The magnitude of the increased PV capacity is evident when compared to alternative renewable energy sources such as hydro and wind power. Where the combined capacity of renewable energy increased with a factor of 2.81 between 2005 and 2019, the renewable energy provided by PV systems went from non-existing to 23% [24]. In fact, the impact of capacities of energy produced by PV systems and wind turbines is so intense that contribution from hydropower has reduced from more than 80% to less than 50% in 14 years, as seen in figure 1.1b, despite

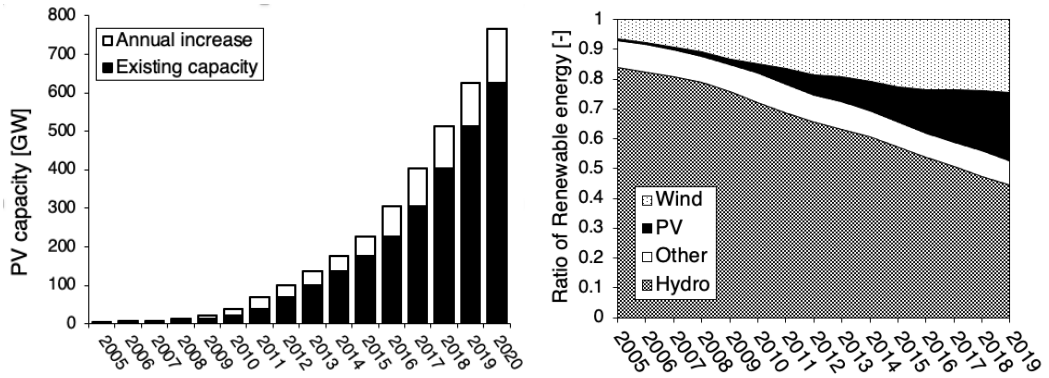

(a) Cumulative power capacity by photovoltaic installations. Based on data from [22, 23]

(b) Production ratio between renewable energy sources. Based on data from [24]

Figure 1.1: Development of the PV market share.

a 67% increase. The swift growth of the technology emphasises the advantage of harvesting energy from the sun. Due to the flexibility of the technology, power can be harvested whenever the sun is present. As an example, off-grid PV systems are, sometimes in combination with generators, used to ensure healthcare facilities in rural areas [25].

1.1.2 Application methods

The flexibility of the PV technology entails that the application methods are extensive. The size of the systems can vary from a single cell on a power bank (figure 1.2a) to terrestrial installations with a capacity of several hundred megawatts (MW), such as the Longyangxia Dam Solar Park (850 MW) [29] in China, or the Kamuthi solar power plant in India (648 MW) [30] (figure 1.2b). However, a land area equivalent to 0.3% of the world is required if PV systems alone should cover the global electricity demand [31]. Thus, implementation of the photovoltaic technology into the built environment is a way to transform passive areas of a property into an active part of the building, generating electricity which has the potential to cover more than 25% of the energy demand in the United States and Europe [31].

Photovoltaic systems implemented in the built environment can be installed in all sizes, from domestic household installations of a few kilowatts (kW) to commercial installations with a production capacity measured in megawatts (MW). Within PV systems in the built environment, there is a clear distinction between building integrated PV (BIPV) and building applied PV (BAPV) systems. As the name implies, the power generating components of a BIPV system is integrated into the building as it should be replaced with a construction component (PV module) with a similar function if removed [32]. BIPV systems can be integrated into all parts of a building façade, such as the windows, balustrades, roofs, or the façade, as seen on Copenhagen International School in Figure 1.2c where each of the small squares is a PV module [33].

(a) PV cell implemented in power-bank.

(b) Terrestrial PV installation in India. (From: [26])

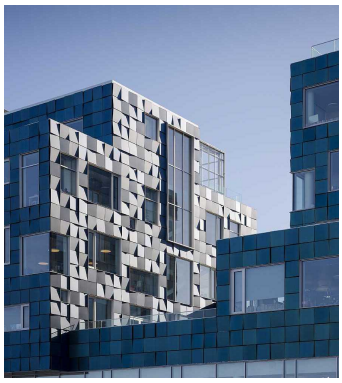

(c) PV integrated in façade. (from: [27])

(d) Building applied PV system on top of IKEA warehouse in Zwolle (NL). (from: [28])

Figure 1.2: Application methods of the photovoltaic technology.

Where some BIPV systems, such as the one installed at the Copenhagen International School, are almost invisible to the surroundings, the presence of a BAPV system can be more evident as it is applied to the roof of an existing construction, such as the IKEA warehouse in Figure 1.2d. Contrary to the BIPV systems, the BAPV systems are not part of the construction but an "add-on" feature that can be removed without any significant consequences for the integrity of the host construction. The potential of utilising the otherwise unexploited roof constructions is supported by the vast amount of BAPV systems installed by companies such as Apple, Amazon and Walmart, whose combined PV capacity accounted for 1.5% of the total capacity in the US [34, 35], and more than the 2019 capacity installed in countries like Portugal or Sweden [23].

The infrastructures of PV systems in the built environment are basically similar for BIPV and BAPV systems, but since the electricity-generating components of BIPV systems are integrated into construction components, the complexity of such systems might be higher and even include custom made façade elements as seen on the Copenhagen International School [33]. From a complexity point of view, BAPV systems are simpler as they are assembled by prefabricated components and because the status as an add-on technology allows installation on existing buildings and thus utilisation of existing roof constructions.

1.2 Building applied photovoltaic installations

In general, implementing a BAPV system consists of three steps, namely the design of the PV system, the installation of the PV system, and finally, the maintenance during the nominal minimum service life of 25 to 35 years [31].

The overall concept of a BAPV system is independent of the system size, and as such, the sketch in Figure 1.3 is representative of all set-ups. The PV modules are the key components in all set-ups as they convert the energy from the sun into direct current electricity. As of 2020, 96.4% of the manufactured PV modules were based on the mono- or poly-crystalline silicon (Si) technology [36]. The modules are fastened to the roof with a mounting system that ensures orientation towards the south (northern hemisphere), north (southern hemisphere) or east/west, depending on the latitude and consumption pattern. Individual modules are connected into a string series to increase the voltage and subsequently in parallel via a combiner box to increase the current and thus the power. The type of PV module determines the number of PV modules in the string, and islands of parallel strings are designated a PV array. From the combiner boxes, the electric power is transferred to a central inverter (also named transformer) where the direct current (DC) is transformed to alternating current (AC) [37]. From the AC side of the inverter, the produced electricity can be consumed directly, transferred to the grid, or stored for later use in battery storage systems.

Isolators are located on both sides of the inverter and are also known as AC- or DC-switches depending on the location. The isolators are used to shut down parts or all of the PV system to facilitate maintenance. However, the PV modules cannot be switched off as the photovoltaic process continues as long as the sun shines, and as a consequence, the switches do not necessarily cut off the current if short circuits occur as an electric arc represents a resistor in a closed simple electric circuit where parallel- or series-connected PV modules forms the energy source.

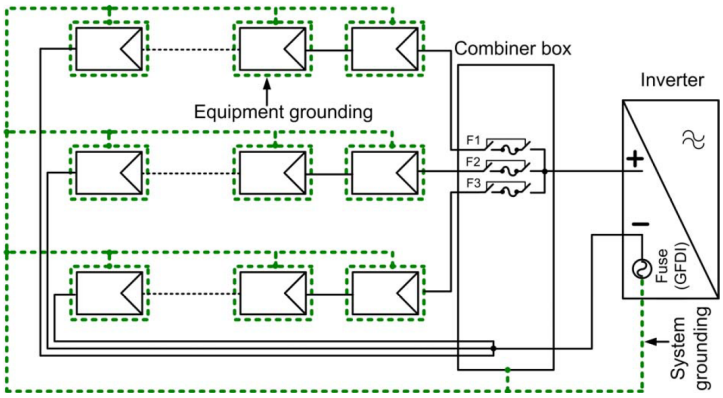

Figure 1.3: Simplified schematic overview of typical PV-system with PV modules, cables, combiner boxes, inverters, and switches (isolators). (From Alam et al. [38])

1.3 Fires related to the photovoltaic system

With electrical components being a generally accepted source of ignition [39, 40], the introduction of a large direct current (DC) system causes a higher risk than the alternating current (AC) power supplied to household plugs. An electric arc formed by a malfunction in a DC system is continuous compared to an AC arc that has to reform with the frequency of the current alternation [39].

With the exponential growth of electricity produced by PV systems, fires caused by, or related to, BIPV or BAPV systems have gained some attention, mainly from the local or national media. However, the magnitude of the issue is currently in a state where only a few national fire and rescue services have some sort of databases of fires related to or caused by the system, and in addition, some data sets based on media reports have been generated.

In Germany, an analysis of internet and media reports, operational reports from fire departments, an internet-based survey, as well as reports from assessors and a single insurance company revealed a total of 430 PV-related fires by January 2013 from where 210 of the fires were caused by the PV system itself [41, 42]. In Italy, PV-related fires were monitored by local authorities, and between 2011 and 2014, the combined number of fires varied between 1800 to 2200 depending on the source [43, 44]. By 2020 PV modules were installed on almost one in four houses in Australia, and the number of PV-related fires five-folded between 2016 and 2021 in the state of New South Wales [45]. In the United States, PV-related fires are classified as "other" according to the National Fire Data Center [46], but limited data based on the PV-system being a suppression factor was published by Meacham and McNamee in 2020 [47]. Finally, a small data set exist for the Netherlands, where 29 PV-related fires occurred in both 2018 and 2019, followed by 39 fires in 2020 [48]

Changing focus from national data to cases described in the media, the e-commerce company Amazon experienced PV-related fires in 2018 [49], 2020 [50], and 2021 [51] with the latter having an estimated cost of $500,000. In 2015, the PV system sparked a fire at an Apple data centre and caused roof collapse [52]. PV-related fires occurred at IKEA warehouses in 2018 [53] and 2020 [54], and as of November 2018, Walmart had experienced seven of their 240 BAPV systems installed by SolarCity catching fire. As a result, Walmart launched a lawsuit against Tesla, which acquired SolarCity in 2016 [55, 56]. Walmart estimated that the fires had cost the $8.2 million [57] and two companies agreed on a settlement in November 2019 [58]. In reports based on a survey of 29 installations, Tesla found 157 "action items" from which 48 reflected conditions that rendered the sites unsafe or potentially unsafe, including improper wiring and broken PV modules [56].

Figure 1.4: Video frame from drone video of the PV-related fire on the museum *We The Curious* in Bristol 2022. (Video: Avon and Somerset Police, from: [59])

Among recent fires is the PV-related fire in Figure 1.4 which occurred on the museum *We The Curious* in Bristol (UK) [59], and the fire on the roof of a print shop in Boston where the damages were estimated at $2 million to $4 million [60]. Severe economic consequences of PV-related fires can also occur without the system being the source of ignition, as seen from the 2017 ASKO fire in Norway. The fire, which initially started in a forklift inside the cold storage facility and caused damages of $23 million, broke through the roof and propagated from one fire compartment to another below the PV modules [61].

Naturally, not all PV-related fires reach the front page of the local newspaper, and not all legal quarrels between a PV contractor and a property owner gain the same level of attention as the dispute between Tesla and Walmart.
Most PV-related fires do probably not reach the media, and thus the overall consequences are largely unknown. The five data sets from Australia, Italy, the Netherlands, the UK, and the

US only quantify the number of fires but neither the cause nor consequence. An exception is the German data set in the report by Sepanski et al., where building damages or complete burndown occurred in respectively 67, and 12 of the 210 fires caused by the PV system [41, 42]. However, it is deemed that the high ratio of severe consequences was caused by the fact that the data was in-homogeneous and partly based on media reports, an internet survey, and data from a single insurance company which might have caused an increased focus on larger fires.

As such, it can be concluded that fires related to PV systems in the built environment occur, but limited data exist on the frequency and consequences of the fires. Based on the dispute between Tesla and Walmart, the fires causing building collapse, or the fires which resulted in damage costs estimated to several million US dollars, the potential consequences of the fires are deemed evident. From the German data set it is noticed that PV-related fires are not always caused by the PV system itself, which indicates that the involvement of a PV system might affect the consequences as well.

1.4 Previous work on PV fire risk

A literature review was carried out to obtain an understanding of the current level of knowledge. The literature review was divided into two sections: i) a review of the existing standards related to photovoltaic systems in the built environment with a focus on BAPV systems, and ii) an evaluation of research related to the fire safety associated with PV installations in the built environment.

1.4.1 Standards [1]

The photovoltaic system

In Europe, photovoltaic modules shall be produced according to the European standards IEC/EN 61730 *Photovoltaic (PV) module safety qualification*, parts 1 [62] and 2 [63], which define the construction and test requirements. The North American standard UL 1703 *Flat-Plate Photovoltaic Modules and Panels* [64] was previously used at a federal level in the US, but in 2018 it was harmonised with IEC/EN 61730 and renamed UL 61730 [65]. Due to the harmonisation of the two standards, the product requirements became similar in North America and Europe, which benefits manufacturers selling their PV modules in both markets. However, the two documents are not identical as UL 61730 parts 1, and 2 only contain the national deviations from IEC/EN 61730. Common for both standards is that the majority revolves around the construction and requirements from an electrotechnical perspective. However, six of the 31

1. All of Section 1.4.1 was written by Jens Steemann Kristensen as part of a journal manuscript. The manuscript was made in cooperation with another research institution and was part of a research methods course that Reidar Stølen completed at the Norwegian University of Science and Technology - NTNU. The manuscript has not yet been submitted to a journal.

test methods in IEC/EN 61730-2 are related to the fire hazards of a PV system. The harmonised standards share the temperature test (Module safety test (MST) 21), hot-spot endurance test (MST 22), bypass diode thermal test (MST 25), and the reverse current overload test (MST 26), which are all considered as electrical stress tests of the modules.

In IEC/EN 61730-2, the ignitability test (MST 24) and fire test (MST 23) introduce test methods from the built environment. MST 24 is based on ISO 11925-2 *Reaction to fire tests – Ignitability of products subjected to direct impingement of flame – Part 2 Single-flame source test* [66], and the deviations between MST 24 and ISO 11925-2 are described in the document. MST 23 does not specify any specific test method, as it states that fundamental requirements for fire safety are not internationally harmonised, so it is not possible to establish general requirements. In case there are no national requirements, a series of national and international tests is mentioned in Appendix B. Two standards highlighted are EN 13501-5 *Fire classification of construction products and building elements - Part 5: Classification using data from external fire exposure to roofs tests* [67], and UL 1703 [64], where the former is the European classification of roof systems, whereas a series of modified UL 790 (*Standard for Standard Test Methods for Fire Tests of Roof Coverings*) [68] test methods are described in UL 1703.
In UL 61730-2, MST 24 is deleted, and MST 23 is replaced by national requirements depending on the application method of the PV system.

Interaction between PV system and roof construction

Photovoltaic modules can be integrated into the built environment by two application methods; respectively, building integrated (BIPV) and building applied photovoltaic systems (BAPV). The term BIPV is defined by EN 50583-1 *Photovoltaics in buildings – Part 1: BIPV modules* [32], where it is stated that the application method is distinguished from BAPV in case the module needs to be replaced with an appropriate construction material if the module is dismounted [32]. BAPV modules are defined as non-BIPV and are often retrofitted on the existing roof constriction.

On a European level, BIPV and BAPV modules are regulated by various standards as BIPV modules are considered as a construction component, whereas BAPV is an additional technology applied to an existing construction and thus, considered as an individual component not related to the building. Although the topic of the thesis is BAPV systems on commercial roof constructions, the relevant standards for both BIPV and BAPV systems are presented in the following Section as it cannot be justified to ignore the standards related to BIPV systems due to the overall similarities.

Because of the national deviations introduced in UL 61730, the standard is more complete than IEC/EN 61730 with respect to the fire safety test required. BIPV systems are to be tested as roof covering systems and separated into classes A, B or C following UL 790. Herein, three different test methods are used to examine the BIPV system at an inclination of no more than

24.6° and an applied wind load of 19 km/h. No matter the test type, a test deck with a width of 1.02 m is used, whereas the length varies from 1.21 m to 3.9 m. In one of the test methods, named intermittent-flame, the location of joints is defined, which seems practically incompatible with many PV products. Although the test decks are relatively large, the dimensions do not necessarily fit with the dimensions of a BIPV system, and since the standard is designed to test conventional roof coverings rather than rigid PV modules, the excess dimensions are not addressed.

A similar approach is noticed in IEC/EN 61730, where it is suggested to consult the European classification standard for external fire exposure to roofs, EN 13501-5, in Appendix B. However, the requirements for BIPV modules and systems are also regulated by EN 50583 parts 1 (modules) [32] and 2 (systems) [69]. Contrary to UL 61730, EN 50583 acknowledge that BIPV is not limited to the roof construction but can also be installed in other parts of the building envelope, such as façades. In the European standard, all BIPV modules are considered construction products, and the reaction to fire must be classified within one of the Euroclasses (A1 – F) – (s1 – s3), (d0 – d3) according to EN 13501-1 *Fire classification of construction products and building elements – Part 1: Classification using data from reaction to fire tests* [70].

If the BIPV modules are not integrated into the main building envelope but are mounted onto the building and represent an additional functional layer, such as balconies, awnings or balustrades, there are no further requirements for safety in case of fire. For inclined systems, the requirements depend on whether it is a BIPV module or a BIPV system [2]. Assuming that all modules are part of a system, they are tested in accordance with CEN/TS 1187 [71], where the classification is divided into $(B – F)_{ROOF}$(t1–t4) based on four different test methods as described in CEN/TS 1187 [67, 71]. The best classification is B_{ROOF} and the subsequent designation, t#, indicate the test method used to obtain the classification. National regulations based on these classifications give different requirements across Europe. Like the test procedures in UL 790, the physical dimensions in half of the CEN/TS 1187 test methods are, most likely, incompatible with BIPV modules. In all four test methods, it is evident that they are intended for conventional roof coverings such as Ethylene Propylene Dien Monomer (EPDM) or Polyvinyl Chloride (PVC) based membranes, as they address the importance of testing joints between overlapping layers.

In addition to CEN/TS 1187, the system is regarded as a window and should comply with EN 14351-1 if it is accessible from inside the building. Finally, it is stated in EN 50583-1 that the fire resistance of all Inclined and vertical BIPV modules should be classified with respect to EN 13501-2 *Fire classification of construction products and building elements – Part 2: Classification using data from fire resistance tests, excluding ventilation services* [72].

---

2. The distinction between BIPV module and system is deemed irrational and probably the result of a human error. A request was sent to the relevant stakeholders in November 2021, but no reply was received by June 2022

In general, two test methods are used to determine the classification based on reaction to fire according to EN 13501-1. A single flame source test (EN ISO 11925-2 [66]) and the single burning item test (EN 13823 [73]). Common for both test methods is that the predefined fixed sample sizes are smaller than most commercially available PV modules. A modified version of the single flame source test is defined in IEC/EN 61730-2 MST 24, where it is accepted to test full-size modules. The modified test method is assumed to be the common test method. For the single burning item test, cutting the modules into smaller Sections might affect the physical stability and, thus, the test result. Furthermore, the corner geometry does not represent a likely end-use scenario, but it is accepted that the corner configuration causes an increased flame height [74], and the test may therefore represent a worst-case scenario.

To summarise the current North American and European standards, it is found that the classifications of BIPV systems are forced into the existing classification regimes given in UL 790 and EN 13501-5, where the products rarely fit within the strict procedures necessary to ensure reproducible and repeatable results. Due to the lack of explanations or modifications related to the physical properties of BIPV systems, the two standards permit interpretations which might result in different classifications of the same product, depending on the test team and location. Such a scenario is undesirable and contrary to the general purpose of standardisation. Finally, it is noted that the potential hazard related to the air gap between the back of the BIPV system and the subjacent layer of insulation in a roof or façade system is not addressed by any of the standards.

For BAPV systems, the European guidance is limited to the technical report CLC/TR 50670 [75] developed by the European Committee for Electrotechnical Standardization (CENELEC), and the test methods described in UL 1703 as suggested in IEC/EN 61730-2 appendix B. Efficiently, the fire safety with respect to BAPV systems in Europe depends on the national requirements, where a French pre-standard from 2012 is the only known document [76]. In the pre-standard, which is based on a modified version of CEN/TS 1187 test 3, it is stated that it was developed due to the inability of CEN/TC 127 to create a single test procedure. As of 2022, it is known that CEN/TC 127 are in the process of designing a test method. As indicated from the quotation below, the fire-related risk associated with renewable technologies was not yet recognised by the responsible authorities in other European countries:

> *Photovoltaic systems and household wind turbines are not considered a special fire risk in the building regulations and are therefore not included in the building regulations' guidelines for chapter 5 - Fire. As such, the installation of photovoltaic systems does not affect the construction's placement in fire classes.*
>
> The Danish Housing and Planning Authority, *answer to a request from the Danish Association of Consulting Engineers*, 2020, Personal mail correspondence

Due to the national deviations in UL 61730, the requirements are more specific. However, the particular requirements do not entail that they are simple. Two terms are essential to understand the classification system related to BAPV systems: i) The definition of PV module "Type", and ii) The System Fire Class Rating (Class A, B, or C) of a PV module or panel with the mounting system in combination with roof coverings.

The definition of PV module "Type" is described in UL 61730-2 and is an optional method to limit the amount of required testing. A PV module can be defined as one of 34 "Types", and PV modules of the same type can replace each other without altering the System Fire Class Rating. The subdivision into the 34 "Types" depends on the materials used for the superstrate layer, the encapsulate, and the frame, as well as classification in accordance with two modified versions of the spread of flame and burning brand test in UL 790 as described in UL 61730-2 annex DVB.1 to DVB.3.

In the modified spread of flame test, it is stated that multiple modules should be used if the dimension of the tested module does not exceed the maximum allowed length of flame spread. It is also stated that the modules should be elevated 127 mm above a non-combustible surface. But it is not described or visualised if the modules should be installed tightly next to each other without any gaps, which would not be representative of the installation method on a roof construction. The method used to elevate the modules is another practical issue which is not addressed, as well as the inclination of the modules with respect to horizontal. As such, the modification allows different interpretations, which might cause the same module to be defined as various "Types" depending on the test personnel and laboratory.

The System Fire Class Rating of the PV module and mounting system in combination with a roof covering can be determined via UL 2703 Section 15. The required number of tests depends on the inclination, where 9.5° separate the definition of low and steep sloped roofs. No matter the inclination, all modules should be tested in accordance with the spread of flame test defined in UL 61730-2 DVB.2, which permit interpretations. Predefined roof constructions, depending on the test method, are used in the additional tests to examine flame spread between the PV module and the roof. The roof constructions are predefined as the System Fire Class Rating is solely linked to the PV module and the associated mounting system. Once

again, the test methods are based on modified versions of the UL 790 spread of flame and burning brand tests, but the written modifications are supported by drawings, which ensure increased consistency. For BAPV systems intended for use on low sloped roof constructions, the only additional test is a spread of flame test (figure 1.5), whereas a spread of flame test and two burning brand tests are required if the module and mounting system are intended for installation on steep-sloped roofs.

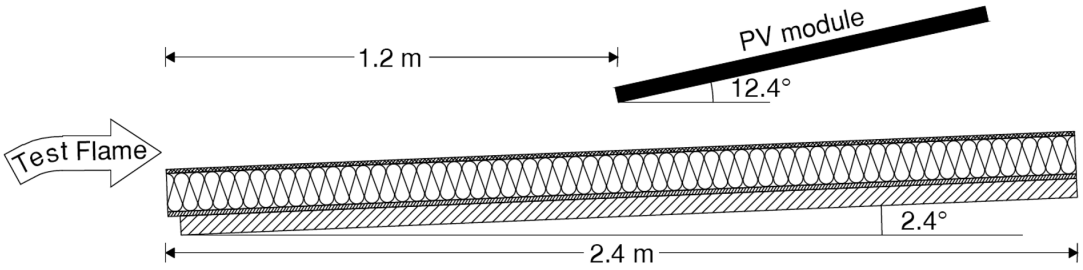

Figure 1.5: Sketch of roof construction and PV module in scale for the spread of flame test for low sloped roof constructions. Notice that the upper layer of the roof construction (roofing membrane) is not in scale as the minimum thickness is 1.5 mm. Based on Figure 15.5 in UL 2703 [77] and Figure 4.9 in UL 790

In the spread of flame test (figure 1.5), a 1.12 m long line burner is used to examine the flame spread between the roof construction and the PV module. Depending on the desired classification, both the exposure time and allowed flame extension are varied. However, a minimum setback distance of 910 mm (1.20 m in all Figures) is required between the lower edge of the roof mock-up and the lower edge of the PV module. Consequently, the width of the test flame is reduced from 90 cm near the line burner to approximately 15 cm below the examined PV module if the gas burner is calibrated per the description in UL 790 appendix A, which defines the ideal flame shape to be an isosceles triangle with a base of 90 cm and an apex of 132 cm [68]. Furthermore, the test method allows a PV system to be tested with a wind deflector, which is defined as “a continuous flame mitigation device which has a significant impact on the flame path and/or airflow direction [64]”.

The acceptance of a flame deflector and the required minimum setback distance indicates that the objective of the test method is to prevent the spread of fire when the system is exposed to an external source of ignition. The test method does not address the fire dynamic system behaviour when the ignition source is located between the PV module and the roof construction, such as multiple components related to the PV system. That does not correspond well to research by Plester et al., Sepanski et al., and Chiaramonte et al., as they found that a significant amount of PV related fires can be linked to an electric malfunction in a component related to the PV system [78, 41, 42, 79].

Ignition between the PV module and roof is addressed in two burning brand tests for steep-sloped roof constructions, but it is omitted if the PV module and mounting system are only intended for installation on low sloped roofs. As no known mounting system is designed for installation on both steep and low sloped roofs, it is assumed that ignition between the PV module and roof construction will not be addressed for any PV module and mounting system designed for use on low sloped roofs.

The limited test scenarios for low sloped roofs are unfortunate as the number of components related to the PV system increase probability of an electric malfunction and thus ignition between the module and roof. On top of that, the probability of ignition increased due to the presence of the DC circuit as defined by Babrauskas:

> “ *Statistically, problems will be fewer in AC than in DC circuits, since in an AC circuit many contact openings will take place during a part of the cycle where worst-case behaviour is not elicited, while opening a DC circuit is always effectively a ‘worst-case’ situation.* ”
>
> V. Babraukas, *Ignition Handbook, Chapter 11*, 2014 [39]

Ignition between the roof construction and the PV module is addressed in one of the two additional test methods for steep-sloped roofs, where a class B burning brand is located in between the PV module and the roof construction. However, a system can pass the test even if fire propagates below the entire system, as failure only is defined as sustained flaming on the underside of the test deck or the formation of flaming or glowing brands, which do not self-extinguish within five seconds. As such, the purpose of the test is not to prevent flame spread along with the building envelope, which is an essential part of building fire safety strategy.

Ignition in between the module and roof construction is also addressed in the European technical report CLC/TR 50670 *External fire exposure to roofs in combination with photovoltaic (PV) arrays - Test method(s)*, where a 15 kW free-hanging gas burner is located between the examined PV module and a non-combustible test deck, which “stimulates an exemplary roof covering” and allow “a free observation of the burning behaviour of the PV module” [75]. Thus, CLC/TR 50670 does not address the system behaviour between various components but only the PV module. That explains the geometry of the test setup for flat roof constructions, where the respective distances between the lower edge of the PV module, the lower edge of a free-hanging gas burner, and the subjacent roof construction are 15 cm and 8 cm. Thus, the gap distance between the PV module and the roof is not representative for the gap distance

on roof-mounted commercial PV systems, which can be as low as 5.5 cm [10]. Moreover, the free-hanging location of the gas burner made by Currenta GmbH und Co. OHG [80] is questionable, as it was designed to replace the wood wool basket from test method 1 in CEN/TS 1187 [71].

Due to the lack of a roof covering, CLC/TR 50670 is basically a single point flame test with a larger flame than the one used in EN ISO 11925-2 [66]. As such, it is deemed that the test methods suggested in CLC/TR 50670 are irrelevant as they do not represent a realistic scenario and because of the similarities to the well-established EN ISO 11925-2.
It is acknowledged that introducing a roof covering and reducing the gap distance might be an efficient method to understand the system behaviour between the roof construction, the PV module, and an ignition source. However, such a test will be a simple pass/fail test where a limited understanding of the underlying fire dynamic system will result in an expensive procedure, where it is necessary to examine every possible combination of roof covering, PV modules, inclinations, and gap heights.

For BAPV systems, it can be concluded that the requirements for the PV system as an electrical component are well regulated by CENELEC in Europe and Underwriters Laboratories (UL) in North America, whereas the implementation in the built environment seems sparse. The limited legislation mainly describes the requirements for a BIPV system, as these fall into the existing definition of building materials and are covered by their current test standards and requirements. Since the existing standards are not designed for testing PV systems, the relevance of the test results may be reduced due to the modifications that are required to fit the PV components into the test setup.

Overall, it is concluded that most of the current legislation is developed as an extension of the existing standards for fire safety related to roof constructions, which implies that very few parameters related to the PV system are addressed. The choice of materials related to the roofing membrane and PV module is addressed in most of the standards, as it is a key parameter with respect to the classification of roofing products according to UL 790 or EN 13501-5. But the transformation from an open to a semi-enclosed fire dynamic scenario is ignored, as the geometry between the building and the PV system is rarely mentioned. It seems to be acknowledged that the introduction of a PV system will change the flame spread behaviour, but the influence of the specific parameters, such as the inclination of the PV modules, the inclination of the roof, or the gap height between the roof construction and the PV modules are rarely addressed.

1.4.2 Current research

Generally, two types of research approaches are associated with PV installations and fire. The first type of research is conducted by mainly electrotechnical engineers who focus on reducing the likelihood of ignition caused by components related to the PV system. Secondly, the consequences of ignition are the focus of fire safety engineers.

Cause of the fire

Common for the research with an underlying basis within electrotechnical engineering is a focus on fault detection through methods based on statistical processing of the signal, analysis of the current-voltage characteristics, analysis of the power loss, or analysis based on artificial intelligence as described in several review papers [81, 82, 83, 84, 85, 86]. The purpose of the analysis methods is to detect when specific failures occur with a focus on efficiency loss and, as a worst-case scenario, component failure, which might result in fire.

From an electrotechnical point of view, there is a clear distinction between different failure types, but direct current arcing is the general outcome of a failure. As described in the review paper by Lu et al. [86], there are mainly two types of arc faults: series arcing and parallel arcing. Parallel arcing often occurs due to degradation, ageing, and mechanical damage of cables and is described as relatively easy to detect, whereas series arcing is deemed more complex [86].

Series arcing is the consequence of poor connection between two terminals and can occur for similar reasons as the parallel arcing, moisture ingress, and improper wiring due to poor workmanship [86, 78]. However, series arcing is deemed more complicated to detect as it might result from a slow degradation progress where a poor connection leads to increased resistance. Heat is generated as a consequence of the resistance, which can cause thermal stress, eventually forming a tiny gap between two terminals. Under the proper environmental conditions, an arc is formed, and the power of the arc depends on the location within the system as the power of the arc depends on the current and voltage [86]. Hastings et al. concluded that DC arcs with effects of 200 W and 800 W caused burn through of a PV cable within respectively 7 seconds and 1.7 seconds, and reported that the concentrated temperature of a DC arc can reach temperatures of 6000K [87].

A visual overview of potential electrical failures was provided by the *International Energy Agency - Photovoltaic Power Systems Programme* (IEA-PVPS) in 2021 [88], and the consequences of each failure type were quantified with respect to performance loss and safety risk. Fire (F), electric shock (E), and physical damage (D) were the three potential safety risks defined for each type of electric failure with the three possible outcomes: i) no effect on F/E/D, ii) may cause a F/E/D, to iii) failure can directly cause F/E/D.

From the overview by IEA-PVPS, it was found that failures related to the i) PV module, ii) the inverter, iii) the combiner box, iv) the connectors, and v) the cables all could act as the direct cause of the fire. The proneness of those components causing a fire was verified in an investigation document of 64 PV-related fires by the Building Research Establishment (BRE), which defined the combiner box as a connector, but added isolator failure, as well as an unidentified or unrelated failure as the sixth and seventh source of ignition [78]. Investigation of the ignition sources have also been conducted in Australia (400 fires) [79] and Germany (394 fires) [41, 42]. In addition to the location of the failure, the German data from 2012 also revealed that most failures occur i) during the first year of installation, ii) between March and August, and iii) between the time of 12:00 and 15:00 [41, 42]. It is assumed that the failures related to the seasons and the time of day correlates with the amount of sunlight.

As such, the significant amount of research summarised in the review papers by Alam et al., Chen et al., Dhere et al., Falvo et al. Mellit et al., and Lu et al. [81, 82, 83, 84, 85, 86] are focused on detecting electrical failures in the components described by IEA-PVPS, Sepanski et al., Plester et al., and Chiaramonte et al. [88, 41, 78, 79]. Based on the similarities between the failing components by IEA-PVPS, the German data by Sepanski et al., and the British data by Plester et al., it was concluded that a total of seven events could lead to a fire related to the PV system, as summarised in table 1.1 where the cause of failure is included as well. The table will be discussed in detail in chapter 2.

Table 1.1: Events and component failures causing ignition which can result in fires related to the photovoltaic system.

Ignition source	Cause of failure
PV module failure:	Cracked PV cells, damaged back-sheet, open circuit bypass-diodes, glass breakage, hot spot, manufacturing failure, cell inter-connection failure, detached or defect junction box, and junction box interconnection failure. [41, 78, 88, 89, 90, 91]
Isolator failure:	AC isolator on DC side, under-rated component, or installation error. [41, 45, 78, 79]
Inverter failure:	Complete failure due to software or hardware issues, moisture ingress, or grounding issues. [41, 49, 78, 79, 86, 88, 92]
Combiner box failure:	Underrated fuses, inadequate connection of DC cables, wrong wiring on-roof. [41, 78, 81, 85, 88, 93, 94]
Cable failure:	Undersized cables, incorrect clamping, incorrect cable routing around sharp corners, too large or incorrect cable glands, insulation degradation, or rodents. [41, 78, 88, 95]
Connector failure:	Connector mismatch/cross-connection/cross-pairing, defect connector, incorrect assembly, or moisture ingress. [41, 78, 88, 91, 96]
Unidentified or unrelated source of ignition:	Fire breaking through roof, arson, fireworks, or firebrands. [61, 41, 78, 88, 97]

Consequence of the fire

From a fire safety engineering point of view, the source of ignition is not necessarily the main focus, as the surrounding environment might have a significantly larger effect on the subsequent development of the fire, no matter if the fire is within the built environment or an urban/wild-fire environment as exemplified by Howard W. Emmons i 1963:

> *“ It wasn’t O’Leary’s cow that burned a third of Chicago and cost 250 lives. It was an exceptionally dry summer and fall and a very strong dry wind on October eighth and ninth of 1871. Nature had loaded the cannon; the cow merely lit the fuse. ”*
>
> Howard W. Emmons, *Fire in the Forest*, 1963, [98]

The research related to mitigation of the ignition consequences can be separated into two subcategories: i) Large-scale experiments and ii) examination of individual parameters.

Sherwood et al. [99] summarised the findings from most of the large-scale experiments which are conducted by Backstrom and various co-authors from Underwriters Laboratories (UL) [100, 101, 102, 103, 104, 105, 106, 107]. The summary was published by the Solar America Board for Codes and Standards and led to national deviations in UL 61730 described in Section 1.4.1. In summary, Backstrom et al. examined whether compliance was achieved when introducing one or multiple PV modules to the test standard for roofing products UL 790. The maximum flame spread distances are examined in six tests with gap heights between 12 in. (30.5 cm) and 24 in. (71 cm) [103]. But the six tests were conducted on an inclined surface with four different gap heights, four different roof coverings, and both a PV module and a surrogate panel. Thus, the influence of the various parameters could not be separated from one another, and as such, the importance of the individual parameters could not be determined.
All of the large-scale experiments by Backstrom et al. were conducted with a line gas burner installed at the edge of the test set-up, and thus the examined scenario assumed external ignition, which could be blocked by a wind deflector/flashing [101, 103, 107].

In addition to the large-scale test, Backstrom and Sloan examined the critical heat flux for various roofing products by the use of the cone calorimeter at fixed heat fluxes of 35 kW/m^2, 50 kW/m^2, and 70 kW/m^2 [102]. Compared to the maximum heat flux of 14 kW/m^2 measured at the UL 790 test set-up with a surrogate roof surface and no panel, the measured critical heat fluxes were similar or higher for all tested roofing products. However, with the introduction of a surrogate panel at a distance of 5 inches (12.5 cm) above the surrogate roof, the maximum heat flux increased to 41 kW/m^2, which was above the critical heat flux for all of the tested products [99, 100, 102].

Because the tests are based on UL 790, and surrogate PV modules are used with success in some tests, Backstrom highlights that introduction of the PV system alters the behaviour of the roof construction. However, the work by Backstrom is not found to be very systematic as the gap height, the setback distance, the roofing material, the panel type (PV module or surrogate board), the inclination of the roof, the inclination of the panel, the presence of a wind deflector, are all varied in relatively few tests. Thus, the tests become pass/fail-test where the importance of the individual parameters such as gap high or inclination of the PV module becomes unknown. In addition, the use of the line gas burner reveals that compliant roofing products become non-compliant with the introduction of the upper surface, but the tests do not reveal whether a smaller source of ignition, such as an electrical arc, can develop into a large fire.

Wood cribs with a theoretical peak heat release rate of 30 kW were used in four large-scale experiments examining roof construction mock-ups with east-west orientated PV arrays of six modules (2 m times 5.1 m) [1]. In all experiments, flame spread was observed below all PV modules, but no self-sustained flame spread occurred on the roofing membrane (B_{ROOF}(t2) compliant) outside the PV array, verifying the influence of the PV modules. The area of self-sustained flame spread was not affected by wind load, and similar to the experiments by Backstrom, the experiments were considered pass/fail-tests, which were used to verify the findings of bench-scale [108].

Bench-scale experiments or extermination of individual parameters enables an understanding of how the studied parameter might affect a more complex system. However, the one-eyed focus on a single parameter does not quantify the significance of the parameter, and thus such experiments cannot stand alone.

Several researchers have examined the PV modules. Despinasse and Krueger applied a gas burner to the front or the back of the PV module and suggested a novel test method where burn-through of the PV module within 15 minutes defined failure of the module [109]. Cancelliere and Liciotti examined the reaction to fire of four different PV module backsheets with a single point flame source (UNI 8457) and in accordance with UNI 9174 (probably the LIFT apparatus), whereupon the products were classified in accordance with the system. Cancelliere and Manzini combined the suggested test set-up from CLC/TR 50670 with a sheet of 0.375 m^2 roofing membrane and fitted it inside the test chamber of the single burning item test (EN 13823 [73]) with the purpose of classifying the PV module as a construction product. But due to the presence of two products, the PV module and the roofing membrane, the suggested method cannot be considered as an examination of the PV module but rather a system which also includes a gap height and a module inclination. As such, the suggested test method is deemed to be pass/fail-test.

In general, it can be questioned if the PV system should be considered a fire load or not. In the large-scale experiments by Kristensen and Jomaas, the plastic supports of the mounting system and the cables connecting the PV modules caught fire and thus, they should be considered as possible fire loads [1].

However, the vast majority of the mono- or poly-crystalline PV modules consist of glass and aluminium. In addition to that, the commonly used encapsulate ethyl vinyl acetate (EVA) and the fluoropolymers (often branded as Tedlar® or Kynar®) are used for the backsheet membrane represent respectively between 6.3% to 8%, and 2.8% to 3.5% of PV modules mass [110]. With a heat of combustion of 41.6 kJ/g, the EVA does represent a fuel load [110]. However, the heat of combustion of the protecting layer of the highly thermally stable fluoropolymers was between 4.1 kJ/g and 5.4 kJ/g [111].

The thermal stability of the PV module backsheet was verified by Yang et al., who used the cone calorimeter to determine a critical heat flux of 26 kw/m^2 for PV modules consisting of a single PV cell [112]. That was supported by Ju et al., who determined a critical heat flux of 18.8 kW/m^2 and 20.8 kW/m^2 for respectively the back- (0.5 mm Tedlar (polyvinyl fluoride)) and front-side (2.5 mm glass) of a poly-crystalline silicon module [113].

The effect of the PV module as a fuel load was also a theme in two of three research papers focusing on how the introduction of a horizontal barrier above a single-point heat source affected the heat flux towards the subjacent surface. Both papers concluded that the effect was limited and no self-sustained flame spread was observed along the backsheet [108, 114].

The three papers used a similar set-up, initially introduced by Kristensen, Merci and Jomaas [1], after which it was refined by Ju et al. [114] and subsequently Tang et al. [115]. The set-up, sketched in Figure 1.6, measured the heat flux received as a function of distance to a central gas burner. Kristensen et al. demonstrated the importance of the deflected flame from the gas burner, causing an additional heat flux towards the subjacent surface. Ju et al. inclined the upper surface ($0^\circ \leq \theta \leq 30^\circ$), varied the gap height ($5\,cm \leq h \leq 15\,cm$), measured heat flux, the up-, and down-stream flame extension, and suggested a model to quantify the re-radiation as a function of a non-dimensional local flame thickness. Reduction of the gap height, h, caused a heat flux increase towards the lower surface. Inclination increase caused an efficient gap height increase at the location of the gas burner, H, and as such, no comparison could be conducted across similar gap heights, h. However, it was evident that increased inclination caused a growth of the upstream heat flux (i.e. below the most elevated part of the surface) [114].

Tang et al. also examined the heat flux towards a subjacent surface as a function of the gap height, H, and the inclination. Contrary to the geometry by Ju et al., the panel was inclined around the centre-line of the gas burner and not the lower edge of the module. As such, the gap height, H, remained constant despite adjustments of the inclination. In addition, the upper

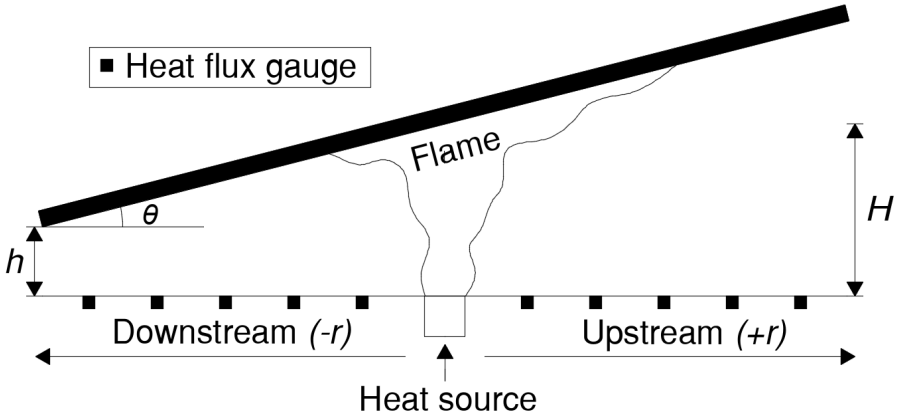

Figure 1.6: Conceptual sketch of the experimental set-up used by Kristensen et al., Ju et al., and Tang et al. [108, 114, 115]. (from Kristensen, Jacobs and Jomaas [7])

panel in the experiments by tang et al. did not represent a PV module but a scaled set-up of an inclined ceiling. Consequently, the gap heights, $25\ cm \leq H \leq 40\ cm$, and heat release rates, $6.72\ kW \leq \dot{Q} \leq 50.40\ kW$, were slightly larger, whereas the inclinations remained in the same range, $0^\circ \leq \theta \leq 20^\circ$ [115]. However, the dimensions were not significantly larger, and thus it was deemed acceptable to make a cross-experimental comparison.

Based on the results, Tang et al. suggested the model in equation 1.1 from where the heat flux, $\dot{q}''_f$, at a distance, r, from the heat source could be estimated as a function of the gap height, H, inclination, θ, and heat release rate from the gas burner, $\dot{Q}$.

$$\frac{\dot{q}''_f\left(H \pm r\,tan\left(\theta\right)\right)^2}{\dot{Q}\left(1 \pm sin\left(\theta\right)\right)} = a\left(\frac{r}{\left(H \pm r\,tan\left(\theta\right)\right)}\right)^b \qquad [115] \tag{1.1}$$

where: $a = 0.074$, and $b = -1.232$

The results are very similar when plotting the data reported by Kristensen et al. and Ju et al. in Figure 1.7. However, they do not correspond well with the model defined in equation 1.1 as that would have required different values of a and b. With a focus on the difference between Ju et al. and the model by Tang et al., at least three factors might have caused the difference: i) the lower ratio between the horizontal distance to the gas burner, r, and vertical distance to the panel, $H \pm r \cdot \tan\theta$, ii) lower heat release rates in experiments by Ju et al. ($3\ kW \leq \dot{Q} \leq 15\ kW$), and iii) the type of gas burner. The significantly lower x-axis values are a consequence of the high initial gap heights at the location of the gas burner in the experiments by Ju et al. [114], and due to the significantly lower heat release rates, the flame extension below the PV module becomes shorter. Consequently, the view factor between the deflected flame and a point on the subjacent surface is relatively small. Thus, it can be concluded that the model by Tang et al. was not developed for large gap heights. The relationship between the view factor and the measured heat flux is illustrated in Figure 1.8. Due to the limited width of the flame from the

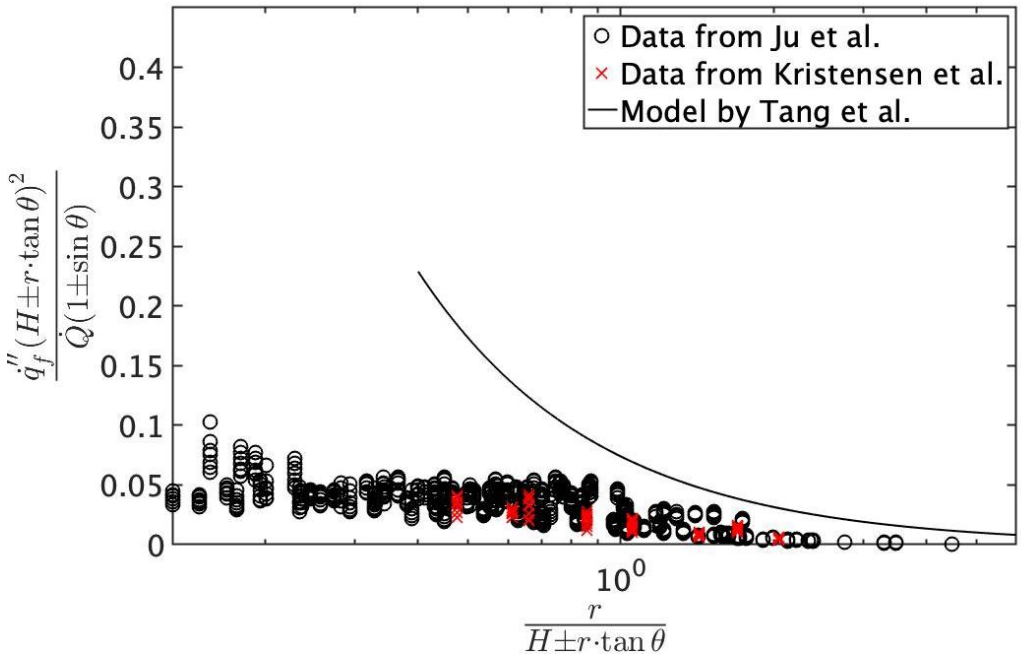

Figure 1.7: Data from work by Kristensen et al. [108] and Ju et al. [114] plotted with the model by Tang et al. (eq. 1.1 [115]). model by Tang et al. is not plotted below a value of $\frac{r}{H\pm r\cdot\tan\theta} = 0.4$. (from Kristensen, Jacobs and Jomaas [7])

gas burner, the view factors in Figure 1.8 were solely calculated for the deflected flame, which was assumed to be an inclined rectangle with a width equal to the upward flame extension, and a combined length similar to the overall lengths of the up- and downstream flame extension [114].

The correlation between the calculated view factors in Figure 1.8 and the measured heat fluxes by Ju et al. were relatively consistent. However, the view factors were a product of the up- and downstream flame extension measured in the experiments by Ju et al., it was not tried to develop any universal model based on the view factor calculations. However, the view factor calculations in Figure 1.8 illustrates that the consequences of 5 cm gap height reductions caused view factor enhancements of approximately 40%. Based on that, it is assumed that small changes of the gap height between a PV module and the subjacent roof construction might significantly affect the heat flux towards the roof.

The view factor from the vertical part of the flame might, along with different Froude numbers, explain the difference between the heat fluxes measured in the experiments by Ju et al. and Tang et al.. The experimental parameters do not enable direct comparison between similar set-ups, but heat fluxes of $\dot{q}''_f \approx 5.3\,kW/m^2$ and $\dot{q}''_f \approx 10\,kW/m^2$ were measured at an upstream distance of $r = 0.2\,m$ in the experiments by respectively Ju et al. [114] and Tang et al. [115]. However, the experiment by Ju was conducted with a lower gap height ($H = 0.194\,m$ vs $H = 0.2\,m$), a higher heat release rate ($7\,kW$ vs $6.73\,kW$), and a higher inclination (10° vs 0°),

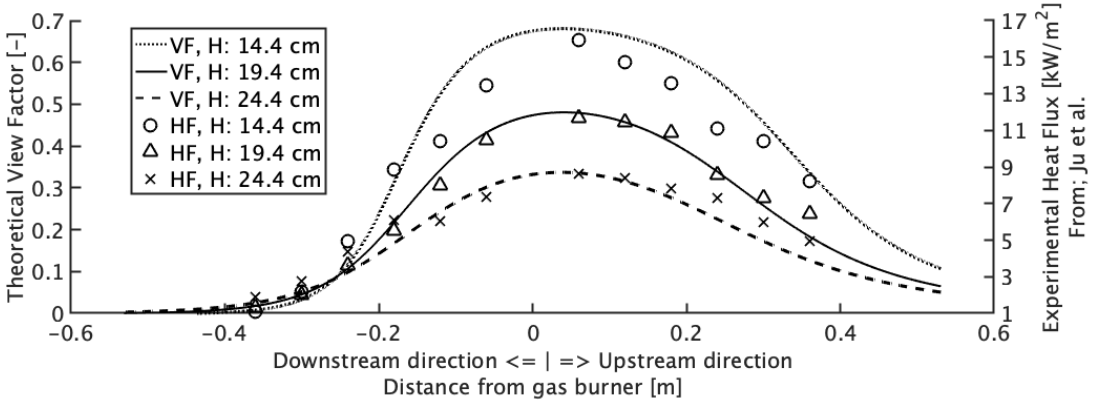

Figure 1.8: Measured heat flux and calculated view factor below module with an inclination of 10°, as a function of distance from the gas burner and gap height, H, as defined in Figure 1.6. **VF:** view factors, **HF:** heat fluxes from Ju et al. [114], **H:** Gap height at location of gas burner, equivalent to h of 5 cm, 10 cm, and 15 cm. The view factor curves were generated by a MATLAB script developed by the author.

which in accordance with both studies indicate that the heat flux measured by Ju et al. should be higher than the $10 kW/m^2$ measured by Tang et al. [114, 115].
With a diameter of 10 mm, the gas burner used by Ju et al. was significantly smaller than the 120 mm side length of the squared gas burner used by Tang et al.. Consequently, the broader flame caused a higher view factor, and thus heat flux, from the vertical part of the flame towards the nearby surface. For similar heat release rates, the smaller cross-sectional area entailed a higher flow velocity, and as such, different Froude numbers [116]. That caused a lower convective heat loss and thus higher heat transfer rate for the buoyancy-driven turbulent flame in the experiments by Tang et al. ($FR = 3.54 \cdot 10^{-10}$) compared to the laminar flow from the small gas burner used by Ju et al. ($FR = 1.55 \cdot 10^{-4}$).

Despite the slightly different outcomes of the three experimental series based on the set-up in Figure 1.6, the trends were similar and very clear. The introduction of a horizontal barrier (non-combustible or a PV module) caused a significant increase in the radiative heat flux towards the subjacent surface. Even for smaller heat release rates, the heat flux exceeded the critical heat flux of $\dot{q}''_{crit} = 7\ kW/m^2$ determined for a B_{ROOF}(t2) (EN 13501-5 [67]) compliant roofing membrane [108]. Combined with the observations of no self-sustained flame spread along the backsheet of the PV modules [108, 114], the findings indicated that the PV module does not necessarily act as a fuel load but rather a facilitator/catalyst. That correlates with the heat of combustion of the fluoropolymer backsheet which Tewarson defined to be between 4.1 kJ/g and 5.4 kJ/g [111]

However, the experiments were steady-state experiments, and as such, the findings only illustrated that an ignition source with a given heat release rate, $\dot{Q}$, below a panel with a defined gap height, H, and inclination, θ, caused heat fluxes, $\dot{q}''_f$, exceeding a given value, $\dot{q}''_{crit}$, within a distance, r, of the gas burner. The experiments did not examine the limitations of self-sustained flame spread below the PV modules as observed in the large-scale experiments summarised by Brooks [117] or Kristensen and Jomaas [1]. Thus, the relevance of the drivers facilitating self-sustained flame spread in those experiments, as well as the actual fires described in Section 1.3 are largely unknown.

1.5 Flame spread

Understanding the importance of parameters affecting flame spread between the BAPV system and the subjacent roof construction require a general understanding of *flame spread*. In general, flame spread along a solid material should be considered as a continuous series of ignitions and the flame spread process over a solid fuel can be separated into four steps [118]:

1. Vaporisation of combustible pyrolysis gases from the solid fuel.
2. Mixing of the oxygen from the ambient air and the pyrolysis gases near the surface of the fuel.
3. Ignition of the mixed oxygen and pyrolysis gases. Thus the formation of a diffusion flame and the establishment of a new flame front.
4. Heating from flame front towards the unignited fuel surface until ignition temperature is reached.

The flame spread rate depends on the material factors of the fuel and the environmental factors as defined by Friedman in table 1.2 according to Drysdale [119]. The influence of the parameters in table 1.2 will be discussed in the following sections with a focus on the experimental part of the research introduced in section 1.4.2. Thus, the basis of the discussion will be flame spread along on a horizontal roof construction and the likely consequences of the material and environmental factors.

1.5.1 Thermal thickness and heat transfer model

James Quintiere separates flame spread into flame spread on thermally thin and thermally thick fuels, and uses the temperature gradient through the fuel to distinguish between the two flame spread models [9]. The thermal thickness of a fuel can be defined by calculating the Biot-number, $Bi = (h \cdot L)/k$, where h $\left[kW/m^2 \cdot K\right]$ is the convective heat transfer coefficient, L $[m]$ is the characteristic length, and k $\left[kW/m \cdot K\right]$ is the thermal conductivity of the solid. A fuel is considered thermally thin if $Bi << 1$ [120].

Table 1.2: Factors affecting flame spread over solid fuels. (from: *Chapter 7: Spread of Flame, An Introduction to Fire Dynamics, D. Drysdale [119]*.

Material factors		Environmental factors
Chemical	Physical	
Composition of fuel	Initial temperature	Composition of atmosphere
Presence of retardants	Surface orientation	Pressure of atmosphere
	Direction of propagation	Temperature
	Thickness	Imposed heat flux
	Thermal capacity	Air velocity
	Thermal conductivity	
	Density	
	Geometry	
	Continuity	

From the large-scale experiments by Kristensen and Jomaas it was seen that the single-ply PVC-based roofing membrane represented the main fuel load and facilitated the flame spread between the BAPV module and roof construction [1]. With a thickness of 1.5 mm, a conductivity of $0.16\,W/m\cdot K$ [121], and a maximum convection heat transfer coefficient for free convection between gas and a surface of $25\,W/m^2\cdot K$ [122], the Biot number is $Bi << 1$. As such, flame spread on a roofing membrane should be considered as flame spread along a thin fuel as the temperature gradient through the membrane can be neglected [120].

For a thermally thin fuel, such as sheets of the reference material polymethyl methacrylate (PMMA), Williams's introduced the fundamental equation of fire spread [123] which was later expanded by Quintiere [9] as seen from the thermal model in figure 1.9 and equation 1.2. Because the fuel is considered thermally thin, Quintiere argues that both conduction through the control volume, $\dot{q''}_{k.p}$ and $\dot{q''}_{k.\infty}$, and convection can be ignored whereupon the right side of equation 1.2 consists of the cumulative radiative heat transfer towards the fuel, $\dot{q}''_f(x)$, minus the radiative heat loss, $\sigma\left(T^4(x)-T_\infty^4\right)$, where σ is the Stefan-Boltzmann constant, $T(x)$ is the temperature of the fuel at the distance x from the flame front, and T_∞ is the ambient temperature.

$$\rho c_p dv_p\,(T_{ig}-T_s)=\int_{x_p}^{\infty}\left[\dot{q}''_f(x)-\sigma(T^4(x)-T_\infty^4)\right]\mathrm{d}x \qquad [9] \tag{1.2}$$

From figure 1.9 it can be seen that the radiative heat flux, $\dot{q}''_f(x)$, is reduced for higher values of x, which corresponds well with the steady-state baseline experiments in the work by Kristensen, Merci, and Jomaas where the heat flux reduced as a function of distance from the gas burner. If the length of the sample is infinite, ∞, as defined by the upper part of the integral in equation 1.2, the radiative heat will in theory be transferred to the full length of the sample, but the insignificant magnitude of the radiative heat transferred towards the fuel at long distances

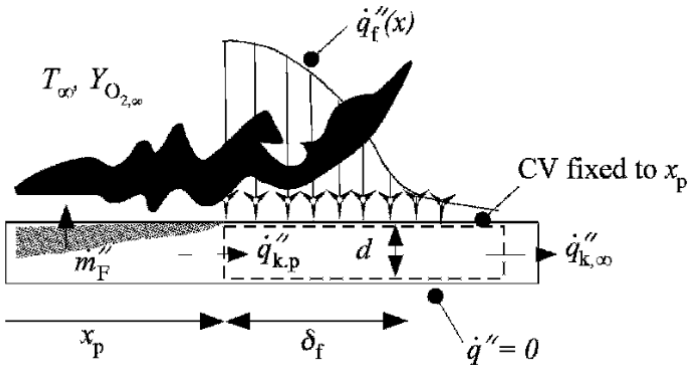

Figure 1.9: Thermal model for surface flame spread. (from: *Fundamentals of Fire phenomena, Chapter 8, J. Quintiere [9]*)

from the flame front justifies the use of a smaller control volume. In a similar way, the heat loss at long distances from the frame front will be negligible as the insignificant heating from the propagating flame will render the difference between the fuel temperature, $T(x)$, and the ambient temperature, T_∞, minuscule.

If the infinite control volume is replaced with a finite volume between the location of the flame front, x_p, and a defined point located $x_{<\infty}$ away from the flame front, the right side of equation 1.2 would represent the net heat transfer, $\dot{q}'_{NET}$ $[kW/m]$, to the defined point when the flame front, x_p, approaches $x_p + x_{<\infty}$.

$$\dot{q}'_{NET} = \int_{x_p}^{x_p+x_{<\infty}} \left[\dot{q}''_f(x) - \sigma(T^4(x) - T_\infty^4)\right] \mathrm{d}x \tag{1.3}$$

With the location of the flame front being a time dependent factor, the unit of the net heat transfer, kW/m, is rather unconventional. However, the location of the flame front depends on the flame spread rate, v_p, at the location $x_p + x_{<\infty}$ and as such, $\dot{q}'_{NET}$, represent the one-dimensional net heat flux necessary to achieve a given flame spread rate, v_p, at a given location, $x_p + x_{<\infty}$.

$$q'' = \frac{\dot{q}'_{NET}}{v_p} = \frac{\int_{x_p}^{x_p+x_{<\infty}} \left[\dot{q}''_f(x) - \sigma(T^4(x) - T_\infty^4)\right] \mathrm{d}x}{v_p} \tag{1.4}$$

As defined by the four step flame spread process on page 24, piloted ignition occurs when a solid fuel is heated to its ignition temperature, T_{ig}. That fits nicely with the left side of equation 1.2 which is the one-dimensional heat flux, $\dot{q}'_{FSR}$, necessary to achieve the flame spread rate v_p for a homogeneous material with a defined density, ρ, specific heat capacity, c_p, solid fuel thickness, d, as well as the ignition- and initial surface temperature of the fuel, T_{ig} and T_s:

$$\dot{q}'_{FSR} = v_p \cdot \rho c_p d \left(T_{ig} - T_s\right) \tag{1.5}$$

Consequently, it is seen that the one-dimensional heat flux necessary to achieve a given flame spread rate, $\dot{q}'_{FSR}$, is proportional with the flame spread rate, v_p, with the proportionality constant being equivalent to the amount of energy necessary to heat an area of a thermally thin solid from the initial temperature, T_s, to the ignition temperature, T_{ig}:

$$q'' = \frac{\dot{q}'_{FSR}}{v_p} = \rho c_p d \left(T_{ig} - T_s\right) \tag{1.6}$$

Based on that it is seen that the energy-balance of Quitiere's expanded version of Williams's fundamental flame spread equation, equation 1.2, is based on an equilibrium between the two one-dimensional heat fluxes in equation 1.7:

$$\dot{q}'_{FSR} = \dot{q}'_{NET} \tag{1.7}$$

Despite the simplicity of the introduced heat transfer model for flame spread on thin fuels, it does include the *thickness*, *thermal capacity*, *initial temperature*, *density*, and *ambient temperature* from table 1.2. In addition, the equation assumes that the influence of the conductivity through the thin fuel can be neglected [9].

1.5.2 Material factors

The material factors can be subdivided into chemical and physical factors, from where the chemical factors such as the ignition temperature (T_{ig}), heat release rate (ΔH_c), and the specific heat capacity depends on the chemical composition and the presence of flame retardants [74]. By rewriting equation 1.2 to 1.8, it can be seen that an increase of either the ignition temperature of the fuel, or the specific heat capacity render a higher $\dot{q}'_{FSR}$ which cause a slower flame spread rate, whereas an increase of the heat release rate will result in a higher heat flux towards the fuel and thus a higher flame spread rate.

$$v_p = \frac{\int_{x_p}^{\infty} \left[\dot{q}''_f(x) - \sigma(T^4(x) - T_\infty^4)\right] \mathrm{d}x}{\rho c_p d \left(T_{ig} - T_s\right)} \tag{1.8}$$

Inert filler materials or chemical additives can, among other products, be used as flame retards as they alter the pyrolysis or heating process by either "diluting" the solid fuel or reduce the combustion efficiency. Thus, flame retardants can be used to to reduce the concentration of pyrolysis gases through either step 1 or 4 in the defined 4-step flame spread process above. The use of inert fillers will, efficiently, increase the specific heat capacity as the energy used

to heat up the fillers, rather than the fuel, is wasted. Reduction of the combustion efficiency will reduce the heat flux, $\dot{q}''_f(x)$ which, once again, will lead to a slower or non-existent flame spread rate. Ultimately, a continues loop-process will cause a continuous reduction of the flame spread rate and finally quench the flame front.

With the physical parameters density and initial temperature also being present in equation 1.8, and a higher density will have similar effect as a higher specific heat capacity, whereas the amount of energy needed to reach ignition temperature will be smaller if the initial temperature of the fuel is higher.

1.5.3 Geometric parameters

Figure 1.10: Upward flame spread on thermally thick polymethyl methacrylate (PMMA) for surface orientations of 0°, 22.5°, 45°, 67.5°, and 90°. Section of the 2011 IAFFS photo competition winning image by Gollner, Huang, Williams, and Rangwala. [124]

The effect of surface orientation, or inclination of the solid fuel, depends on the defined direction of flame spread and is closely related to the difference between concurrent and opposed flame spread. If an inclined homogeneous fuel is ignited at the centre, the upwards flame spread will be faster than the downwards flame spread and due to the reduced heat flux downwards, the result might be a negative heat feedback-loop resulting in a quenched downwards flame front and thus only one-directional upward flame spread.

The effect of surface orientation was visualised by Gollner, Huang, Williams, and Rangwala in their competition winning image from the IAFSS 2011 symposium. The part of the image in figure 1.10 illustrates flame spread along a fuel with different inclinations and it should be noticed that an increase of inclination cause a reduction of the distance between the right side of the flame front and the fuel. The smaller distance leads to a higher view factor and thus a higher heat flux, $\dot{q}''_f(x)$, from the flame towards the solid fuel to right side of the flame. For thin fuels, studies showed that the upward flame spread rate increased with a magnitude of respectively 3 and 10, when the fuel orientation were changed to 45° and 90° [125, 126].

Similarly, negative inclinations reduce the heat flux and flame spread rate as a result of the reduced view factor between the flame front and fuel. Although figure 1.10 originates from an experimental campaign studying upward flame spread [127], the visualisations are also representative for downward flame spread by considering the interaction between the left side flame fronts and the non-ignited PMMA. From a visual point of view, the angle between the left side flame front and the fuel is almost similar for the samples with inclinations between -22.5° to -90°, which corresponds well with the findings by Hirano in 1974. Hirano observed an almost constant flame spread rate when the inclination was varied between -30° and -90°, whereas the change from 0° to -30° caused a 1/3 reduction of the flame spread rate [125].

In addition to the fuel orientation, other geometric parameters can affect the flame spread rate. The most known effect among fire safety engineers is probably the trench effect where the vertical barriers at the edges of the fuel, parallel to the flame spread direction, cause re-radiation and a changed airflow pattern which accelerates the flame spread rate significantly. The effect is often linked to the fatal King's Cross fire in 1987 [126].

The 2017 Grenfell Tower fire was another London based fire where the fuel geometry played a major role as flame spread was possible within the ventilated façade system [128]. Vertical steady-state experiments of flame extension between two non-combustible surfaces showed flame extension and an increased heat flux towards the surface closest to the heat source with a reduction of the distance between the surfaces [129, 130, 131, 132]. As such, there is a close link between the fire dynamics in vertical cavities and the horizontal cavities that was discussed in section 1.4.2 [108, 114, 115].

1.5.4 Environmental factors

The effect of wind is almost similar to the effect of the orientation of the solid fuel and depends on the defined direction of flame spread. The term *concurrent flame spread* is used when the wind direction is similar to the direction of flame spread, whereas *opposed flame spread* is used to describe the case where the wind direction and flame spread direction are opposite of each other. The result of concurrent flame spread is that the flame is tilted closer towards the fuel ahead of the flame front which resembles the introduction of a positive inclination of the fuel and as such, results in a faster flame spread rate. The same type of comparison is valid is valid

for opposed flame spread and fuel orientation with negative inclinations, which can also lead to quenching of the opposed flame front if the heat transferred to the fuel ahead of the flame front is insufficient. That was illustrated in the flame spread studies by Fernandez-Pello and Hirano, when they studied opposed flame spread on the thermally thick polymethyl methacrylate (PMMA) and thermally thin filter paper sheets [133].

In the same paper, Fernandez-Pello and Hirano described the effect of modified composition of the atmosphere and an examination of the flame spread rates on the same materials at different opposed flow velocities and oxygen concentrations between 21% and 100%. In general, the flame spread rate increased for higher concentrations of oxygen, which was related to gas kinetics [133].

Obviously, high wind loads can dilute the concentration of combustible pyrolysis gases below the lower flammability level and thus quench the flame front.

An imposed heat flux from i.e. a radiant panel increase the fuel temperature, T_s before the arrival of the flame front, whereupon a smaller temperature increase of the fuel is necessary to reach the ignition temperature, T_{ig} in equation 1.2. The imposed heat flux does not necessarily originate from a radiant panel, but can be an interaction with another object - combustible or non-combustible. The imposed heat flux from the nearby burning logs in a bonfire is for example requisite for continues burning of the individual logs within the bonfire, which is confirmed by the self-extinguishing behaviour of the bonfire if the logs are separated.

1.5.5 Reference materials

Common for the majority of the parameters discussed in the previous part of section 1.5 is the use of materials such as paper sheets, computer cards, or PMMA [126, 133, 134, 135]. Those materials are defined as reference materials since their material properties permit self-sustained flame spread under most conditions. As such, it s possible examine the flame spread behaviour at all angles, at severe air velocities, temperatures, or atmospheres. PMMA tends to be the most often used reference material due to the lack of a charring phase [136] and because it absorbs very limited amounts of water at even high relative humidity (0.8% at RH: 80% [137] and 2.1% when immersed in water [138]). That makes it significantly easier to model the flame spread behaviour when compared to other materials such as wood where humidity and charring affects the conductivity and thus heat transfer through the material [139].

1.6 Flame spread below the BAPV module

With an understanding of the parameters affecting flame spread along a solid fuel, the influence of the building-applied PV module above the roof, which generate a semi-enclosure, or horizontal cavity, can be considered.

1.6.1 Horizontal cavity or semi-enclosure?

The term *semi-enclosure* will be used throughout the thesis rather than *cavity* which is more generic and thus covers both horizontal, vertical, and tilted cavities. Cavities are in general referring to a hole or space inside *something* [140], which fits well with the smaller air gap behind a BIPV façade module or BIPV roof module, but not necessarily the gap height of 5 cm to 30 cm [10, 108] between a roof mounted BAPV module and the subjacent roof constriction as seen in figure 1.11.

With an enclosure fire being a fire within a room with one or several openings, the space in between the BAPV modules and the subjacent roof could qualify as an enclosure. However, it was decided to use the term *semi-enclosure* as the opening factor was assumed higher than for a conventional enclosure.

Figure 1.11: East-west orientated BAPV system on flat roof construction. From: [10].

1.6.2 Flame spread between two vertical surfaces

The flame spread scenario between a BAPV system and a flat roof construction is, to some degree, similar to the flame spread scenario in ventilated façade systems. With a focus on façades, Torero defined three fundamental performance requirements for the building envelope from where *flame spread* was one of them which he also defined as the most complex when compared to *Fire ingress* and *compartmentalization* [128].

No matter the orientation, the high complexity within the cavity is a result of the combination of external parameters and multiple materials with different material parameters. Consequently, the parameters in table 1.2 are no longer sufficient to define the flame spread scenario since material factors can be ascribed to each component of the system whereas each of the environmental factors depends on the interaction between the materials.

When combustion occurs within a cavity, in the form of a ventilated facade system or a horizontal semi-enclosure below a BAPV system, the combustion process alters the composition of the available atmosphere and reduces the concentration of oxygen and thus the combustion efficiency. The non-oxidised fuel is driven by the buoyant flow and causes an extension of the flame when the fuel mix with air. The length of the extension depends on the velocity of the entrained air which relies on the opening widths of the cavity and the temperature within the cavity which induce a pressure difference and thus entrainment. Besides supplying oxygen to the combustion process, the flow velocity and relative low temperature of the entrained air absorbs energy from the heated materials which causes a reduction of the heat flux towards the components of the system.

Despite only discussing a limited number of the processes affecting the flame spread between two surfaces it is clear that quantification of the heat flux towards an individual component within a system is very complex. Contrary to flame spread along a single material, the flame spread scenario does not only depend on the material parameters of the solid fuel, but also the parameters of all the other components of the system and the external factors defined in table 1.2.

1.6.3 Flame spread between two horizontal surfaces

Obviously, the orientation is different between a ventilated facade system and BAPV system on a flat roof construction, but the level of complexity is similar. Although it is studied how the introduction of a horizontal barrier affects the heat flux towards the subjacent surface in steady-state experiments (see section 1.4.2), the horizontal barrier's influence in a transient flame spread scenario is unknown as well as the influence of the parameters associated with such system.

In addition to the horizontal distance between the two surfaces, the material parameters of the surfaces can affect the flame spread scenario in various ways. Because the steady-state experiments described in section 1.4.2 defines snapshots, the influence of time-dependent factors such as thermal thickness, conductivity, or emissivity are not as essential as in a transient scenario.

By substituting the specific engineering problem, flame spread below BAPV modules on flat roof constructions, with a simpler scenario, flame spread between two components, a thermally thin solid fuel below a horizontal barrier, the influence of the component material parameters can be discussed with Quintiere's version of the simple flame spread equation as the focal point (equation 1.2).

The influence of the horizontal barrier is sketched in figure 1.12 where figure 1.12a represents a simplified version of Quintiere's model of flame spread on a thin fuel (figure 1.9).

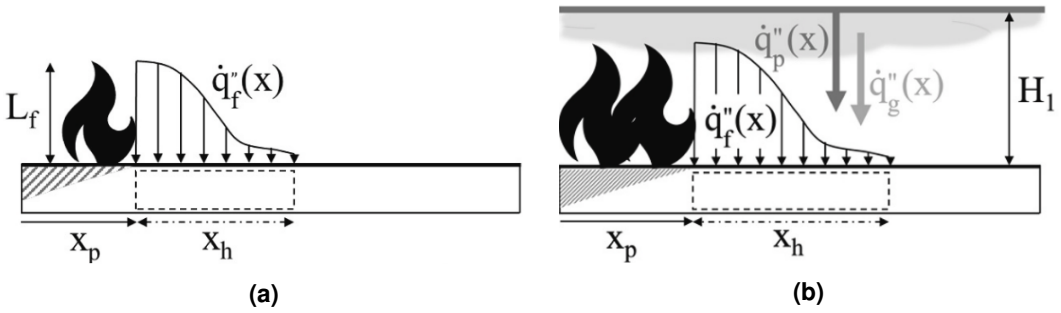

Figure 1.12: Simple heat transfer models of flame spread on thin fuel and the effect of a horizontal barrier above thermally thin fuel. **a)** Simplified figure 1.9. X_p: pyrolysis zone, X_h: preheating zone, $\dot{q}''_f(x)$: heat flux from flame to fuel, L_f: flame height. **b)** Introduction of horizontal barrier at the vertical distance H_1. $\dot{q}''_p(x)$: heat flux from the heated horizontal barrier, $\dot{q}''_g(x)$: heat from hot gases. (form: Kristensen, Faudzi and Jomaas [6])

If the vertical distance between horizontal barrier, H_1, and the fuel is larger than the flame height, L_f, convective and radiative from the flame will heat up the horizontal barrier at a rate depending on the barriers appearance and material parameters. The barrier will, simultaneously, emit radiation towards the fuel, $\dot{q}''_p(x)$ (figure 1.12b) and away from the system (not included in figure 1.12b).

The amount of energy absorbed by the barrier depends on the fraction of energy absorbed (α), reflected (ρ), and transmitted (τ) [141]. If the material is opaque, all the energy that is not reflected will be absorbed by the material and thus increase the temperature of the barrier. The fraction of energy absorbed by a material is strongly dependent on the wavelength and thus the colour of the material as well the emitter [141]. A black body have an absorption of 1 and consequently a reflection and transitivity of 0.

Other materials are more complex and for some materials, the temperature of the emitter, thus wavelength of the radiation, is significant. For example, white polystyrene absorbs 86% of the radiation from a black body emitter with a temperature of 1000 °C, only 40% of the radiation from a black body emitter with a temperature of 3500 °C, but 88% from flames which do not have black body behaviour [141].

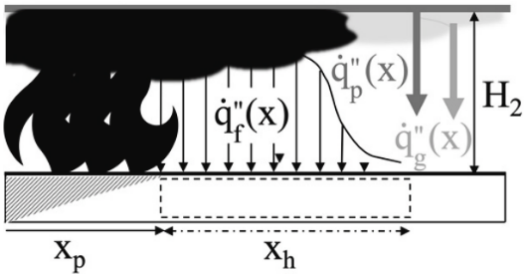

Figure 1.13: Continuation of figure 1.12. Reduction of the vertical distance H_2 and thus deflection of the flame below the horizontal barrier. (from: Kristensen, Faudzi and Jomaas [6])

Without knowing the exact material of the horizontal barrier, it can be assumed to be a black body in figure 1.12b. If so, and if the barrier is thermally thin, then the upwards radiation not defined in figure 1.12b, is similar to the downwards radiation, $\dot{q}''_p(x)$, emitted from the barrier and thus an energy loss from the system to the surroundings.

Focusing on the radiation emitted towards the system, the heat flux depends on the temperature of the barrier which depends on the material's specific heat capacity, c_p, and conductivity, k. A hypothetical material with a very high conductivity and a very low specific heat capacity will be heated up fast and have a relatively homogeneous temperature and thus homogeneous radiative heat transfer towards the subjacent fuel. In figure 1.12b, that would lead to the right edge of the preheating zone, X_h, being extended to the right edge of the sample. If the conductivity is low, only a localized area of the horizontal barrier will increase in temperature and thus the heat flux contribution from the heated barrier, $\dot{q}''_p(x)$, will reduce as a function of distance to the flame front, x.

In a similar way, the contribution from the smoke layer in figure 1.12b, $\dot{q}''_g(x)$, depends on the smoke temperature which is expected to reduce as a function of distance to the flame front, x, due to entrainment of air.

The magnitude of both $\dot{q}''_p(x)$ and $\dot{q}''_g(x)$ in figure 1.12b depends on the vertical distance, H_1, due to the influence of view factor described in section 1.4.2. If the vertical distance becomes lower than the flame height, L_f, as sketched in figure 1.13 it is, based on the knowledge from the steady-state experiments, expected that the flame deflects below the barrier whereupon the heat flux from the flame towards the subjacent material, $\dot{q}''_g(x)$, increase.

Obviously, increased heat fluxes from the flame, smoke, or heated horizontal barrier will enhance heating rate of the thermally thin fuel and thus result in faster flame spread in accordance with equation 1.2. But for the sake of simplicity, Quintiere's flame spread model in equation 1.2 assumes no heat losses from the solid fuel to the material below ($\dot{q}'' = 0$ in figure 1.9). Such boundary conditions would only be possible with a vacuum, since there would be no mass to heat, whereas an actual horizontal flame spread scenario would require some sort of physical support.

Only a limited amount of energy is required to heat up a small mass with a low specific heat capacity and thus such materials, combined with a low conductivity, will result in boundary conditions closest to a vacuum. An increase of one the three material parameters will lead to a growing heat transfer from the thermally thin fuel to the material (i.e. heat loss) and thus slower heating of the fuel leading to slower flame spread rate or quenching of the flame front.

Without taking the fuel properties, convective heat transfer, nor consideration for temperature dependent thermal properties of the horizontal barrier and the material below the fuel into account, the discussion within this section verify the complexity of a system with more components.

1.7 Problem identification

1.7.1 Frequency and cause of ignition

Based on the current level of knowledge regarding fires associated to the photovoltaic system in Section 1.3, it can be concluded that fires related to the photovoltaic system, including BAPV systems, occur. The consequences of the fires are rarely quantified, but in some cases, the loss is estimated to be several million US dollars. In addition, only a few data sets associated with PV-related fires exist, and consequently, the frequency of the fires remains unknown.

From an electrotechnical point of view, it is accepted that the PV system represents a potential ignition source due to the nature of direct current and the consequences of direct current arcing. Based on forensic investigations and a detailed overview of potential electric malfunctions related to the PV system, a directory of seven potential ignition sources is found in Table 1.1. However, the failure frequencies are not quantified, and even if no electric failures occur, ignition from a non-PV-related ignition source is possible.

1.7.2 Influence of BAPV module

From a regulation or standard point of view, a BAPV system is not considered a part of the building but rather a technological add-on in Europe. Thus, the consequences of the interaction between a BAPV system and the hosting roof construction are not generally accepted, and further regulations should be made on a national level. In the United States, the interaction between the BAPV system and roof construction is accepted, and test methods are developed. However, the tests are based on existing test methods, and implementing the PV module(s) within the existing tests is deemed to permit interpretations. As such, the outcome of the tests might vary across different test laboratories. In addition, all existing and suggested test methods can be conducted with fixed gap heights, and as a result, the potential influence of the geometry is ignored.

Focusing on the flame spread in an horizontal semi-enclosure, the basic understanding of why the fire is propagating in the semi-enclosure is defined in section 1.4.2, but there is no understanding of the complex system behaviour discussed in section 1.6.2. From the discussion of flame spread between two horizontal surfaces in section 1.6.2 it is seen than the installation of the PV module on the roof introduce an additional radiative heat transfer, $\dot{q}''_{add}$, towards the roof. The additional heat transfer originates from many sources including the heated PV module and deflected flame, but it could also come from combustible components of the PV module.

If it is assumed that the simple flame spread equation (eqn. 1.2) is valid for flame spread in the semi-enclosure, the simplified heat flux towards the fuel ahead of the flame front, $\dot{q}''_{fl}$, can be substituted by two components: i) a baseline heat flux corresponding to the heat flux from the flame without the horizontal barrier, $\dot{q}''_{bas}$, and ii) the additional heat flux, $\dot{q}''_{add}$, which depends on the complex system behaviour discussed in section 1.6.2. Thus, it is possible to redefine the heat flux from the flame as $\dot{q}''_{f,re} = \dot{q}''_{bas} + \dot{q}''_{add}$ in the simple flame spread equation (eqn. 1.2).

The high level of complexity when more components are combined into a system require a fundamental understanding of, at least, all the factors discussed in sections 1.5 and 1.6.2. However, the influence of the BAPV module and thus the redefined heat flux, $\dot{q}''_{f,re}$, is estimated to be equivalent to the difference between the sketches in Figs. 1.14 and 1.15.

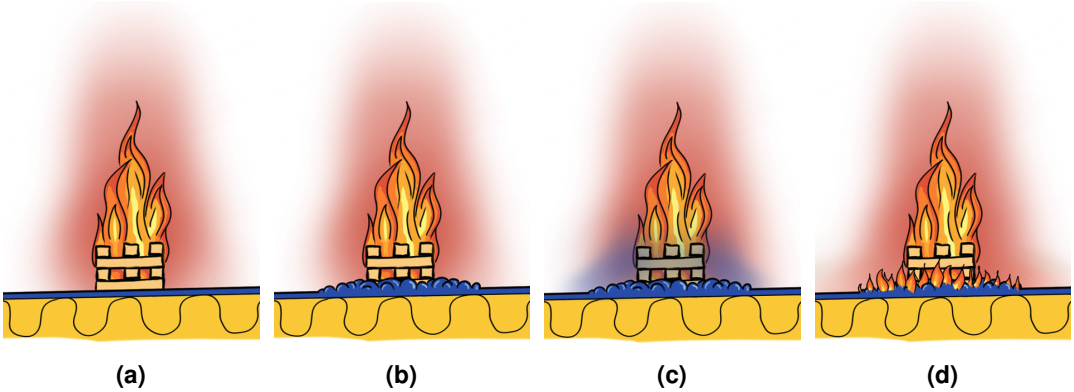

Figure 1.14: Sketched ignition process of roof construction (blue roofing membrane, yellow insulation) with wood crib. **a)** Radiative heat transfer from ignited wood crib (fading red cloud). **b)** Heating of nearby roofing membrane. **c)** Release of combustible pyrolysis gases (fading blue cloud), **d)** Ignition of pyrolysis gases, additional radiative heat transfer, but no self-sustained flame spread.

For a commercial flat roof construction, compliant with the European test standards described in EN 13501-5 or the North American UL 790 [67, 68] (see section 1.4.1), flame retardants in the roofing membrane prevent self-sustained flame spread as visualised in figure 1.14. The heat flux from the ignited wood crib is sufficient to heat up the upper layer of the roof

(figure 1.14b) to a temperature where the concentration of pyrolysis gases exceed the lower flammability level whereupon ignition occur (Figs. 1.14c and 1.14d). But the heat release rate from the burning membrane is so limited that the flame front is quenched and no flame spread occur outside the domain of the ignition source.

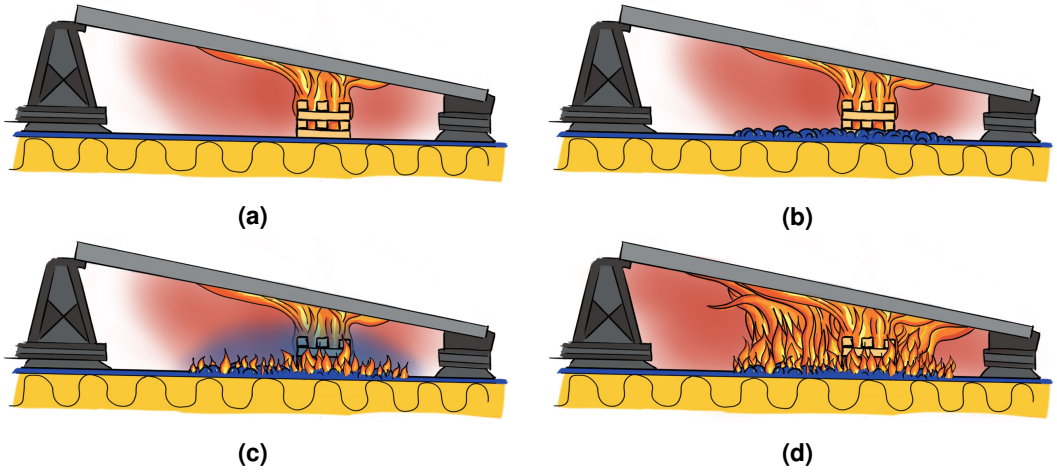

Figure 1.15: Sketched ignition process of roof construction (blue roofing membrane, yellow insulation) with wood crib below BAPV module (inclined grey rectangle). **a)** Radiative heat transfer from deflected flame (fading red cloud). **b)** Heating of nearby roofing membrane. **c)** Release of combustible pyrolysis gases and initial ignition (fading blue cloud). **d)** High heat release rate due to higher concentration of pyrolysis gases, heating of nearby materials and self-sustained flame spread.

The additional heat flux, $\dot{q}''_{add}$, is sketched as a larger and more intense red cloud (i.e. radiative heat transfer) in figure 1.15a when compared to figure 1.14a. That leads to heating of a larger area, release of more combustible pyrolysis gases, higher heat release rate and finally, self-sustained flame spread below the BAPV module (Figs. 1.15b-1.15d).

The two illustrations indicate that the introduction of the BAPV module, which is the only difference between Figs. 1.14 and 1.15, results in a magnitude of the redefined heat flux, $\dot{q}''_{fl,re}$, that per default enables self-sustained flame spread. But the additional heat flux, $\dot{q}''_{add}$, have to exceed a given magnitude to enable self-sustained flame spread and it is expected that the magnitude depends on parameters associated with the complex relationship between the semi-enclosure geometry and the material properties of the roof construction and PV module.

Identification of the parameters and quantification of their significance could enable efficient mitigation of the consequences associated with PV-related fires on flat roof constructions. But the influence of the semi-enclosure geometry is only studied in steady-state bench-scale experiments and the system behaviour of the materials are unknown as the system components

have only been tested on component level or as pass/fail-tests as described in section 1.4.2. Thus, the significance of the geometry and the material parameters are unknown in a transient flame spread scenario and enable a quantified discussion of potential mitigation strategies it is deemed essential to understand the significance of:

- The PV module type
- The PV module inclination
- The horizontal distance between the roof construction and the PV module
- The material parameters within the semi-enclosure

1.8 Thesis aim

PV systems in the built environment will be part of a fossil-free energy mix which is essential in reducing the release of greenhouse gasses and thus a key player in limiting the future consequences of the climate changes. However, the unintended consequences might be a showstopper, which can slow down further market penetration by the technology. To reduce the fire-related risk of BAPV systems, it is essential to understand the frequency and the cause of flame propagation associated with PV-related fires, so the unexpected consequences of the technology do not overshadow the benefits. The larger the building, the larger the risk. As such, commercial installations on warehouses and production buildings have the highest potential gain and consequences due to the size of the systems.

The thesis aims to consolidate a continuous growth of building applied photovoltaic (BAPV) systems on commercial flat roof constructions by providing research and thus building knowledge to highlight where measures should be taken to ensure the fire-related risk associated with the technology and the application method is negligible. The hope is that the thesis will deliver a scientific contribution to render a long-term sustainable green transition from fossil-based to renewable energy production.

1.9 Objectives

A total of six objectives are defined based on the aim of the thesis:

1. To quantify the frequency of fires related to photovoltaic systems as well as the cause of the fire.
2. To design and construct a novel experimental set-up to enable measurement of relevant parameters related to flame spread in a semi-enclosure defined by a PV module and the subjacent roof construction.
3. To quantify and discuss the significance of the individual parameters influence on the fire dynamic scenario consisting of the development of an initial fire inside the semi-enclosure.

4. To simplify the complexity of the fire dynamic system by detaching the material parameters from the geometric parameters.
5. To examine the influence of geometric parameters.
6. To suggest and test different mitigation methods to reduce the consequences of an initial fire related to a building applied PV system.

These six objectives create the main direction of the thesis. The frequency analysis of fires related to the photovoltaic systems (Objective 1) can be found in chapter 2 whereas the rest of the objectives are approached through the substantial experimental effort presented in Chapters 3 and 4.

Chapter 2

Frequency and fault analysis

For building applied PV (BAPV) systems, the PV system is installed on a building compliant with the required standards defined in the national building regulations. As such, the basis of a BAPV system is a building that generally can be defined as safe, with the term safe indicating that the fire-related risk is low. Based on the literature review, it is evident that the PV system introduces a source of ignition, but to understand the inherent fire-related risk of introducing a PV system into the built environment, it is essential to quantify the frequencies as well as consequences of a fire related to a BAPV system.

The analysis in the chapter is based on the paper published in cooperation with a team from Putra University in Malaysia [3]. A few adjustments have been implemented concerning the cause of the PV-related fires in Germany, but the overall outcome is similar. Thus, all of the tables and figures are based on tables and figures from the published paper. The idea of plotting the national annual frequency of fires based on capacity originated from the Malaysian team, as well as a preliminary manuscript. The data analysis and re-writing of the manuscript was conducted by Jens Steemann Kristensen in cooperation with Nur Aliah Fatin Mohd Nizam Ong.

2.1 Analysis methods

To quantify the fire-related risk associated with a BAPV system, using a bow-tie analysis, defined as a combined fault tree analysis and event tree, would be ideal [142]. In such analysis, the occurrence of an initial fire on the roof could be defined as a major hazard of the fault tree analysis, after which the frequencies of potential consequences could be quantified as a function of safety functions implemented on the hosting roof construction and the BAPV system [142].

However, such analysis requires extensive knowledge about a system's failure modes and the safety measurements implemented to mitigate the consequences of an initial fire. Knowledge which is provided for extensive chemical and biochemical production facilities [142], but not for the rapid implementation of a novel technology into the built environment. In addition, the

potential consequences could be related to the design of the roof construction, the geometry of the PV system, material properties of the individual components and external factors as defined in the literature review. Thus, properties which were undefined or unknown in the vast majority of reported fires.

Based on the literature review, a total of five data sets reporting PV-related fires from Australia, Germany, Italy, the United States of America (US), and the Netherlands were found [79, 41, 44, 47, 48]. The cause of a PV-related fire was quantified in three data-sets from respectively Australia, Germany, and the United Kingdom (UK) [79, 41, 143], and finally, the consequences of 213 PV related fires in Germany were reported by Sepanski et al. [41]. However, all of the German data, including the extent of damage associated with PV-related fires, were based on non-uniform reports from several sources, including internet and media reports, assessor reports, and internet-based surveys. As a result, it is assumed that the consequences are biased towards fires with a greater extent of the damage. The assumption was deemed valid as it was stated that burndown of the building occurred in 6% of the reported cases, which was considered highly unlikely. As a result, it was decided that this data would not increase the accuracy of the overall analysis.

Because it was not deemed possible to conduct the event-tree analysis, the events *fire* and *no fire* were the only obtainable outcomes of which the outcome *no fire* was not possible, with the major hazard being an initial fire related to the PV-system. As a result, the event-tree analysis was reduced to a frequency analysis which could be linked to a fault tree analysis examining the probability of an event causing the initial fire, after which the frequency of an event causing a PV-related fire could be estimated. The chapter is therefore separated into a frequency analysis followed by a fault tree analysis.

2.2 Frequency of PV-related fires

2.2.1 Available data and method

The five data sets in table 2.1 represented all the publicly available data, including the duration and methods used to collect the data. None of the data sets differentiated between the installation method of the PV system, and thus the fire could have developed in a terrestrial (ground based), a building integrated, or a building applied PV system. Consequently, the fires are referred to as PV-related, and the calculated frequency represents an overall frequency of fires related to a PV system and not exclusively fires related to PV systems implemented in the built environment. The data from the Netherlands are the most recent, but due to the limited period of years, it was excluded from the frequency analysis. Instead, it was used for comparison and thus comparison with the calculated frequency.

Table 2.1: Overview of data-sets on PV-related fires, the duration of years where the data were collected, and the methods used to collect the data. ♠: Up to and including October 28th 2020 [48]

Country	Period of years	Source(s) used for collection
Australia:	2009-2015	Australian Fire & Emergency Service Authorities Council (AFAC) [79]
Germany:	2008-2012	Internet and media reports, operational reports from fire departments, assessor reports and statements, damage reports from Mannheimer insurance, and an Internet-based survey [41]
Italy:	2008-2015	Italian National Fire Corporation [44, 43]
The Netherlands:	2018-2020 ♠	Media and social media [48]
United States:	2009-2018	National Fire Incident Reporting System (NFIRS) Raw Structure Fire Data for: Equipment Power = 55-Solar by Year [47]

The frequency could be defined as a function of two parameters. Sepanski et al. and Fiorentini et al. calculated the frequencies in respectively Germany and Italy based on the number of photovoltaic systems [41, 44]. Nevertheless, such a method does not take the size of the PV system into account, and consequently, it could be derived that the frequencies are similar for small domestic installations, large systems on flat commercial roofs, and terrestrial PV systems. That does not correspond well with Lu, Phung, and Zhang, who stated that large PV systems could have thousands of connection points and that each of those points could cause an arc fault, and for this reason, a higher probability of an initial fire [86].

An alternative was to calculate the amount of annual PV-related fires as a function of the national cumulative capacities, which are available in annual reports from the International Energy Agency Photovoltaic Power Systems Programme (IEA-PVPS) [23]. Such definition was deemed more accurate as proportionality was expected between the system capacity and the number of components.

Based on the plot in figure 2.1, it became evident that the data was in-homogeneous as significantly more fires were observed in Australia and Italy compared to Germany and the United States. Common for the Australian and Italian data was that the National fire and rescue services had provided the data (see table 2.1). Thus a reporting system was assumed to be accessible for the national firefighters, and as a result, consistent data was provided. As strongly indicated by the name, the National Fire Incident Reporting System (NFIRS), PV-related fires in the US were reported in a similar system. However, Kinsey and Ahrens

stated that there were consistent challenges with obtaining input data into the NFIRS system [47, 144] and as a consequence, the data is probably underestimated. An underestimation is also expected for the German data as the use of multiple sources indicates that no coordinated system existed when the data was gathered in 2015.

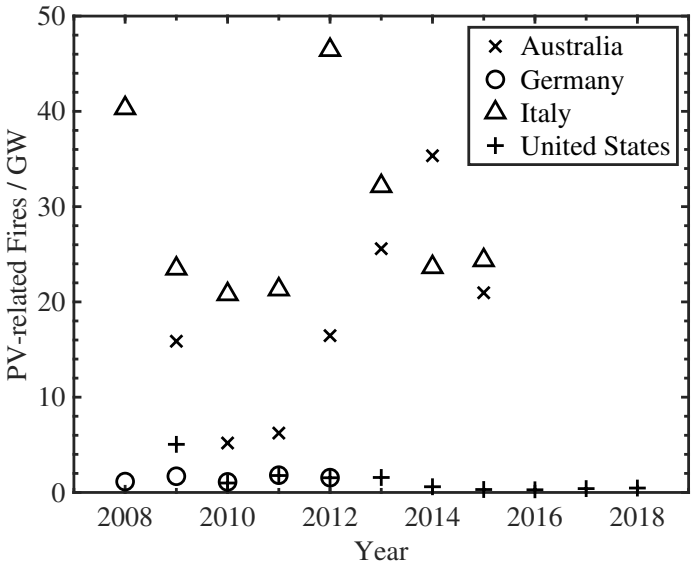

Figure 2.1: Annual PV-related fires per GW installed capacity ranging from 2008 to 2018 for Australia, Germany, Italy and the United States.I accordance with table 2.2 (from Mohd Nizam Ong et al. [3])

To work around the inconsistent data, the national and global frequencies were calculated as weighted averages instead of arithmetic averages, as seen in table 2.2. By using the weighted average, equal values were ascribed to every reported fire. That would not be the case if the averages were calculated by the arithmetic method as such an approach would assume that all fires were investigated and all fires related to a PV system were reported. Otherwise, the use of the arithmetic average ascribes equal values to reported and non-reported fires, which causes a reduction in the frequency if the quality of the collected data is poor.

2.2.2 Results

As seen from table 2.2, an annual global frequency of almost 29 PV-relates fires per gigawatt (GW) capacity was calculated. Based on the Dutch cumulative PV capacities of 4.5 GW and 6.9 GW, the equivalent amount of PV-related fires would be 131 and 199 in respectively 2018 and 2019, which are considerably higher than the 29 fires reported both years by Leene and van den Dikkenberg [48].

It was assumed that the significant difference was related to respectively: i) The Italian data dominating the annual global frequency and ii) the difference between the methods used to determine the number of fires in Italy and the Netherlands.
As seen from table 2.2, the vast majority of the reported fires occurred in Italy ($\approx 80\%$), and consequently, there was a clear link between the Italian frequencies and the annual global frequency. With the Italian data being collected by their National Fire Corporation, it was assumed that all fires related to the PV system were reported, no matter the size of the fire. Consequently, it could have included fires with minimal consequences. The PV-related fires in the Netherlands were, to some extent, described in the appendix of the report and in general, the magnitude of the fires was substantial and mostly related to some type of roof fire [48].

Such Interpretation of the significant difference could indicate a ratio between severe fires and minor incidents, where the global annual frequency of 29.3 fires/GW represents the latter and the annual frequencies of 0.98 fires/GW, 1.58 fires/GW, and 5.3 fires/GW from respectively the US, Germany and the Netherlands represents the more extensive fires. However, such a bold assumption cannot be stated based on the limited data available, and it should be challenged when more comprehensive data sets are generated or become available.

Despite the uncertainty related to the calculated annual frequency of 29.3 PV-related fire/GW, the analysis was the first analysis based on all data available. Consequently, it was also the most comprehensive estimation of how many PV-related fires a country or a property owner should expect during the anticipated lifetime of the PV system, which is between 25 and 40 years [31]. With the expected lifetime in mind, the global cumulative capacity in 1997 was 204 MW which represents 0.27‰ of the capacity in 2020 [36], and for this reason, it is currently unknown if the failure rate of the PV components increase when the current systems reach the end of the expected lifetime.

Table 2.2: Input data and calculation of the overall number of PV-related fires per gigawatt (GW) capacity per year for Germany, Italy, Australia, and the US. Note the change from megawatt to gigawatt between columns with cumulative capacity and frequency. (from Mohd Nizam Ong et al. [3])

Country	**Year**	**Number of Fires**	**Cumulative Capacity** [23] $[MW]$	**Frequency** $\left[\frac{fires}{GW}\right]$	**National Annual Average** $\left[\frac{fires}{(GWyear)}\right]$	**Global Annual Frequency** $\left[\frac{fires}{(GWyear)}\right]$
Germany [41]	2008	7	6120	1.14	1.58	29.34
	2009	18	10566	1.70		
	2010	20	18006	1.11		
	2011	47	25916	1.81		
	2012	53	34077	1.56		
Italy [145]	2008	20	496	40.32	32.59	
	2009	30	1277	23.49		
	2010	75	3605	20.80		
	2011	280	13141	21.31		
	2012	780	16796	46.44		
	2013	585	18198	32.15		
	2014	440	18607	23.65		
	2015	461	18915	24.37		
Australia [79]	2009	3	189	15.87	26.75	
	2010	3	578	5.19		
	2011	9	1444	6.23		
	2012	41	2491	16.46		
	2013	84	3283	25.59		
	2014	146	4131	35.34		
	2015	106	5057	20.96		
United States of America [47]	2009	6	1188	5.05	0.98	
	2010	2	2017	0.99		
	2011	7	3937	1.78		
	2012	11	7130	1.54		
	2013	19	12076	1.57		
	2014	11	18321	0.60		
	2015	8	25821	0.31		
	2016	14	49973	0.28		
	2017	21	51818	0.41		
	2018	29	62498	0.46		

2.3 Fault tree analysis

2.3.1 Available data and method

With an estimation of the frequency of PV-related fires, a fault tree was designed to enable an understanding of the initial ignition source. The possible ignition sources were summarised and classified into seven major events in the literature review (table 1.1). Based on that, a fault tree diagram in figure 2.2 was established where the top event, *PV-related fire*, could be activated by any of the previously defined major events (S01-S07) of which the first six events were related to an ignition caused by the PV system and the final, S07, was defined as an unknown component or an external source of ignition.

Common for the major events related to the PV system was that they were only activated when arcing or overheating of a component was not observed due to a failure or absence of a protective device detecting or interrupting the failure. Thus, the activation of S01 to S06 relied on an *and-gate* where the intermediate event X2 depended on an *or-gate* that could be activated by any of the reasons summarised in table 1.1 or the initial events A1 to F7 in table 2.3. As the data-sets only consisted of events which caused a fire, the *and-gate* between the major and intermediate events could be disregarded as arcing or overheating (X2) was never detected (X1), and consequently, all of the initial events (A1 to F7) activated the major events (S01 to S06).

Because the level of detail was inconsistent across the three data sets, the reported failure types were sorted into the major event following table 2.4. The selection of the major events was based on the categories in the British investigation report, and the failure types are described in the report by IEA-PVPS [143, 88]. As such, the failure types from the 80 fires (64 fires related to the PV system, 16 caused by external ignition source) reported in the UK matched perfectly. The amble amount of failure types (S01-S06) from the German data-set came from an overview which was strictly focused on ignition caused by components from the PV system (174 fires), which were previously detached from the total number of PV-related fires. As such, S07 consisted of the 220 PV-related fires caused by an external source of ignition. Finally, the 400 fires described in the Australian data-set were not described very detailed, and as a result, fires originating from the direct current (DC) combiner box, the DC cables, or the DC connectors (major events S04, S05, and S06) were not registered.

Table 2.3: Overview of major events (S01-S07), intermediate events (X1-X3), and initial events (A1-F7), which can lead to a PV-related fire in accordance with the Fault Tree Diagram in figure 2.2. (from Mohd Nizam Ong et al. [3])

Code	Event	Code	Event
S01:	Ignition caused by PV module	**B4:**	Manufacturing defects
S02:	Ignition caused by isolator	**B5:**	Damaged component
S03:	Ignition caused by inverter	**C1:**	Moisture ingress
S04:	Ignition caused by combiner box and fuse	**C2:**	Cable damage
S05:	Ignition caused by cable	**C3:**	Installation error
S06:	Ignition caused by connector	**C4:**	Lack of ventilation
S07:	Unidentified or unrelated source of ignition	**C5:**	Manufacturing defects
X1:	Failure/Absence of fault detection and interrupting devices	**D1:**	Water ingress
X2:	Arcing/Overheating	**D2:**	Loose screw terminals
X3:	Module damage	**D3:**	Component damage
A1:	Corrosion	**D4:**	Installation error
A2:	Bypass diode failure	**E1:**	Pulling out of cables
A3:	Installation error	**E2:**	Weathering effects
A4:	Manufacturing defect	**E3:**	Damages from animals
A5:	Damages from frame distortion	**E4:**	Installation errors
A6:	Damages from mountings	**F1:**	Moisture ingress
A7:	Excessive snow loads	**F2:**	Loose screw terminals
A8:	Vandalism	**F3:**	Incorrectly crimped contacts
A9:	Thermal expansion	**F4:**	Physical damage
A10:	Metallisation distortion	**F5:**	Installation error
B1:	Moisture ingress	**F6:**	Incompatible plugs and sockets
B2:	Loose screw terminals	**F7:**	Poorly soldered joints
B3:	Installation errors		

For each data-set, the ratio of PV-related fires caused by the seven major events was calculated and presented in table 2.5. In both Australia and Germany, the major event S07 represented the vast majority of cases and in the UK, ignition from an undefined or unrelated ignition source was the second most frequent cause of PV-related fires.

The major event S02 (Ignition caused by isolator) accounts for 35% of the PV-related fires in the UK, which is significantly more than the 6% and 8% in Australia and Germany (see table 2.5). The significant difference cannot be explained based on the available data, but the fire-related risk of especially the DC switches is acknowledged in both Australia and Germany. In the German report, it is noticed that some manufacturers recommend switching the DC isolator at least ten times a year to rub off any oxide layers, and thus a source of increased resistance [41]. The use of DC isolators had been mandatory in Australia since 2012, but during inspections

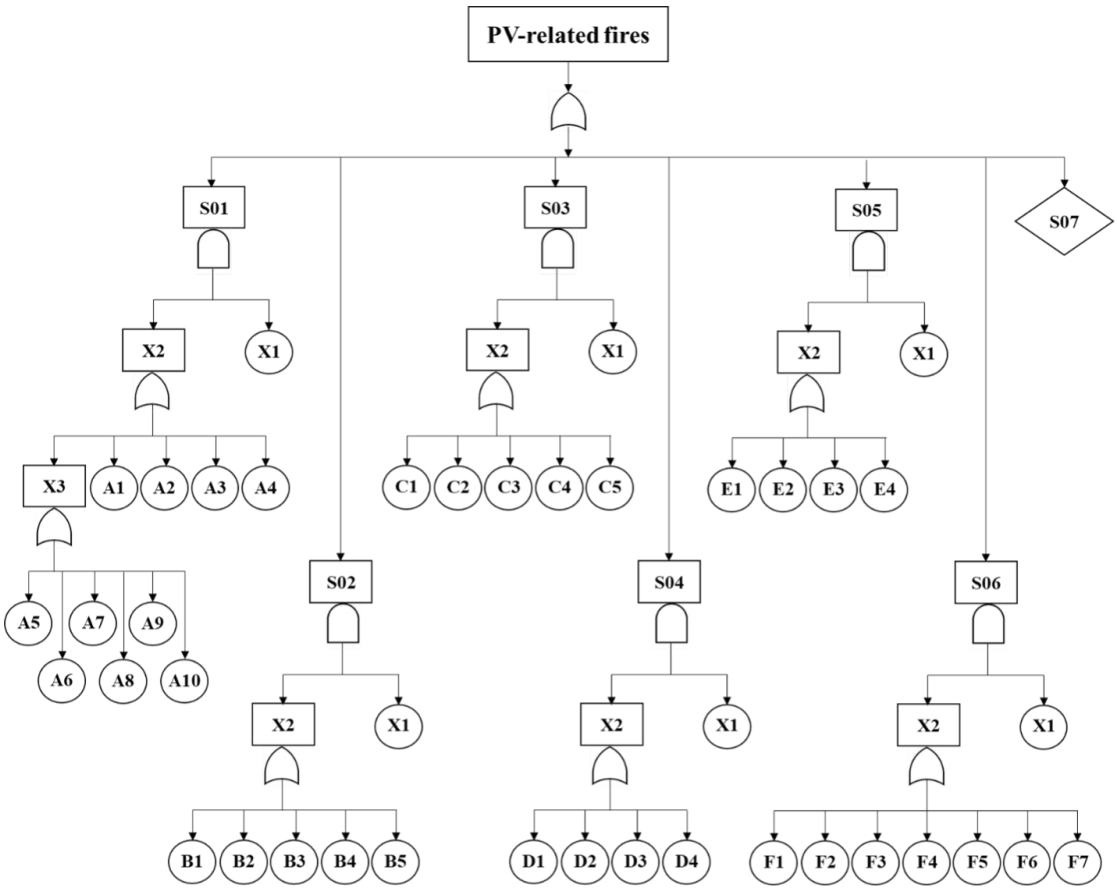

Figure 2.2: Qualitative fault tree diagram with a PV-related fire as the top event. Description of the major events (S01-S07) leading to the top event, as well as the intermediate (X1-X3) and initial events are found in table 2.3. *or-* and *and-gates* in accordance with Crowl and Louvar [142]. (Figure based on, but not similar to figure from Mohd Nizam Ong et al. [3])

of active PV systems, the isolator was deemed to represent the most significant risk [146], and in 2021 the mandate was removed. During the inspections, water ingress into the isolator represented the most common failure type, which corresponds well with the failures analysed by the British Research Establishment (BRE) in the UK [143]. In the British report, it was found that the fires had occurred due to poorly designed products (1/12 cases), incorrectly specified DC isolators (2/12 cases), or poor installation practices (9/12 cases).

The method used to collect the ignition data might also have caused the significantly lower stake of PV-related fires caused by an unknown component or an ignition source not related to the PV-system for the British data (S07 in table 2.5). In addition to 33 historical events, the remaining 47 forensic investigations were only carried out if the Fire and rescue service deemed that the PV system was clearly implicated as a possible cause of the fire or a significant hazard for the Fire and rescue service (FRS) [143]. Thus, fires related to, but not caused by, the PV system and fires which, according to the FRS, did not represent a significant hazard were not included in the data set.

Table 2.4: Qualitative Fault Tree Diagram for PV-related fires. (Table based on, but not similar to figure by Mohd Nizam Ong et al. [3])

Major event	Failure type grouping		
	UK [143]	**Germany** [41, 42]	**Australia** [79]
S01:	PV modules	Module, Junction box, Cell connector	Exterior roof/Solar panel
S02:	DC isolators	DC switch, AC switch	Isolator
S03:	Inverters	Inverter electronics, Inverter, Transformer, AC distribution	Inverter or switchboard overload
S04:	DC combiner box	Generator junction box, AC fuse, DC fuse	N/A
S05:	DC cables	DC cable	N/A
S06:	DC connectors	Crimping, DC terminal, AC terminal, DC plug, AC plug	N/A
S07:	Unidentified components	External causes of fire	Batteries, Exterior Other, In-House, Other, Deficiency/Failure, Electrical, Unknown

Table 2.5: Annual frequency of PV-related fires caused by the seven major events. (Table based on, but not similar to figure by Mohd Nizam Ong et al. [3]).

Major event		National PV-related fires in accordance with table			Normalised average	Frequency of major event
		UK	**Germany**	**Australia**		
		$[\%][143]$	$[\%][42]$	$[\%][79]$	$[\%]$	$\left[\frac{fires}{GW \cdot year}\right]$
S01:	Ignition caused by PV module	6	11	4	6.5	1.9
S02:	Ignition caused by isolator	35	8	6	13.9	4.0
S03:	Ignition caused by inverter	11	11	13	10.9	3.1
S04:	Ignition caused by combiner box and fuse	1	5	N/A	3.0	0.9
S05:	Ignition caused by cable	6	3	N/A	4.5	1.9
S06:	Ignition caused by connector	15	11	N/A	12.1	3.5
S07:	Unidentified or unrelated source of ignition	25	56	77	49.2	14.2

In Australia, the major event S07 occurred three times more often than in the UK, equivalent to 77% of the registered PV-related fires. From table 2.4 it was seen that nine categories were present in the Australian data-set, but that only three of the categories were related to components of the PV system, whereas the remaining six categories were ascribed to "batteries" (0.5%), "exterior other" (2.5%), "in-house" (4.5%), "other" (5.0%), "Deficiency failure" (15.5%), or the subcategory "unknown" (40.0%). It was expected that the high ratio of S07 in Australia could be linked to the fact that more than 30% of Australian homes had PV systems installed in 2020 [147] compared to around 3.5% of homes in the UK [148, 149]. Thus, PV systems are present in a substantially larger part of Australian homes and consequently involved in more fires. Depending on the sizes of those fires caused by sources other than the PV system, the system might get involved, whereupon the FRS have to consider it due to the risk related to DC current systems.

2.3.2 Results

Based on the above considerations, the fires caused by each of the seven major events were deemed acceptable for the three data sets, after which normalised averages were calculated for each event. The use of a normalised average was preferred due to the various inputs for each major event. Hence, the averages of S01, S02, S03, and S07 were calculated as an average of three data sets, whereas the averages of the major events S04, S05 and S06 were solely based on the data from the UK and Germany (see table 2.5). Subsequently, the normalised averages were multiplied with the global annual frequency of PV-related fires, and as such, the frequency of fires caused by the major events could be estimated.

Obviously, the data from Germany and Australia affected the normalised average of 49.2% and thus an annual frequency of 14.2 fires/GW for major event S07. With a reasonable expectation of a significant part of the Australian PV-related fires being caused by external fires in domestic installations, it can be questioned if the use of the capacity-based frequency, *fires/GW*, rather than the installation-based frequency, *fires/PV-installation*, was correct for this part of the analysis. If the global market penetration of PV systems implemented into the built environment reach levels similar to or higher than Australia's, PV systems will be present in at least every third household fire. Consequently, it might be necessary to separate future data into domestic and industrial/commercial PV-related fires. Despite the underlying limitations of the study, the current confined level of data does not permit hard conclusions to be drawn, and thus, the major event S07 - *Unidentified or unrelated source of ignition* are deemed the most likely source of ignition.

Ignition caused by the *isolator* (S02), *inverter* (S03), or *connector* (S06) were all deemed as runner-ups with annual frequencies of respectively 4.0 fires/GW, 3.1 fires/GW, and 3.5 fires/GW (see table 2.5). Common for those three major events was that the probability of failure depended on the workforce quality. As highlighted by Coonick [143], the consequences

of incorrect installation of the isolators could be severe. The same goes for the installation and maintenance of the inverter [143, 88, 41]. For the connectors, cross-connection accounts for parts of the fires [41, 96, 143, 150], and improper assembly of the connectors are among the other likely failure scenarios as defined in table 1.1.

2.4 Uncertainties

It is acknowledged that the calculated frequencies are subject to many uncertainties. They uncertainties could have been addressed by calculating the variance of the frequencies in table 2.2 and adding error bars to the plot in figure 2.1.

The introduction of error analysis methods such as calculation of the variance, and thus standard deviation, associated with the annual frequencies in table 2.2 would result in intervals that depending on the confidence interval would define the annual frequency in the given country. As such, the purpose of calculating the uncertainty would be to ensure that the actual annual frequency of fires/GW are within the defined interval and thus validate the accuracy of the frequency.

However, the value of error analysis is limited when the quantity and quality of the original data is as poor as discussed in section 2.1 and it is decided that there is no value in including the standard deviations of $0.12\ fires/GW/year$, $3.87\ fires/GW/year$, $3.20\ fires/GW/year$ and $0.35\ fires/GW/year$ for respectively Germany, Italy, Australia, and the US in table 2.2.

Using the data from Germany as an example, the maximum annual frequency would be less that $2\ fires/GW$ with a confidence interval of 99% (three standard deviations). But as long as it is unknown whether the *fires* define large roof fires or smaller incidents, the validity is as limited as without the added standard deviations

As such, it is decided that the use of error analysis would add an incorrect sense of certainty to the calculated frequencies, which is far from certain due to the various data collection methods defined in table 2.1. Instead, the limited quality and quantity of the data are emphasised as a factor that leads to a high degree of uncertainty.

2.5 Preliminary conclusion based on frequency analysis

A frequency and fault tree analysis were conducted with eight data sets from five different countries. It was accepted that the data quality could be questioned as the collection methods were inhomogeneous and conducted by different methods and stakeholders. However, the data-sets represented all of the available public data-sets associated with PV-related fires, and the analysis represented the first comprehensive analysis incorporating several data-sets.

The term PV-related fire was introduced because the PV system does not always cause fires involving the PV system. Based on data sets from Australia, Germany, Italy and the US, an annual frequency of 29.3 fires per GW installed capacity was calculated. It was estimated that the calculated frequency included fires of all sizes, and as a consequence, it over-predicted the number of fires compared to data sets based on media and social-media reports, such as small data sets from the Netherlands and the data-set from Germany. The estimation is based on the assumption that only fires of significant sizes would be included in (social) media reports.

In addition, it was concluded that most PV-related fires were caused by an unknown component of the PV system or an ignition source not related to the PV system. Runner-up ignition sources were the DC switches, inverters and connectors, which are all prone to poor workmanship. As such, it was verified that a reduction of the PV system acting as an ignition source might not be able to efficiently mitigate the overall fire risk related to PV systems in the built environment. Thus, focusing on mitigating the consequences might have a more significant mitigation effect.

In general, it was deemed that the analyses were the best possible based on the available data. However, a focus on an increased and homogeneous collection of data related to fires in the built environment, including PV installations, is highly recommended as such data will enable more accurate quantification of the risk associated with PV systems. Two questions are suggested for the National Fire and Rescue Services post-fire report systems: i) Was a PV system involved in the fire, and if so ii) what caused the fire? A total of eight options should be available based on the seven major events from the fault tree analysis, with the final major event being separated into the two options: a) fire caused by an unknown PV component and b) fire caused by an ignition source not related to the PV system.

Chapter 3

Experimental designs and methods

3.1 Chapter overview and organization

A total of three experimental set-ups, Set-up A, Set-up B, and Set-up C, were constructed to approach the five objectives related to the fire dynamic system consisting of a propagating flame front within a semi-enclosure defined by a horizontal roof construction below an inclined or horizontal PV module. As defined in the objectives, three set-ups were designed to quantify the influence of the geometry and material parameters of the upper and lower surfaces of the semi-enclosure.

Table 3.1 presents a general overview of the semi-enclosure geometric parameters examined in the three set-ups as well as the materials used in the experiments. By altering the parameters within, and across, the three experimental set-ups, the effect of each parameter could be quantified and discussed. Subsequently, the relevance of the individual parameters could be quantified and thus enable a discussion of their potential to mitigate the consequences of PV-related fires.

To support Table 3.1, a brief introduction of the three experimental set-ups are found in section 3.1.1 to Section 3.1.3. Subsequently, the two different panel types used throughout the three experimental set-ups are described in Section 3.2, followed by detailed descriptions of the set-ups in Sections 3.4 to 3.6.

3.1.1 Set-up A: Flame spread on PMMA in horizontal semi-enclosures

To quantify the consequences of the geometry, the influence of the gap height between the upper and lower semi-enclosure surface was examined. By substituting the roof construction with the well-studied reference material polymethyl methacrylate (PMMA) [135, 134, 133, 151, 152], the influence of the upper surface could be quantified. Besides the panels and panel rig, the set-up consisted of a second rig facilitating installation and instrumentation of the PMMA, which is described in Section 3.4 together with a general description of the combined

set-up and an experimental matrix. A total of 50 experiments were conducted, of which 11 experiments were baseline tests used to validate the set-up. All experiments were conducted with PMMA as the lower surface, and to reduce the material complexity, the stainless-steel board substituted a PV module in the majority of the remaining experiments.

Table 3.1: Overview of variables and data collected for the three experimental set-ups. Set-up A: Flame spread on PMMA in horizontal semi-enclosures, Set-up B: Flame spread on roof construction mock-up in semi-enclosure, and Set-up C: Medium-scale experiments with and adjacent roof.

	Geometric parameters ($\times$: parameter varied)		
	Set-up A:	**Set-up B:**	**Set-up C:**
Gap height:	$\times$	$\times$	-
Panel inclination:	-	$\times$	-
(unintended) Wind flow:	-	-	$\times$
Sample size:	$\times$	-	$\times$
	Upper surface of semi-enclosure (number of experiments)		
None (baseline):	11	-	-
Stainless-steel board:	34	18	-
PV module (new):	5	24	6
PV module (re-used):	-	-	6
	Lower surface of semi-enclosure (number of experiments)		
Polymethyl methacryate (PMMA):	50	-	-
PVC-based roofing membrane:	-	9	12
Roof construction mock-up:	-	33	-
	Data types ($\times$: data collected)		
Temperature $[^{\circ}C]$**:**	$\times$	$\times$	-
Heat Flux $[kW/m^2]$**:**	$\times$	-	$\times$
Mass Loss $[g]$**:**	$\times$	-	-
Location of flame front $[mm]$**:**	$\times$	$\times$	-
Location of burn out zone $[mm]$**:**	-	$\times$	-
Heat Release rate $[kW]$**:**	-	-	x

3.1.2 Set-up B: Flame spread on roof construction mock-up in semi-enclosure

By gradually increasing the complexity of the fire dynamic system studied with set-up A, the influence of the material parameters and geometry between roof construction mock-up and a horizontal barrier were studied through 42 experiments. The flexible experimental set-up enabled a gradual transition from the parametric studies conducted with set-up A to a mock-up roof construction with interchangeable insulation materials.

Twenty-four of the experiments were conducted with PV modules, and the stainless-steel board were used in the remaining experiments. Compared to the experiments conducted with set-up A, more parameters were introduced, and thus the experiments were significantly practical with a focus on *need to know* rather than *nice to know*. They were not experiments designed to develop or elaborate new theory but rather experiments where the results could be explained with existing knowledge, after which the importance of specific parameters could be discussed. Besides the panels and panel rig described in Sections 3.2 and 3.3, set-up B consisted of an instrumented roof construction mock-up described in Section 3.5 together with the experimental matrix.

3.1.3 Set-up C: Medium-scale experiments with adjacent roof

Finally, a small series of 12 experiments conducted with set-up C is presented in Section 3.6. Contrary to set-ups A and B, which were both the product of patient pre-experiments and subsequent modifications, set-up C was a set-up in development which turned out to be unfit for the laboratory and had too many parameters. However, the experiments are included in the thesis as they highlight the holistic behaviour of the system. As such, the heat release rate and heat flux inside and outside the semi-enclosure were quantified as a function of, mainly, the volumetric flow from the extraction hood. However, the roofing membrane area and brand, PV module condition, and location of the ignition source served as additional variables.

3.2 Panels

Two types of panels, or horizontal barriers, were used during the experimental campaigns; photovoltaic modules, or a stainless-steel board.

3.2.1 Black-body stainless-steel board

The black-body stainless-steel board was used in two of the three experiments and introduced for three reasons.

- It was a non-combustible substitute for the PV modules,
- which reduced the fire dynamic complexity of the system.
- It was reusable.
  - The number of experiments were unlimited.
  - The number of experiments were not limited by the number of PV modules.
  - It reduced the cost significantly.

Construction

The non-combustible stainless steel was constructed as a substitute for the PV modules. Thus, the board's geometry was similar to the geometry of a standard PV module, 1000 mm times 1700 m. The thickness of the stainless-steel sheet was 3 mm and the thickness was solely chosen with a focus on structural integrity.

The frame, constructed of Bosch Rexroth compatible aluminium profiles with a cross-section of 45 mm, supported the stainless-steel sheet on the non-exposed side. The sheet was attached to the frame along the edge of the sheet and the centre line to ensure a plane surface during the experiments. Holes were drilled and lowered, so the screws were flush with the surface of the lower side of the board (see Figure 3.1). Finally, the board was painted with a ceramic-based, black-pigmented coating for carbon and stainless steel with a maximum service temperature of 1316 °C (Aremco HIE-coat 840-MX [153]). Similar to the PV modules, the board was installed in the Panel Rig described in Section 3.3 and behaved similarly. The board was only installed horizontally as it was considered too heavy (> 40 kg) for inclined installations. As the board was re-used for a vast amount of experiments and tests, contrary to the single-use of the PV modules, it was subject to minor reuse-dependent changes.

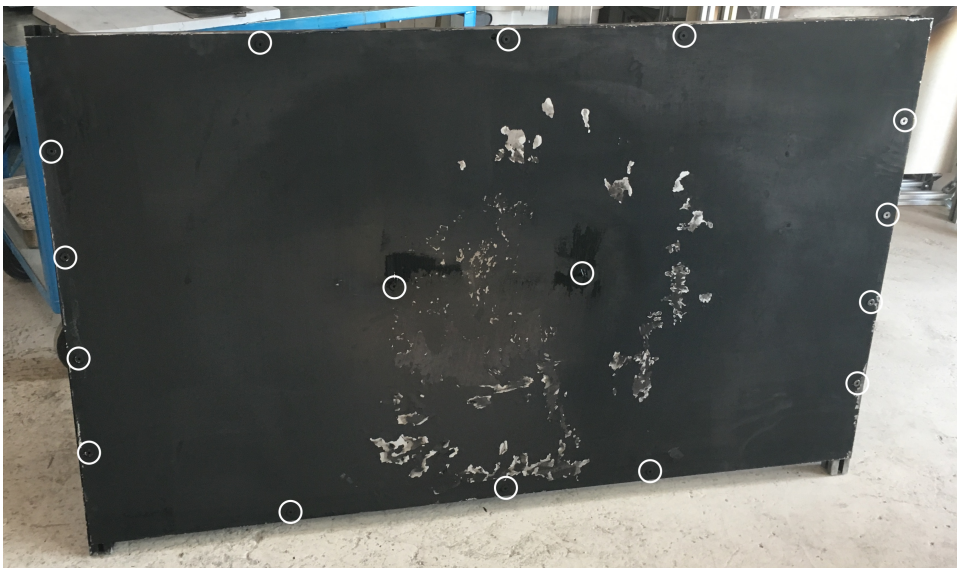

Figure 3.1: Paint damages at the stainless-steel board when brushed down after experiments. The lowered screws are visible on the right side of the board and are marked by white circles.

Deflection

Like the PV modules, the stainless-steel board deflected downwards during an experiment and regained the original shape when it cooled down. The deflections were not significant but visible during video analysis. Due to the reuse, the board was exposed to many temperature cycles. Combined with the fixation points, they caused some permanent local deflections with a maximum of 2 cm along the board's edges. The deflections along the edges were considered insignificant, as the experiments were conducted below the centre of the board.

If the experiments are reproduced, the use of rectangular holes should be considered to allow the two-dimensional expansion of the stainless-steel board along the edges of the frame.

Black body behaviour and soot production

When impinged by flames, the robustness of the Aremco HIE-coat 840-MX was limited, and in some spots, the paint burned or flaked off, as seen in Figure 3.1. The missing paint was only visible when the board was brushed thorough before removal from the panel rig. During the experiments, the board remained utterly black due to the combustion products from the subjacent fire. As such, the missing paint was not considered to affect the behaviour of the board. However, it was necessary to brush the board lightly between each experiment to ensure a plane surface, as several experiments without cleaning caused a vast buildup of soot below the board. Consequently, the soot caused an extremely uneven surface, and thus, the total surface area of soot increased, as seen in Figure 3.2, which caused inconsistent results for similar experiments.

Figure 3.2: Soot buildup below the stainless-steel board due to inadequate cleaning between experiments. Video frame from initial experiments from the MEng thesis of Benjamin Jacobs [5]

3.2.2 Photovoltaic modules

A total of 40 PV modules were used during the three experimental campaigns presented herein. The PV modules which were pre-used, or faulty, but non-damaged, were obtained from installers and therefore not a uniform collection. Thus, the five different mono- or poly-crystalline silicon PV modules presented in Table 3.2 were used.
Ideally, the same PV module brand and model were used through all experiments since the use of different modules introduced a variable related to the physical dimensions and material parameters of the PV modules.

Table 3.2: Overview of PV module brands used for the three experimental campaigns. PV1 modules were used in the experiments with flame spread on PMMA in horizontal semi-enclosures (see Section 3.4), and PV2 to PV4 modules were used in combination with the roof mock-up (see Section 3.5), and PV5 were were used in the medium-scale experiments (see Section 3.6).

PV#	Brand	Length [mm]	Width [mm]	Frame depth [mm]	Certification
PV1:	SolarWorld Sunmodule Plus SW Poly 250 [154]	1675	1001	22	CT2
PV2:	SUNTECH [155]	1950	990	40	Application Class A
PV3:	GCL Solar [156]	1645	990	28	NA
PV4:	AUO [157]	1560	1046	39	IEC 61215, IEC 61730, Fire Class C
PV5:	AXITEC, AC-250P/156-60S [158]	1640	992	30	IEC 61215, IEC 61730, DIN:ISO 9001:2008

3.3 Panel Rig

Although being a simple structure, the design of the rig had to comply with a list of requirements as it had to:

- support the panels with lengths between 1650 mm and 1950 mm.
- support the PV modules at inclinations from 0° to 15°.
- enable modification of gap height between the panels and the test rigs.
- permit easy buildup of the test rigs.

The solution was to divide the experimental rig into two components, as seen in Figure 3.3: i) the panel rig and ii) the test wagon. The test wagon was a rolling laboratory Table made of stainless steel, and the panel rig was a stationary rig with a permanent location below the extraction hood during test days, enabling a stable construction design. The use of the test wagon made it possible to prepare each experiment outside the extraction hood, whereupon it was rolled below the panel before the start of each experiment. That enabled easy access to the remaining part of the experimental setup, a cleaner installation process, better documentation opportunities, and better working conditions.

Due to the weight of the stainless-steel board (see Section 3.2.1), it was considered unwise to use an easily adjustable support system, as it increased the risk. As such, the rig (see Figure 3.3), which consisted of components from the Bosch Rexroth system, consisted of two 1900 mm tall frames (A and B), where the panels were supported at four locations (a3, a4, b3, and b4). A structure below the camera view stabilized the frames, and frame A was open at floor level to enable an accessible entrance and exit of the test wagon. A cross-sectional beam with two small aluminium profiles ensured the test wagon was located in the same position at each experiment.

The panel rig was modular, and depending on the dimensions of the PV modules, the distance between frames A and B could be adjusted as each frame was attached at four locations (a1, a2, a5, a6, and b1, b2, b5, b6 in figure 3.3). The inclination of the modules could be adjusted as a function of the height difference between the support-sets a3-a4 and b3-b4, as well as the distance between frames A and B. Definition of the inclination was based on standard geometric calculations of the ratio between the adjacent and opposite lengths with the panel acting as the hypotenuse in a right-angled triangle. In experiments with positive inclination, the height of b3-b4 was larger than a3-a4. The four support points were made of 100 mm aluminium profiles, each attached to the frames with a single bracket. When the PV modules were inclined, additional brackets were installed at the top of the aluminium profiles at a3 and a4 to prevent the PV modules from sliding. The internal width of frames A and B was 1 meter, making it possible to slide the PV modules in from the side of frame B when replaced for each experiment. The distance between frame A and B was 1.7 m in experiments with the stainless-steel board, but varied in the experiments with PV modules as a function of their dimension.

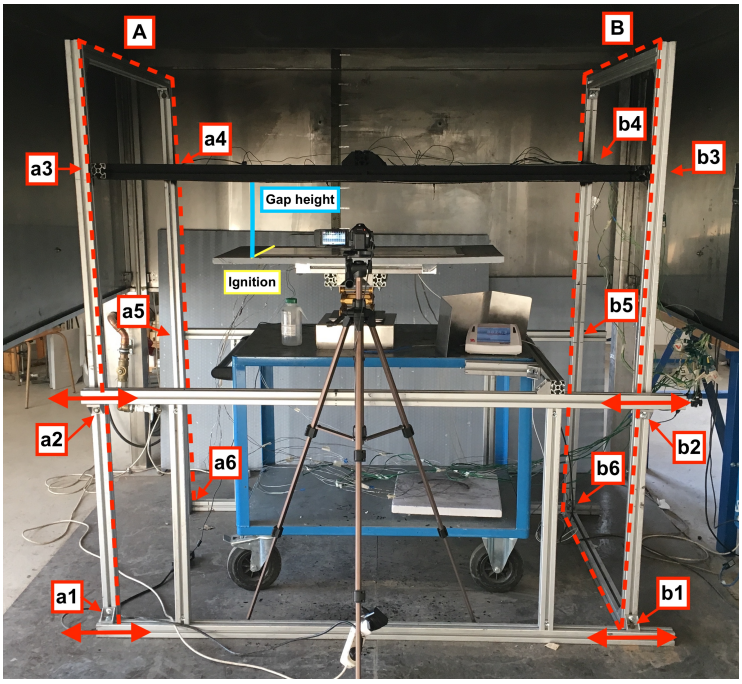

Figure 3.3: The panel rig, the test wagon, and the lower surface from set-up A (see Section 3.4). The capital letters A & B denote the two cross-sectional frames highlighted with dotted red lines. Lower case letters indicate the location of brackets and support used to modify the rig. The location of the camera depended on the combined experimental set-up.

3.3.1 Location of camera

Due to presence of the horizontal barrier, the camera could only record the from the side of the experimental set-up with a view perpendicular to the length of the PMMA and orientated towards the centre as seen in figure 3.3. Consequently, the camera recorded one-dimensional flame spread despite the two-dimensional surface of the thermally thin solid fuel. The viewpoint of the camera is used in the thesis to define objects to the left or right side of the centre, such as frames A and B in figure 3.3.

3.3.2 Adjustment and definition of gap height

To prevent endless adjustment and re-location of the panel supports a3, a4, b3, and b3 at the panel rig (see figure 3.3), the lower surfaces of set-ups A and B were installed on respectively one and two laboratory jacks. Both used laboratory jacks were the model SwissBoy 115 manufactured by Rudolf Grauer AG with a maximum static capacity of 40 kg and a range of 200 mm [159].

The adjustment of the laboratory jacks was very exact. They were stable in the direction perpendicular to the adjustment spindle and had minimal flexibility in the opposite direction when fully extended. The test rigs' inclination was secured by using a bubble leveller in both directions before ignition.

As the gap heights in some experiments were as low as 8 cm, they could not be measured at the centre-line of the test rigs. Thus, all gap heights, including experiments with inclined PV modules, were measured on the side of the test rigs at the location of the ignition source as illustrated by the blue and yellow lines in figure 3.3 . In the experiments where wood cribs were used as the ignition source (see Section 3.5), the centre of the wood crib was defined as the location of ignition.

3.4 Set-up A: Flame spread on PMMA in horizontal semi-enclosures

The experimental rig was designed to conduct an analysis of flame spread on a solid, thermally thin, fuel in horizontal semi-enclosures with various gap heights. By replacing the roofing membrane with a 2 mm thin sheet of polymethyl methacrylate (PMMA), the complex material parameters varying between different roofing products was eliminated. In addition, the use of PMMA enabled comparison of the flame spread rate between experiments with and without the horizontal barrier, which would not be possible with conventional roofing products as they are designed to prevent selfsustained flame spread as described in section 1.5.5. In combination with the Panel Rig (see Section 3.3) as well as the Black-body Stainless-steel Board (see Section 3.2.1) or a PV module, the experimental rig facilitated quantification of the following parameters:

- One-dimensional flame spread rate of the flame front.
- Temperature of the PMMA as a function of distance to the flame front.
- Heat flux as a function of distance to the flame front.
- Mass loss as a function of flame front location.

3.4.1 Design concept

The rig consisted of two components. A 22 mm thick non-combustible calcium silicate board (CSB) [160] for installation of the PMMA sample, and subjacent aluminium support to facilitate instrumentation, attachment to laboratory jack (see Section 3.3.2) as well as the structural support of the friable CSB. Thermocouples (TCs) were embedded in the PMMA and installed at a distance of 50 mm along the centre line of the CSB. A single heat flux gauge (HFG) was installed at the end of the TCs, as seen in figure 3.4. The rig was installed on top of an Ohaus laboratory scale with a precision of 0.1 g (see figure 3.5). To prevent flame spread along the edges of the PMMA sheet, ceramic paper with a height of 2 mm and a width of 20 mm was placed along the edges of the PMMA samples. The PMMA was ignited at the left side of the video camera view (see figure 3.4), which was used to track the location of the flame front as a function of time.

By analysing the recorded video(s) from each experiment, the flame front location could be determined as a function of time (see Section 4.2). As such, the time-dependent data related to temperature, heat flux, and mass loss were determined as a function of flame front location. A detailed description of the experimental rig is found in the following subsections.

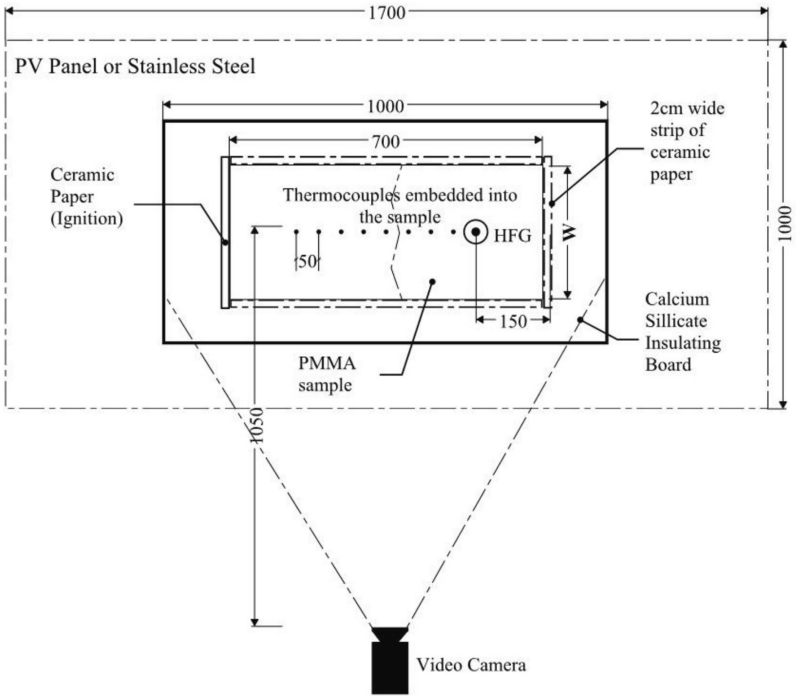

Figure 3.4: Top view of the experimental setup. Measurements in millimetres unless otherwise indicated. (from Kristensen et al. [6]).

3.4.2 The aluminium support

The aluminium support of the calcium silicate board (CSB) was made from Bosch Rexroth compatible brackets and aluminium profiles with a width of 45 mm. The CSB was supported by two 75 cm long profiles with a distance of 16 cm. The distance between the two profiles enabled the installation of the heat flux gauge as well as the thermocouples in the CSB (see Section 3.4.3). An aluminium bracket was designed to ensure that the upper surface of the HFG was level with the top of the calcium silicate board. Photos of the bracket and a description of the bracket and aluminium support are found in Appendix A.

3.4.3 Instrumentation

To enable embedding of the eight shielded thermocouples (type-k, gauge 14) into the PMMA, they were installed through eight bores in the calcium silicate board with 1 mm exposed at the upper surface. Pre-heating the thermocouple (TC) tips with a gas burner to at least 600 ℃ made it possible to melt the PMMA locally, and by applying a constant pressure until TC temperatures reached a maximum temperature of 60 ℃, the TCs were embedded along the centre-line of the PMMA.

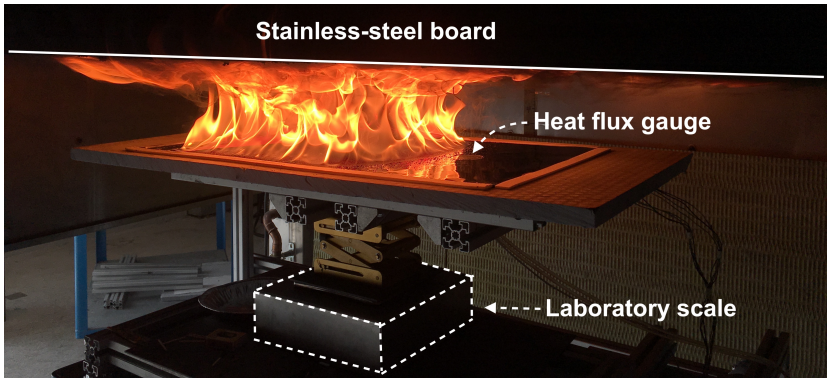

Figure 3.5: Image from an experiment in progress. The location of the stainless-steel board, heat flux gauge, and laboratory-scale are highlighted. Sample width of 400 mm. The photo is taken next to the video camera in figure 3.4.

The TCs were installed from the underside of the calcium silicate board. A stapler was used to fasten each TC to the board to prevent deflection when pressure was added to the tip of the TCs. The shielded cables from the TCs were stapled along the centre of the board for two reasons: i) To prevent the vertical drag of the TC tips from the weight of the shielded cables, ii) to ensure that the shielded cables are located in the gap between the two upper profiles in figure of the aluminium support. Detailed photos can be found in Figures A.3a, A.2a, and A.2b) in Appendix A.

A Hukseflux SBG01 heat flux gauge (HFG) with a range of 20 kW/m^2 was installed through a ø26 mm bore (see Figure 3.8. The HFG was connected to a water pump with a flow of 60 l/h installed in a basin with 50 litres of water to ensure a constant temperature of the instrument. Because of the temperature difference between the water-cooled HFG and the hot combustion products in the semi-enclosure, soot was expected to condense on top of the HFG. To protect the HFG from soot and direct flame impingement, a ø50 mm quartz disc with a thickness of 1.5 mm was placed above the HFG. To prevent conductive heat transfer from the HFG to the quartz disc and thus reduce the temperature difference between the smoke and the upper surface of the disc, an air gap was formed by placing the quartz disc on a ø50 mm metal ring with a height of 2 mm as seen in Figure A.3b. To measure the heat flux towards the PMMA, levelling the top of the HFG with the upper surface of the PMMA would be most accurate. But such installation causes increased exposure to the HFG housing, as well as the need of a metal ring with a larger height. A larger area of exposure increases the probability of a non-constant reference temperature for the HFG, whereas the use of a higher metal ring cause shadowing of the HFG censor. However, it was decided to avoid unintended shadowing of the HFG sensor, and thus the upper surface of the HFG was installed flush with the calcium silicate board instead of the PMMA.

An Ohaus laboratory scale monitored the mass loss rate of the PMMA with a precision of 0.1 grams. As seen in Figure 3.5, a steel cover was designed to protect the body of the scale, whose external control unit was connected by a single cable protected by aluminium foil.

3.4.4 Polymethyl methacrylate (PMMA) samples

Sheets of extruded opaque black PMMA with a thickness of 2 mm were cut into three different sample sizes with a laser cutter. As seen from Figure 3.4, all samples had a length of 700 mm, whereas the width of the three sample sizes was 200 mm, 300 mm, and 400 mm. A ø50 mm hole was laser-cut at the location of the heat flux gauge along the centre line with a distance of 150 mm to the edge of the sample. To avoid deflection of PMMA samples when applied on top of the heated thermocouples, the total length of 700 mm was laser-cut into two. The partition line was shaped like a large zigzag to prevent an abrupt passage from one sheet to another and facilitate easy assembly. In addition, splitting the samples into two transformed embedding of the TC tips in the PMMA samples to a two-step process where only four TC tips were heated at a time. Ensuring the correct temperature of four TCs, rather than eight made the installation process significantly more straightforward. Datasheet for the used PMMA can be found in Appendix B.4.

3.4.5 Experimental matrix

A total of 50 experiments were conducted, focusing on the sample width of 30 cm as seen from Table 3.3. The remaining 18 experiments were conducted with the sample widths of 20 (10) cm and 40 cm (8) as the flame emissivity, according to Kirchhoff's law [141], is linked to the emission coefficient and the characteristic length of the sample. Thus, the radiative fraction of the heat transfer became more dominant with increased sample width, whereupon the flame spread rate increased when Jiang et al. studied flame spread on PMMA samples with widths of 5 cm to 10 cm [6, 134, 133]. The eleven experiments conducted without any kind of panel served as reference experiments for comparison with previous research, the extended fundamental flame spread equation by Quintiere (see equation 1.2), and as baseline results for the remaining experiments.

Table 3.3: Experimental matrix of experiments conducted with different sample widths and gap heights. Experiments conducted with PV module type PV1 (table 3.2) are shown in parentheses [6].

Sample Width	Gap height						
	12 cm	**15 cm**	**17 cm**	**20 cm**	**22 cm**	**25 cm**	**No Panel**
20 cm:	1	2	3	1	1	-	4
30 cm:	1	7 + (2)	6 + (1)	6 + (2)	2	-	4
40 cm:	-	-	1	1	1	1	3

All but five of the experiments were conducted with the non-combustible stainless-steel board (see Section 3.2.1) to prevent an additional heat flux from the back sheet of the PV module. As such, the experiments were solely a study of how the introduction of the upper barrier affected the flame spread rate along the PMMA.

3.4.6 Ignition of the PMMA

To facilitate one-dimensional flame spread along the PMMA samples, the samples were ignited along the full sample width, whereupon an initial straight flame front was formed as seen in Figure 3.6. For ignition, the ceramic paper was soaked with 5 grams of methanol for each 10 cm of sample width. As such, consistent ignition was achieved across the three sample widths. The flame front remained straight in experiments with a fast flame spread rate (FSR), whereas a curved flame front formed in experiments with a slower FSR. In all experiments, the direction of flame spread occurred from the left to the right side of the PMMA sample. In each experiment, the methanol was applied after the ceramic paper was installed on the calcium silicate board and weighed by resetting the scale before application. After the application of the methanol, the scale was reset again to ensure a similar initial mass.

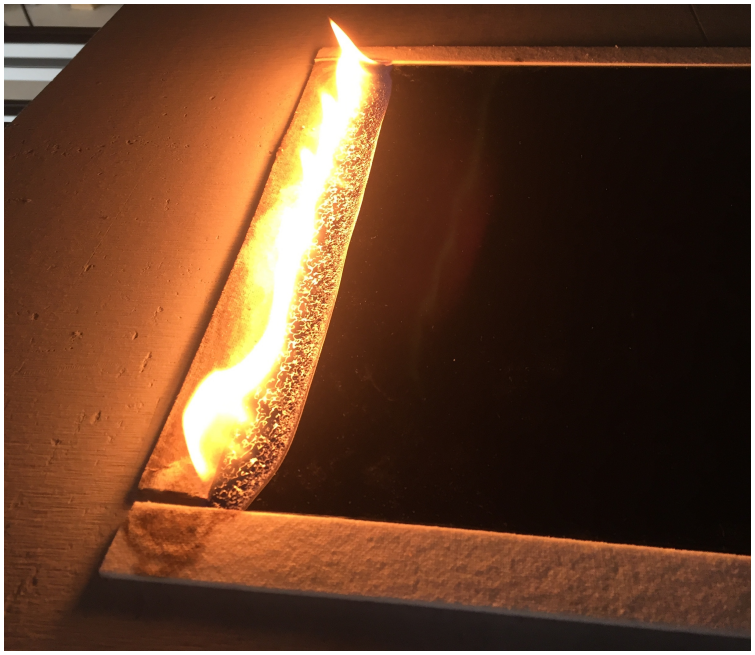

Figure 3.6: Flame front after ignition of a PMMA sample with a sample width of 400 mm.

3.5 Set-up B: Flame spread on roof construction mock-up in semi-enclosure

The difference between the roof construction mock-up (RCMU) and the first experimental rig in Section 3.4 was the materials used as well as the dimensions of the rig. Where the first rig was designed to obtain a fundamental understanding of flame spread on the reference material PMMA in a horizontal semi-enclosure. The purpose of the RCMU was to study the fire dynamics of a system representative of a flat roof construction. In addition, it was of interest to measure the temperature development in different insulation materials subjacent to the roofing membrane with the aim of quantifying their potential mitigation of the consequences. In combination with the panel rig (see Section 3.3) as well as the stainless-steel board (see Section 3.2.1) or a PV module, the rig was designed with the focus on:

- Facilitating an understanding of flame spread and temperature development in the subjacent insulation, as a function of:
  - Panel type: Stainless-steel board or PV module.
  - Gap height between panel and roof.
  - Inclination of panel.
  - Thermal parameters of the material below roofing membrane.
- Constructing a tree-dimensional roof mock-up consisting of:
  - A roofing membrane compliant with a test method in EN 13501-5 [67].
  - The use of different insulation materials.
  - Separation of potential fire-related consequences and the source of ignition.

3.5.1 Design concept

As it was decided to separate the source of ignition from the consequences of ignition, the length of the RCMU was separated into tree Sections as seen in Figure 3.7. Highlighted by the red triangle were a box with a length of 70 cm, a width of 30 cm, and a depth of 13 cm, where the three different roof constructions (RC-A, RC.B, and RC-C) could be installed in accordance with Table 3.4. Two flanges were installed on each side of the roof mock-up to facilitate ignition (left side) and the installation of a heat flux gauge (right side). With a length of 118 cm, the upper layer of roofing membrane almost covered the full length of the RCMU, whereupon the initial fire could propagate from the left flange, over the roof construction, and onto the right flange. By separating the ignition source and the heat flux gauge from the roof constructions, conductive heat transfer between the two components and the roof construction mock-up would be insignificant, as heat transfer through the roofing membrane was negligible according to section 1.5.1. However, it was acknowledged that the change of the material subjacent to the roofing membrane efficiently was an increase of the fire dynamic system complexity due to the change of the material properties of a system component, which was taken into account during the results analysis by only considering flame spread above the roof construction mock-up.

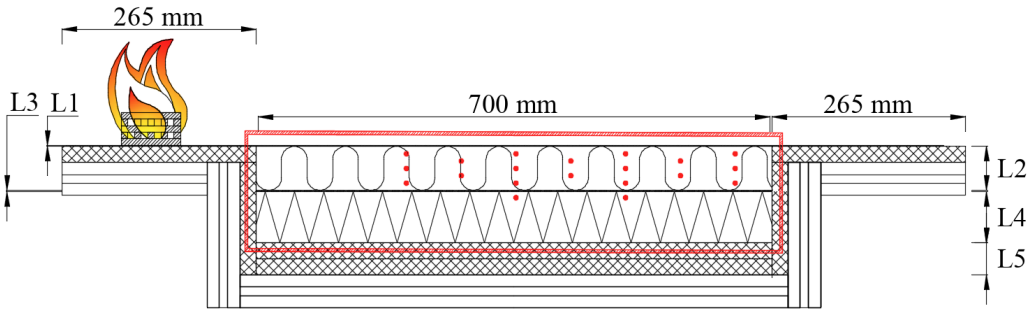

Figure 3.7: Sketch of the roof construction mock-up (RCMU). The location of the tested roof constructions are highlighted by the red square, where the thickness and material in each of the layers L1 to L5 are defined in Table 3.4. The red dots indicate the location of the thermocouples (TCs) installed along the centre-line of the insulation. Note that the location of the HFG is not visible in the sketch, but it is located at the centre line at a distance of 175 mm from the left side of the left flange (from Kristensen et al. [7]).

3.5.2 Ignition source

Based on the fault tree analysis and the frequency of a PV-related fire being caused by one of the seven major events in Table 2.5, the ignition sources can be grouped into two categories: i) ignition from direct current arcing caused by an electric malfunction in a component of the PV system (51.8%), and ii) an unknown ignition source or an ignition source not related to the PV system (49.2%).

With common temperatures of 6000 - 12,000 K [39] in ambient conditions the potential of direct current arcing as an ignition source is indisputable. However, the development of such fire can be a slow process developing over several days [78, 96]. The potential use of direct current as an ignition source was examined in cooperation with a certified electrician from the Danish Institute for Fire and Technology. Ignition of the membrane was possible, but the repeatability of the method was unsatisfactory, as small changes in the ambient conditions, such as humidity or temperature, rendered different outputs. Combined with the direct current risk, the method was decided to be unfit as an ignition source for the experimental set-up.

As self-sustained flame spread below building, applied PV systems were observed in genuine PV-related fires on commercial roof constructions (see Section 1.3), as well as large scale experiments [1], the fire can propagate outside the domain of the initial source of ignition. Thus, flame spread within the semi-enclosure was independent of the type of ignition, as long as the initial fire could detach from the ignition source.

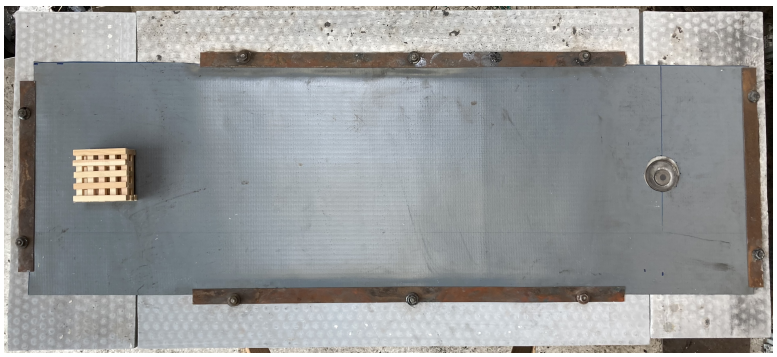

Figure 3.8: Top view of the mock-up roof construction before ignition of the wood crib. The membrane was fastened along the edges to prevent shrinkage, and the four metal rulers were attached to the below aluminium profiles.

Due to the reputation of being a well-tested ignition method with a high repeatability [74], it was decided to use a wood crib. The wood cribs were made of pine sticks with a length of 81 mm and a squared cross-section with a side length of 9 mm. Each wood crib consisted of four layers of five sticks. The four layers were elevated by two additional sticks parallel with the flame spread direction, which enabled ignition with a 50 mm times 80 mm sheet of ceramic paper soaked with 10 grams of methanol. The ceramic paper, with a thickness of 2 mm, was soaked with methanol and pushed below the wood crib just before ignition.

The wood crib was installed along the centre-line of the roofing membrane as seen from Figure 3.8. The wood crib was displaced one stick length (81 mm) from the left side of the membrane to ensure a consistent location and ignition of the roofing membrane corresponding to the expected domain of the wood crib. If the displacement of the wood was smaller, a smaller area of roofing membrane would be ignited and thus cause a lower initial heat release rate. A larger displacement would result in two flame fronts propagating to respectively the right and left side of the set-up.

Based on three measurements, the heat of combustion, ΔH_C, of the pine sticks was 18.6 kJ/g. The peak heat release rate measured by oxygen calorimetry and mass loss rate were measured to respectively 5.4 kW and 0.36 g/s [5]. The findings were slightly lower than the mass loss rate of 0.47 g/s calculated for the upper four layers of the wood crib in accordance with the method by McAllister and Finney [161]. With a combustion efficiency of around 80% based on the heat of combustion and the measurements in the cone calorimeter, the calculated mass loss rate corresponds to a peak heat release rate of 7 kW. However, the measured values are used throughout the thesis as they represent the specific wood crib.

With the assumption of a turbulent flow, the peak heat release rate of 5.4 kW corresponded to a flame extension below the upper surface of around 24 cm for gap heights of 8 to 12 cm, according to the method by Hasemi et al. [162, 163]. That is slightly higher than the experimental findings by Ju et al., who measured a flame extension of 15 cm below a panel

with a gap height of 10 cm and 10° inclination for a 5 kW laminar flame [114]. No data exists for horizontal upper surfaces, but at a distance of 12 cm from the gas burner, a heat flux of approximately 5.5 kW/m^2 was measured for the geometry in the studies by Ju et al. [114]. Without the horizontal barrier, the heat flux was measured to 1.5 kW/m^2 at a distance of 11 cm from a gas burner with a heat release rate of 5 kW [108]. As such, radiative heat transfer from the flame was expected towards the initial part of the insulation in the roof mock-up when a horizontal surface was installed above the roof construction mock-up.

3.5.3 The aluminium support and instrumentation

The rig was made from a combination of Bosch Rexroth compatible aluminium profiles (45 mm) and 22 mm thick non-combustible calcium silicate boards (see Appendix B.1). To enable adjustment of the gap height, the rig was installed on two lab jacks (see Section 3.3.2).

A Hukseflux SBG01 heat flux gauge (HFG) with a range of 20 kW/m^2 was installed through the flange on the right side of the roof construction. The installation and protection of the HFG were similar to the first experimental rig described in Section 3.4.3. The HFG was installed along the centre-line of the roof construction mock-up at a distance of 90 mm from the right side of the roof construction.

Temperatures in the insulation were monitored by 20 thermocouples installed along the centre-line as seen in Figures 3.7 and 3.9. The purpose of the TCs was to quantify the heat transfer through the insulation materials, the effect of the aluminium foil on the PIR insulation, as well as monitoring possible ignition of the EPS insulation. The installation of the gauge 14 shielded type-k thermocouples. Four arrays of TCs (depth; 10 mm, 30 mm, and 50 mm) were located at 50 mm, 200 mm, 350 mm, and 500 mm, and three TC sets (depths of 20 mm and 40 mm) were located at 125 mm, 275 mm, and 425 mm from the right side of the roof construction. Two additional TCs were installed in the EPS at a depth of 70 mm below the two TC arrays located at 200 mm and 350 mm. The thermocouples were shifted to the right of the roof mock-up to prevent heating from the wood crib and thus ensure that temperature changes were a result of the self-sustained fire inside the semi-enclosure rather than heat transfer from the source of ignition.

The TCs were permanently installed through a calcium silicate board, which lowered the likelihood of installing a TC at the wrong location. Before installation of the TCs, the intended location was marked on the side of the insulation material (see Figure 3.9a). All TCs were pulled almost out of the calcium silicate board, whereupon the tips of the TCs gradually were pushed into the insulation materials. With all TCs installed, the calcium silicate board was next to the side of the insulation, where it was fixed with a transverse aluminium profile fastened to the main frame, as seen in Figure 3.9b. Two smaller flanges with a width of 10 cm were installed along the length of the RCMU to reduce edge effects and to facilitate the installation of the upper layer of the roofing membrane (L1).

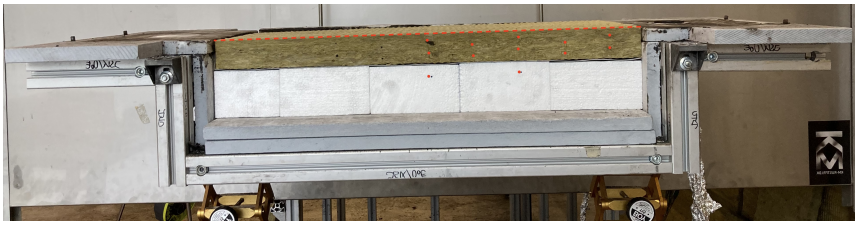

(a) Sample of roof construction in accordance with the layers L5 to L2 in RC-B (table 3.4). The intended location of the thermocouples is highlighted with red dots.

(b) Thermocouples (TCs) installed through a single board of 22 mm thick calcium silicate. The board and the TCs were locked in place by an aluminium profile.

Figure 3.9: Side view of the roof mock-up during preparation. Note that the images are of the side opposite the camera view during the experiments and therefore flipped horizontally to correspond with the view in Figure 3.7 and the direction of flame spread.

3.5.4 Roof constructions and materials

The experimental rig was designed to host three different roof constructions as defined in Table 3.4. The three roof build-ups were governed by three objectives:

- To quantify the difference between flame spread on PMMA and flame spread on roofing membrane compliant with EN 13501-5 in a horizontal semi-enclosure.
- To quantify the interaction between the burning roofing membrane and the subjacent materials.
- To test different mitigation solutions to prevent downward flame spread.

Table 3.4: Overview of the layers in the roof mock-up. The layers L1 to L5 are located as sketched in Figure 3.7. Note that the layer L2 in RC-A are installed on top of the roof mock-up, which causes an air gap of 131.5 mm. The thermal properties of the calcium silicate board and the insulation products can be found in Table 3.5. (from Kristensen et al. [7])

	RC-A	RC-B	RC-C
L1:	PVC-based Roofing membrane - 1.5 mm		
L2:	CSB - 22 mm	MW - 50 mm	PIR - ° mm
L3:	Air - 131.5 mm	PVC-based Roofing membrane - 1.5 mm	
L4:		EPS - 80 mm	EPS - 70 mm
L5:	Calcium Silicate Board (CSB) - 44 mm		

Roof construction A

RC-A stood out from the remaining roof constructions as the membrane was installed on a 22 mm thick calcium silicate board, which does not represent a commercial insulation product. However, RC-A facilitated a direct comparison with flame spread experiments on PMMA and material with significantly different thermal properties than the mineral wool and PIR insulation used in RC-B and RC-C.

Roof construction B and C

Neither the build-up of roof construction B nor C, represents a conventional solution of insulation on a light roof construction. They are simply attempts to mitigate the consequences if a property owner wishes to retrofit a PV installation on an existing flat-roofed commercial building insulated with an unknown material. In the experiments, the existing roof construction consisted of a roofing membrane (L3) on top of a layer of expanded polystyrene (L4) which was assumed to represent a worst-case scenario. As an initial fire on such roof construction would, most likely, result in burn down of the roof, two mitigation solutions were tested. The concept of the mitigation solutions was similar and consisted of an additional layer of insulation material (L2) and roofing membrane (L1) installed directly on top of the existing roof construction (L3 and L4).

It is accepted that the tested mitigation solutions had a one-eyed focus on fire safety. It did not consider the consequences with respect to moisture transport, as the existing roofing membrane in layer L3 will act as a moisture barrier that could affect the health of the existing insulation. As a complex analysis of moisture transport within the building was not within the scope of the thesis, it was decided to ignore the derived consequences of the suggested mitigation methods. The method was found relevant, as it was considered to be a simple solution preventing downward flame spread. If implementing the method into the built environment, a multidisciplinary analysis of the consequences should be performed.

Materials

A Bauder thermofol U15 FR roofing membrane was used in layer L1 through all experiments, as well as layer L3 in RC-B and RC-C. It was a 1.5 mm thick single-ply PVC-based roofing membrane with flame retardants. The membrane was classified B_{ROOF}(t4) in accordance with EN 13501-5 [67] when used in standard roof build-ups solely insulated with PIR insulation or mineral wool [164]. The heat of combustion, ΔH_C, for the roofing membrane was determined to $24.6 kJ/g$ via three tests conducted in an IKA C200 bomb calorimeter (see Table B.1 in Appendix B.5).

To fit the box hosting the roof construction, the roofing membrane in layer L3 had a width of 30 mm and a length of 700 mm. Width a length of 1180 mm and a width of 350 mm, the membrane used in layer L1 covered almost the entire length of the roof construction mock-up, whereas the width made it possible to fasten the membrane. To mimic a large roof construction, the membrane was fastened along all sides with metal rulers attached to the subjacent aluminium profiles. The fastening was performed to prevent shrinkage of the membrane, which could result in a forced increase of the flame spread rate and a local increase of fuel load if the membrane contracted when heated. The relevant thermal properties of the mineral wool, PIR insulation, EPS insulation and calcium silicate board (CSB) are available in Table 3.5. As noticed from Table 3.4, the thickness of the PIR insulation is 10 mm higher than the thickness of the mineral wool. Naturally, a similar material thickness would be ideal for a comparison between the two materials. However, it was decided that only products available on the market could be used as a mitigation layer.

Table 3.5: Thermal properties of the mineral wool (MW), PIR insulation (PIR), expanded polystyrene (EPS), and calcium silicate board (CSB). $\star$: Data obtained from correspondence with the manufacturer. Data sheets for the MW, PIR and CSB are presented in Appendix B.1, B.2, and B.3.

	Conductivity $k[mW/(mK)]$	**Density** $\rho[kg/m^3]$	**Specific Heat** $c_p[J/(kgK)]$
MW:	36 [165]	118 [165]	850 $\star$
PIR:	22 [166]	35 $\star$	1400 $\star$
EPS:	38-39 [167]	15 [167]	1210 [168]
CSB:	60 [160]	250 [160]	748 [169]

The PIR insulation board was a Kingspan Therma TR26 with a core of 60 mm PIR foam protected by aluminium foil on both surfaces. The mineral wool was a 50 mm thick batts of unprotected ROCKWOOL sold under the product name *stålunderlag 50*. Both materials were cut to fit the box in the roof construction mock-up with a length of 700 mm and a width of 300 mm. A jigsaw was used for the PIR insulation, whereas a large table-installed circular saw was used for the mineral wool. The cutting method choice depended on the insulation product's initial size, but both methods ensure smooth surfaces.

Due to the different thicknesses of the mineral wool and PIR insulation, the thickness of the EPS in layer L4 deviated between RC-B and RC-C. To ensure that the upper surface of layer L2 was flush with the calcium silicate board on the two flanges, a hot-wire EPS cutter was used to cut the material with high accuracy.

3.5.5 Experimental matrix

A total of 42 experiments were conducted with the roof construction mock-up. As seen from Table 3.6, one of the three roof constructions defined in Table 3.4 were used in all experiments. All of the experiments with the stainless steel board (SS) and PV module type 2 (PV2) (B1-B35) were repeated to examine whether the reproducibility was satisfactory, with 19 being the only exception. That experiment was conducted for comparison with a similar experiment conducted with the stainless-steel board but not repeated due to the results of experiments with a lower gap height (B20-B21) which did not result in flame spread. Consequently, using the additional PV module for an experiment with different geometry was preferred.

For the experiments conducted with PV module types PV 3 and PV4 (B36-B42), the experiments were not repeated due to the limited number of each PV module type, and thus it was expected that the repeatability of the previous studies with inclined modules (B28-B35) could represent these experiments as well.

As seen from the experimental matrix in Table 3.6, the roof construction type with mineral wool as the upper layer (RC-B) was used for the majority of the experiments (24) as it represented a link to the experiments conducted with the calcium silicate board (B1-B9), and a link between the experiments conducted the stainless-steel board (B10-B18) and PV module type PV2 (B19-B21, B24-B25, B28-B29, B32-B33). Furthermore, the type of roof construction was preferred for the non-repeated experiments with inclined PV modules of type PV3 and PV4 (B36-B42).

The mineral wool was preferred rather than the PIR insulation in the final seven experiments (B36 - B42) as a consequence of the behaviour in the series of experiments where the two insulation materials were compared against each other (B22 - B35). When exposed to heat, the PIR insulation is designed to swell, which increases the thickness of the product and thus the distance between the fire and the core of the intact PIR foam. That mechanism, combined with the delamination of PV cells from the PV modules, caused a significant obstruction of the camera view, which yielded a less reliable analysis of the video. Thus, it was decided to use the roof construction RC-B in those experiments as the use of both roof constructions (RC-B and RC-C) was not possible due to the limited amount of modules type PV3 and PV4. If more PV modules were available, a rerun of experiments B36 to B42 should have been preferred above experiments across different roof construction types as the influence of the parameter was examined.

Table 3.6: Experimental matrix for the experiments conducted with the roof construction mock-up. Two panel types were used for the experiments: i) a stainless-steel board (SS) as defined in subsection 3.2.1, and ii) three types of PV modules (PV2, PV3, and PV4) as defined in Table 3.2 (p. 60). The three roof construction types (RC-A, RC-B, and RC-C) are defined in Table 3.4 (p. 73.).

Experiment	Panel type	Roof construction	Gap height H	Inclination θ
B1, B2:	SS	RC-A	8 cm	0°
B3, B4:			10 cm	
B5, B6:			12 cm	
B7, B8, B9:			11 cm	
B10, B11:		RC-B	8 cm	
B12, B13:			10 cm	
B14, B15:			12 cm	
B17, B18:			11 cm	
B19:	PV2		12 cm	
B20, B21:			11 cm	
B22, B23:		RC-C		
B24, B25:		RC-B	10 cm	
B26, B27:		RC-C		
B28, B29:		RC-B	8 cm	
B30, B31:		RC-C		
B32, B33:		RC-B		10°
B34, B35:		RC-C		
B36:	PV3	RC-B		
B37:				13°
B38:				15°
B39:	PV4			10°
B40:			10 cm	
B41:			11 cm	
B42:			12 cm	

3.6 Set-up C: Medium-scale experiments with adjacent roof

A third, small series of experiments were conducted to quantify the heat release rate (HRR) and heat flux towards the roof construction in- and outside the semi-enclosure composed of the PV module and the roof construction, which in combination with an initial fire, generated a system with complex fire dynamics. The experimental set-up was, compared to the other experimental set-ups described in Sections 3.4 and 3.5, more provisional as the instrumentation and various parameters were modified continually. The experimental set-ups used for those two experiments were the outcome similar test runs where analysis of the initial test results

facilitated the final design of the set-ups and experimental matrices. They were the results of continuous testing in the fire laboratory at the Technical University of Denmark, where time in the laboratory was undisturbed and almost unrestricted since the experiments represented the vast majority of the ongoing research.

The initial concept of these experiments, conducted at the University of Edinburgh, was to design a large multi-parameter set-up consisting of a roofing membrane-covered lower surface of around $3.4\,m^2$ with half of it covered by a PV module (1.0 m times 1.7 m). However, the physical size of the experimental set-up within the extraction hood of 2.5 m times 2.5 m, combined with the volumetric flow from the extraction hood, probably caused high flow velocities along the lower surface. Thus, it was necessary to change the volumetric extraction flow during the experiments, as a too high initial flow prevented ignition, whereas a too low flow caused the formation of a heavy smoke layer that spread outside the extraction hood for even smaller areas of roofing membrane. Due to the limited area of the roofing membrane and the influence of the extraction hood, it was concluded that the experimental set-up was not ideal as the basis for the intended experimental campaign.

Still, the issues related to the extraction flow revealed the flow sensitivity of the ignition process where the initial ignition source transformed into a self-sustainable fire detached from the point of origin. The experiments also quantified the heat release rate and the radiative heat flux towards the lower surface in- and outside of the semi-enclosure. Thus, the initial test runs provided some data which, unintended, represented valuable inputs to the overall understanding of flame spread in the semi-enclosure between a PV system and a flat roof construction.

As such, the experimental set-up is not presented with a focus on the intended, unachieved outcome but rather on the actual outcome of the conducted tests, which, to some extent, provided an initial understanding of:

- The heat flux inside the semi-enclosure.
- The heat flux near the edge the PV array.
- The influence of flow on the ignition and flame spread phase.
- Determination of heat release rate of the fires.

3.6.1 Design concept

The experimental set-up was designed to mimic a small roof construction with two similar-sized areas. As seen in Figure 3.10, one half of the roof was covered by a PV module, and the other half represented the adjacent roof construction.

The set-up consisted of a large aluminium frame made of components from the Bosch Rexroth system, 22 mm thick boards of non-combustible calcium silicate were installed on top of the aluminium frame (see Appendix B.1), and a PVC-based roofing membrane was installed os the upper layer.

As the experimental set-up was designed for the crowded fire laboratory at the University of Edinburgh, the aluminium system consisted of four two-dimensional frames with a length of 1900 mm connected by 750 mm long aluminium profiles equipped with quick-connectors. Such construction enabled easy set-up and dismantling and reduced the storage space significantly.

The non-combustible calcium silicate board was preferred instead of a roof construction mock-up as the latter would cause a more complex experimental set-up. As such, the set-up did not reassemble an actual roof construction, but since the roofing membrane was expected to be the main fire load on the roof, the overall fire dynamic scenario with flame spread in a semi-enclosure was achieved.

Since the presented set-up was not a final experimental set-up but rather a set-up in development, the sketched experimental set-up in Figure 3.10 did not represent all experiments conducted. The frame's dimensions remained constant through all experiments, whereas the instrumentation, dimension of the roofing membrane, location of the ignition source, and the initial state of the PV modules varied.

3.6.2 Location of the PV module

A total of six PV modules (PV5 in sec. 3.2.2) were used in the 12 experiments presented herein. As a consequence, all of the PV modules were reused, which enabled comparison of the results and thereby discussion of the PV module's role as a potential fuel load. In all experiments, the PV modules were installed with an inclination of 13° and a distance of 9 cm between the module's lowest point and the roof's upper surface, similar to previous large-scale experiments [1]. The distance of 9 cm between the frame and roof was equivalent to a gap height of 12 cm, as the depth of the PV module frame was 3 cm (see Table 3.2) and $\cos(13^\circ) \approx 1$. The PV modules were supported by four brackets as seen in Figure 3.10.

3.6.3 Source of ignition

A three-layer wood crib with three sticks in each layer was used for ignition. The squared side length of the sticks was 2 cm, whereas the length was 10 cm. The sticks were hand-cut with a jigsaw from a board of medium density fiberboard. Despite the fact that wood cribs are considered a reliable and reproducible ignition source [74, 170], the use of hand-cut sticks reduced the reproducibility as roughly cut edges caused variation of the stick surfaces and thus a variation between the individual wood cribs. All in all, the roughness of the sticks was not expected to have a significant impact on the outcome of the experiments, and since they

(a) Side view of the experimental set-up with the roofing membrane and wood crib installed in correspondence with the sectional top view in Figure 3.10b.

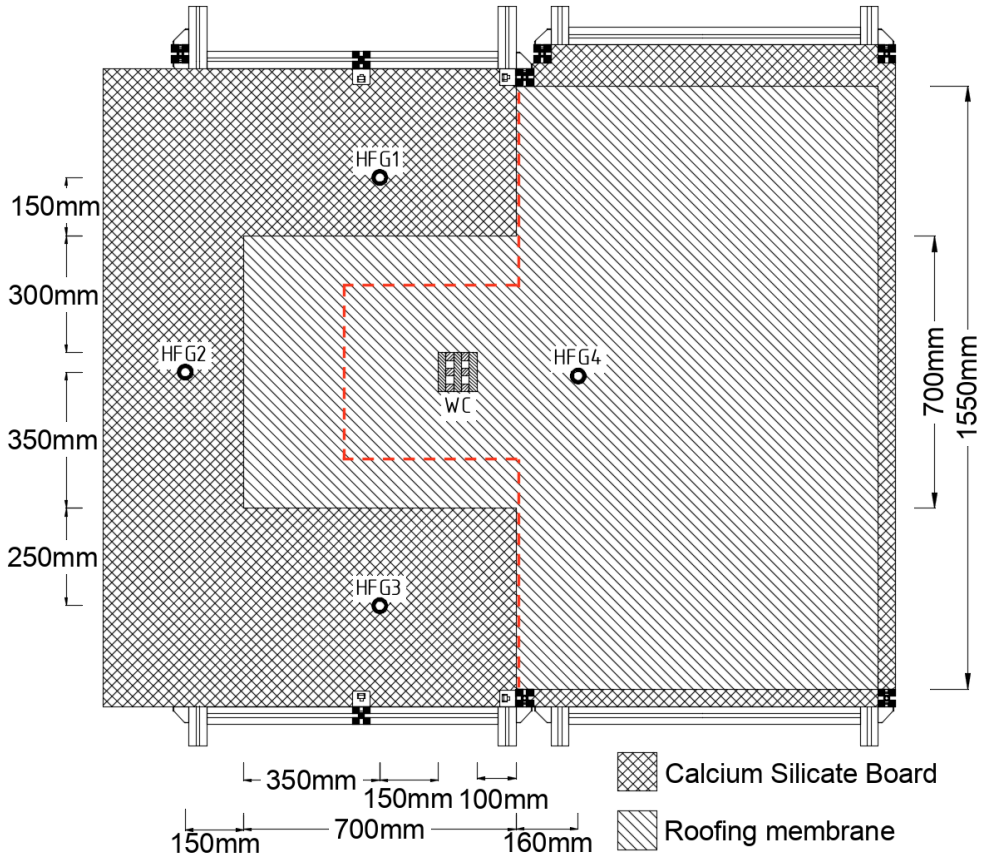

(b) Sectional top view of the experimental set-up with a 700 mm times 700 mm (shaded), or 450 mm times 450 mm (marked with dashed red lines) area of roofing membrane below the PV module and 10 cm displacement of the wood crib from the edge of the PV module similar to the setups C7 to C10 in Table 3.8. **HFG:** Heat Flux Gauge. **WC:** Wood Crib.

Figure 3.10: Visual overview of the medium-scale experimental set-up used to analyse the influence of flow and heat flux in- and outside the semi-enclosure formed by the PV module and the subjacent surface.

were provisional rather than carefully planned, the wood cribs were accepted as a preliminary ignition source made from the materials available. 10 g of barbeque firelighters were used for the ignition of the wood cribs, which had a peak heat release rate (pHRR) of 5.1 kW when tested without a PV module on a sheet of roofing membrane. Ideally, the pHRR was measured

for the wood crib alone, but given that the wood crib was located on the roofing membrane in all experiments, the development of the initial fire was similar since the ignition of the roofing membrane would be inevitable. As such, the measured pHRR was considered representative of the ignition source used in the experiments.

3.6.4 Maximum size and type of roofing membrane

Due to the capacity of the extraction hood in the fire laboratory at the University of Edinburgh and an unclean combustion process of the burning roofing membrane, the area of the roofing membrane below the PV module did not cover all of the lower surfaces in the semi-enclosure. To prevent smoke outside the extraction hood, a squared area of roofing membrane was gradually increased to a maximum side length of 70 cm. The side length of 70 cm is illustrated in Figure 3.10, whereas the. Two roofing membranes were used in the experiments; The 1.5 mm thick membrane from Bauder was used for experimental set-up B (see Section 3.5.4) as well as a 2 mm thick membrane from SIKA. Data sheets and a detailed description of the membranes can be found in Appendix B.5, but as seen in Table 3.7, the critical heat flux and heat of combustion of the two membranes were almost similar.

Table 3.7: Parameters of the two used PVC-based roofing membranes. The critical heat fluxes are based on Figure B.1 (see Appendix B.5). Measurements of the critical heat flux for the Bauder membrane are found in Table B.1 (see AppendixB.5), whereas the heat of combustion for the SIKA membrane is based on previous tests conducted by Kristensen [2].

Membrane	Product	Thickness	Mass per area	Critical heat flux	Heat of combustion
Bauder:	Thermofol U15 FR	1.5 mm	$1.83\ kg/m^2$	$\approx 7\ kW/m^2$	$24.6 kJ/g$
SIKA:	Sikaplan S20	2.0 mm	$2.60\ kg/m^2$	$\approx 7\ kW/m^2$	25.3 kJ/g

However, the mass per area of the SIKA membrane was more than 40% higher than the mass of the Bauder membrane. If it is assumed that the combustion efficiency and the mass loss rate of the two roofing membranes were similar, the significantly higher fuel load of the SIKA membrane will result in a longer duration of the fire, which might cause a higher heat release rate due to a larger area being ignited.

The part of the set-up representing the open roof construction adjacent to the PV module was covered by roofing membrane in the majority of the experiments, as seen in Figure 3.11. Below the PV module, a stapler was used to attach the roofing membrane to the calcium silicate board, whereas the membrane was bolted to the aluminium frame on the part of the roof not covered by the PV module, as seen in Figure 3.11. Additional staples were used on edge between the semi-enclosure and the open surface.

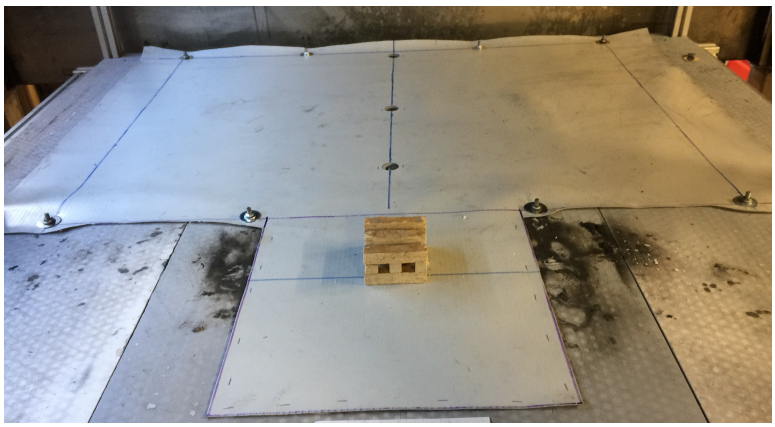

Figure 3.11: Bauder roofing membrane installed on the calcium silicate board. The squared section below the wood crib had a side length of 45 cm, and the wood crib was displaced 10 cm from the edge of the PV, similar to the set-up in fígure 3.10. Three heat flux gauges (HFG) are seen along the centre-line above the wood crib, but only data from the nearest HFG, equivalent to HFG4 in Figure 3.10b, is presented in the thesis.

3.6.5 Instrumentation

The heat release rate was measured in all experiments and calculated using the method by Janssens [171]. One or four heat flux gauges (HFGs) were attached to the aluminium frame (see Appendix A) and installed through ø26 mm holes drilled in the calcium silicate board (CSB) as seen in Figure 3.10b. The upper surface of the HFGs was installed flush with the CSB, and a quartz disc protected the sensor of the HFGs below the PV module. The HFGs were water-cooled Hukseflux SBG1 with measurement ranges of $50\,kW/m^2$ and $100\,kW/m^2$. The heat flux gauge HFG4 was located outside the semi-enclosure with a horizontal distance of 16 cm perpendicularly to the line below the edge of the PV module as illustrated in Figure 3.10b. The remaining heat flux gauges HFG1, HFG2 and HFG3 were located inside the semi-enclosure as seen from Figure 3.10b. Because the HFGs were installed through the calcium silicate board, their location was permanent, and thus HFG1, HFG2, and HFG3 were installed after the maximum side length of the roofing membrane in the semi-enclosure was determined to be 70 cm.

3.6.6 Experimental matrix

Based on all of the experiments conducted through the initial test cycle of the set-up, a total of 12 experiments are presented in the thesis, as they represented two sets of experiments with constant dimensions of the roofing membrane below the PV module. Other experiments were conducted with different dimensions of the roofing membrane, but they were primarily stand-alone experiments, whereupon cross-experimental comparison was not possible. As such, only experiments conducted with side lengths of 45 cm (C1 to C6) and 70 cm (C7 to C12) are presented in Table 3.8.

Table 3.8: Experimental matrix of the 12 medium-scale experiments. In all experiments, the area of the roofing membrane was squared with a side length of either 45 cm or 70 cm. Displacement of the wood crib was defined as the distance between the right side of the wood crib and the lower edge of the PV module, as seen in Figure 3.10. ⋆: The roofing membrane and the wood crib were displaced 10 cm, and thus the right side of the wood crib was located on the edge of the roofing membrane.

Experiment	Membrane Side length	PV Condition	Displacement of wood crib	Membrane manufacturer	Heat Flux Gauges
C1:	45 cm	New	10 cm	Bauder	1
C2:					
C3:		Used			
C4:				Sika	
C5:				Bauder	
C6:					
C7:	70 cm	New		Sika	
C8:		Used	10 cm ⋆		
C9:		New	10 cm		4
C10:		Used			
C11:		New	-5 cm		
C12:			0 cm		

Based on the experimental matrix, the variation in the experiments with a side length of 45 cm (C1 to C6) is limited as C1 and C2, as well as C3, C5, and C6, are similar, whereupon they should facilitate verification of the results, and comparison between similar experiments conducted with respectively a new PV modules (C1 and C2), and re-used PV modules with a burned back sheet membrane. In the experiments where the roofing membrane had a side length of 70 cm, five different experimental set-ups were tested, with C7 and C9 being the only repetitions. As such, comparison across experiments was limited.

Despite the similarities across some of the experiments in the Table 3.8, a final parameter, being the volumetric flow from the extraction hood, affected the outcome of the experiments. In all experiments, the initial flow was around 500 litres per second. However, the smoke production from the burning roofing membrane caused the necessity for a higher extraction flow. Adjustment as a function of time as well as a manual adjustment as a function of heat release rate considered unsuccessful. At the same time, a higher initial flow affected the initial ignition process as the concentration of pyrolysis gases was diluted by the extraction flow, whereupon flame spread was not achieved.

Thus, no extensive experimental series was conducted with the set-up.

Chapter 4

Results and analysis

4.1 Chapter overview and organization

The three experimental set-ups rendered various experimental outputs, which required different levels of data processing before the raw data could be presented and subsequently analysed. Based on the instrumentation of the three set-ups, six different types of data were obtained, as seen in Table 4.1.

Table 4.1: Data types extracted from the three experimental set-ups. $\times$ marks that the data type was quantified. $(\times)$ indicates that the magnitude was estimated but not quantified.

	Temperature (°C)	**Heat Flux (kW/m^2)**	**Mass Loss (g)**	**Location of flame front (mm)**	**Location of burn out edge (mm)**	**Heat release rate (kW)**
Set-up A: Flame spread on PMMA in horizontal semi-enclosures	$\times$	$\times$	$\times$	$\times$		
Set-up B: Flame spread on roof construction mock-up in semi-enclosure	$\times$	$(\times)$		$\times$	$\times$	
Set-up C: Medium-scale experiments with adjacent roof		$\times$				$\times$

Overall, the six types of data could be separated into two groups: i) data types proportional to the raw data and ii) data types which needed post-experimental processing.

The measured temperatures, heat flux, and mass loss were within the first category. The mass loss was logged directly on the computer through the software provided by the scale manufacturer Ohaus. Similarly, the temperatures measured by the type-k thermocouples were logged directly by the Keysight BenchLink software used for the Agilent data loggers. Each of the Hukseflux SBG01 heat flux gauges was calibrated by the manufacturer, and by utilizing the computational option in the Keysight BenchLink, the heat fluxes were calculated during the experiments. Both the raw data voltage and the calculated heat fluxes were saved for each experiment in case of mistakes.

The remaining three types of data, the heat release rate and flame front and burn out edge, were a result of post-experimental processing of the data. The heat release rates were based on the concentration of oxygen (O_2), carbon-monoxide (CO), and carbon dioxide (CO_2) and were calculated by the method of Janssens [171], whereas the one-dimensional location of the flame fronts and burn out edges were determined through analysis of the videos in MATLAB.

The analysis process developed as a simple method to track the flame front in the experiments conducted with set-up A, and subsequently refined and developed further for the experiments conducted with set-up B. The concept of the analysis method is presented in Section 4.2, after which the results from the individual experimental campaigns are presented in Sections 4.3 to 4.5.

4.2 Recording and analysis of one-dimensional flame spread

In the experimental set-ups A and B, the location of the flame was recorded by a single video camera (Panasonic HC-V770 HD, 24 fps), which rendered an ample amount of data as some experiments lasted for almost two hours. To ensure an objective and precise analysis and to reduce the amount of data, a series of MATLAB scripts were developed to determine:

- The one-dimensional location of the flame front in experiments conducted with set-ups A and B.
- The one-dimensional location of the burnout edge in experiments conducted with set-up B.
- The one-dimensional width of the pyrolysis-zone in experiments conducted with set-up B.

The automatic analysis enabled pixel-precise location with almost infinite time steps and thus generated data sets without any interpolations. Such precision was not deemed possible if the data was tracked manually as both the definition and location of the flame front and burn out edge was a subjective decision. Furthermore, a manual process requires manual data transfer with the potential for human errors. The scripts were written from scratch to have full control of the analysis process, as well as the option to overwrite parts of the outcome if they did not correspond with the visual observations. The latter was necessary for some of the experiments conducted with PV modules as PV cells delaminated from the glass plate and blocked parts of the view as seen in Figures 4.1e to 4.1g.

4.2.1 Location of the camera and video output

Because the fire propagated within a semi-enclosure, the upper surface prevented recording the two-dimensional development of the fire from above. Thus, it was only possible to track the development of the fire in the gap between the two surfaces. For experiments conducted with large gap heights, it was deemed possible to record the two-dimensional propagation of the flame front by installing the camera level with the upper surface and tilting it towards the lower surface. However, some of the experiments were conducted with visual gaps of only 4 cm between the two surfaces as a consequence of gap heights as low as 8 cm (see Table 3.6) and PV modules with a frame depth of up to 4 cm (see Table 3.2).

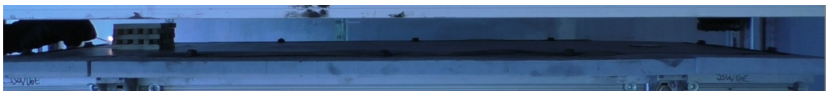

(a) Time from ignition: 0 seconds

(b) Time from ignition: 300 seconds

(c) Time from ignition: 600 seconds.

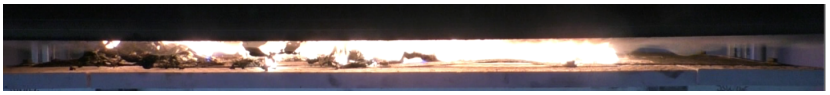

(d) Time from ignition: 750 seconds.

(e) Time from ignition: 900 seconds.

(f) Time from ignition: 1200 seconds.

(g) Time from ignition: 1500 seconds.

Figure 4.1: Flame spread along the roof construction mock-up (Set-up B) in a horizontal semi-enclosure with a 10 cm gap between a horizontal PV module and the roofing membrane. (experiment B25 (see Table 3.6)). For reference, Figure 4.1g shows the roof construction mock-up from set-up B.

To achieve a consistent point of view, the camera was kept level with the top of the lower surface in all experiments. As such, recording the one-dimensional flame front was only possible from the two sides of the experimental set-ups. The one-dimensional approach required the assumption of a linear flame front perpendicular to the direction of flame spread, which would render mirrored recordings from the front and back of the set-ups. Thus, a single camera in front of the set-up was deemed adequate. The camera view covered the entire length and aimed towards the centre of the lower surface, as seen inFigure 4.1.

The general concept of the visual output from all experiments conducted with the experimental set-ups A and B was similar to Figure 4.1, with the duration of the experiments as the only difference. The video frames inFigure 4.1 will serve as the reference experiment in the remaining part of the Section, withFigure 4.2 as the only exception.

Camera exposure settings

The automatic exposure feature was switched off to simplify the MATLAB analysis process. From a subjective point of view, the feature indeed rendered some impressive shots of the developing fire (seeFigure 4.2b), but the change of colour scheme from white/yellow to orange (seeFigures 4.2a, 4.2b) was not ideal for the automatic processing of the video. A more constant colour scheme was achieved when the automatic exposure was deactivated, as seen inFigure 4.2c and 4.2d.

(a) Auto exposure: ON - 10 min after ignition.

(b) Auto exposure: ON - 23 min after ignition.

(c) Auto exposure: OFF - 10 min after ignition.

(d) Auto exposure: OFF - 20 min after ignition.

Figure 4.2: Set-up A: Similar experiments with different camera locations and exposure settings for experiments conducted with 30 cm wide PMMA sheets with a gap height of 15 cm to the stainless-steel board. Note thatFigures 4.2a and 4.2b are from a test of the experimental set-up A. View and exposure settings similar toFigures 4.2c and 4.2d were used throughout all experiments conducted with set-ups A and B.

Import of video frames

The videos were imported with frame intervals of one second, and each frame's height was cut to the gap's height to prevent excess data. Despite the availability of 24 frames per second, single second intervals were deemed sufficient. If the interval was too long, fluctuation of the flame front could cause stammering data, whereas too short intervals caused unnecessarily long computation times.

4.2.2 Transformation from video frames to binary matrix

To extract the desired data from the two-dimensional and time dependent video frames, each experiment was transformed into a single binary matrix from which the flame front, the location of the burnout edge, and thereby the width of the pyrolysis zone could be tracked as a function of time.

Definition of length

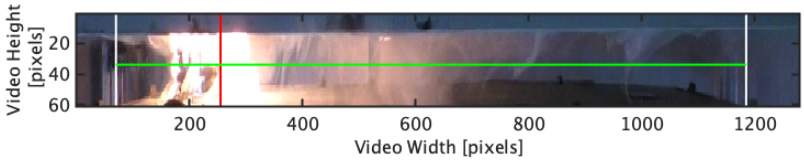

Figure 4.3: Set-up B: Video frame from experiment B25 (see Table 3.6) 300 seconds after ignition. The white lines define the edges of the roofing membrane, and the red line defines the right side of the wood crib used for ignition. The green line's length corresponds to the roofing membrane's length, whereas the height corresponds to the single-pixel line inFigure 4.4a. Note that the y-axis is scaled and this video frame is not the same as inFigure 4.1b.

By defining the edges of the PMMA or roofing membrane as the white lines inFigure 4.3, the number of pixels per millimetre could be calculated. A constant relationship between length and pixels was verified by the use of a patterned chess board with squares of 1 cm by 1 cm. The chess board was temporarily installed at the location of the experimental rigs, and thorough analysis in MATLAB, it was concluded that the camera lens did not alter the dimensions, as the number of pixels per square was consistent along the width of the camera. When the wood crib was used for ignition, an additional vertical line defined the right side of the wood crib as seen inFigure 4.3.

Construction of three-dimensional matrix

The height of the one-dimensional pixel-line, defined by the green line inFigure 4.3 was constant during each experiment. However, the specific pixel-line height was specified for each experiment after a visual comparison between various heights. Stacking the defined pixel-line for each second on top of each other, a two-dimensional RGB image could be generated as seen inFigure 4.4a and 4.4b. The image was a three-dimensional matrix with time on the y-axis, and pixels on the x-axis, whereas the z-axis defined the saturation of red, green, and blue (RGB). Determination of the pixel-line height used for further analysis depended on the plot's exposure, as the final step was converting the three-dimensional matrix to a two-dimensional binary matrix as seen inFigure 4.4b.

Conversion to binary matrix

MATLAB's *Color Thresholder* app was used to design a filter that generated the binary matrices. As seen from Figure 4.4b and 4.4c, the filter was designed to locate colours associated to the flame, without including reflections as seen between pixel 400 to 600 in Figures 4.3 and 4.4b. In general, the same filter was used through each experimental series, but some experiments required a slightly modified filter to ensure a satisfactory conversion to the binary matrix. Such reasons could be extreme gap heights (different reflection of light) or reflection of the flame upon the PMMA surface, as seen in Figure 4.2c.

4.2.3 Analysis of binary matrix

During the duration of the PhD, the analysis methods were refined, and new methods were developed. The initial intention was to track the flame front as a function of time, which was the only method used to analyze flame spread on the PMMA sheets. Subsequently, the burnout edge was defined, and finally, the width of the pyrolysis zone was calculated. In general, the analysis method utilized the structure of a binary matrix as each location had the value 1 or 0, representing respectively the presence or absence of the flame visualized by white and black pixels in Figure 4.4d.

A general understanding of the binary plot and its source is necessary before conducting any kind of analysis. With basis in the experiment plotted in Figure 4.4 (and Figure 4.1), the relevant parts are described in the following passages.

The upper boundary, marked with yellow crosses in Figure 4.4c is the passage from the fire to the non-ignited roofing membrane or PMMA. During the initial 300 seconds, the edge between the fire and the un-ignited roofing membrane is very steep. Thus, the flame font only moves a minimal distance each second after the ignition of the wood crib. During that period, the

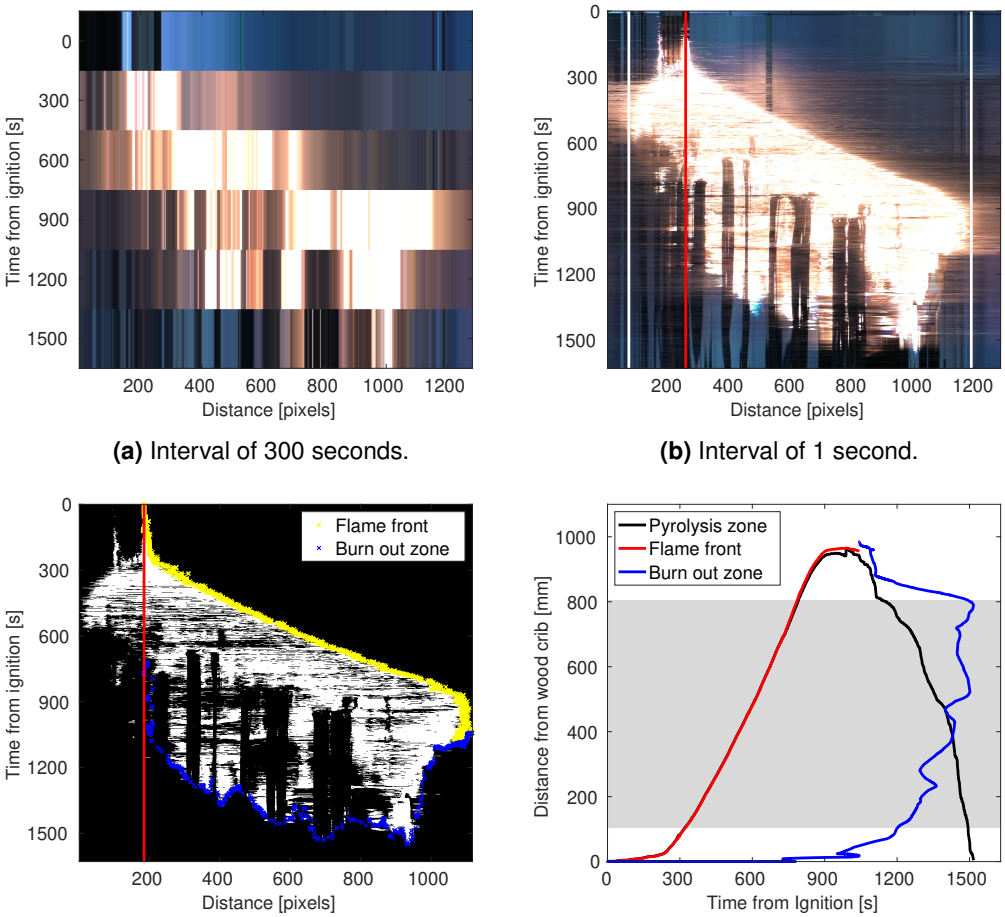

(a) Interval of 300 seconds.

(b) Interval of 1 second.

(c) Analysed binary conversion.

(d) Final data

Figure 4.4: Relevant steps of the video processing in MATLAB for experiment B25. The individual pixel-lines in subfigure a corresponds to the individual frames inFigure 4.1. The two vertical white lines and the single red line in subfigure b mark the roofing membrane's end edges and the wood crib's right side, as defined inFigure 4.3. The location of the wood crib is also marked in subfigure c, where the width corresponds to the distance between the two vertical white lines in subfigure b. Note that the axes are switched in subfigure c where the distance in pixels is replaced by millimetres. The grey box in subfigure d corresponds to the width of the roof construction mock-up as defined in 4.1g.

fire in the ignited wood crib intensified, after which it pre-heats and ignites the nearby roofing membrane in a larger and larger radius. After 300 seconds, the inclination of the line is reduced, indicating an acceleration of the flame front, which reaches the end of the roofing membrane after approximately 800 seconds.

The lower and less distinct boundary is the burnout edge. In some experiments, the burnout edge is a displaced line similar to the flame front, which indicates a constant width of the pyrolysis zone, as seen in some of the experiments with PMMA. In the given experiment, B25, burnout was not a one-directional phenomenon, and the plural term *burn out edges* seems to be more suitable as the fire within the semi-enclosure burned out from behind the pyrolysis zone and from the front of the pyrolysis zone as the flame front withdrew around 1000 seconds after ignition.

Finally, a specific phenomenon happened in the experiments conducted with PV modules as well as experiments conducted with PIR insulation (RC-C in Table 3.5), as one or multiple black columns with various widths occurred within the area (mostly) dominated by the presence of the flame. The lines appeared very sudden, which did not indicate partial fire extinguishing but rather blockage of the camera view. The video recordings verify that, and the *blind spots* either occur due to delamination of the PV cells from the PV modules or due to swelling of the PIR insulation when exposed to heat. The consequences of the swelling PIR insulation were mostly avoided by increasing the height of the pixel-line. However, it was not possible in the experiments with low gap heights as heating caused deflection of the panels, which also blocked the view. As such, the blind spots were unavoidable, and the analysis method had to take them into account.

Flame front

The height and width of each binary matrix corresponded to respectively the time duration of the experiment, t, and the length, d, of the sample (initially in pixels), as seen from the y- and x-axes in Figure 4.4b and 4.4c. Thus, each matrix consisted of t rows and d columns. The flame front was localised by analysing the individual rows. Since the one-dimensional movement of the flame front was a continuous process, the script was designed with the assumption that the flame front location on the x-axis in one row was within +/- 20 pixels of the flame front location in the previous row. The assumption served two purposes: i) to ensure a continuous movement of the flame front even if the filter had rendered a coincidental and non-representative location of the flame (white pixel) in the binary matrix. ii) To reduce the computational time. If the location of the flame front was within the first or last 20 pixels in the previous pixel-line, the script was modified to analyse the first or last 40 pixels to ensure that the defined span of +/- 20 pixels did not exceed the length of the individual pixel-lines. The result was an array with the location of "the last white pixel" as a function of time, which was filtered by the use of MATLAB's *smooth* function with a high span in the direction of the y-axis

and a low span in the direction of the x-axis to ensure a smooth line. Finally, the smoothed data was multiplied by the ratio between length and pixels, whereupon the flame front location was known as a function of time as seen in Figure 4.4d. If the burn out zones of the fire were defined as well, the location of the flame front was trimmed to the time when the flame front withdrew from the location of the maximum flame spread length, after which it was defined as a burn out edge.

Burn out edge

The definition of the burnout edges was less straightforward than the definition of the flame front and required manual correction in some cases. Three factors increased the complexity:

- Burn out from two sides.
- The presence of *blind spots*.
- Less constant concentration of white pixels

The combination prevented the reuse of the single row analysis used to detect the flame front. Instead, each column was analyzed. Using the individual flame front coordinates as the starting point for each column analysis, the black triangular shape in the upper right corner of Figure 4.4c was left out of the analysis. Thus, the burnout edge was defined as the transition from white to black pixels. To set apart singular white pixels caused by reflections from the fire itself, burnout was defined as the location where only 10% of the following 200 pixels were white. However, no method was found to work around the blind spots, and thus, a script was developed to manually remove pixels that should be ignored and replace them with pixels at a more likely location, as seen in Figure 4.5.

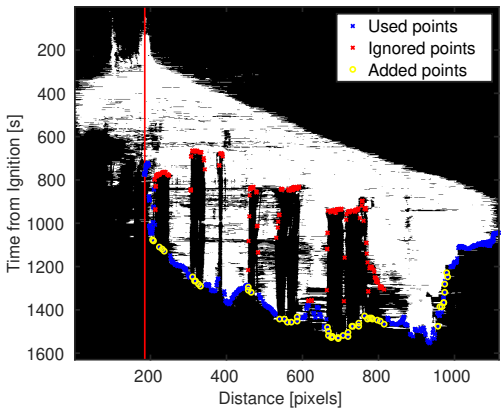

Figure 4.5: Example of the manual selection process. Both the blue and red crosses were the outcome of the automated localisation of the burnout zone. The red crosses were manually ignored and replaced by the yellow circles, which in combination with the blue crosses, formed the basis of the subsequent analysis as seen in Figure 4.4c.

It was accepted that overruling the automatic analysis did not correspond with efficiency and objectivity being the overall arguments for designing a method transforming the videos into relevant data for the analysis. Naturally, using a single pixel-line to represent each second was part of the reason manual editing of the automatic outcome was necessary. However, the combination of the single pixel-line method and the video recordings was significantly faster and deemed more exact than standalone manual analysis, as the binary plot formed the framework of the burnout edge location, which was refined manually by comparison with the corresponding videos.

The overall method was rendered good based on the very exact frame front analysis and the decent definition of the burnout zone.

Width of pyrolysis zone

The original binary plots could not be used to determine the width of the pyrolysis zone, as the blind spots, as well as the motley areas, prevented counting the number of white pixels in each pixel-line. However, as the boundaries of the pyrolysis zone were already defined as the flame front and burnout zone, the data was re-arranged and used to define a new, simplified binary matrix as seen in Figure 4.6. As such, the width of the pyrolysis zone as a function of time was defined as the number of pixels per second times the ratio between pixels and length, as seen in Figure 4.4d.

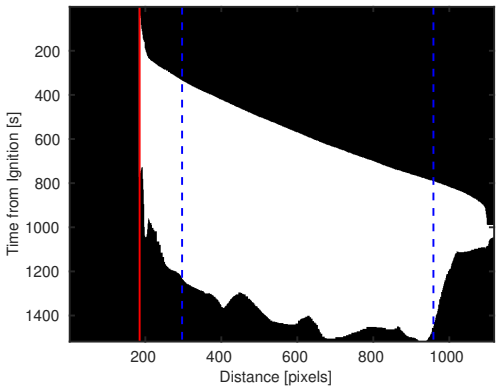

Figure 4.6: Example of an idealised binary plot based on the non-smoothed data points defining the flame front and the burnout edge. The red line marks the point of ignition (right side of the wood crib), and the two dotted blue lines define the edges of the roof construction mock-up in set-up B (see Section 3.5).

4.3 Set-up A: Flame spread on PMMA in horizontal semi-enclosures

The experimental output was separated into two parts for the experiments with flame spread on 2 mm thick PMMA sheets. i) The baseline experiments where no panel were installed above the PMMA, and ii) The experiments with various gap heights between the PMMA sheet and a horizontal panel represented by either a stainless-steel board or a PV module.

The baseline experiments served two purposes since they were used to validate the set-up through comparison with existing theory and, as the name implies, as baseline experiments for the experiments conducted in horizontal semi-enclosures. As such, the results of the baseline experiments are presented in Section 4.3.1 after which the influence of the horizontal barrier is presented in Section 4.3.2.

4.3.1 Baseline experiments

All ten baseline experiments behaved similarly. After ignition of the methanol soaked ceramic paper, the PMMA was ignited, and a self-sustained flame front was formed perpendicular to the camera view. As seen from Figure 4.7), the pyrolysis zone's width remained constant throughout the experiment.

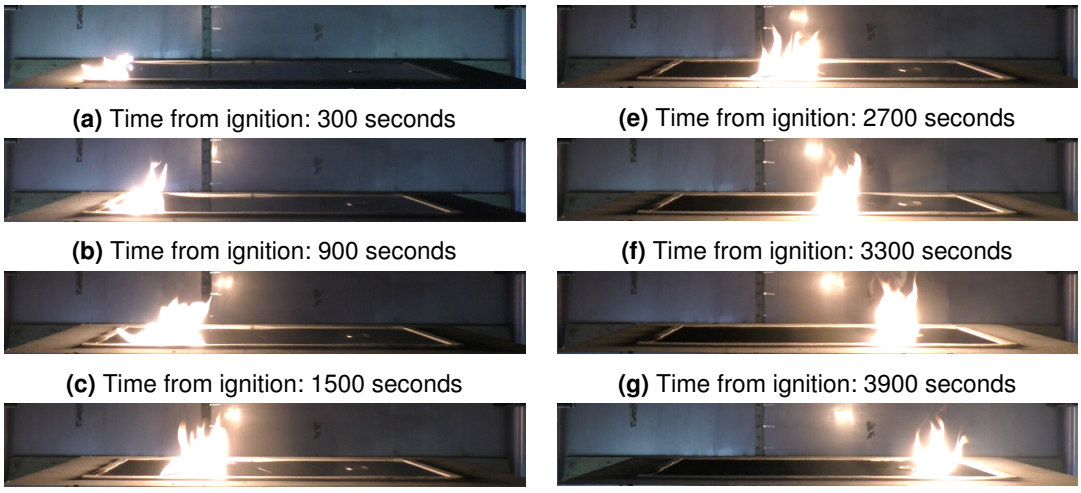

(a) Time from ignition: 300 seconds

(e) Time from ignition: 2700 seconds

(b) Time from ignition: 900 seconds

(f) Time from ignition: 3300 seconds

(c) Time from ignition: 1500 seconds

(g) Time from ignition: 3900 seconds

(d) Time from ignition: 2100 seconds

(h) Time from ignition: 4500 seconds

Figure 4.7: Set-up A: Baseline experiment with flame spread on PMMA with a width of 30 cm and no panel. Time interval of 10 minutes between each frame.

Flame spread

A constant flame rate (FSR) for the baseline experiments was verified through the results from the video analysis presented in Figure 4.8. It can be seen that a larger sample width generally resulted in a fster FSR. However, the baseline experiments also highlighted the sensitivity of the system as the unevenness of the plotted lines, as well as the different FSR for similar sample widths, indicate changes in the ambient conditions either between or during the experiments as seen in Table 4.2. The influence of changed ambient conditions is observed for the second slowest experiment conducted with a sample width of 20 cm (A1 in Table 4.2), where the FSR increased from 0.082 mm/s to 0.135 mm/s around 5700 seconds after ignition. From the recorded video of the experiment, it is seen that the significant change of FSR was related to an unintended modification of the flame spread mode from opposed to concurrent flame spread (defined in section 1.5.4). The reason for the changed flow pattern along the PMMA sheet was unknown, and the magnitude was most likely very small. However, the concurrent flame spread leads to an increased heat flux towards the pre-heating zone ahead of the flame front and thus a faster flame spread rate. Consequently, the length of the pyrolysis zone might have increased slightly, resulting in a higher heat release rate and thereby heat flux.

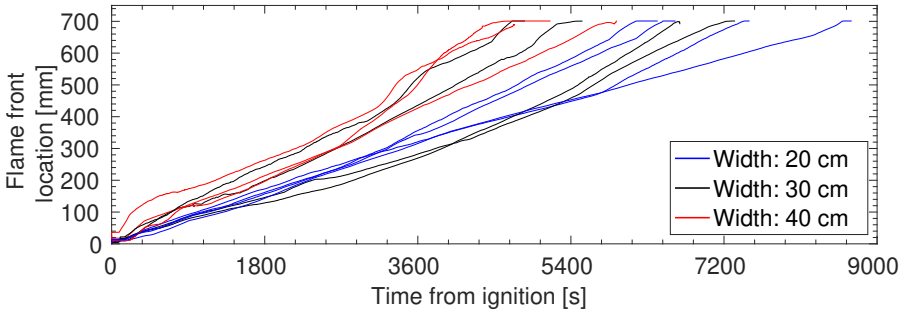

Figure 4.8: Flame front location as a function of time for the baseline experiments conducted without any horizontal barrier (from Kristensen et al. [6]).

The sensitivity of the system is confirmed when looking at the average flame spread rates (FSRs) in Table 4.2. With overlaps between neighbouring sample widths and the similarity between the fastest and slowest FSRs for the sample widths of respectively 20 cm and 40 cm, it can be discussed if the sample width is a significant parameter which affects the FSR.

However, the cross-sample width similarities only indicate that minor ambient changes can have a significant influence on the flame spread behaviour when the flames are propagating freely in the boundary area between opposed and concurrent flame spread. Despite the cross-sample width similarities and the diversity across baseline experiments with the same sample width, the overall trend is clear, as seen from the average FSRs for each sample width.

Table 4.2: Average flame spread rate (FSR) in mm/s for the baseline experiments. The flame spread rates are calculated as the average flame front velocity for the central 600 mm of the PMMA samples.

20 cm		30 cm		40 cm	
Exp:	**FSR:**	**Exp:**	**FSR:**	**Exp:**	**FSR:**
A1:	0.098 mm/s	A5:	0.132 mm/s	A9:	0.119 mm/s
A2:	0.082 mm/s	A6:	0.104 mm/s	A10:	0.170 mm/s
A3:	0.110 mm/s	A7:	0.155 mm/s		
A4:	0.118 mm/s	A8:	0.117 mm/s	A11:	0.177 mm/s
Avg:	0.102 mm/s	**Avg:**	0.127 mm/s	**Avg:**	0.155 mm/s

Naturally, it would be of great interest to design an experimental set-up with complete control of every parameter as such a set-up could form the basis of developing a unified model. However, a simple model for flame spread on thermally thin fuels is already developed (see Eq. 1.2) and serves for validation of the experimental set-up. Nevertheless, based on the current stage of knowledge, or lack thereof, it is necessary to have an initial understanding of how the introduction of a horizontal barrier affects the flame spread. Besides that, the experimental set-up serves as a simplified substitute for a BAPV system on a flat roof which is a significantly more complex system that includes several stochastic variables. By accepting the wind load as a stochastic parameter, it is accepted that similar experiments do not necessarily yield similar outcomes. However, as seen from the average FSRs in Table 4.2, the wind load does not affect the overall outcome of the experiments, and thus the results are deemed satisfactory.

Besides cross-experimental comparison, the flame front location as a function of time was used to transform the time-dependent results measured by the mass loss scale, heat flux gauge, and thermocouples into location-dependent values. Due to the non-consistent duration of similar baseline experiments, calculation of average values was not possible, and thus the transformation enabled the calculation of location-dependent averages.

Mass loss

Based on the mass loss measurements, the mass loss rates (MLR) were in accordance with ISO 5660-1 [172]. For the sample widths of 20 cm, the assumption of constant flame spread rate for the baseline experiments correspond well with the average constant normalised MLR of $0.12\ (g/s)\,m^{-1}$ (Figure 4.9). After ignition, the normalised MLR increase until a flame front location of 200 mm from the point of ignition, indicating a small increase of the FSR and width of the pyrolysis zone. After the 200 mm, an equilibrium between the flame spread rate and energy absorbed by the pre-heating zone ahead of the flame front, after which the average

normalised MLR becomes constant until 520 mm from the point of ignition, where it drops due to the presence of the water-cooled heat flux gauge. The initial increase of the normalised MLR and the following reduction when the flame front reaches 520 mm are the two commons across all baseline experiments (See Figure 4.9).

Contrary to the sample width of 20 cm, the normalised MLR for the wider sample widths continue to increase from $0.12\ (g/s)m^{-1}$ to $0.21\ (g/s)m^{-1}$ at the flame front location of 520 mm from the point of ignition.

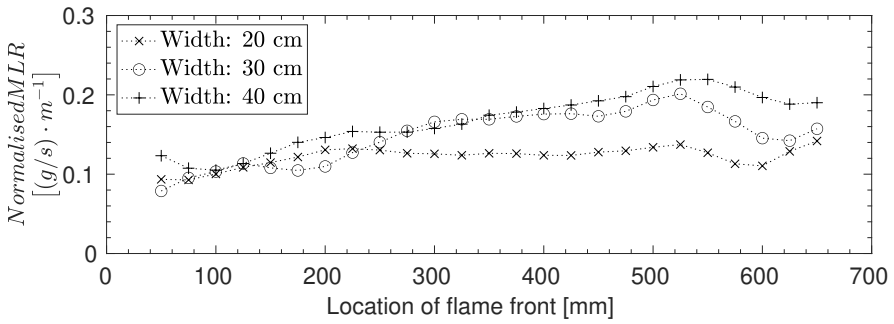

Figure 4.9: Moss loss rate (MLR) for the baseline experiments normalised for the three sample widths as a function of flame front location. The MLRs were normalised for cross-experimental comparison, and they were calculated as an average across all baseline experiments conducted with the same sample widths. (from Kristensen et al. [6])

Because the MLRs in Figure 4.9 were normalised, the MLRs were similar when a stable flame front was established on the PMMA after 100 mm, whereas the normalised MLRs closer to the point of ignition probably were affected by pre-heating from the burning methanol soaked ceramic paper. As both the view factor from the flame towards the PMMA [134, 173], as well as the flame emissivity [134, 174, 40, 175], increase as a function of the sample width (characteristic length), the experiments with larger sample widths will have higher normalised MLRs, which corresponds well with the overall faster flame spread rates (FLRs) in Figure 4.8.

However, the constant increase of the normalised MLR for the sample widths of 30 cm and 40 cm reveals that none of them reaches equilibrium as seen from Eq. 1.2 and thus that the FLRs in Figure 4.8 cannot be considered constant. As the mass loss rate is proportional to the heat release rate [174] and thereby the heat flux towards the PMMA ahead of the flame front [108, 114], the increased heat flux corresponds to a slowly increasing flame front velocity.

If the PMMA sheet was longer, it is expected that the MLRs and FLRs for the sample width of 30 cm and 40 cm would reach constant levels. However, the overall MLRs and FLRs are deemed so low that they are assumed constant for the remaining part of the thesis.

Net radiative heat transfer

The transformation from time- to flame front location-dependent variables were also made for the measured temperature of the PMMA and the heat fluxes. Subsequently, the basis of the flame front location where changed so that the distance to the flame front was measured from the location of the heat flux gauge (550 mm from the point of ignition) and the embedded thermocouple (500 mm from the point of ignition), rather than the point of ignition. The heat flux and temperature as a function of distance to the flame front could be plotted as exemplified in Figure 4.10. Because both the heat flux gauge and the embedded thermocouple were installed along the centre line of the PMMA sheet (see Figure 3.4), they were installed 5 cm apart. Ideally, the temperature and heat flux were measured at the location, but due to the almost constant flame spread rate, the temperatures measured 5 cm ahead of the heat flux gauge were assumed to be representative for the temperature at the location of the heat flux gauge.

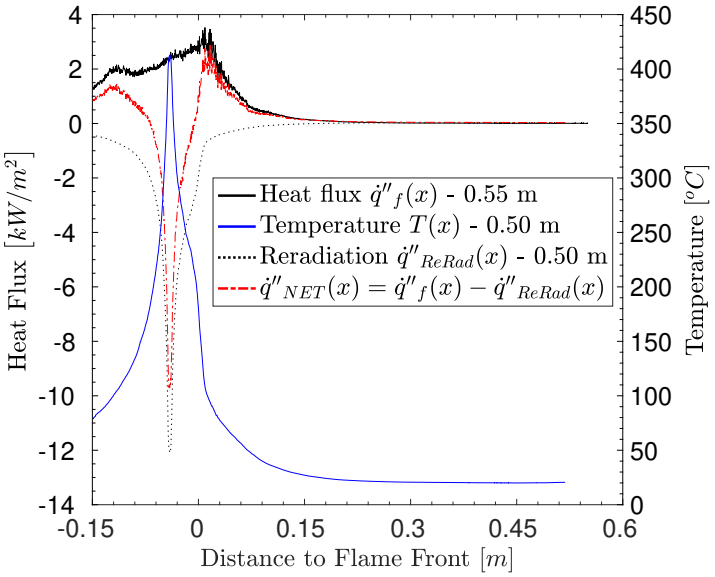

Figure 4.10: Measured heat flux and temperature plotted as a function of distance to the approaching flame front for baseline experiment conducted with a PMMA sample width of 30 cm (A8 in Table 4.3). Negative values on the x-axis indicate that the flame front, not the pyrolysis zone, has passed the measurement location. Re-radiation from the heated PMMA and the net heat flux is calculated as a function of the measured data. Plot of time-dependent temperature, heat flux, and flame front location in Figure A.4. (modified Figure from Kristensen et al. [6])

.

In Figure 4.10, the development of the heat flux can be separated into four phases as a function of distance to flame front (DFF): i) for $DFF > 0.2\ m$, no significant heat flux (HF) is measured, ii) for $0.2\ m > DFF > 0\ m$ the HF increase almost exponentially to a maximum HF of approximately $3.5\ kW/m^2$, iii) for $0\ m > DFF > -0.12\ m$ an uneven, less steep, reduction occur, and iv) for $-0.12\ m > DFF > -0.15\ m$ an even, slightly faster, reduction of the HF occur.

The initial two phases are the flame front approaching corresponding to first six or seven video frames in Figures 4.7a to 4.7f. The peak heat flux occurs a few centimeters before the flame front reaches the location of the heat flux gauge (HFG) sensor, which corresponds well with the ø50 mm diameter of the quartz disc installed to protect the heat flux gauge sensor. The quartz disc was a necessary physical barrier to prevent direct flame impingement and protect the HFG sensor from debris in the experiments conducted with PV modules. However, the radius of the quartz disc also defined a safety distance of 25 mm to the centre of the HFG sensor, and as a consequence, the maximum measured heat fluxes are not equivalent to the heat flux just before the concentration of pyrolysis gases permits ignition.

In the third phase, the flame pass around the HFG and quartz disc. Until the peak heat flux is reached, the flame is perpendicular to the HFG sensor view, but when a thin pyrolysis zone pass around the HFG (see Figure 4.7g-4.7h), the flame front becomes parallel with the sensor and thus the majority of the received HF is emitted from the two edges of the passing pyrolysis zone. If the width of the pyrolysis zone, defined as the dimension perpendicular to the flame spread direction, were constant when the flame passed the HFG, a symmetrical HF would be expected as the distance from the edge of the quartz disc to the HFG sensor would be constant whereas the flame length facing the HFG sensor would change as a function of flame location. As such, the minimum of the symmetric heat flux would be expected when the centre of the pyrolysis zone was in line with the HFG sensor.

However, the the heat flux decrease when $0\ m > DFF > -0.09\ m$, whereupon a small increase is noticed between $-0.09\ m > DFF > -0.12\ m$. It is expected that the HF decline is caused by a pyrolysis zone width reduction, as the view factor towards the PMMA ahead of the flame is reduced as a consequence of the partitioned flame, which efficiently is a local reduction of the sample width. The peak of the subsequent increase is most likely, related to an increased view factor when the flame front reassembles, whereupon the HF reduction in the fourth phase occurs when the distance to the back of the flame (burn out edge) increases.

When the distance to the flame front is 0 m in Figure 4.10, the measured temperature is 180 ℃, which is below the ignition temperature of PMMA ($T_{ig} = 278\ ^\circ C$ [9]). The significant temperature difference can be caused due to one or both of the following reasons: i) A limited precision of the flame front tracking method, or ii) that the PMMA was not perfectly thermally thin.

From the time- and the flame front location-dependent data, the ignition temperature is reached 168 seconds later, or when the flame front had travelled 25 mm further. A displacement might occur depending on the height of the single-pixel line used to track flame front. If the displacement is assumed to be correct, the additional distance was covered by the additional time, which entails an average flame spread rate (FSR) of 0.149 mm/s. Such flame spread rate is higher than the average FSR of 0.117 mm/s for baseline experiment A8 (see Table 4.2), but corresponds well with Figure 4.10 where the FSR of the second slowest baseline experiment with a sample width of 30 cm increase at the end of the experiment.

With a sample thickness of 2 mm, the Biot number is $Bi = (h \cdot l)/k \ll 1$ [174], as the maximum convection heat transfer coefficient for free convection between gas and a surface is $25\,W/m^2 \cdot K$ [122], whereas the conductivity for PMMA is $k = 019\,W/m \cdot K$ [174]. Thus, the assumption of the PMMA slab being thermally thin is correct, and the in-depth temperature variation should be negligible. Thus, the low temperature is probably caused by the 25 mm displacement of the flame front.

Based on the two data sets, the net radiative heat flux as a function of distance from the flame front towards the PMMA, $\dot{q}''_{NET}(x)$, could be calculated, at which point the cumulative net radiative heat transfer, $\dot{q}'_{NET}$, towards a specific point on the PMMA is equivalent to the right side of the simple flame spread equation, previously discussed in section 1.5.1, as seen from Eq. 4.1.

$$\dot{q}'_{NET} = \int_{x_p}^{\infty} \left[\dot{q}''_{NET}(x)\right] dx = \int_{x_p}^{\infty} \left[\dot{q}''_f(x) - \sigma(T^4(x) - T_\infty^4)\right] dx \tag{4.1}$$

Thereby, the net radiative heat flux is $\dot{q}''_{NET}(x) = \dot{q}''_f(x) - \sigma(T^4(x) - T_\infty^4)$ as seen from the calculated values in Figure 4.10. Because the minimum distance between the flame front and the given point on the PMMA is 0 m before ignition, the lower limit of the bounded integration in see Eq. 4.1 is $x_p = 0\,m$.

Theoretically, the upper limit of the integral is predefined as unlimited, which does not correspond well with the confined length of the PMMA samples. However, as seen from the plotted re-radiation and heat fluxes in Figure 4.10, the magnitudes are insignificant when the distance to the flame front exceeds 0.3 meters. Thus, an upper boundary of 0.5 meters corresponding to the maximum distance between the embedded thermocouple and the ignition point is deemed sufficient.

Similar to the average flame spread rates (FSRs) for the individual baseline experiments in Table 4.2, the cumulative net radiative heat transfer ($\dot{q}'_{NET}$) fluctuated within experiments conducted with similar sample widths as seen from Table 4.3. Contrary to the average FSRs, some of the $\dot{q}'_{NET}$ are calculated for the sample width of 20 cm were within range of the $\dot{q}'_{NET}$

Table 4.3: Calculated cumulative net radiative heat transfer towards the PMMA, $\dot{q}'_{NET}$ $[W/m]$. Calculated in accordance with see Eq. 4.1.

20 cm		**30 cm**		**40 cm**	
Exp:	$\dot{q}'_{NET}$	**Exp:**	$\dot{q}'_{NET}$	**Exp:**	$\dot{q}'_{NET}$
A1:	28 W/m	A5:	174 W/m	A9:	110 W/m
A2:	14 W/m	A6:	98 W/m	A10:	177 W/m
A3:	121 W/m	A7:	76 W/m		
A4:	123 W/m	A8:	122 W/m	A11:	81 W/m
Avg:	71 W/m	**Avg:**	117 W/m	**Avg:**	122 W/m

calculated for the maximum sample width of 40 cm and vice versa. Several factors cause the lack of distinction between the three sample widths: i) The design of the set-up, ii) the complexity of the system, and iii) ambient parameters as discussed in the flame after the spread analysis on page 96 as well as in section 1.5.

For the baseline experiments conducted with a sample width of 20 cm, the different $\dot{q}'_{NET}$ between A2 and A3 or A4 is almost in the order of a magnitude and consequently, the repeatability of those experimental set-up and the specific experiments can be questioned. The significant difference is a consequence of the flame spread mode combined with the ø50mm hole in the PMMA at the location of the heat flux gauge. From table 4.2, it is known that the FSRs of A3 and A4 are 30% to 40% larger the FSR for A2, which is a significantly smaller difference than the calculated $\dot{q}'_{NET}$.

However, the calculated flame spread rates in table 4.2 were average over the central 600 mm, whereas the calculated $\dot{q}'_{NET}$ were a result of the measured heat flux and temperature of the PMMA at specific locations based on the distance to the flame front as defined on page 99. As plotted in Figure 4.10 a significant heat flux was only measured when the flame front was close to the HFG and due the lower FSR it is expected the heat flux emitted from the flame front, $\dot{q}''_f(x)$, in experiment A2 would be lover than in A3 and A4. That would cause a lower onset distance of the significant heat flux increase and due to the 25 mm distance from the edge of the ø50 mm hole in the PMMA to the centre of the HFG, that results in a smaller ratio of the heat flux, $\dot{q}''_f(x)$, being measured in experiments with lower flame spread rates (i.e. A2) and thus a lower cumulative radiative heat flux from the flame, $\dot{q}'_f$, which leads to a much lower $\dot{q}'_{NET}$.

As such, it can be explained why $\dot{q}'_{NET}$ is almost a magnitude lower for experiment A2 than A3 or A4, and it is accepted that the difference between the four calculations for a sample width of 20 cm would be significantly lower if the distance between the edge of the PMMA and HFG was shorter. It is accepted that the calculation of an average $\dot{q}'_{NET}$ for the baseline experiments with a sample width of 20 cm is questionable, but it is done because it found more correct to compare trends rather than the individual experiments due to local variations of the FSR and thus heat flux towards the PMMA at a specific location.

As concluded when discussing the location-dependent temperature development for baseline experiment A8 in Figure 4.10, the analysis method might have caused a 25 mm displacement of the flame front. It can be argued that the lower boundary of the integral in see Eq. 4.1 should have been $x_p = -0.025\ m$ rather than $x_p = 0\ m$ for the specific experiment. Due to the $50\ mm$ diameter of the quartz disc protecting the heat flux gauge (HFG), the minimum distance between the HFG sensor and the flame front will never be smaller than the radius of the quartz disc. Thus, the use of $x_p = -0.025\ m$ will not yield a more correct result as the net heat flux, $\dot{q}''_{NET}(x)$, drops significantly when $-0.12\ m < x_p < 0\ m$ due to the re-radiation from the PMMA (see Figure 4.10).

Based on the flame front analysis, the conceivable displacement might vary across the individual experiments and thus yield different outputs as the consequence of minor x_p might have a significant influence on $\dot{q}'_{NET}$ due to the exponential behaviour of both the re-radiation, $\dot{q}''_{ReRad}(x)$, and radiant heat flux, $\dot{q}''_f(x)$.

As for the flame spread rate, it could have been of interest to optimise the analysis method, which would require a considerable increased number of baseline experiments. Both to optimise the experimental set-up further and increase the number of baseline experiments to a level where the cumulative net radiative heat flux for each sample width could be determined with a defined statistical variance. Because the set-up served as a novel tool to examine an unknown feature within fire safety engineering, flame spread in a small horizontal semi-enclosure, it was deemed acceptable that the average $\dot{q}'_{NET}$ increased as a function of sample width as expected. It was accepted that parameters and details related to the experimental set-up could influence the outcome of the individual baseline experiments, but the overall trend was deemed clear.

Energy balance - Validation of the baseline experiments

By comparison between the energy necessary to obtain the measured flame spread rate with the net energy received by the PMMA, equivalent to respectively the left, $\dot{q}'_{FSR}$, and right, $\dot{q}'_{NET}$, side of see Eq. 1.2, it can be determined if behaviour of the baseline experiment corresponds to the existing theory. Since $\dot{q}'_{FSR}$ is proportional to the FSR as seen in Eq. 4.2, the average $\dot{q}'_{FSR}$ is calculated for each of the sample widths in Table 4.4, with a density, specific heat capacity, ignition temperature, and ambient temperature of respectively, $\rho = 1190/m^3$ [174], $c_p = 1420\,J/kg \cdot K$ [174], $T_{ig} = 278\,^{\circ}C$ [9], and $T_{\infty} = T_s = 25\,^{\circ}C$.

$$\dot{q}'_{FSR} = \rho c_p d v_p (T_{ig} - T_s) \tag{4.2}$$

Table 4.4: The energy necessary to obtain the average flame spread rates (FSR), $\dot{q}'_{FSR}$, for the three sample widths in Table 4.2 calculated via Eq. 4.2. The average cumulative net radiative heat transfer, $\dot{q}'_{FSR}$, for each sample width as defined in Table 4.2, and the ratio between the two values for each sample width.

Sample width:	**20 cm**	**30 cm**	**40 cm**
$\dot{q}'_{FSR}\ [W/m]$:	87	109	133
$\dot{q}'_{NET}\ [W/m]$:	71	117	122
$\dot{q}'_{NET}/\dot{q}'_{FSR}\ [-]$:	0.82	1.07	0.92

In the discussions regarding the measured flame spread rates as well as the cumulative net radiative heat fluxes, it was decided to use the average values for each sample width (see Table 4.4) for comparison. The stochastic parameters affecting the individual experiments could be ignored by comparing the trends rather than the individual experiments. Based on the simple flame spread equation (see Eq. 1.2), the calculated ratios between $\dot{q}'_{FSR}$ and $\dot{q}'_{NET}$ in Table 4.4 indicates an acceptable correlation. For the sample widths of 30 cm and 40 cm, the difference between $\dot{q}'_{FSR}$ and $\dot{q}'_{NET}$ is insignificant. For the sample width of 20 cm, the difference between the heat flux required to obtain the measured flame spread rate, $\dot{q}'_{FSR}$, and the heat flux measured at the location of the heat flux gauge, $\dot{q}'_{FSR}$, might be related to the calibration range of the heat flux gauge (HFG) which was not ideal for such small values.

Considering the limitations of the heat flux measurements caused by the protective quartz disc, which restricted the distance between the sensor of the HFG and the flame front and thus the maximum heat flux, the $\dot{q}'_{NET}$ was surely lower than the actual cumulative net radiative heat flux gained when the flame front reached a point on the PMMA parallel to the HFG. Thus, the the calculated ratios, $\dot{q}'_{NET}/\dot{q}'_{FSR}$, in Table 4.4 should all $\dot{q}'_{NET}/\dot{q}'_{FSR} > 1$ if $\dot{q}'_{FSR}$ was determined for the specific location. As the flame spread rate for the baseline experiments was expected constant, $\dot{q}'_{FSR}$, the values calculated for the sample widths of 30 cm and 40 cm were most likely below the actual value, as the normalised mass loss rate (NMLR) (Figure 4.9) indicated

an overall NMLR increase and thus an increase of the flame spread rate. Consequently, the FSR used to calculate the $\dot{q}'_{FSR}$ were also lower than the actual values for the sample width of 30 cm and 40 cm, whereas $\dot{q}'_{FSR}$ might be correct for the sample width of 20 cm, which could be an additional reason for the lack of correlation between $\dot{q}'_{NET}$ and $\dot{q}'_{FSR}$.

Based on that, it should be noticed that the calculated ratios are between two under-measured or -estimated values, which are a consequence of the measurement method and decisions made with respect to assuming constant flame spread rates.

Taking the uncertainties into account, it can be concluded that the findings of the baseline experiments were in line with known theory. They were not perfect experiments where each parameter was defined nor quantified, but the relation between sample width, flame spread rate, and energy gained by the PMMA was deemed acceptable, and thus the findings were used as baseline experiments for similar experiments below a horizontal panel.

4.3.2 Flame spread below horizontal panels

Two experimental outcomes occurred when a panel was installed above the PMMA sheets. Either a constant flame spread rate (FSR) occurred along the 700 mm long PMMA sample, or the FSR slowly increased until it accelerated very rapidly, as seen from the video frames in Figure 4.11. Compared to the baseline experiment with a similar sample width of 30 cm in Figure 4.7, the initial frames 300 second after ignition are almost similar (see Figures 4.7a and 4.11a). However, the flame height in Figure 4.11a is significantly higher and continues to grow until it reaches the above panel 900 seconds after ignition in Figure 4.11c. The deflection of the flame below the horizontal barrier caused a rapidly developing heat feedback loop where a constantly increasing heat flux towards the PMMA causes an increase of the pyrolysis zone length and thus a significant increase of the flame spread rate. Consequently, the final 2/3 of the 700 mm sample length was covered by four minutes (see Figures 4.11d to 4.11h), whereas the initial 1/3 was covered in 20 minutes (Figures 4.11a to 4.11d).

In the following subsections, the influence of the horizontal barrier will be quantified with respect to the flame front development, flame spread rate in comparison with the baseline experiments, and normalised mass loss rates. Finally, the energy necessary to obtain the measured flame spread rates at the location between the embedded thermocouple and the heat flux gauge was compared to the cumulative net radiative heat flux gained at the same location.

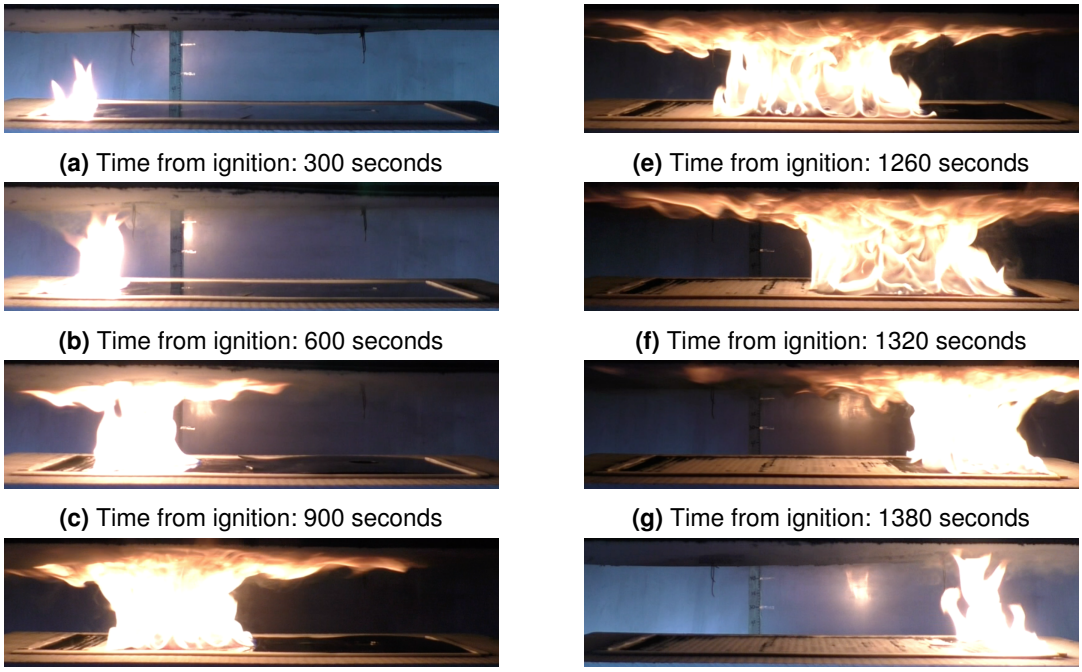

(a) Time from ignition: 300 seconds

(b) Time from ignition: 600 seconds

(c) Time from ignition: 900 seconds

(d) Time from ignition: 1200 seconds

(e) Time from ignition: 1260 seconds

(f) Time from ignition: 1320 seconds

(g) Time from ignition: 1380 seconds

(h) Time from ignition: 1440 seconds

Figure 4.11: Set-up A: Flame spread on PMMA with a width of 30 cm and a gap distance of 15 cm between the stainless-steel board and the PMMA surface. Note that the time span is reduced from 300 seconds to 60 seconds between Figure 4.11d and 4.11e.

Flame front location

Based on the analysis introduced in Section 4.2, the location of the flame fronts was tracked in all of the 38 experiments conducted below either the stainless-steel board or a PV module as defined in the experimental matrix (table 3.3).

Because the sample width of 30 cm represented the vast majority of the experiments as seen from Figure 4.12, they are the focal point of the analysis. Consequently, they will also serve as reference experiments for the sample widths of 20 cm and 40 cm, as differences or similarities can facilitate a discussion about how the finite dimensions of the PMMA samples affect the experimental outcome.

For gap heights of 22 cm (see Figure 4.12a), the flame spread rates (FSR) remained relative constant and compared to the baseline experiment, the flame spread rates of around 1.6 mm/s were similar to the fastest baseline experiment (A7) and slightly faster than the baseline average of 1.27 mm/s (table 4.2). The experimental outcome were less uniform and constant when the gap height was reduced with 2 cm. As seen in Figure 4.12b, the FSR in three experiments with a PMMA sample width of 30 cm remained almost constant, whereas a gradual increase occurred in the remaining three experiments conducted with the stainless-steel board.

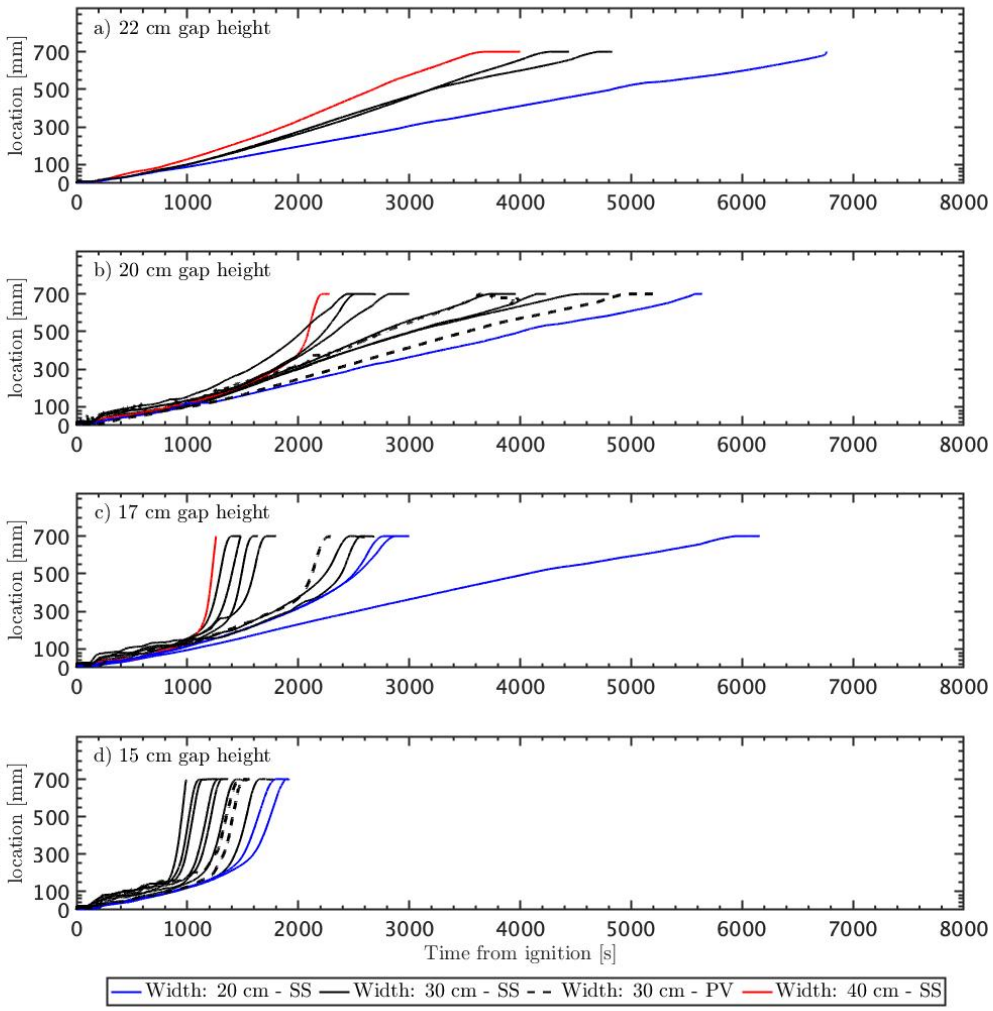

Figure 4.12: Location of the flame front plotted against time for flame spread on PMMA samples in horizontal semi-enclosures with gap heights between 22 cm and 15 cm. Three sample widths of respectively 20 cm, 30 cm, and 40 cm were tested. **SS:** Experiment conducted with stainless-steel board. **PV:** Experiment conducted with PV module. (Based on plot from Kristensen et al. [6])

Further reduction of the gap height to 17 cm (see Figure 4.12c) made it clear that the diverse results seen for the gap height of 20 cm (see Figure 4.12b) defines a transition zone where minor ambient differences had a significant influence on the experimental output. As a consequence of the gap height reduction to 17 cm, no constant FSR occurred for the sample widths of 30 cm. Instead, the FSR gradually increased until a transition occurred and it started accelerating rapidly as visualized by the video frames in Figure 4.11e to 4.11h. The transition from a slow FSR rate to a rapidly accelerating FSR occurred even faster when the stainless-steel board was lowered to 15 cm (see Figure 4.12d).

The phenomena where a slow FSR transitioned to a significantly faster FSR was caused by a self-enhancing heat feedback loop where an increased heat flux towards the pre-heating zone ahead of the flame front prompted a faster FSR and longer pyrolysis zone. Consequently, the longer pyrolysis zone entailed a higher mass loss rate and thus higher heat release rate which caused an additional heat flux increase. As seen from the video frames in Figure 4.11, the accelerating phase was a consequence of the flame deflection below the horizontal barrier, which corresponded with the findings in steady state experiments [1, 114, 115].

The link between the deflection of the flame and the accelerating phase might also explain why the transition occurs significantly later for some experiments, that others. In four of the six experiments with a sample width of 30 cm (see Figure 4.12c), the transition occurs after 1200 seconds to 1400 seconds, whereas the acceleration onsets are delayed with around 1000 seconds for the remaining two experiments conducted with the stainless-steel board. Similar to the baseline experiments, ambient parameters might have affected the initial development of the flame front. Despite the introduction of a horizontal barrier, the initial process of the experiments were similar to the baseline experiments and as a consequence, the sensitivity were comparable. Thus, it was expected that an opposed flow in the initial phase would affect the heat feedback loop whereupon the transition to the accelerating FSR would be delayed, or completely absent as seen for the sample width of 20 cm with a 17 cm gap height (see Figure 4.12c).

To look at the trends rather than the behaviour of the individual experiments, the relative flame spread rates were plotted as a function of flame front location and gap height in Figure 4.13. Herein, the relative flame spread rates were calculated for flame front location intervals of 5 cm until it reached the location of the heat flux gauge. At each flame front location, the average flame spread rate (FSR) for all similar experiments (i.e. same gap height, width, and panel type) were calculated for the traversed 5 cm and compared to the average baseline FSR for the given sample width (table 4.2).

Based on the relative flame spread rates (see Figure 4.13) it was clear that the gap height were a governing factor which caused a phenomena where the FSR transitioned from being slow and constant to rapidly accelerating if the gap height was lower than a *critical gap height*. For the sample widths of 30 cm and 40 cm (see Figures 4.13b, 4.13c, and 4.13d), the location of the critical gap heights were very distinct as relative FSRs were relatively constant for gap height of respectively 20 cm and 22 cm, whereas further reduction caused an acceleration. Besides the increased relative FSRs for low gap heights, the gap height reduction also moved the onset of the phase-transition which caused flame spread rates almost 40 times faster (see Figures 4.13b and 4.13c) than the FSR for the corresponding baseline experiments.

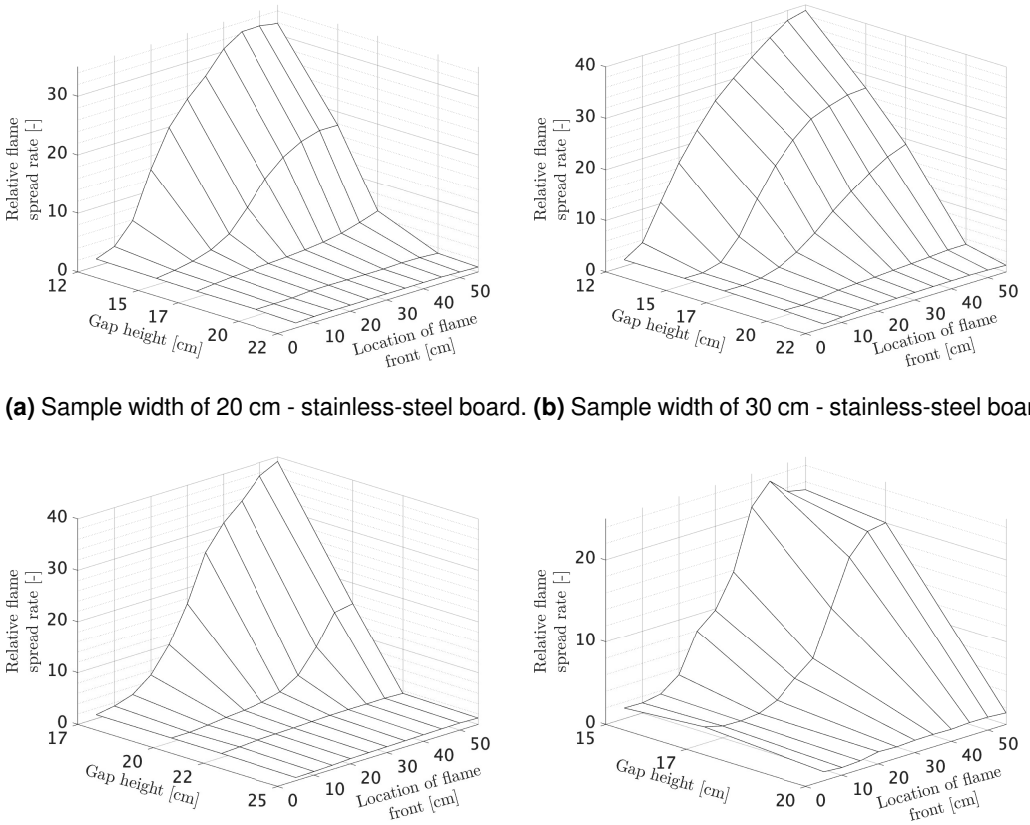

(a) Sample width of 20 cm - stainless-steel board. **(b)** Sample width of 30 cm - stainless-steel board.

(c) Sample width of 40 cm - stainless-steel board. **(d)** Sample width of 30 cm - PV module.

Figure 4.13: Relative flame spread rate compared to the average flame spread rate for the baseline experiments defined in Table 4.2. Note that the length of the y- and z-axis vary across the plots. (from Kristensen et al. [6]).

Because of the onset delay, exemplified by the sample width of 20 cm after 45 cm for a gap height of 17 cm (see Figure 4.13a), the consequence of a longer sample length can be discussed. Based on Figure 4.12c, the critical gap height for the sample width of 20 cm is below 17 cm. But for the sample width of 30 cm, the relative FSR for the sample width of 30 cm could be above 20 cm due to the inconsistent flame front location in Figure 4.12b. An increased sample length could also reveal whether the FSR continues to accelerate or if a new equilibrium is reached where FSR remains constant which the relative flame spread rate indicates when the flame front have passed 45 cm in experiments with a 20 cm sample width and gap height of 15 cm and 12 cm (see Figure 4.13a).

From the experiments conducted with PV modules, the backsheet on the backside of the PV modules did not cause significant different behavior as the flame front location as a function of time (see Figure 4.12), and thus the critical gap height similar to the experiments conducted with the stainless-steel board (see Figure 4.13d). In the experiments with PV modules, the polymer back sheet were ignited and dripping were observed as highlighted in Figure 4.14.

Figure 4.14: Experiment conducted with PV module, sample width of 30 cm, and a gap height of 17 cm. The highlighted flames were molten plastic from the back of the PV module, which continued burning. (From Kristensen et al. [6])

Despite the continuous burning of the dripping polymer, the similarities with the experiments conducted with the stainless-steel board indicated that the burning droplets did not accelerate the flame spread rate. Based on the experiments conducted with the PV modules, the slower relative flame spread rate indicate the opposite behaviour a seen in Figure 4.13d. As such, the experiments cannot verify that the PV modules represent a fire load, which corresponds with previous steady-state experiments by Krisensen, Merci, and Jomaas [108].

Normalised mass loss rate

The effect of the critical gap height is verified when calculating the average normalised mass loss rate as function of flame front location for the experiments conducted with a sample width of 30 cm as plotted in Figure 4.15. The findings, as a function of gap height, correspond well with the calculated relative flame spread rates in Figure 4.13b and the normalised mass loss rate for the baseline experiments in Figure 4.9. For gap heights of 20 cm and above, the normalised mass loss rate were constant and no higher than $0.5 g\,s^{-1}\,m^{-1}$, which was to two to three times the normalised mass loss rate for the baseline experiments (see Figure 4.9). That is equivalent to the constant relative flame spread rate of two to three in Figure 4.13b. Similar relationship is seen for the experiments with a gap height below the critical gap height as the maximum normalised mass loss rate of $7 g\,s^{-1}\,m^{-1}$ is approximately 40 times the normalised mass loss rate for the baseline experiments.

As such, the constant normalised mass loss rates for all gap heights could indicate a constant flame spread after the flame front pass 500 mm. However, the presence of the heat flux gauge reduce the overall mass (thus mass loss rate) near the location of 550 mm, whereas edge effects might affect the final Section of the PMMA, which corresponds well with the reduced flame spread rates before the flame fronts reaches 700 mm in Figure 4.12.

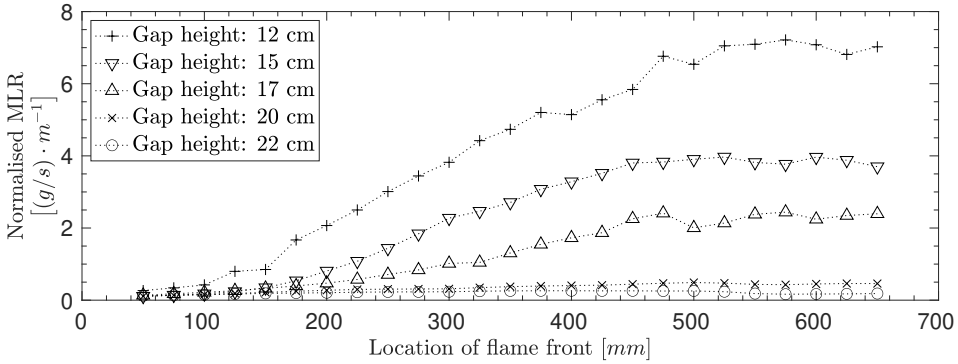

Figure 4.15: Normalised mass loss rate (MLR) as a function of gap height to the stainless-steel board for the PMMA samples with a sample width of 30 cm. (From Kristensen et al. [6])

Energy balance in the semi-enclosure

The net energy heat flux $\dot{q}'_{NET}$, and the heat flux required to obtain the flame spread rate (FSR) at the location of the heat flux gauge (HFG), $\dot{q}'_{FSR}$, were calculated for all the experiments. As the FSRs were not constant as expected for the baseline experiments, the calculation of $\dot{q}'_{FSR}$ were based on the FSR measured 500 mm from the point of ignition. Similar to the baseline experiments, $\dot{q}'_{NET}$ and $\dot{q}'_{FSR}$ were calculated via respectively see Eq. 4.1 and 4.2.

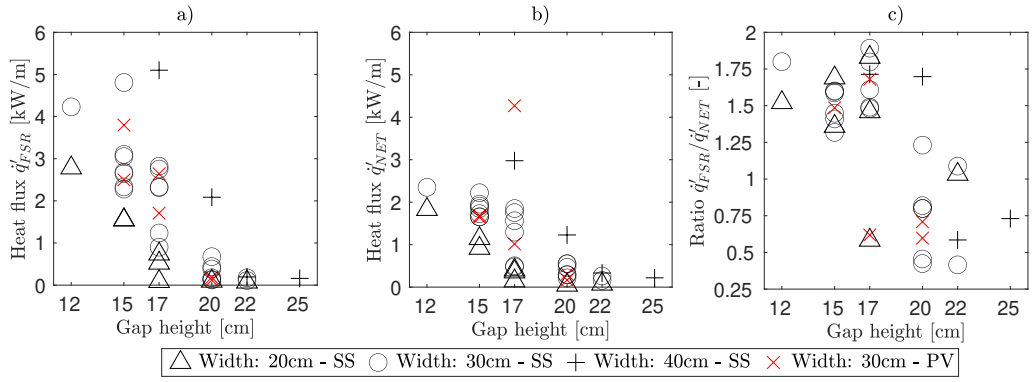

Figure 4.16: Heat flux near the location of the heat flux gauge. **a)** Heat flux required to obtain the measured flame spread rate, $\dot{q}'_{FSR}$, (based on Eq. 4.2). **b)** Cumulative heat flux gained, $\dot{q}'_{NET}$, (based on Eq. 4.1), **c)** Ratio between $\dot{q}'_{FSR}$ and $\dot{q}'_{NET}$. (From Kristensen et al. [6]).

Common for $\dot{q}'_{NET}$ and $\dot{q}'_{FSR}$, were an increase as a function of gap height reduction. The fluctuation related to the FSR caused some variation of the calculated $\dot{q}'_{FSR}$ in Figure 4.16a, but an acceptable relation was observed between the sample width and $\dot{q}'_{FSR}$ as wider PMMA samples caused a higher heat flux. The same trend was evident for the cumulative gained heat flux in Figure 4.16b, but the proportionality coefficient between the gap height and $\dot{q}'_{NET}$ was lower than for the $\dot{q}'_{FSR}$ (see Figure 4.16a), which is evident when the ratio between two heat fluxes are plotted in Figure 4.16c.

Looking at the ratio between $\dot{q}'_{FSR}$ and $\dot{q}'_{NET}$, it is evident that the ratio of 1 is almost non-existent as the majority of the ratios are either below 1.0 or above 1.2 (see Figure 4.16c). As such, the energy balance in Eq. 1.2 is rarely satisfied, and it can be discussed if it is representative of the flame spread scenario in horizontal semi-enclosures. But the grouping tends to be related to the critical gap height for the individual sample widths as the transition occur around the intervals of respectively 17 cm to 20 cm for the sample widths of 20 cm and 30 cm, as well as 20 cm to 22 cm for the sample width of 40 cm.

For the experiments with a gap height below the critical gap height, the vast majority of the ratios are below 0.75 and thus the FSR were below the expected FSR based on the cumulative net radiative energy, $\dot{q}'_{NET}$, received at the location of the heat flux gauge. But because $\dot{q}'_{NET}$ is only based on radiative heat transfer (see Eq. 4.1), it is expected that an additional convective heat transfer caused the consistent underestimation due to flow changes caused by the introduction of the panel which obstructed the flow in the extraction hood. The installation of pressure probes could probably confirm the influence of the convective heat transfer along the PMMA sample at the location of the heat flux gauge, whereupon the influence of the additional heat transfer mode could be added to the calculation of the cumulative net heat transfer:

$$\dot{q}'_{NET} = \int_{x_p}^{\infty} \left[\dot{q}''_f(x) - \sigma(T^4(x) - T_\infty^4) - \dot{q}''_{conv}(x)\right] dx \tag{4.3}$$

However, the installation of a pressure probe would, similarly to the heat flux gauge, affect the overall energy balance as it might obstruct the flow and block the radiation from the flame. Based on the current experiments, the reduced ratio, $\dot{q}'_{FSR}/\dot{q}'_{NET}$, is therefore accepted when the gap height is below the critical gap height.

Naturally, the additional convective heat loss in Eq. 4.3 was probably also present when the gap heights were below the critical gap height, but due to the re-radiation and significant increase of $\dot{q}''_f(x)$, it was expected to be less dominant. Despite the increase of the radiative heat flux from the flame, $\dot{q}''_f(x)$, the overall increase of the net radiative heat transfer did not correspond to the FSR increase as $\dot{q}'_{NET}$ was consistently lower than $\dot{q}'_{FSR}$ when the gap height was below the critical gap height as seen in Figure 4.16c.
Thus, the measured flame spread rate (FSR) was significantly higher than the FSR expected based on the cumulative heat transfer towards the PMMA. It was expected that the unsatisfied heat transfer model was caused by one or both of the following: i) reduced transparency of the quartz disc, and/or ii) an increased convective heat transfer [6].
Due to the constant temperature of the water-cooled heat flux gauge (HFG), the temperature of the protective quartz disc was significantly lower than the flame when the pyrolysis zone passed the location of the HFG. Consequently, the smoke and soot particles condensed on the surface of the quartz disc, reducing the transparency and thus the measured heat flux. At the same

time, the combination of a small gap distance and high heat release might have increased the overall temperature within the semi-enclosure and thus contributed to the preheating of the PMMA ahead of the flame front rather than reducing it, as assumed when the gap height was above the critical gap height.

4.3.3 Conclusion based on experimental campaign

The influence of a horizontal barrier was examined by tracking the flame spread rate, radiative heat flux, and temperature as a function of gap height between sheets of 2 mm thick opaque PMMA and a horizontal barrier represented by either a stainless-steel board or a PV module. The findings revealed that minuscule (2-3 cm) changes of the gap height caused a significant change of the flame spread behaviour, as the flame spread rate remained slow and constant if the gap height was above a critical gap height but transitioned into a rapidly accelerating fire if the gap height were below the critical gap height. Compared to the baseline experiments, without any panel, the introduction of the panel resulted in flame spread rates up to 38 times faster. The transition from a steady to an accelerating flame spread behaviour was the consequence of an enhancing heat feedback loop, which accelerated significantly when the flames deflected below the panel and thus increased the view factor towards the un-ignited PMMA ahead of the flame front.

The simple flame spread equation (see Eq. 1.2) was used as a heat transfer model and verified the general trends in the baseline experiments. The simple flame spread equation was not satisfied when the panel was installed as it probably introduced additional convective heat transfer when the panel was above the critical gap height. On the other hand, the measured heat flux towards the PMMA was not representative of the actual heat flux when the gap height was below the critical gap height, as soot condensed on the cold surface of the quartz disc, which reduced the transparency. Despite the unsatisfied energy balance (based on the quantified parameters), the experimental set-up's instrumentation verifies that the introduction of a horizontal barrier causes a significant increase in the net heat flux towards the PMMA when the gap height is below the critical gap height.

The experiments also reveal that the width of the sample is relevant as the critical gap height increase together with the sample width. Thus, the results from experiments with restricted sample widths does not represent an infinite two-dimensional surface such as a roof surface. That is relevant because the flame front width can be, relatively, unlimited on a roof construction below a BAPV module and thus the flame front width can grow as the fire propagates which, according to the findings from the experiments, leads to a higher heat flux towards the roof construction. As such, the fire can propagate below inclined PV modules with a local gap height which is higher than the critical gap height for the initial ignition source.

Finally, the few experiments conducted with PV modules did not differ significantly from those conducted with non-combustible surrogate stainless-steel board. Burning droplets were observed from the back sheet of the PV modules, but since the flame spread rate was lower than for the experiments conducted with the stainless-steel board, they were not expected to affect the overall outcome.

4.4 Set-up B: Flame spread on roof construction mock-up in semi-enclosure

In the second experimental campaign, the 2 mm thick polymethyl methacrylate (PMMA) sheets were replaced by the roof construction mock-up described in Section 3.5. In all experiments, a 1.5 mm thick polyvinyl (PVC) based roofing membrane was installed along the upper surface, and three different roof constructions were used to examine how the heat transfer affected the flame spread behaviour and protected the subjacent construction. A 22 mm non-combustible calcium silicate board (CSB), 50 mm mineral wool (MW), or 60 mm polyisocyanurate (PIR) was used as the upper layer below the roofing membrane in the three different mock-up roof constructions as described in detail in Section 3.5.4 and Table 3.4.

The experimental matrix in Table 3.6 was designed to enable a gradual increase in complexity. Therefore the initial experiments were conducted with the CSB (see B1 to B9 in Table 3.6) and as such they were similar to the experiments conducted with PMMA although the PMMA were replaced with roofing membrane. By subsequently replacing the CSB with MW or PIR insulation and the stainless-steel board (see Section 3.2.1) with a PV module, the influence of the subjacent insulation material and combustible back sheet of the PV modules could be examined step by step (B10 to B18 in Table 3.6). Most of the experiments were conducted with horizontal PV modules (B10 to B31) to reduce the parameters. Inclinations between 10° and 15° were introduced in the final 11 experiments (B31 to B42).

The overall visual observations will be presented and discussed in the following Section, whereas the flame spread length and flame spread rate as a function of gap height, panel type (stainless-steel board or PV module), panel inclination and insulation material are found in Sections 4.4.2 and 4.4.3. The necessity of the term Exposure is discussed and introduced in Section 4.4.4 and finally, the maximum temperatures measured within the mineral wool and PIR insulation are presented in Section 4.4.5.

4.4.1 Visual observations

A wood crib was used to ignite the roof construction mock-up (see Section 3.5.2), and one of two flame spread scenarios occurred after ignition: i) The fire did not propagate outside the domain of the ignition source, or ii) the fire propagated along the majority of the roofing membrane. As such, the change from PMMA to the PVC-based roofing membrane caused a binary flame spread scenario where a critical gap height determined if the fire propagated or not.

When the gap height was above the critical gap height, and the fire did not propagate, there was no significant difference between the experiments conducted with the stainless-steel board and the experiments conducted with a PV module, as seen from Figure 4.17. In the two experiments, the area affected by the ignition source was very similar to each other, and in

both experiments, the maximum flame spread length was around 15 cm from the centre of the wood cribs with a displacement towards the right side. A convective heat loss probably caused the displacement due to the presence of edge effects along the left side of the roof construction mock-up, and similar behaviour was expected along the right side of the mock-up.

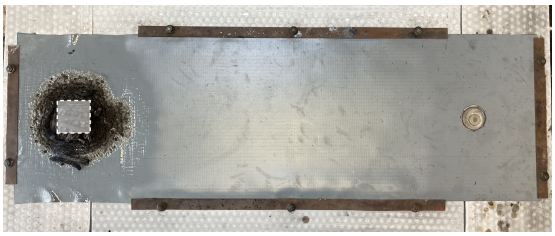

(a) Experiment conducted with stainless-steel board (B14 in Table 3.6).

(b) Experiment conducted with PV module (B19 in Table 3.6).

Figure 4.17: Top view of flame spread on roofing membrane from left to right with a gap height of 12 cm between the roofing membrane and a horizontal panel. The shaded area highlighted with dotted white lines marks the location of the wood crib used for ignition (from [7]).

When the gap height was below the critical gap height, a self-sustained fire propagated along all of, or a significant part of, the roof construction mock-up as seen from Figures 4.1 and 4.18 were the fire propagates below respectively a horizontal and an inclined PV module. If the self-sustained flame was achieved, the fire propagated with a constant flame spread rate and the fire did not accelerate due to a self-enhancing heat feedback loop as seen in the experiments conducted with PMMA (see Figure 4.12).

In all of the experiments conducted with a PV module (B19 to B42), the PV cells delaminated from the back when the polymer back sheet was heated, as seen in Figure 4.19. However, all PV cells were either mono- or poly-crystalline silicon cells, and as such, they did not increase fire load, and in some cases, they might have blocked radiative heat transfer from the flame towards the roof surface, thus reducing the flame spread. In some cases, the PV cells also blocked the camera view, which affected the video analysis as discussed in Section 4.2. The glass panel of the PV modules remained intact in all experiments except B26, and only the back sheet affected by direct flame impingement burned away (see Figure 4.19a). As such, no self-sustained flame spread occurred on the PV module and thus, the experiments indicated that the PV module should not be considered a fire load. However, burning droplets were observed in all four experiments conducted with PV module type 4 (Experiments B39 to B42 in

Table 3.6). The droplets fell from the lower edge of the inclined PV modules to a sheet of mineral wool protecting the experimental set-up, and self-sustained burning was observed for more than one minute. Under normal conditions, the droplets would land on the upper surface of the roof construction and thus act as an increased fuel load contributing to the existing fire. When modules are installed on a horizontal surface, it is expected that the droplets will not cause additional flame spread as previous large-scale experiments revealed that no self-sustained flame spread occurred outside the semi-enclosure due to the lack of the additional heat caused by re-radiation [1]. If the PV modules were installed as a part of a building integrated facade system, the burning droplets might affect the flame spread behaviour. However, PV modules used for building integrated PV systems will have to pass the appropriate test methods (ISO/EN 13823 [73], and EN 11925-2 [66]) for the construction product they replace and thus, it is not expected that such PV modules would be installed as a part of a facade system.

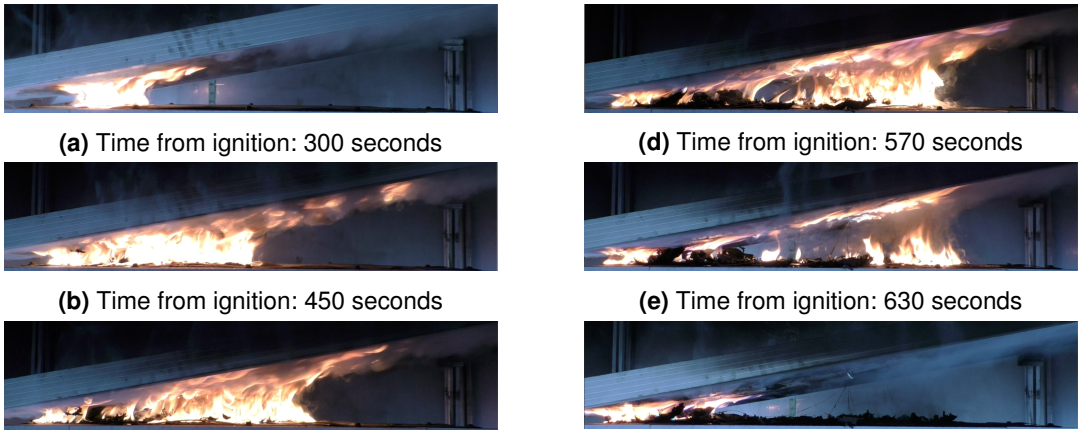

(a) Time from ignition: 300 seconds

(b) Time from ignition: 450 seconds

(c) Time from ignition: 510 seconds

(d) Time from ignition: 570 seconds

(e) Time from ignition: 630 seconds

(f) Time from ignition: 690 seconds

Figure 4.18: Flame spread on roof construction mock-up with mineral wool below the roofing membrane, a gap height of 8 cm, and an inclination of 10° (Experiment B32 in Table 3.6) (from Kristensen et al. [7]).

4.4.2 Flame spread length (FSL)

The location of the flame front, burn out edge, and width of the pyrolysis zone were tracked by analysing the recorded video via the developed single-pixel line method described in Section 4.2. Quantifying the flame spread length (FSL) was used to determine the critical gap height because the flame spread rate remained constant if the flame front detached from the ignition source. The FSL was defined as the longest distance between the right side of the wood crib and the flame front. As such, the maximum FSL was 102 cm, as indicated by the dotted lines in Figure 4.20.

For the experiments conducted with horizontal modules, it is clear that a critical gap height is below 12 cm as the FSL were consistently below 20 cm when the gap height was 12 cm, whereas a gap height of 11 cm rendered significantly longer FSLs (Figure 4.20a).

(a) Backside of PV module type 2 (see Table 3.2). The dotted line indicates the dimensions (37 cm times 118 cm) and the location of the roof construction mock-up below the module. Most of the polymer back sheet inside the dotted square was burned, and the white area was the transparent glass front sheet. The remaining part of the module was sooted, and the areas near the edge of the dotted lines were charred.

(b) Top view of roof mock-up. The shaded white square with the dotted line marks the location of the wood crib used for ignition. The scattered blue pieces are the non-combustible mono- or poly-crystalline cells delaminated from the PV module.

Figure 4.19: The backside of the PV module and top view of the roof construction mock-up (from Kristensen et al. [7]).

The length of the enhanced flame spread length depended on the panel type, as the FSL for the experiments conducted with the stainless-steel board were consistently lower than the FSL for the experiments conducted with PV modules. For the experiments conducted with the stainless-steel board, the FSL were inconsistent for the gap height of 11 cm, after which an FSL increase occurred when the gap height was reduced further. The inconsistent FSLs for the gap height of 11 cm were expected to result from a transition phase where the additional radiative heat flux was not yet dominating the heat transfer model, after which other un-quantified factors affected the outcome. As such, the inconsistent FSLs for the gap height of 11 cm were deemed acceptable.

Convective heat transfer was expected to be one of the un-quantified parameters as the panels obstructed the forced flow from the extraction hood. As the FSL increased with a gradual gap height reduction from 11 cm to 8 cm, it was expected that the convective heat transfer increased with a reduction of the distance to the right side edge of the roof construction mock-up. As such, an increase of the heat transfer from the flame to the roofing membrane as a function of a gap height reduction would enable increase of the FSL.

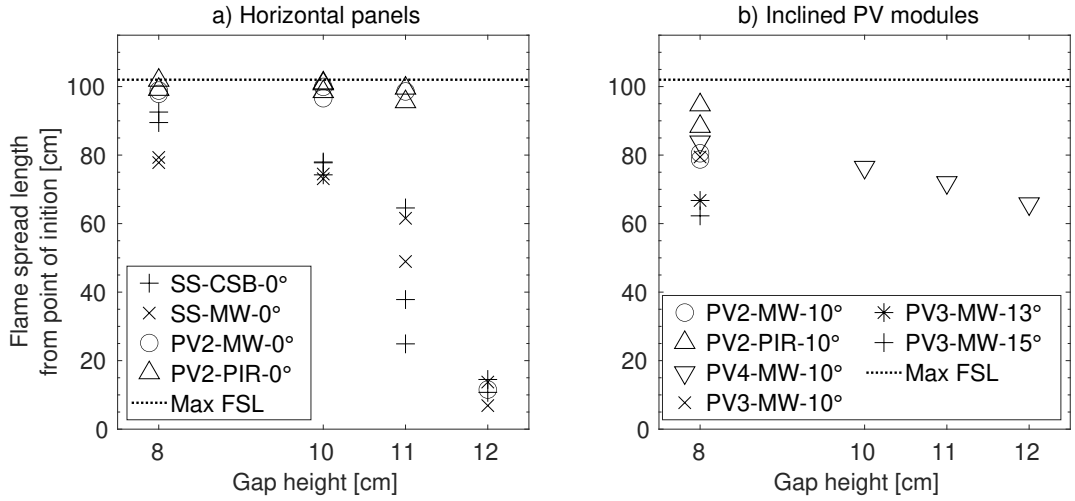

Figure 4.20: Flame spread length (FSL) as a function of gap height, panel type (Stainless-steel board (SS) or PV module (PV2, PV3, or PV4)), and insulation material (Calcium silica board (CSB), mineral wool (MW), or PIR insulation) for experiments conducted below: **a)** Horizontal panels, or **b)** Inclined PV modules.(From Kristensen et al. [7]).

When the PV modules replaced the stainless-steel board, the results were significantly more consistent and for gap heights of 11 cm and below, the FSL almost reached the maximum FSL of 102 cm as seen from Figure 4.20a. Like the experiments conducted with the stainless-steel board, convective heat transfer caused by edge effects were expected to affect the flame spread behaviour at the end of the roof construction mock-up.

Because self-sustained flame spread along the PV module back sheet membrane was not observed in any of the experiments (see Figure 4.19a), the significant difference between the two panel types was not expected to occur due to an increased fuel load but rather a geometric difference between the two panel types.

The PV module type 2, which was used for all experiments with horizontal PV modules, had a 40 mm aluminium frame along the edges (see Table 3.2). The frame restricted the buoyant flow of combustion products from the flame, and as a consequence, a layer of hot and black smoke was formed below the PV module in all of the experiments. It is expected that the smoke-induced a constant heat flux along the full length of the roof construction mock-up, whereupon the contribution from the flame, $\dot{q}''_f(x)$ to the combined net heat flux, $\dot{q}'_{NET}$ (see Eq. 4.1), could be defined as $\dot{q}''_f(x) = \dot{q}''_{flame,rad}(x) + \dot{q}''_{flame,conv}(x) + \dot{q}''_{smoke,rad}(x)$. Because the thickness of the smoke layer was constant along all of the PV module, $\dot{q}''_{smoke,rad}(x)$ could probably be considered a constant rather than a location-dependent variable when the length of the PV module exceeds the length of the roof construction mock-up. Consequently, the frame as a physical barrier caused an increased heat flux towards the roofing membrane ahead of the flame front and significant pre-heating along the full length of the roof mock-up, rather than only the part closest to the flame front. The inclination of the PV modules caused two significant

changes, as seen from Figure 4.20b. First, the critical gap height could not be identified as the flame front propagated outside the domain of the ignition source in all experiments. Secondly, the FSL never reached the end of the roofing membrane, and it was noticed that an increase of both the gap height or module inclination caused a reduced FSL.

The non-identified critical gap height in the experiments with inclined modules (see Figure 4.20b) indicated that the critical gap height was above 12 cm. That corresponds well with the model developed by Tang et al. (see Eq. 1.1) where the upstream (below the most elevated of the module) heat flux from the flame, $\dot{q}''_f$, to a certain extent will grow as a function of an increased inclination if the remaining variables, including the heat release rate, $\dot{Q}$, are kept constant.

The visual observations also corresponded very well with the assumed increased upstream heat flux as the upstream flame spread in Figure 4.18a was significantly longer than the downstream flame spread. In addition, the inclination also caused a significantly faster flame spread rate as the flame front had travelled 80 cm after 570 seconds when the module was inclined 10° in experiment B32 (see Figure 4.18d), whereas the same distance was covered in 750 seconds when the PV module was installed horizontally in experiment B25 (see Figure 4.1d).

For the experiments conducted with mineral wool, the FSL were similar (79 cm to 84 cm) for all experiments conducted with a gap height of 8 cm and an inclination of 10°(B32, B33, B36 and B39 in Table 3.6). In addition, a reduction of the gap height increased the FSL, whereas an increase of the inclination from 10° to respectively 13° and 15° reduced the FSL from 79 cm to 66 cm and 62 cm.

From the video frames in Figure 4.18 it is seen that the pyrolysis zone detached from the ignition source after 510 to 570 seconds from the time of ignition (see Figures 4.18c and 4.18d). Despite the wide pyrolysis zone and thus an expected high heat release rate, the flame front did not propagate any further and 630 seconds after ignition, the fire had almost self-extinguished (see Figure 4.18e).

The self-extinguishing behaviour was observed throughout all the experiments conducted with inclined modules (see Figure 4.20b) and did not correspond well with the binary flame spread scenario observed when the PV modules were installed horizontally (see Figure 4.20a). However, the different flame spread behaviour can be explained via the model by Tang et al. (see Eq. 1.1), where the flame spread rate, v, were proportional to the net cumulative heat flux gained during the preheating phase, $\dot{q}'_{NET}$ (see Eq. 4.1. Because of the binary flame spread scenario, flame spread only occurred when the magnitude of $\dot{q}'_{NET}$ exceeded a given, but

undefined, value. If assumed that the finite width of the roofing membrane entailed a maximum heat release rate independent of the pyrolysis zone length when the length exceeded a given value, the heat flux, $\dot{q}''_f$, towards a point at a distance r from the flame front would only depend on the vertical distance between the flame front and the PV module (see Eq. 1.1).

Because the FSLs in Figure 4.20b are similar to the location of the flame front when self-extinguishment occurred, $H_{FSL} = H + FSL \cdot tan(\theta)$ corresponds to the local gap height. As such, the local gap height, H_{FSL}, should be independent of the initial gap height, H, if the remaining parameters are constant. That is verified in the four experiments with an inclination of 10° and initial gap heights of 8 cm to 12 cm, as the local gap heights, H_{FSL}, are between 22.8 cm and 23.7 cm.

Based on the above, it was concluded that the limited flame spread length in the experiments conducted with inclined PV modules was the consequence of a restricted heat release rate, $\dot{Q}$, caused by the limited width of the roofing membrane (see Figure 4.20b). The assumption of a constant heat release rate for pyrolysis zone lengths above a certain length should be validated via oxygen calorimetry of the combustion products [171]. As such, it is expected that the flame front would have propagated along the entire length of the roof mock-up if the width of the roofing membrane had been considerably wider and thus represented an actual roof construction.

In general, the materials below the roofing membrane did not significantly influence the FSL. For the experiments conducted with horizontal PV modules (see Figure 4.20a), the FSL were similar for all experiments conducted with the same gap height. Below the stainless-steel board, the calcium silicate board (CSB) yielded slightly longer FSLs than the experiments conducted with mineral wool (MW) for the gap heights of 8 cm and 10 cm but did not affect the magnitude of the critical gap height. As the specific heat, c_p (see Table 3.5), for the CSB ($748\ J/(kg\ K)$) and MW ($850\ J/(kg\ K)$) were relatively similar, it was expected that the higher density of the CSB ($250\ kg/m^3$ vs. $118\ kg/m^3$) allowed more energy to be stored within the material during the pre-heating phase. Consequently, the heat loss from the heated roofing membrane to the subjacent material were smaller when the convective heat transfer increased as a function of the flame front location, whereupon longer FSLs were achieved.

4.4.3 Flame spread rate (FSR)

Except from the onset and the decay phase of the flame spread scenarios, flame spread rates (FSRs) remained almost constant if the fire propagated outside the domain of the ignition source, as seen in Figure 4.4d for experiment B25 and in Figure 4.21 for the experiments with both horizontal and inclined PV modules with gap heights between 8 cm and 12 cm. The slow FSR below the horizontal module with a gap height of 8 cm (Figure 4.21a) varied slightly more than the other flame spread rates which corresponds well with the trend seen for the slower FSRs in the experiments with PMMA (see section 4.3).

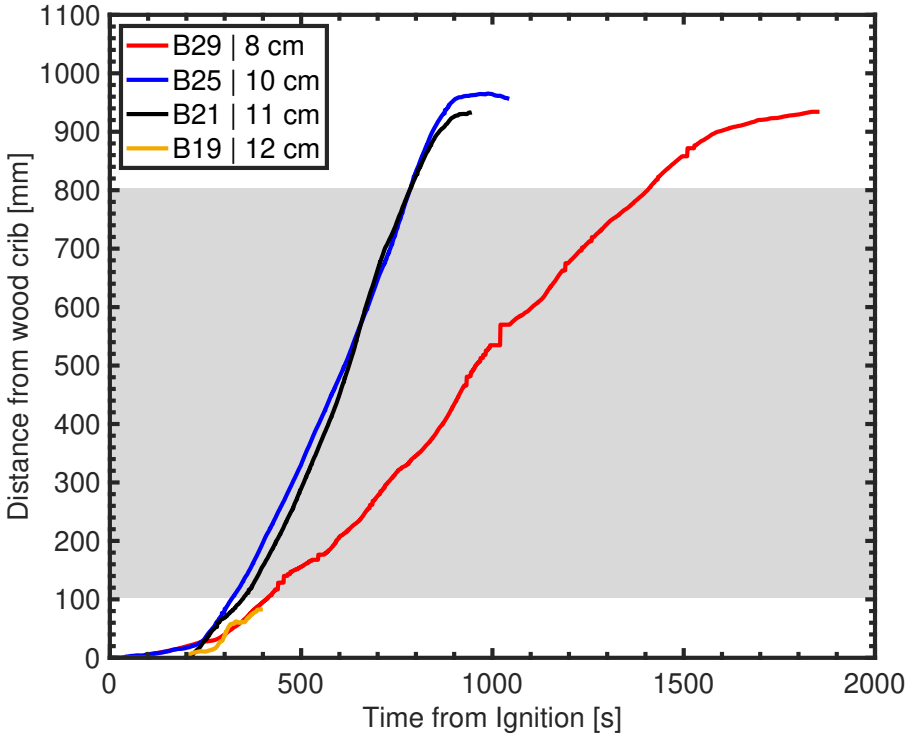

(a) Horizontal PV modules

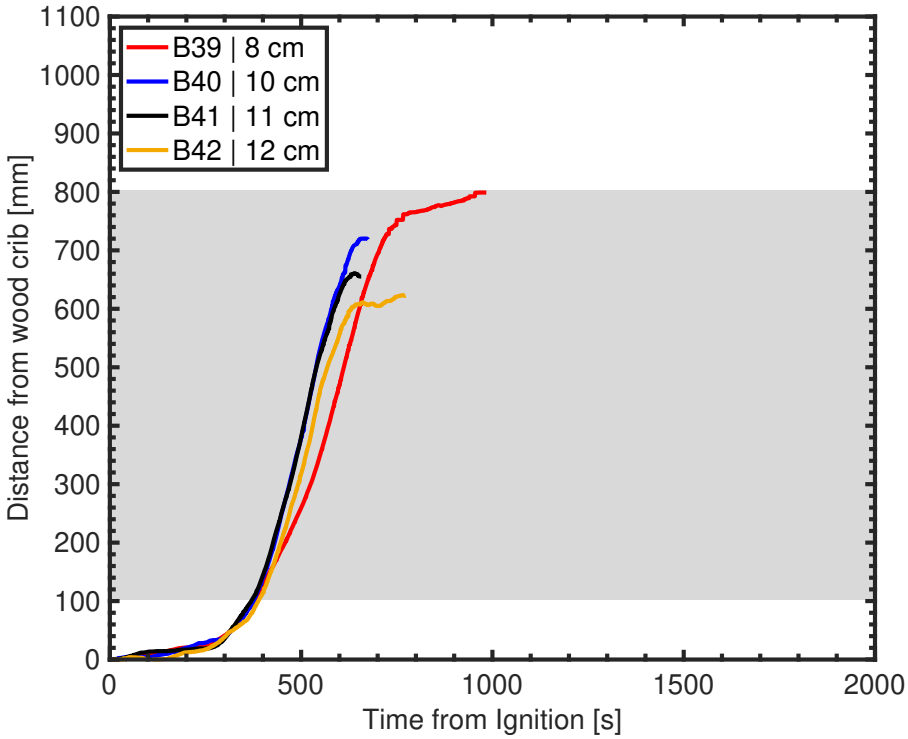

(b) PV modules with an inclination of 10°

Figure 4.21: Flame front location as a function of time from ignition for experiments with **(a)** Horizontal PV modules, and **(b)** PV modules with an inclination of 10° at gap heights between 8 cm and 12 cm. All experiments were conducted with mineral wool below the roofing membrane and further details can be found in the experimental matrix (see table 3.6). The grey box corresponds to the width of the roof construction mock-up.

Due to the consistent flame spread rates below the horizontal barriers, it was decided to determine the FSRs as a constant calculated as the average speed between the two points reached 30 seconds before and after the flame front reached a distance of 450 mm from the edge of the wood crib. The measured constant flame spread rates are plotted in figure 4.22.

The FSRs measured for the experiments below horizontal panels (see figure 4.22a) indicated a dependency of the gap height, panel type and the material below the roofing membrane. When the fire propagated outside the domain of the ignition source, the FSR was reduced as a function of a gap height reduction for experiments with a gap of 11 cm and below when the panel was a PV module and for 10 cm and below when the panel was the stainless-steel board. The FSRs at a gap height of 11 cm were ignored for the experiments conducted with the stainless-steel board due to the inconsistency of the results.

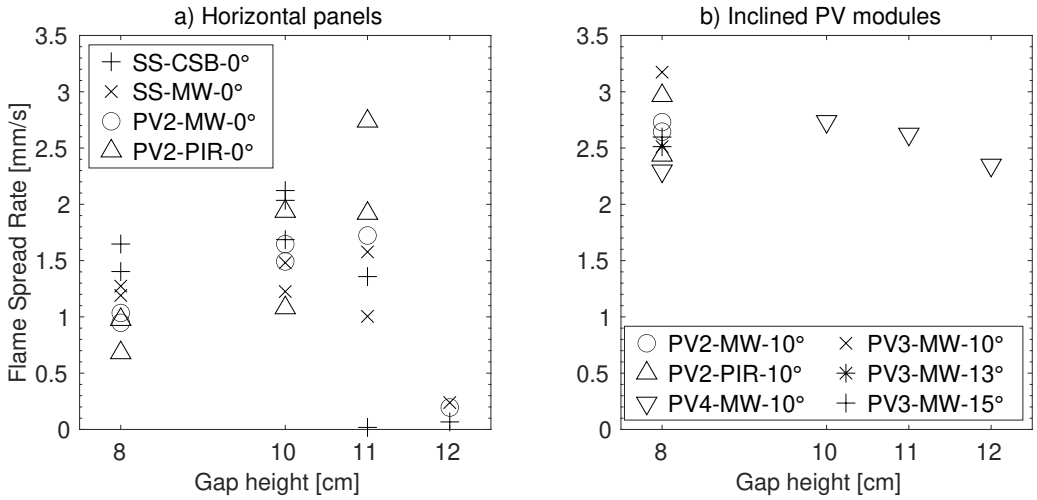

Figure 4.22: Flame spread rate (FSR) as a function of gap height, panel type (Stainless-steel board (SS) or PV module (PV2, PV3, or PV4)), or insulation material (Calcium silica board (CSB), mineral wool (MW), or PIR insulation) for experiments conducted below: **a)** Horizontal panels, or **b)** Inclined PV modules.(From Kristensen et al. [7]).

Focusing on the experiments conducted with the stainless-steel board, the influence of the specific heat was verified as the FSR achieved with the calcium silicate board (CSB) was consistently faster than the FSR for similar experiments conducted with a subjacent layer of mineral wool (see Figure 4.22a).

Again, it is expected that the lower heat loss from the roofing membrane towards the upper layer of the CSB, compared to the mineral wool, caused faster heating of the roofing membrane and thus a faster FSR. Subsequently, the lower conductivity of the mineral wool might have caused a lower conductive heat loss from the pyrolysis zone.

Similar to the flame spread length (FSL), the panel type also affected the flame spread rate (FSR), as the FSRs were consistently faster in the experiments conducted with the stainless-steel board for gap heights of 10 cm and below. Once again, it was expected that the difference between the two panel types was related to the geometry of the PV module rather than the polymer backsheet. As the 40 mm aluminium frame of the PV modules, as well as the enclosed smoke layer, efficiently reduced the gap height of the semi-enclosure, it was expected that one or both of the following phenomena occurred: i) an increased velocity of the entrained air, which caused an enhanced convective heat loss and thus a lower FSR, or ii) a reduction of the overall amount of ambient air entrained into the fire plume and thus a reduction of the combustion efficiency, which might have caused a lower heat release rate and thereby a reduction of the FSR.

Except for the experiments conducted with PIR insulation below the horizontal panels, the repeatability of the experiments was deemed satisfactory (see Figure 4.22a). It was expected that aluminium foil on the upper surface of the PIR insulation would affect the flame spread rate. However, the inconsistent FSRs for similar experiments indicated a very sensitive system which probably depended on the possible air gap between the roofing membrane and the PIR insulation.

If a small air gap between the roofing membrane and the PIR insulation was present, the aluminium foil would reflect the radiative heat transfer from the heated roofing membrane back towards the membrane. That would lead to a reduced heat loss and thus a high FSR. A lower FSR was expected if no air gap existed between the roofing membrane and the PIR insulation, as the aluminium foil would have no effect whereupon conductive heat transfer would occur between the roofing membrane and the PIR insulation.

The inconsistent results for the experiments conducted with PIR insulation were also observed in the experiments with inclined PV modules, where a difference of 0.6 mm/s was seen for two similar experiments conducted with an inclination of 10° and a gap height of 8 cm (see Figure 4.22b). In addition to the consequence of a potential air gap between the roofing membrane and the insulation, the PIR insulation started swelling when exposed to heat, as seen in Figure 4.23 where the thickness had increased by more than 30%. As such, the thickness of the material and thus the gap height was not constant, whereupon the final height might have varied across similar experiments, which would have affected the flame spread rate.

For the remaining part of the experiments conducted below inclined modules, no significant trend was observed between the FSR, gap height, and inclination of the PV modules (see Figure 4.22b). In general, the flame spread rates were significantly faster than the FSRs below the horizontal panels in Figure 4.22a. The difference was ascribed to two changes caused by the inclination of the PV modules: i) Based on the model by Tang et al. (see Eq. 1.1), the upstream radiative heat flux, $\dot{q}''_f$, should increase for positive inclinations if the heat release rate, $\dot{Q}$, remained constant. As the wood cribs were considered an ignition source with a high

Figure 4.23: Post experiment sectional view along the centre-line for an experiment conducted with PIR insulation and a gap height of 11 cm to a horizontal PV module type 2 (B23 in Table 3.6). The thickness was 80 mm, and the image was mirrored horizontally to ensure a consistent flame spread direction from right to left.

reproducibility, the initial upstream preheating was more prominent when the modules were inclined. Subsequently, the increased preheating caused a longer pyrolysis zone and thus a higher heat release rate, subsequent upstream heat flux, and FSR. ii) When the PV modules were inclined, the buoyancy-driven combustion products were allowed to follow the back of the PV module, which permitted a higher entertainment of air into the fire along the roofing membrane, as well as an elimination of the suggested convective heat loss caused by the high-velocity air entertainment for the horizontal modules.

Finally, the four experiments conducted with mineral wool, a gap height of 8 cm, and an inclination of 10°, but with three different PV modules (B32, B33, B36, and B39) yielded different flame spread rates (see Figure 4.22b). The two experiments conducted with PV2 achieved similar flame spread rates of 2.63 mm/s and 2.73 mm/s, whereas the FSRs in the experiments with PV3 and PV4 were respectively 3.17 mm/s and 2.30 mm/s. Thus, the latter were significantly different from each other as well as the experiments conducted with PV2. As the overall repeatability of the FSRs for the experiments conducted with mineral wool was high (see Figure 4.22), it was expected that the different PV modules caused the different flame spread rates due to various geometries (see Table 3.2) or back sheet materials. However, such a statement would require repeated experiments to verify that the results were part of a general trend.

4.4.4 Exposure

The use of three different roof constructions below the roofing membrane enabled a gradual increase in the complexity, and as such, the use of a roofing membrane instead of a PMMA sheet was the only difference between the experiments in Section 3.4 and the experiments conducted with roof construction type RC-A (B1 to B9 in Table 3.6). Subsequently, the calcium silicate board in RC-A was replaced with the more complex RC-B (B10 to B18 in Table 3.6). The replacement enabled examination of two things: i) How the subjacent layer of mineral wool (MW) in RC-B affected the flame spread behaviour, and ii) How the 50 mm MW projected the existing roof construction with expanded polystyrene (EPS) and a single layer of roofing membrane, which was expected to be a worst-case scenario.

The flame spread behaviour, as a function of panel type and roof construction type, were quantified by the flame spread length and flame spread rate in Sections 4.4.2 and 4.4.3. Due to the in-consequent flame spread lengths (see Figure 4.20) and since the delamination of the PV cells prevented quantification of the heat flux towards the roofing membrane and subjacent insulation material, it was deemed necessary to quantify the magnitude of the heat transfer in a different way.

The quantification of the heat transfer towards the insulation materials in roof construction RC-B and RC-C was found necessary to generate a link between the fire in the semi-enclosure and the temperature development in the insulation materials (see Section 3.5.3). The fireline intensity [176, 177] in see Eq. 4.4 was defined by Byram [178] and is frequently used to quantify the energy, $I\ [kW/m]$, released from a forest fire which similar to the conducted experiments are not heavily instrumented. As such, the fireline intensity was deemed a acceptable way to quantify the magnitude of energy transferred from the fire towards the subjacent insulation materials.

$$I = HWR \qquad [178] \tag{4.4}$$

By reusing the nomenclature by Byram in see Eq. 4.4, the intensity was the product of the heat of combustion, $H\ [kJ/kg]$, the density of the fuel per area, $W\ [kg/m^2]$, and the flame spread rate, $R\ [m/s]$. The roofing membrane was expected to be homogeneous, and consequently, both the density and the heat of combustion were considered constants, after which the fireline intensity would be proportional to the flame spread rate.

Despite similar flame spread rates (FSR) for the flame front, the post-experimental video analysis of the experiments (see Section 4.2) revealed that there was no relation between the FSR and the length of the pyrolysis zone as exemplified in Figure 4.24. Because the width and duration of the pyrolysis zone for the experiment conducted with the horizontal PV module (see Figure 4.24a) was significantly larger than below the inclined PV module (see Figure 4.24b), it was expected that the amount of energy transferred towards the insulation material would be significantly larger. However, the behaviour of the pyrolysis zone was not considered by the fireline intensity (see Eq. 4.4), and thus the equation was deemed unfit for the intended use.

The importance of the pyrolysis zone was taken into account by replacing the flame spread rate, $R\ [m/s]$, with the area of the pyrolysis zone, $A_{pyro}\ [m^2/s]$. As the one-dimensional length of the pyrolysis zone were known as a function of time, $l_{pyro}(t)\ [m]$, the area was defined as a square with a width, $w\ [m]$, equivalent to the width of the roofing membrane: $A_{pyro} = w \cdot l_{pyro}(t)$. Consequently, the fireline intensity ($[kW/m]$) became independent of the distance and was renamed *intensity* ($[J/s]$).

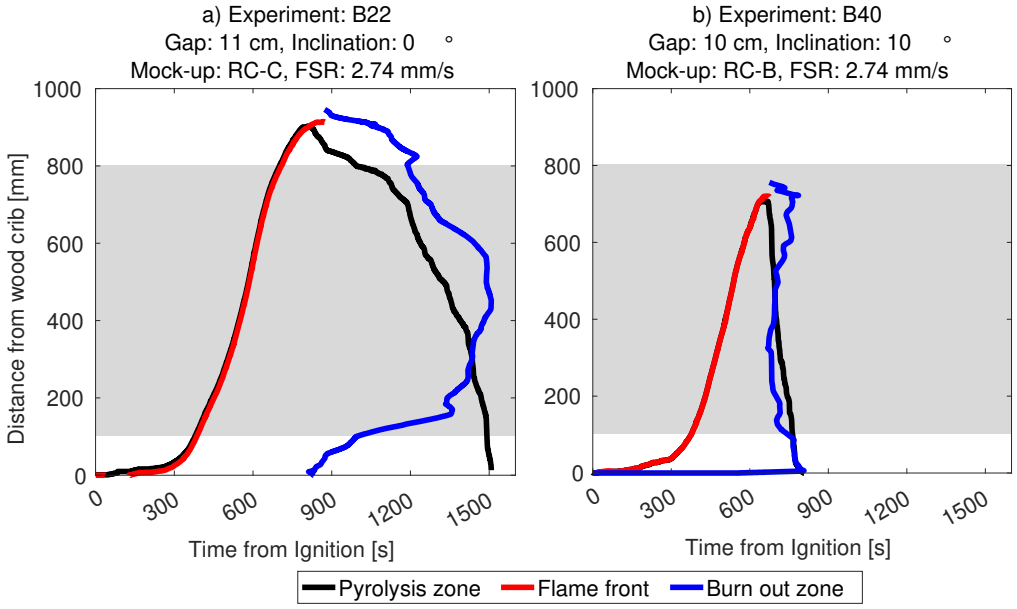

Figure 4.24: Location of the flame front, burn out zone, and width of pyrolysis zone as a function of time. The 700 mm long areas highlighted in grey indicate the location of the subjacent roof mock-up (From Kristensen et al. [7]).

As the intensity was time-dependent, a cross-experimental comparison was only possible by comparing the overall amount of energy transferred from the fire towards the insulation material. That was enabled by integrating the intensity, $I\ [J/s]$, over the duration of the experiment, as seen in see Eq. 4.5, which yielded the fire load, $q_f\ [J]$.

$$q_f = \int_{t_{ig}}^{t_{end}} (HWA_{pyro}(t))\, dt \tag{4.5}$$

However, the definition of the fire load expected a constant heat of combustion, H, across all of the experiments, which was deemed unlikely as the limited gap heights in some experiments probably restricted the air entrainment into the fire plume and thus the combustion efficiency. Due to the unknown combustion efficiency, the fire load, q_f, was deemed unfit for cross-experimental comparison as the assumption of a constant combustion efficiency would be inaccurate. Instead, the magnitude of the heat transfer was by term Exposure, $E\ [m\,s]$, which was equivalent to the integral of the time-dependent pyrolysis zone length, $l_{pyro}(t)\ [m]$ as defined in Eq. 4.6:

$$q_f = HWw \int_{t_{ig}}^{t_{end}} (l_{pyro}(t))\, dt = HWwE \tag{4.6}$$

The Exposures were only defined for the part of the pyrolysis zone located above the roof construction mock-up as highlighted in grey in Figure 4.24, which entailed the maximum length of the time-dependent pyrolysis zone was 700 mm.

The Exposures for all of the experiments, including the experiments conducted with the calcium silicate board, were plotted in Figure 4.25. In general, the repeatability of the calculated exposures was very high in the experiments conducted below the horizontal panels (see Figure 4.25a), as well as the two sets of experiments conducted with a gap height of 8 cm, an inclination of 10°, and subjacent insulation materials of respectively PIR insulation or mineral wool (see Figure 4.25b).

Most remarkable was the significant difference between the experiments conducted with the horizontal stainless-steel board and the PV modules (see Figure 4.25a), as the exposure of all experiments conducted with the PV modules was significantly higher for gap heights of 11 cm and below. Similar to the FSL and FSR, it was expected that increased Exposures were related to the additional gap height reduction caused by the PV module frame and the concomitant restricted air entrainment into the fire plume. Assuming an inefficient combustion process caused by the lack of entrained air, the heat release rate might have been reduced significantly, resulting in a lower mass loss rate. In case of a reduced mass loss rate of the pyrolysis zone, the velocity of the burnout zone would drop correspondingly and yield a longer pyrolysis zone.

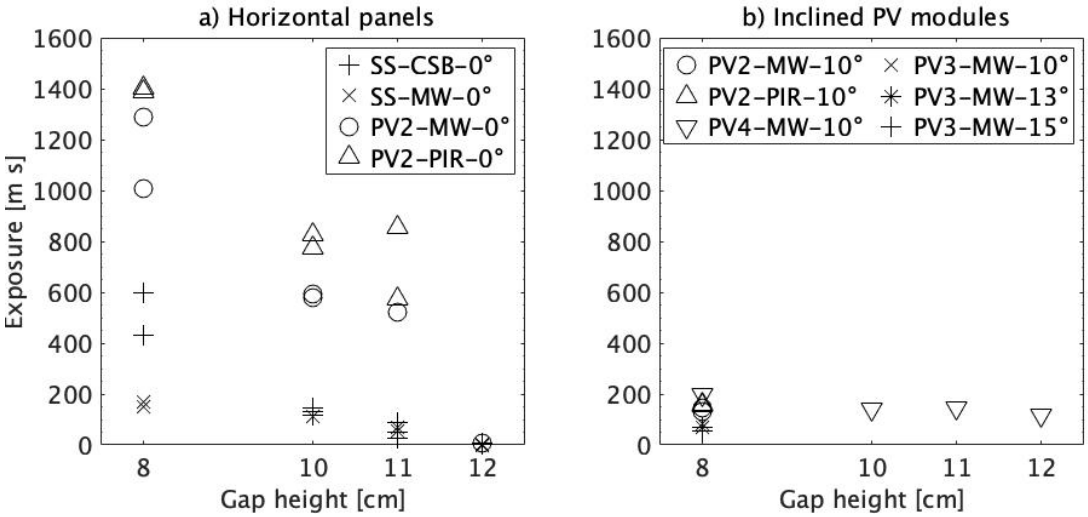

Figure 4.25: Exposure plotted against gap height, panel type (Stainless-steel board (SS) or PV module (PV2, PV3, or PV4)), or insulation material (Calcium silica board (CSB), mineral wool (MW), or PIR insulation) for experiments conducted below: **a)** Horizontal panels, or **b)** Inclined PV modules. (From Kristensen et al. [7]).

The expected relation between the restricted air entrainment for the horizontally installed PV modules (see Figure 4.25a) and high Exposure, was verified when the PV modules were inclined (see Figure 4.25b), as it caused a significant reduction of the Exposure. It was accepted that the reduced flame spread lengths (FSL) for the inclined PV modules (see Figure 4.20b) would result in a lower Exposure if the FSLs were below 80 cm (i.e. right side of roof mock-up). For experiments conducted with an inclination of 10°, the FSL was 72 cm for a gap height of 11

cm, equivalent to a 12% reduction of the exposed areal, whereas the Exposure of $145\ ms$ was almost four times lower than the lowest Exposure calculated for the similar experiment below a horizontal module ($576\ ms$). When the gap height was reduced to 8 cm, a FSL of 80 cm or above was achieved for all experiments with an inclination of 10° (see Figure 4.20b) and thus, the flame front covered the entire length of the subjacent insulation material. However, the lowest Exposure calculated for the horizontal PV modules ($1005\ ms$) was five times larger than the highest Exposure calculated for the semi-enclosure below a PV module with an inclination of 10° ($197\ ms$).

As such, it was concluded that the panel type and inclination had a significant influence on the Exposure $[ms]$, which was a parameter developed as neither the flame spread length (FSL) nor flame spread rate (FSR) was deemed adequate to quantify the magnitude of the heat transfer towards the roof construction mock-up. Similar to the quantification of the FSL and FSR, the frame of the PV modules was expected to cause the difference rather than the PV module backsheet.

4.4.5 Maximum temperature in insulation materials

The temperatures were measured by 20 thermocouples installed at six different depths between 10 mm and 70 mm as defined in Figure 3.7. As the maximum temperatures were the product of a time-dependent, transient heat transfer from the propagating fire in the semi-closure between the panel and the subjacent roof construction, they were plotted against the Exposure rather than the gap height, which was used when plotting the flame spread length and flame spread rate (see Figures 4.20 and 4.22). By doing so, it was possible to compare the temperature development through the subjacent roof construction as a function of a parameter which quantified the *magnitude* of heat transferred towards the insulation, but not the actual values due to the limited instrumentation of the roof construction mock-ups.

The comparison between the Exposure and temperature development was of interest because the two roof construction types, RC-B and RC-C (see Table 3.4) represented an existing roof construction insulated with expanded polystyrene (EPS), which were protected by mitigation layers of respectively 50 mm mineral wool (MW) or 60 mm PIR insulation.

As the purpose of the mitigation layers was to reduce the temperature of the EPS insulation, it was interesting to know the maximum temperature achieved as a function of depth. Because the maximum temperatures were determined as a function of depth, the temperatures were the maximum value of several thermocouple (TC) measurements, as four TCs were installed at the depths of 10 mm, 30mm, and 50 mm, whereas three TCs were installed at the depths of 20 mm and 40 mm, and only two TCs were installed at a depth of 70 mm as defined in Figure

3.7. The thermocouples were shifted towards the side furthest away from the wood crib to prevent eventual pre-heating from the ignition source. Consequently, the number of TCs used to determine the maximum temperatures at the different depths might have been reduced in the experiments with shorter flame spread lengths (see Figure 4.20).

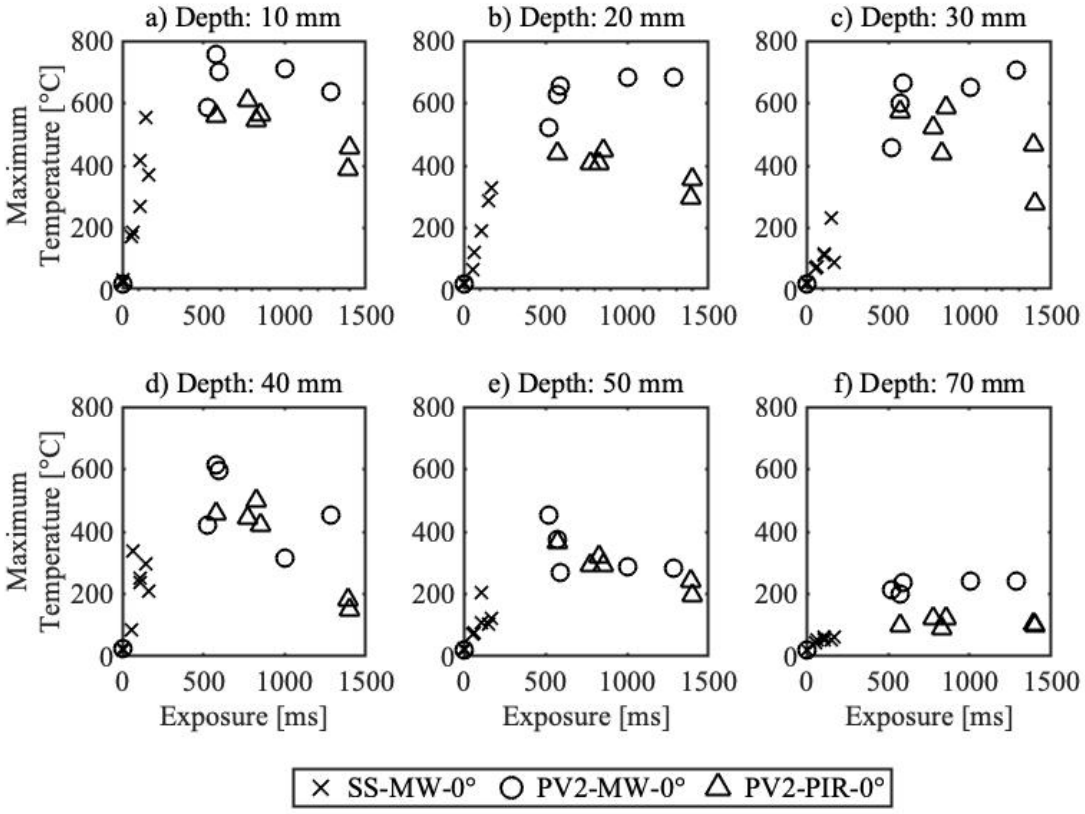

Figure 4.26: Maximum temperature below the horizontal panels plotted against Exposure [m s], depth [mm], panel type (stainless-steel (SS) or PV module (PV2)), and insulation material (mineral wool (MW) or PIR). (From Kristensen et al. [7]).

In the experiments conducted with horizontal panels, there was a relatively clear trend between the Exposure at the maximum temperatures measured in the upper 30 mm of the insulation materials. For Exposures below $250\ ms$, there were an almost linear relation to the maximum temperature which increased when plotted against Exposure. For Exposures above $500\ ms$, the maximum temperatures stabilised with significantly lower maximum temperature measured in the PIR insulation than the mineral wool (see Figure 4.26a-c). The material-dependencies were less evident at a depth of 30 mm (see Figure 4.26c) and almost eliminated at the depths of 40 mm and 50 mm (see Figure 4.26d-e). However, local minor maximum temperature rises occur as a function of depth in the experiments conducted with mineral wool, such as seen for

an Exposure of $523\ ms$, where the temperatures were 423 ℃ and 454 ℃ at the depths of 40 mm (see Figure 4.26d) and 50 mm (see Figure 4.26d). It was expected the the temperatures rise occurred due to one or both of the following reasons: i) smouldering combustion within the mineral wool, or ii) precision of thermocouple location.

In some of the experiments with mineral wool, sudden local temperature increases occurred after self-extinguishment of the fire in the semi-enclosure. That indicated smouldering combustion within the insulation product due to an exothermic reaction from the binders [179]. That was verified when the mineral wool samples were cut along the centre line, as the grey areas seen in Figure 4.27 were less rigid and thus indicated the lack of binders.

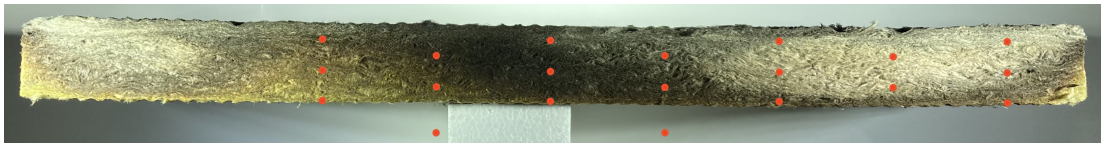

Figure 4.27: Sectional view of the mineral wool after an experiment conducted with a gap height of 11 cm to a horizontal PV module (B20 in Table 3.6). The mineral wool was cut along the centre line, flame spread occurred from left to right, and the red dots mark the location of thermocouples (TCs) in accordance with Figure 3.7. The two red dots below the mineral wool indicated the location of TCs in the expanded polystyrene (EPS).

The thermocouples (TCs) were installed with great care, but since they were inserted from the side of the 300 mm wide insulation product, the tip of the individual thermocouples might not have been located as intended (see Figure 4.27). The metal shielded 14 gauge TCs were relatively rigid, but they were able to deflect due to material resistance when they were installed. Even if the TCs were completely rigid, the final location of the TC tip was very sensitive to the angle between the insulation and TC. If the TC were not inserted precisely perpendicular to the surface of the mineral wool, an angle of 4° in any direction would cause a final displacement of 10 mm. As such, thermocouple tips with an intentional depth of 40 mm could have been located at a depth of 50 mm, and vice versa.

The influence of the insulation thickness becomes evident at a depth of 70 mm, where the maximum temperatures were measured in the expanded polystyrene subjacent to the mitigation layers of 60 mm PIR insulation or 50 mm mineral wool. Because of the additional thickness of the PIR insulation, the temperatures at a depth of 50 mm were mitigated further before reaching the upper layer of the roofing membrane above the expanded polystyrene (EPS). Thus, some of the experiments affected only a limited area of the EPS.

Due to the lower thickness of the mineral wool (MW), the roofing membrane between the MW and the EPS was exposed to temperatures measured at a depth of 50 mm. Consequently, parts of the subjacent EPS insulation melted and vaporised, after which the cavity was heated and more EPS vaporised, as seen in Figure 4.28. None of the EPS showed any sign of ignition in all cases, but it was expected that the vaporised EPS increased the fuel load. That could probably have been verified if oxygen calorimetry had been carried out on the exhaust gasses and the mass loss had been monitored.

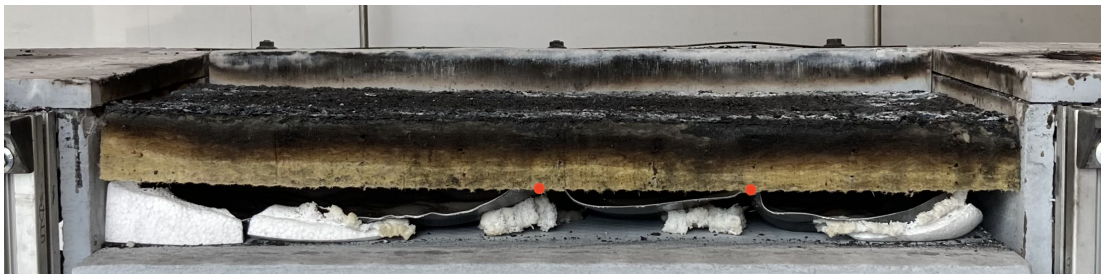

Figure 4.28: Side view of an experiment conducted with mineral wool (MW) and a gap height of 10 cm to a horizontal PV module (B24 in Table 3.6). The upper surface of the mineral wool was flush with the side flanges during the experiment but moved downwards due to the set-up disassembly. The roofing membrane above the EPS is seen below the MW, and the two red dots indicate the location of the two TCs at a depth of 70 mm. Flame spread from left to right.

The temperatures in the insulation materials dropped significantly when the PV modules were inclined, as seen in Figure 4.29. The reduction corresponded well with the lower Exposure, but contrary to the experiments conducted below horizontal modules (see Figure 4.29), there was no correlation between the Exposure and the measured maximum temperatures. It was expected that temperatures at the very top of the insulation materials were similar for all experiments where self-sustained flame spread occurred. However, due to the short duration of local Exposure caused by the fast flame spread rate and short length of the pyrolysis zone (see Figure 4.24b), the measured maximum temperatures at a depth of 10 mm and 20 mm were 100 °C to 150 °C lower than below the horizontal modules. That yielded lower temperatures in the subjacent layers, where temperatures above 100 °C in the EPS insulation were only measured in three experiments (see Figure 4.29).

Based on the measured temperatures, it was concluded that high Exposures, in general, caused higher temperatures within the insulation materials. For the conducted experiments below horizontal PV modules, the 60 mm PIR insulation protected the EPS insulation significantly better than the 50 mm mineral wool as the temperatures were at least 75 °C lower (see Figure 4.26f). It was expected that the temperature difference measured at the depths of 10 mm and 20 mm was a consequence of the aluminium foil on the PIT insulation (see Figures 4.26a-b). Despite the initial temperature difference, there was no significant difference at a depth of 50 mm (see Figures 4.26e), which indicated that the actual conductivity of the mineral wool was lower than the conductivity of the PIR insulation when the products were exposed an actual fire.

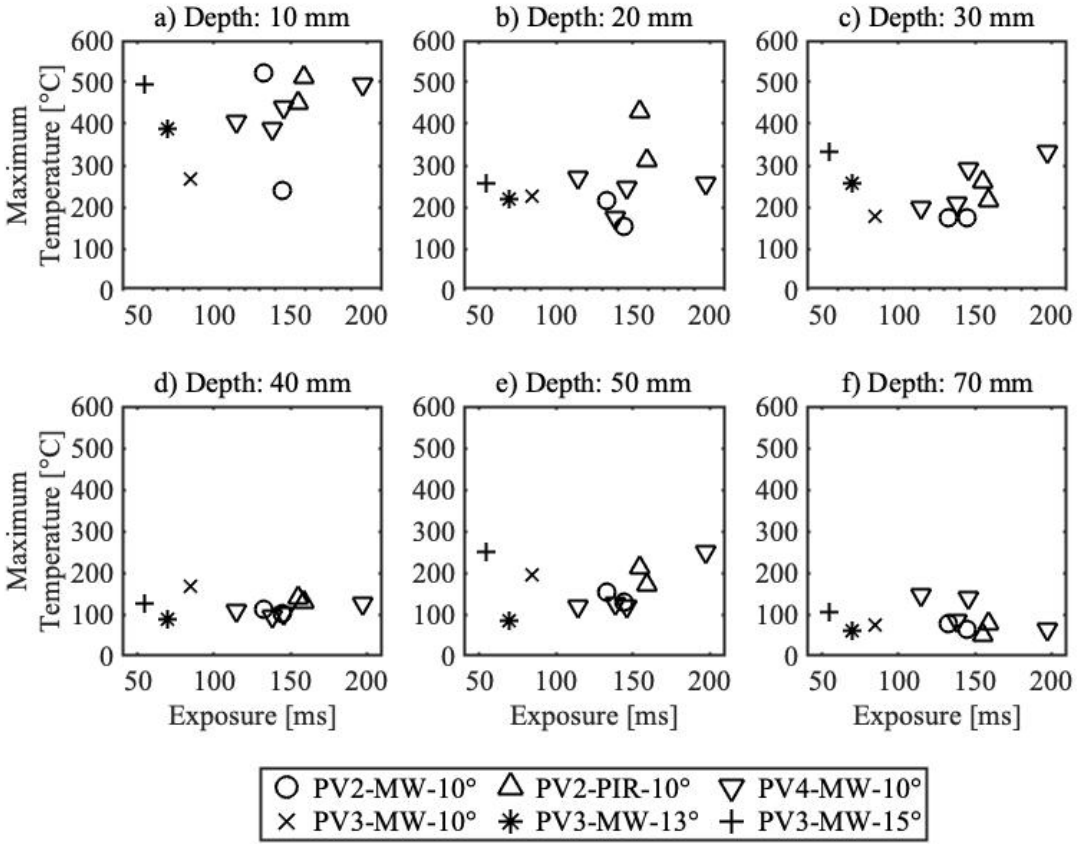

Figure 4.29: Maximum temperature below the inclined PV modules plotted against Exposure [m s], depth [mm], inclination, PV module (PV2, PV3, or PV4), insulation material (mineral wool (MW), or PIR insulation). (From Kristensen et al. [7]).

That did not correspond with the conductivities at room temperature where the PIR insulation ($0.022\,W/(mK)$) outperformed the mineral wool ($0.036\,W/(mK)$) (see Table 3.5). As such, it was expected that the mineral wool would perform (i.e. protect the subjacent EPS insulation) as good as, if not better than, the PIR insulation if the products were tested with the same thickness.

4.4.6 Conclusion based on experimental campaign

An experimental set-up representing a flat roof construction with a building applied PV system was designed to examine how four different parameters affected the flame spread length and flame spread rate in a semi-enclosure between a roof construction mock-up and a panel, as well as the heat transfer towards and temperature development in the roof construction mock-up. PV modules or a stainless-steel board were used as the panel, and the gap height and panel inclination formed the second and third parameters. A PVC-based roofing membrane (B_{ROOF}(t4)) was used throughout all the experiments, and three different roof constructions below the membrane represented the fourth parameter. A calcium silicate board

was used in the initial experiments, whereas the use of either 60 mm PIR insulation or 50 mm mineral wool was examined with the purpose of reducing the heat transfer towards a layer of expanded polystyrene (EPS) which represented an original, assumed worst-case scenario, roof construction.

The use of PIR insulation as a mitigation layer caused significantly lower temperatures within the EPS insulation. However, the difference between the temperatures measured below the PIR insulation and mineral wool was ascribed to the different thicknesses of the two products, as the overall conductivity of the mineral wool was better at high temperatures. As such, it was expected that the mineral wool would perform as good, or better than, the PIR insulation if they were tested at the same thickness.

For the experiments conducted with horizontal panels, no self-sustained flame spread occurred for gap heights of 12 cm, whereas a 1 cm reduction of the PV module caused flame spread along the entire length of the roofing membrane. For the experiments conducted with the stainless-steel board, consistent results required further reduction of the gap height to 10 cm. As the polymer backsheet of the PV modules only burned away at the location of direct flame impingement, it was not considered a significant increase of the fuel load, which affected the flame spread in the semi-enclosure.

Instead, the lower critical gap height for the PV modules was ascribed to their aluminium frame as it hindered the flow of buoyancy-driven combustion products and thus formed a continuous layer of hot smoke which had multiple effects: i) It enhanced the preheating along the entire length of the roof mock-up, which increased the flame spread length, and ii) it limited the efficient gap height of the semi-enclosure, which caused a velocity increase of the air entrained into the fire and thus reduced the flame spread rate.

The effects of the hot smoke layer were eliminated when the PV modules were inclined as the inclination permitted upstream flow of the buoyancy-driven combustion products along the back of the modules. But the inclined PV modules also caused an increased heat flux below the elevated part of the module, whereupon self-sustained flame spread occurred in all experiments. Thus, it was concluded that the critical gap height was above 12 cm for inclined PV modules.

It is important to highlight, that the critical gap heights defined are only valid for a fire dynamic system with the specific components used within the experiments. If the 2mm thin opaque PMMA is replace with another material, or a different thickness, the energy balance for the system changes and consequently the critical gap height. If the PMMA was thicker, the pyrolysis zone would be wider and result in a longer flame height which is expected to increase the critical gap height. Likewise, a material with similar properties as the used PMMA, but with a lower heat of combustion, is expected to result in slower heating of the fuel ahead of the flame front and thus, a narrower pyrolysis zone, a lower flame height, and a lower critical gap height.

The experiments clarified that PV modules can facilitate flame spread on a roofing membrane compliant with current European standards (EN 13501-5 [67]). As such, introducing a building applied PV system on a flat roof represents a potential breach of fundamental fire safety strategies. As a result of the re-radiation from the deflected flame below the module, an initial small fire can intensify and propagate along the building envelope, which might result in severe consequences.

Therefore it is suggested that a new test standard is developed, which takes the re-radiation from the deflected flame into account. Until then, the potential consequences of building applied PV systems should be known by relevant stakeholders so that future installations take the consequences of the modified fire dynamic system into account.

4.5 Set-up C: Medium-scale experiments with adjacent roof

A surface of calcium silicate boards equivalent to twice the area of a PV module represented a flat roof construction that was partly covered by a PVC-based roofing membrane (B_{ROOF}(t4)). Half of the area was covered by a PV module with an inclination of 13° and a minimum gap height of 9 cm. The lower edge of the PV module was located next to the uncovered part of the flat roof. As described in detail in Section 3.6, the experimental set-up was constructed in the initial phase of the PhD project, and the number of unknown or unmanageable parameters limited the overall quality of the outcome. However, some of the experiments did, to some extent, provide an initial understanding of:

- How the flow from the extraction system affected the ignition phase and the heat release rate.
- Quantification of the heat flux transferred from the fire inside the semi-enclosure towards a point 16 cm from the edge of the PV module.
- Quantification of the heat flux below the PV module

Due to a high smoke production from the burning roofing membrane, the area below the PV modules was limited for safety reasons. Two series of experiments were conducted with squares of roofing membrane with a side length of respectively 45 cm (experiment C1-C6) and 70 cm (experiment C7-C12 in Table 3.8) inside the semi-enclosure. The heat release rate and heat flux towards the open roof construction were quantified in all experiments, whereas the heat flux below the PV modules was only quantified in the experiments with a membrane side length of 70 cm (C7 to C12).

As such, the overall visual observation from the experiments will be presented in Section 4.5.1, after which the extraction flow and heat release rate are discussed in Section 4.5.2. Finally, the measured heat fluxes out- and inside the semi-enclosure are presented in Sections 4.5.3 and 4.5.3. Savitzky-Golay filtering with a span of 5 and a frame length of 151 were used for all data types to increase the readability of the plots.

4.5.1 Visual observations

In general, fire propagated below the PV module in most of the experiments, but the severity of the fire and the area of the roofing membrane affected depended on the PV module condition and the extraction flow. For the experiments conducted with a side length of 70 cm (C9-C12), the intensity of the fire in the semi-enclosure was significant, and the flame spread occurred relatively fast, as seen from Figure 4.30.

When flame spread occurred outside the wood crib's domain, the onset occurred after approximately eight minutes when the burning wood crib had ignited a significant area of the roofing membrane (see Figure 4.30b). Subsequently, a self-enhancing heat feedback loop causes a continuous area increase of burning roofing membrane and thus an increased heat

(a) Time of ignition.

(d) Time from ignition: 600 seconds

(b) Time from ignition: 480 seconds

(e) Time from ignition: 660 seconds

(c) Time from ignition: 540 seconds

(f) Time from ignition: 720 seconds

Figure 4.30: Flame spread in semi-enclosure between a sheet of roofing membrane with a side length of 70 cm and a new PV module. The displacement of the wood crib was 10 cm from the lower edge of the PV module (C9 in 3.8)

release rate (see Figures 4.30c-4.30d). Self-extinguishment occurred when the flame front reached the edges of the membrane as the further flame spread was not possible as no other combustible material was located in the semi-enclosure (see Figure 4.30f). Self-sustained flame spread was not observed on the back of PV modules in any of the experiments, and only the back sheet membrane affected by direct flame impingement burned away, as seen in Figure 4.30d.

In the experiments where self-sustained flame spread occurred in the semi-enclosure, no significant flame spread continued to the open roof construction. As seen from Figure 4.31, the roofing membrane outside the semi-enclosure was only affected at a distance of a couple of centimetres. That corresponded well with previous large-scale experiments where no self-sustained were observed outside the PV array, but the adjacent roofing membrane was occasionally ignited when the flame from the fire inside the semi-enclosure was deflected by the wind towards the adjacent roof [1].

Similar to the experiments examining the influence of gap height and inclination of the PV module (see Section 3.5), the PV cells delaminated from the PV module when the back sheet burned away. As the PV cells were non-combustible mono- or poly-crystalline silicon, they did not increase the fuel load. However, the delamination of the cells indicates that both the polymer membrane and encapsulate burned away and thus increased the fuel load, although probably to a limited extent.

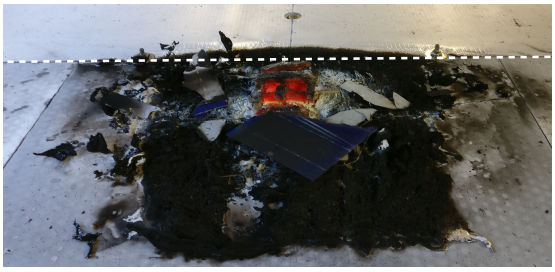

Figure 4.31: Smouldering wood crib and location of flame spread on roofing membrane with a side length of 45 cm (C2 in Table 3.8). The dotted white line indicates the location of the PV module's lower edge. The sooted blue and white debris with sharp corners were respectively the front and back of the PV cells, which were delaminated from the PV module. The heat flux gauge outside the semi-enclosure is seen at the top of the image.

4.5.2 Heat release rate below PV modules

Membrane side length of 45 cm

The influence of the PV module back sheet was, to some extent, quantified through the heat release rate (HRR) measurements as the condition of the PV module, together with the extraction flow rate, were the two main variables in experiments conducted with a roofing membrane side length of 45 cm (C1-C6) in Figure 4.32a. Because the extraction flow rate was a time-dependent variable that was adjusted manually, it was plotted separately in Figure 4.32b, whereas the condition of the PV modules was stated in the common plot legend.

For all of the experiments conducted with a roofing membrane side length of 45 cm (see Figure 4.32), the initial phase of the experiments were similar, with a steady rise in the heat release rate (HRR) until 480 seconds after ignition, after which a considerably increase of HRR began. The magnitude of the increase varied as the peak heat release rates (pHRR) were between 22 kW to 27 kW for the experiments C3, C4, and C5, and between 41 kW and 45 kW for experiments C1, C2, and C6.

Focusing on the three experiments with the highest HRRs, the HRRs are almost identical until 540 seconds after ignition, where a drastic HRR decline begins for experiment C6, while the HRR remains high for experiments C1 and C2 despite slight declines. Except for the initial extraction flow of 800 l/s for experiment C2 (see Figure 4.32b), the input variables of

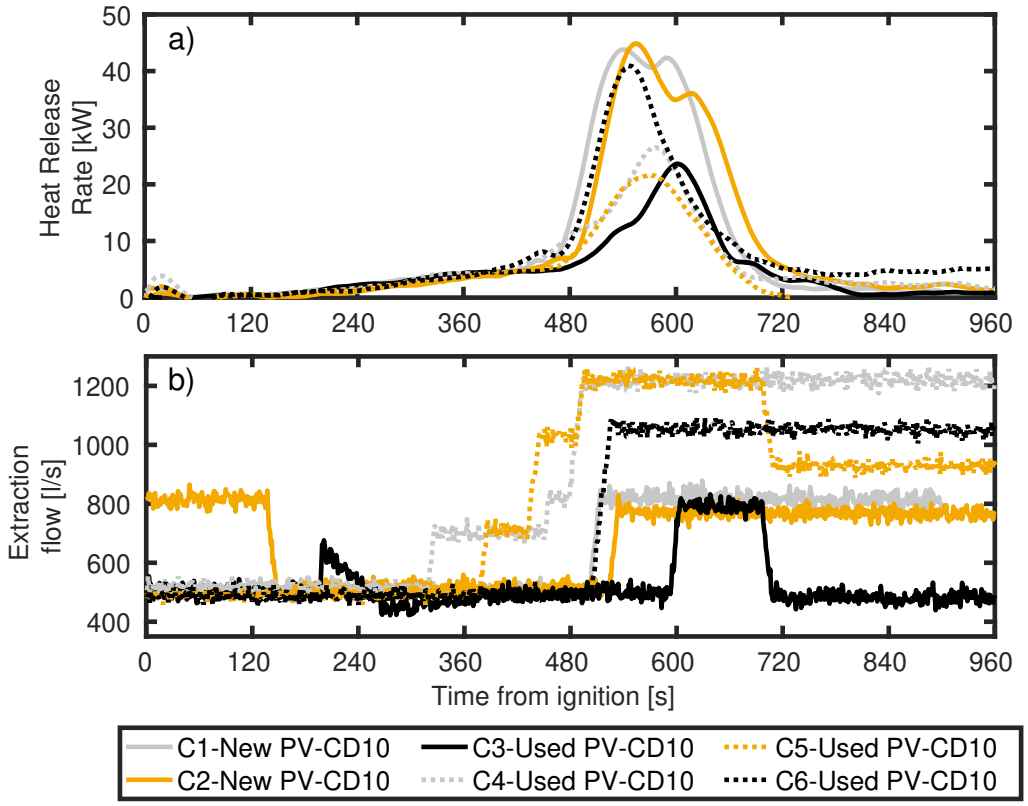

Figure 4.32: Heat release rate (Figure 4.32a) as a function of time, PV module condition (New/Used), and extraction flow (Figure 4.32b). Squared sheets of roofing membrane with a side length of 45 cm were used in all experiments, and the wood cribs used for ignition were displaced 10 cm (CD10) from the edge of the PV module as defined in Table 3.8.

experiments C1 and C2 were similar with new PV modules and an extraction flow onset from 500 l/s to approximately 800 l/s after respectively 500 seconds and 520 seconds. As such, the repeatability of the experiments seemed acceptable as similar results were obtained for similar experimental inputs.

For experiment C6, the onset time to a higher extraction flow rate was the same as in experiment C1, but the final flow rate of 1080 l/s was more than 200 l/s higher than the final extraction flow rate for experiment C1 (see Figure 4.32b). In addition, a previously tested PV module was used in experiment C6, whereas new modules were used in C1 and C2. Based on that, it was impossible to determine whether the fast decline of the HRR could be ascribed to the different extraction flow rates or the lack of combustible polymers that made up the PV modules back sheet. However, the high pHRR of experiment C6 did verify that the lower pHRRs measured in experiments C3, C4, and C5 could not be ascribed to the condition of the PV modules.

For experiments C4 and C5, the limited PHRRs were probably caused by the high extraction flow rate of 1200 l/s after 480 seconds from the ignition time (see Figure 4.32b). Based on the HRRs (see Figure 4.32a), the rises of the extraction flow between 320 seconds and 480 seconds after ignition had no distinct influence on the initial HRRs as the magnitudes for experiments C1 and C4, as well as C2 and C5 were similar at respectively 10.3 kW and 7 kW after 480 seconds (see Figure 4.32a). The initial similarities and following differences indicate a strong link between the pHRR and extraction flow rate increase 480 seconds after ignition as a too high extraction flow probably might have caused a convective heat loss or reduced the concentration of combustible pyrolysis gases.

Finally, experiment C3 revealed that the increased extraction flow rate in experiments C1, C2, and C6 acted as an accelerator. Despite the identical set-up between experiments C3 to C6, the delayed onset of increased extraction flow reduced the pHRR, and the speed of the HRR increase (see Figure 4.32). As seen in Figures 4.31, 4.33a and 4.33b, the whole area of the roofing membrane burned away in the experiments, which resulted in a high pHRR (C1, C2, and C6). Because of the delayed increase of the extraction flow rate in experiment C3, the flame front was not forced to propagate below the most elevated part of the PV module as pictured lower part of Figure 4.33c.

(a) Experiment C1, pHHR: 43.7 kW.

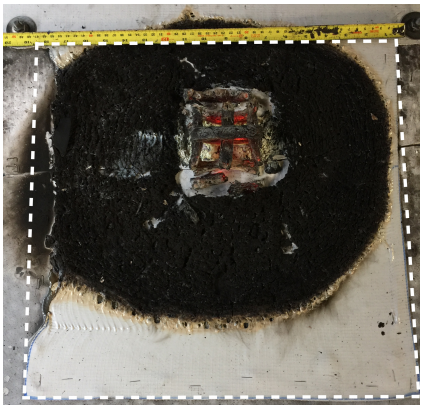

(c) Experiment C3, pHHR: 23.8 kW.

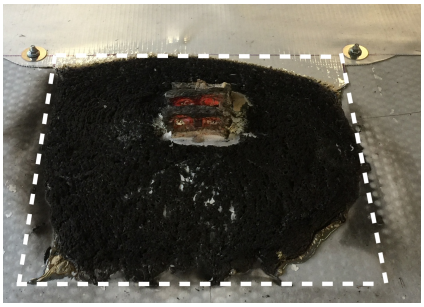

(b) Experiment C6, pHHR: 40.9 kW.

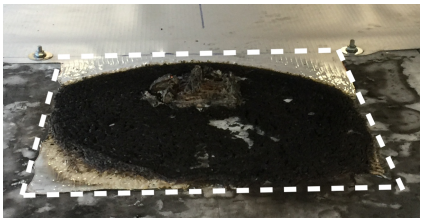

(d) Experiment C5, pHHR: 21.6 kW.

Figure 4.33: Area affected by flame spread and corresponding peak heat release rate (pHRR) for experiments conducted with a roofing membrane side length of 45 cm. The top of all images corresponds to the location of the lower PV module edge.

As the low thickness of the membrane caused a limited duration of the fire in the semi-enclosure, the flame front self-extinguished at an upstream distance (i.e. towards an enhanced elevation of the PV module) of approximately 35 cm from the lower edge of the PV module as the pre-heating of the membrane ahead of the flame front became in-sufficient. With a gap height of 13 cm, a PV module inclination of 13°, and a maximum upstream flame spread length (FSL) of 35 cm, the local gap height, H_{FSL}, at the location of the maximum FSL was around 21 cm, which was slightly lower than the local gap heights defined on page 121 in Section 4.4.2.

Membrane side length of 70 cm

The importance of the extraction flow rate was verified when the side length of the roofing membrane in the semi-enclosure increased to 70 cm in Figure 4.34. Similar to the experiments conducted with a side length of 45 cm, the initial extraction flow rate was around 500 l/s in the majority of the experiments (see Figure 4.34c), and steady growth of the HRR took place until a common onset time of 520 seconds after ignition.

The influence of the extraction flow rate was verified when comparing the identical experiments C7 and C9, as the delayed two-step increase to a higher extraction flow resulted in a significantly faster developing and higher pHRR of 160 kW for experiment C7 when compared to the pHRR of 84 kW for experiment C9. Despite the almost similar set-up with experiments C7 and C9, the pHRR of 20 kW in experiment C10 was deemed very low. Besides the lack of polymer back sheet and thus a potential fuel load, the delayed onset of the increased extraction flow rate was similar to experiment C3 in Figure 4.32 and thus, the reduced pHRR cloud also be the consequence of a too low initial acceleration of the upstream flame front. However, the HRR at the time of the extraction flow increase was 8.6 kW in both experiments, but the extraction flow increase was made 70 seconds later in experiment C10. With the condition of the PV module being the only difference between experiments C9 and C10, the presence of the PV module back sheet polymer in experiment C9 might have caused a faster development of the HRR, after which a sufficient amount of roofing membrane (i.e. fuel) remained for the subsequent development of the fire. Thus, the PV module back sheet could have been the decisive factor between considerable flame spread or not.

In the experiments C8 and C12, and C11, the location of the wood crib were slightly different than in the remaining experiments as its displacements were respectively 0 cm and -5 cm, compared to the general displacement of 10 cm. The initial high extraction flow rate of 1200 l/s in experiment C8 revealed that it yielded a pHRR similar to the wood crib itself (see Section 3.5.2), and thus the high flow rate probably diluted to the concentration of flammable pyrolysis gases to an extent where the roofing membrane could not be ignited.

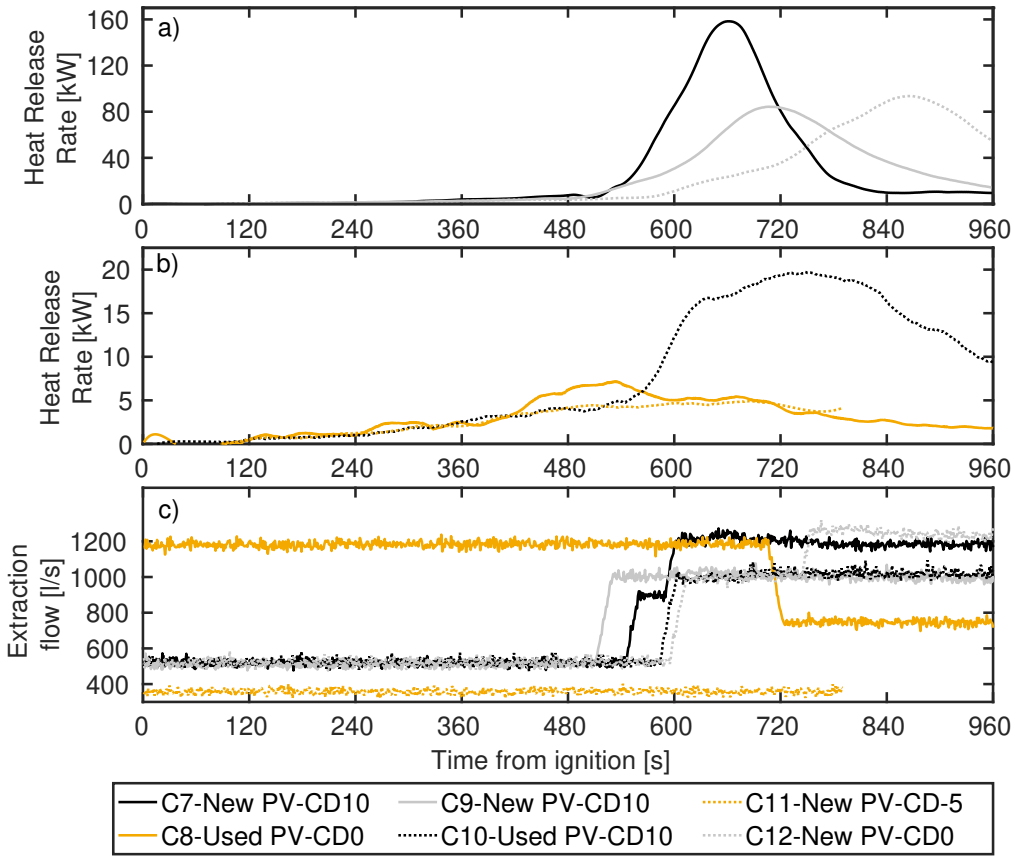

Figure 4.34: Heat release rate (HRR)(figs. 4.34a & b) as a function of time, PV module condition (New/Used), displacement of the wood crib from the lower edge of the PV module (CD-5: -5 cm, CD0: 0 cm, CD10: 10 cm), and extraction flow (Figure 4.34c). Squared sheets of roofing membrane with a side length of 70 cm were used in all experiments. Notice that the HRRs are plotted in both Figures 4.34a & b due to the different magnitudes.

Similar output occurred in experiment C11, where the wood crib was located below the lower edge of the PV module due to a displacement of -5 cm. Thus, only half of the ignition source was located below the PV module, which efficiently caused a reduced initial HRR below the PV module, which appeared unable to cause self-sustained flame spread along the roofing membrane in the semi-enclosure.

The self-sustained flame spread was achieved in experiment C12, which resulted in a pHRR of 94 kW (see Figure 4.34a). Compared to experiment C9, the ignition source in experiment C12 was moved 10 cm, whereupon one side of the wood crib was parallel with the lower edge of the PV module. As a result, only the roofing membrane on the three sides of the wood crib was ignited, which caused a slower initial growth of the fire below the PV module. Consequently, the pHRR occurred later than the in experiment C9, despite the overall development of the HRR as a function of time were similar for the two experiments.

Comparing the time-dependent development of the HRRs between experiments C10 (pHHR: 20 kW) and C12 (pHRR: 84 kW), they were identical until 615 seconds after ignition (see Figure 4.34a and b), and in addition, the onset to a higher extraction flow rate took place within a difference of 10 seconds from each other. Similar to the discussion regarding the difference between experiments C9 and C10, it was expected that the back sheet membrane of the PV module could have been the decisive factor. Because the wood crib was parallel to the lower edge of the PV module in experiment C12, the ignited roofing membrane formed a single upstream flame front rather than a flame front propagating in all directions. In addition, the 10 cm downstream displacement of the wood crib in experiment C12 was efficiently a gap height reduction of 2.3 cm Thus, the different outcomes between experiments C10 and C12 could have been related to i) the PV module back sheet, ii) the shape of the flame front, and iii) the efficient gap height reduction.

4.5.3 Heat flux outside semi-enclosure

The heat fluxes measured outside the semi-enclosure at a distance of 16 cm from the lower edge of the PV modules were, in general, very low with maximum values of no more than 1.6 kW/m^2 for both the experiments conducted roofing membrane side lengths of 45 cm (see Figure 4.35) and 70 cm (see Figure 4.36). The experiments verify the visual observations of the nearly unaffected roofing membrane outside the semi-enclosure in Figure 4.33. For experiments C1 to C6, there was an acceptable correlation between the higher release rates within the semi-enclosure and the higher fluxes plotted in Figure 4.35. However, the peak heat release rates (pHRRs) in Figure 4.32 were slightly delayed when compared to the peak heat fluxes (pHFs) in Figure 4.35.

The time of the pHFs was deemed most accurate as the HRR measurements relied on the transport time of the combustion products from the semi-enclosure to the measurement points located inside the duct of the extraction hood. Consequently, the measured flow, temperature, oxygen-, carbon monoxide-, and carbon dioxide concentration were not real-time measurements as the PV module obstructed the flow within the extraction hood.

No increase of the peak heat flux measured outside the semi-enclosure was noticed when the heat release rate in the semi-enclosure enhanced as a consequence of the side length increase of the roofing membrane (see Figure 4.36). For three experiments with a significant heat release rate (see C7, C9 and C12 in Figure 4.34), there was a acceptable relationship between the HRR and the HF. Despite similar low heat release rates for experiments C8 and C11, the heat flux received outside the semi-enclosure was significantly different as a constant heat flux of 0.1 kW/m^2 was measured for experiment C8, whereas a peak heat flux of 1.2 kW/m^2 was the of a consistently high and increasing heat flux from the time of ignition in experiment C11. Naturally, the heat flux measured in experiment C11 resulted from the wood crib location below the lower edge of the PV module and thus the heat flux gauge measured

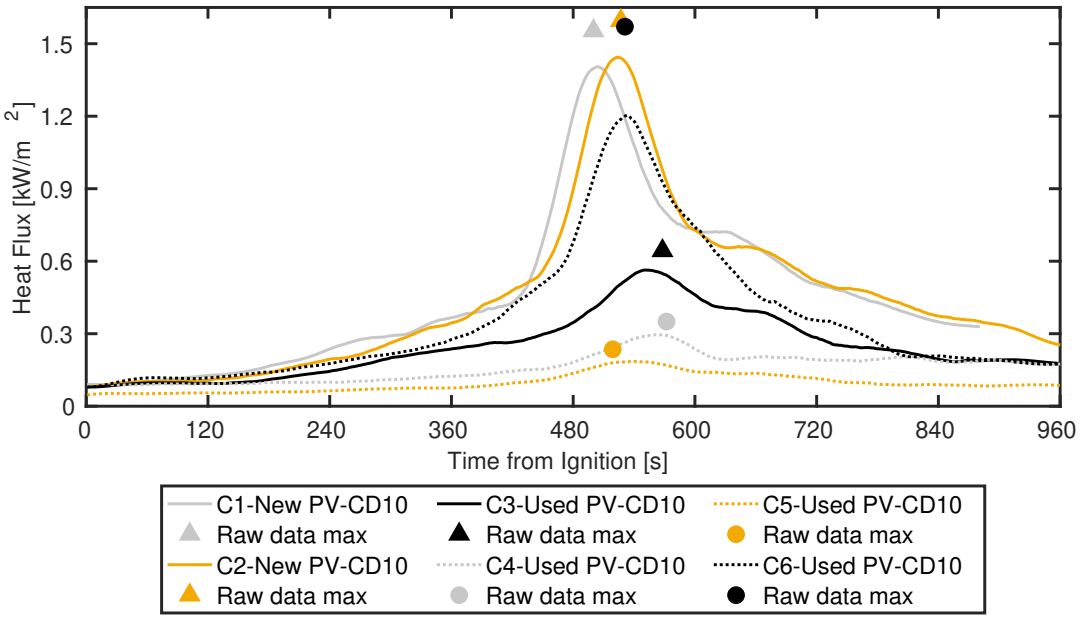

Figure 4.35: Heat fluxes measured outside the semi-enclosure with a distance of 16 cm to the PV module for experiments with a squared roofing membrane side length of 45 cm. The heat fluxes were measured as a function of time from the ignition, condition of the PV module (new/used), and the location of the wood crib (CD10: Crib Displacement of 10 cm from the lower edge of the PV module). *Raw data max* marks the maximum non-filtered heat flux measured.

the heat flux from the wood crib itself rather than the non-existing fire inside the semi-enclosure. A similar but less distinct, enhanced initial heat flux was noticed for experiment C12, where one edge of the wood crib was parallel to the lower edge of the PV module. The wood crib was located at the exact location in experiment C8, but it was expected that the heat flux remained low as a consequence of the initial high extraction flow rate (see Figure 4.34c)

4.5.4 Heat flux inside semi-enclosure

The heat flux was measured at three locations inside the semi-enclosure in experiments C9 to C12 (see Table 3.8). Three heat flux gauges (HFGs) were located per Figure 3.10b and the distance between the HFGs and the nearest part of the roofing membrane were 15 cm for HFG1 and HFG2, and 25 cm for HFG3.

A acceptable correlation was found between the heat release rate (HRR), and the heat flux (HF) measured below the PV modules as substantially higher heat fluxes were measured in experiments C9 and C12 (see Figures 4.37a and d), compared to experiment C10 (see Figure 4.37c), which corresponded well with the peak HRRs of 84 kW, 93 kW, and 20 kW (see Figures 4.34a and b).

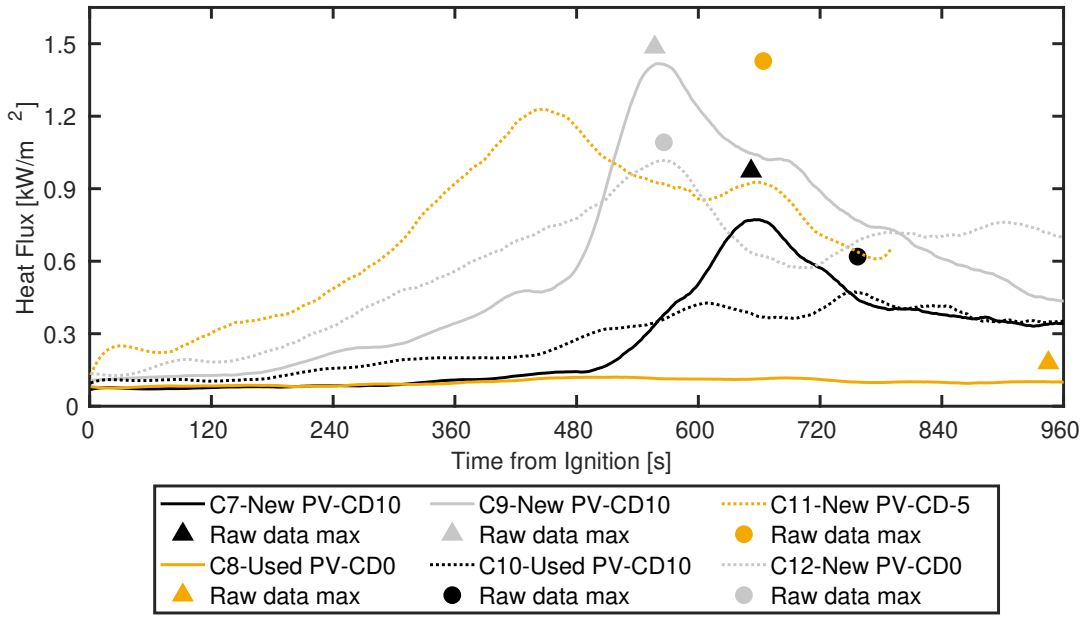

Figure 4.36: Heat fluxes measured outside the semi-enclosure with a distance of 16 cm to the PV module for experiments with a squared roofing membrane side length of 70 cm. The heat fluxes were measured as a function of time from the ignition, condition of the PV module (new/used), and displacement of the wood crib from the lower edge of the PV module (CD-5: -5 cm, CD0: 0 cm, CD10: 10 cm). *Raw data max* marks the maximum non-filtered heat flux measured.

For experiments C9 and C12, the peak heat fluxes of 23 kW/m^2 and 13 kW/m^2 indicated that continuous flame spread would have occurred if the area of the roofing had been larger. The assumption of continuous flame spread in the two experiments was based on two reasons: i) as the heat fluxes were measured at a distance of 15 cm from the burning membrane, a significant increase would have occurred as the flame front approached the location of the HFGs, and ii) because the 7 kW/m^2 (see Table 3.7) critical heat of the membrane were already surpassed with a sufficient margin for a substantial duration of time.

Comparing the HF measured by HFG1 in experiments C9 and C12, the assumption of a single flame front propagating in one direction from the lower edge of the PV module in experiment C12 (CD0) was verified as the time duration was longer and the HF increased gradually with the expected upstream movement of the flame front. That was expected to be the opposite of experiment C9, where the more central location of the wood crib (CD10) allowed up- and downstream flame spread.

A final relevant comparison was the initial development of experiments C9 and C10 (see Figure 4.37b) as the condition of the PV modules (new/used) was previously stated as the only difference between the two experiments which expected to be the decisive factor between flame spread and no flame spread (p. 141). The assumption was verified as the heat fluxes

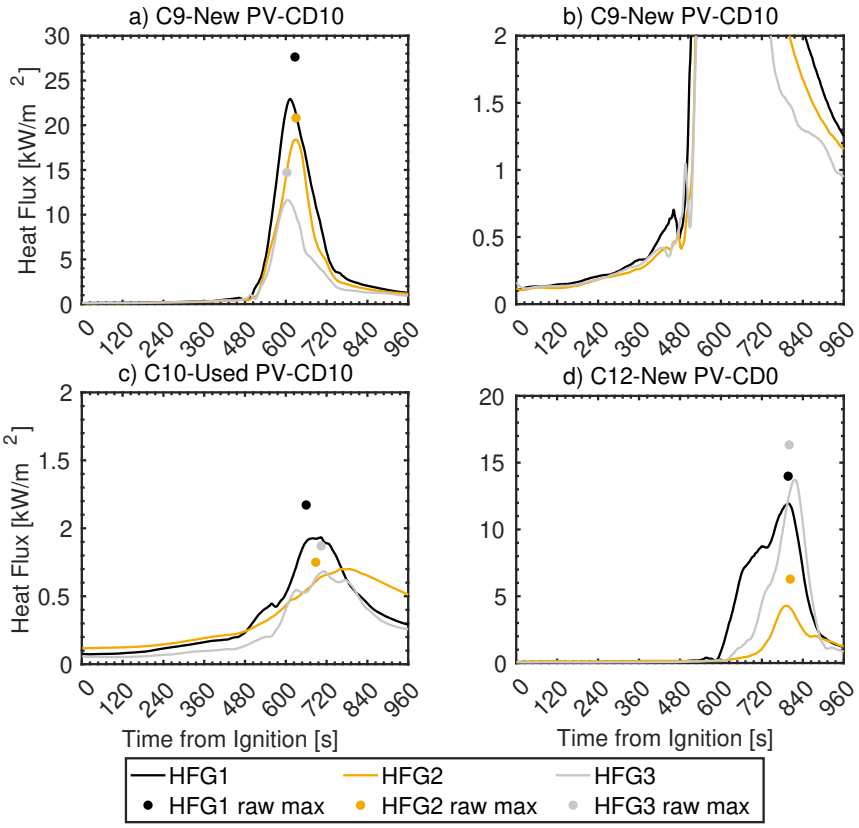

Figure 4.37: Filtered heat fluxes measured inside the semi-enclosure for experiments C9 (a & b), C10 (c) and C12 (d). Heat flux gauges were installed in accordance with Figure 3.10b. Notice that experiment C9 is plotted in Figures a and b with different scales on the y-axis. *HFG# raw max* mark the maximum non-filtered heat flux measured.

measured in experiment C9 until 480 seconds after the ignition was consequently higher than the heat fluxes measured in experiment C10. As such, it was concluded that the ignited PV module back sheet caused a slightly higher heat flux towards the roof construction, which was most likely the decisive factor that caused a faster development of the HRR in experiment C9 and thus enabled the subsequent development.

4.5.5 Conclusion based on experimental campaign

In twelve experiments, the heat release rate (HRR) from a fire inside a semi-enclosure consisting of a horizontal surface with an area of roofing membrane and an inclined PV module were quantified together with the heat fluxes (HF) in- and outside the semi-enclosure. Two squared areas of roofing membrane with side lengths of respectively 45 cm and 70 cm were ignited inside the semi-enclosure during a total of 12 experiments. In addition to the membrane side length, the experimental outcomes depended on the condition of the PV module (new/used), the extraction flow rate, and the location of the wood crib used for ignition.

Two sets of experiments were repeated on a satisfactory level (C1/C2, and C5/C6), and the repeatability was deemed acceptable. The remaining experiments were one-off but verified the importance of the gap height and indicated that the additional fuel load from the PV module backsheet could be decisive for the development of the fire (C9/C10). However, the latter was only indicated from a single experiment, and the contribution from the backsheet was deemed minuscule compared to other parameters.

Finally, it was concluded that the extraction flow rate was crucial for the outcome of the experiments. A too high initial flow caused dilution of the pyrolysis gases from the heated roofing membrane, which prevented ignition (C8), whereas a constant extraction flow (C3) caused a slower flame spread rate than a flow increase to the right level at the right time (C1, C2, C6).

In total, the twelve experiments highlighted the sensitivity of the fire dynamic system within the semi-enclosure where minuscule differences, such as the slightly higher heat flux caused by the burning roofing membrane in experiment C9, prompted significantly different results from nearly identical experiments.

Chapter 5

Flame spread between two surfaces

Based on the results from the three experimental campaigns described in chapter 4, the relevance of the findings with a focus on the fire safety science rather than the specific engineering problem associated to flame spread below BAPV systems is discussed. As such, the chapter functions as a follow-up on the discussion of flame spread between two surfaces in section 1.6.2.

The experiments were essentially a series of system flame spread experiments with three components; i) a horizontal barrier, ii) a thermally thin solid fuel, and iii) a material supporting to the fuel, from where the geometry was changed between barrier and the fuel, but remained constant between the fuel and the supporting material in set-up A and B (sections 4.3 and 4.4). Finally, the influence of slightly more stochastic factors, such as the location of the ignition source or the introduction of an (unintended) wind load, were introduced in set-up C.

The influence of the horizontal barrier and the geometry between the barrier and thermally thin fuel will be considered in the chapter followed by a discussion of the relevance for flame spread between two non-horizontal surfaces.

5.1 Orientation of the fuel

The two types of thermally thin fuel, the 2 mm thick polymethyl methacrylate (PMMA) used in set-up A and the flame retardant PVC-based roofing membranes used in set-ups B and C, where all examined horizontally. As such, opposed flame spread was the inherent flame spread mode since ambient air was entrained into the flame front as described in by Fernandez-Pello, Ray, Glassman, and Hirano [133, 180]. The opposed flame spread scenario was in general verified in the baseline experiments for set-up A as self-sustained flame spread was only possible without the presence of the horizontal barrier when the thermally thin fuel was represented by the PMMA. However, minuscule changes of the flow within the laboratory changed the flame spread mode to concurrent flame spread during few of the baseline experiments resulting in a significantly faster flame spread rate as seen in Figure 4.8.

5.2 Influence of horizontal barrier

5.2.1 Gap height to horizontal surface

The introduction of a horizontal barrier increased the complexity of the flame spread scenario significantly due to a more complex fire dynamic system. Similar to the baseline experiments radiation was the dominating heat transfer mode, but the additional radiation from the heated horizontal barrier and the combustion products had a significant effect on the initial development of the experiment and thus the final flame spread scenario. In the experiments conducted with PMMA, the horizontal barrier caused an increase of the flame spread rate for all the examined gap heights between 12 cm and 25 cm (see Fig. 4.13).

It was verified that the re-radiation caused by the deflection of the flame, and identified in steady-state experiments [108, 114, 181], had a significant influence on the heat transfer towards the fuel. The higher heat flux caused a transition from slow and constant flame spread rate to an rapidly accelerating flame front which resulted in a flame spread rate that was 38 times faster than the constant flame spread rate measured in the baseline experiments without the horizontal barrier.

The small gap heights differences between the gap height that enabled an accelerating flame spread and the gap height that did not, is one of the major findings of the project and was identified as the *critical gap height*. But in addition to the function as a flame deflector, the horizontal barrier also functioned as an emitter that caused an additional radiative heat flux, $\dot{q}''_p$, towards the PMMA in the experiments conducted with set-up A, as defined in the scenario sketched in figure 1.12b and discussed in section 1.6.2. Because the relative flame spread rate was above 1 in all experiments conducted with the stainless-steel board (see Fig. 4.13), the combined heat flux was higher than in the baseline experiments and thus the horizontal barrier must have caused an additional heat flux, $\dot{q}''_{add}$.

The ratio between the three radiative heat transfer sources contribution to the additional heat flux, $\dot{q}''_{add}$; the heated horizontal (or inclined) barrier, $\dot{q}''_p$, and the hot combustion products (i.e. smoke), $\dot{q}''_g$, and the increased contribution from the deflected flame, $\dot{q}''_f$, was not possible to quantify. However, the similarities between the relative flame spread rates for the similar experiments conducted with the stainless-steel board and the PV module (see Figs. 4.13b and 4.13d) indicated that the emissivity from the heated barrier was less dominant than the emissivity from the smoke and deflected flame.

If the emissivity from the barrier was dominating, the black stainless steel board should have absorbed more energy than the white backsheet of the PV module [141]. The stainless steel board should also have reached a higher temperature due to the lower heat capacity of stainless steel than both the glass, the PV cell encapsulate (ethylene-vinyl acetate) and the fluoropolymer backsheet membrane of the PV module [169, 182]. It is expected that the temperature of the combustion products were the same for similar sized areas of ignited PMMA and thus the

radiative heat transfer from the smoke towards the fuel must have been similar no matter the type of horizontal barrier. In that way, the hot combustion products have the same effect as the deflected flame, but the magnitude depends on the gap height. During the initial part of all the experiments, the width of the pyrolysis zones are similar and as such the temperatures of the combustion products. But the different gap heights render different view factors and consequently lower gap heights leads to the positive heat feed-back loops that results in flame heights that exceeds the gap height.

As such it can be concluded that the radiative heat transfer from the smoke is a more dominating factor than the radiative heat transfer from the horizontal barrier in the pre-heating phase of the fire, whereupon heat transfer from the deflected flame becomes dominant in the subsequent phase.

5.2.2 Geometry of horizontal barrier

The importance of the combustion products' effect on the initial part of the fire dynamic scenario was verified in the experiments conducted with a more complex fuel than PMMA. Due to the presence of flame retardants, the combustion of the PVC-based roofing membrane was less efficient which caused the formation of a significantly darker smoke with a higher emissivity than the smoke formed during the combustion of the PMMA.

Because of that, the geometry of the horizontal barrier became significant parameter since the frame of the PV module restricted the flow of the combustion products and thus caused a built-up of hot smoke with a higher emissivity. The built-up efficiently reduced the distance between the smoke and the thermally thin fuel and thus caused an efficient increase of the view factor. Consequently, the heat flux towards the surface was higher in experiments where the horizontal barrier were surrounded by an edge.

5.2.3 Inclination of barrier above horizontal surface

Inclination of the barrier reduced the effect of the smoke layer during the pre-heating phase since the view factor between the smoke and and the fuel decreased with the gradual increase of the vertical distance between the two components.

Similarly, the heat flux towards the fuel was reduced when the vertical distance to the barrier, at the location of the flame front, increased. But as found in the discussed steady-state experiments in section 1.4.2, the heat flux towards the surface was significantly higher below the most elevated part of the inclined barrier than below the horizontal barrier. Consequently, the critical gap height was also higher when the barrier was inclined, and the width of the thermally thin fuel was the only reason that the heat flux decreased when the local gap height increased since the width limited the maximum area of the pyrolysis zone and thus heat release.

5.3 Influence of fuel properties

5.3.1 Material parameters of fuel

With only two, very different, types of thermally thin fuels studied, no conclusions can be drawn regarding the material properties of the fuels except the inadequacy of the test standards developed to prevent self-sustained flame spread on roofing products. However, the experiments conducted with set-up B illustrated that the soot production can have significant effect during the pre-heating phase as the consequences of radiation from the smoke layer was significantly more evident in the experiments conducted with the PVC-based roofing membrane, than the PMMA.

5.3.2 Fuel geometry

In the experimental set-ups A and B, the fuel width was a limiting parameter. In the baseline experiments experiments with PMMA, increase of the fuel width decreased the critical gap height which was a result of the wider pyrolysis zone and thus higher heat release rate, radiative heat flux towards the fuel and thus, flame spread rate.

Due to the material properties, the limited width of the PMMA did not cause quenching of the flame front but only a reduced flame spread rate. Contrary, the flame front was quenched due to the presence of the flame retardants when the heat flux decrease due to the increase of gap height as described in section 5.2.3.

As such, none of the conducted experiments were representative for flame spread on a wider surface and the findings illustrate the issues of scaling large fire spread scenarios down when the system complexity is high.

5.4 Flame spread between surfaces with non-horizontal orientation

The findings related to flame spread in horizontal semi-enclosures, or cavities, is most likely not only relevant for the examined horizontal configuration as flame spread between a solid fuel and an adjacent surface is also seen in other parts of the built environment.

As discussed in section 1.6.2, the studied flame spread scenario reassembles flame spread in ventilated facades. Similarly, the effect of the distance between the two surfaces have been studied by several authors [129, 130, 131, 132], but like the steady-state experiments related to the influence of a horizontal barrier [108, 114, 115], the only heat source was a gas burner. Obviously, an adjacent surface will not have the same effect on vertical flame spread as for horizontal flame spread since the inherent vertical flame spread mode is concurrent.

But it is expected that a reduction of the distance between the two surfaces will limit the entrainment of air and thus result in a less efficient combustion. In lower mass of entrained air with a lower temperature might result is a higher smoke temperature and thus a larger extend of radiation emitted from the smoke. That corresponds well with the findings by Mendez et al. [132] who studied steady-state heat transfer between to vertical surfaces with at different gap widths between the surfaces. In the experiments with a 15 cm gap width, the radiative heat contribution reduced was reduced form $\approx 82\%$ at a distance of 4 cm from the gas burner to $\approx 43\%$ when measured 124 cm upwards, whereas a reduction from $\approx 88\%$ to $\approx 83\%$ was observed for the gap width of 5 cm. As the total heat flux also decreased significantly more as a function of the dimensionless height in the experiments with a gap width of 15 cm compare to the gap width of 5 cm, the conclusion of radiation being the dominant heat transfer mode for flame spread between two surfaces seems correct no matter the orientation of the two surfaces.

No known research have examined the influence of gap width for a transient flame spread scenarios as all of the previously mentioned work have been steady-state experiments with a gas burner. It is expected that such experiments will be significantly more complex than for a horizontal flame spread scenario since it will be harder to distinguish the contribution from the three heat transfer modes, instrument the set-up, and monitor the flame front.

As such, the experiments conducted for horizontal flame spread in the thesis probably also adds value for flame spread between two surfaces with other orientations than horizontal. Because the significant influence of the distance between the two surfaces is found crucial in steady-state experiments with both horizontal and vertical orientation, it expected that parts of the knowledge found within the thesis can be applied for the vertical scenario.

Chapter 6

Conclusion

The introduction of building applied photovoltaic (BAPV) systems on commercial flat roof constructions represent an increased fire-related risk. Besides the probability of ignition inherent to a direct current system, a semi-enclosure is formed between the photovoltaic (PV) modules and the flat roof construction.

The thesis aimed to provide an enhanced understanding of the fire-related risk associated with BAPV systems on commercial flat roof constructions. To do so, a minor frequency analysis was conducted to support the major part of the thesis being a series of experiments focused on understanding the fire dynamics in the semi-enclosure formed by a flat roof construction covered by a PV module.

Based on an extensive literature review, six objectives were established, of which the first objective i) was to quantify the frequency and potential causes of PV-related fires, whereupon the experimental work was the focal point of the remaining five objectives, which were: ii) To design and construct a novel experimental set-up which would permit measurement of relevant parameters, iii) to quantify how geometric variables affected flame spread in a semi-enclosure based on fundamental flame spread equations. iv) To detach the material parameters from the geometry, thus enabling v) the selection of crucial parameters affecting flame spread, after which vi) different mitigation methods could be discussed and tested to reduce the consequences of an initial fire related to a BAPV system.

6.1 Frequency analysis

A fault tree analysis based on all publicly available data was conducted, and an annual frequency of 28.9 fires per gigawatt capacity was estimated. 51% of the fires were caused by an electric failure of a component related to the PV system. Among these, the inverters, connectors, and isolators represented the most likely ignition sources, being responsible for respectively 11%, 12%, and 14% of all incidents. The three component types were prone to human errors as incorrect installation practice or assembly could lead to component failure and thus fire, which corresponded well with a recent quantification of risks in PV systems published by the International Energy Agency.

The remaining 49% of the fires were caused by an unknown component or an ignition source unrelated to the PV system. Thus, a significant reduction of the fire-related risk associated with PV systems in the built environment cannot be achieved by a one-eyed focus on the PV systems' possible role as an ignition source. The reason for that is that the involvement of a PV system in a fire can modify the fire dynamic system and facilitate flame spread on the roof. Consequently, a BAPV system should not be exonerated from the responsibility of fire propagation despite not being the initial cause of the fire.

Despite the room for improvement in the data quality, the analysis was the first of its kind to quantify the fire-related risk of PV systems in the built environment. It revealed that understanding how a BAPV system affects the building fire safety, besides representing an additional ignition source, is essential to obtain a fire-safe implementation and thus long-term sustainability of the technology.

6.2 Experimental work

A total of three experimental set-ups, denominated set-ups A, B, and C, were designed to address the stated objectives related to the fire dynamics within the semi-enclosure represented by a flat roof construction below a PV module.

The experiments confirmed that the interaction between an initial fire and the semi-enclosure formed by the flat roof construction and a PV module is highly complex, as minute differences might significantly influence the fire's development. However, the identification of a critical gap height and, as a result, the flame spread facilitating behaviour of compliant roofing membranes stood out as crucial findings of the thesis. The two findings are essential as they represent a barrier to long-term sustainable implementation of photovoltaic installations in the built environment if the issue is not addressed.

The influence of the horizontal barrier was examined by detaching the material parameters from the geometry of the semi-enclosure by substituting the roof construction and PV module with respectively opaque polymethyl methacrylate (PMMA) on a non-combustible surface and a horizontal stainless-steel board. With this set-up, a constant slow flame spread rate (FSR) for gap heights above the critical gap height was differentiated from a gradually increasing FSR that transitioned into a rapidly accelerating flame front for gap heights below the critical gap height.

Similar behaviour was observed when the PMMA was replaced with a roof construction mock-up with an upper surface of PVC-based roofing membrane compliant with European standards (EN 13501-5 (B_{ROOF}(t4))). However, the flame retardants in the roofing membrane caused a binary flame spread scenario with *no flame spread* and *flame spread outside the domain of the ignition source* as the possible outcomes.

When PV modules replaced the stainless-steel board, it was concluded that the polymer back sheet of the PV modules represented a minuscule fuel load, which had an insignificant influence on the flame spread in the semi-enclosure. In all experiments, the membrane was only burned away at the location of direct flame impingement, and no self-sustained flame spread was observed. When experiments with horizontal PV modules were compared with similar experiments conducted with a non-combustible stainless-steel board, the critical gap heights were similar for flame spread on PMMA and the roofing membrane. However, in the experiments conducted with roofing membrane, the boundary was more distinct, as a gap height reduction of a single centimetre determined the difference between no flame spread and flame spread along the entire length of the roof construction mock-up. The distinct boundary between *flame spread* and *no flame spread* was caused by the PV modules' aluminium frame, which restricted the buoyant flow of combustion products. Thus, a layer of hot smoke caused pre-heating along the entire length of the roof mock-up.

In the experiments with horizontally installed PV modules above the roof construction mock-up where self-sustained flame spread was achieved, further gap height reduction caused slower flame spread rates, longer pyrolysis zones and thus a higher magnitude of heat transferred towards the insulation materials below the roofing membrane.

The inclination of the PV modules caused higher critical gap heights than for horizontally installed modules, as longer upstream flame extension caused an increased heat flux towards the roofing membrane below the most elevated part of the PV modules. The increased heat flux also caused a significantly faster flame spread rate and thus a lower overall magnitude of the heat transfer towards the material below the roofing membrane.

To enable the installation of BAPV systems on existing flat roof constructions, the use of 50 mm mineral wool or 60 mm polyisocyanurate (PIR) insulation was examined in the roof construction mock-up on an assumed worst-case scenario with an existing roof insulated with expanded polystyrene (EPS). The temperature within the insulation was measured at six depths between 10 mm and 70 mm from the upper surface of the mock-up by a total of twenty thermocouples. Due to the difference in the heat transfer magnitude, significantly higher temperatures were measured below the horizontal PV modules compared to the inclined modules.

The experiments conducted with the 60 mm of PIR insulation caused lower temperature measurements in the EPS insulation, but the difference was solely considered to be a result of the different material thickness. Based on the temperature development through the two insulation products, the conductivity of the mineral wool was better at high temperatures, and thus, it is expected that it would performed as good or better than the PIR insulation if tested with a similar thickness.

Finally, the initial extraction flow and adjustments of the extraction did influence the ignition and flame spread phase of the experiments. However, the wind load on a flat roof construction was deemed a stochastic parameter and thus a parameter that could not be used to ensure an acceptable level of fire safety.

6.3 Recommendations and further work

Since a BAPV system is not considered part of the building in many countries but rather an add-on technology, it is expected that compliance with the regulations will not permit flame spread along the roof. However, as highlighted within the thesis, *compliant behaviour* are not granted when the effect of the semi-enclosure is taken into account, whereupon the additional heat flux from the deflected flame can facilitate flame spread. As such, it can be concluded that if *compliant behaviour* corresponds to no flame spread along the roof, the current test methods are not adequate for flat roof constructions with BAPV systems.

Based on the current level of knowledge from previous research and the research conducted during the PhD project, a total of six recommendations are suggested. The recommendations are focused on how to increase the knowledge regarding PV-related fires, and the necessary steps which should be taken to reduce the consequences of an initial fire and thus ensure the long-term sustainability of building applied PV installations.

6.3.1 Quantification of frequency

Improved quantification of the frequency and consequences associated with PV systems in the built environment is necessary to facilitate a wider acceptance of the risk and thus an increased focus on the topic. To do so, improved data sets are essential, and the knowledge can, most likely, be supplied from two reliable sources: i) The insurance companies or ii) the national fire and rescue services.

Existing data sets most likely exist within the insurance industry, where each company has data on incidents related to the property they insure. The data is probably considered intellectual property of the companies or a trade secret. However, an agreement within the insurance industry to share such data in the interest of an efficient and safe transition to a higher ratio of renewable energy would indicate a genuine interest in a sociological and ecologically sustainable world.

To increase the global pace of data collected regarding PV-related fires, it is suggested to follow the recommendations from the paper *Fault tree analysis of fires on rooftops with photovoltaic systems* by Mohd Nizam Ong et al., which states that a uniform data require a response from similar respondents. Thus, the national fire and rescue services are ideal respondents to answer the two suggested questions. Because the PV system can facilitate the spread of fire

without being the reason for the fire, the main interest is to know if a PV system was involved in a fire. Subsequently, the cause of the fire is of interest, and three options should be available: i) Ignition source unknown, ii) Ignition source not related to the PV-system, or iii) Ignition caused by a component of the PV system. For the latter case, the six major events from the fault tree analysis should represent the possible components of failure.

Based on the findings within the thesis, it is recommended that the national fire and rescue services start to collect data regarding PV-related fires, which will permit the development of an improved model to estimate the risk associated with PV-related fires. In addition, it should be of interest to monitor if the failure frequency increases when PV systems reach the end of the expected service life.

6.3.2 Acceptance of building applied PV systems as part of the building

In some current regulations in European countries, a building applied PV system is not considered to be a part of the building, but rather a technological add-on. As such, there are no additional requirements to the hosting roof construction that represents a significant fire-related risk due to the non-compliant behaviour of the compliant materials. Thus, it is found necessary that relevant stakeholders and governmental institutions understand and accept the consequences of the rapid introduction of the photovoltaic technology into the built environment.

6.3.3 Development of standard test method for roofing products

The development of a test method is an essential step in ensuring the long-term sustainability of roof-mounted PV systems. However, the development of such a test method without an adequate understanding of how different parameters affect flame spread within the semi-enclosure is deemed unwise. Based on the findings in the thesis, it can be concluded that test methods conducted with a given gap height are not representative of all gap heights.

It is concluded that fuel load is minimal for PV modules with fluoropolymer backsheets such as Tedlar or Kynar. Thus, it is necessary to develop a test method to examine the products installed on the lower surface of the semi-enclosure. One of the failure criteria of the developed test method should be self-sustained flame spread within a semi-enclosure. The minimum gap height not causing self-sustained flame spread within the semi-enclosure could be a variable used to categorise the tested membranes for safe use at gap heights above a specified height.

6.3.4 Compartmentalisation of roof

PV arrays with uninterrupted side lengths of 45 meters separated by walk paths of minimum of 1.2 meters are the maximum size allowed by the global insurance company Allianz. If the fire cannot spread from PV array to PV array across the walk paths, the entire array could cover an area up to more than 2000 m^2. Naturally, the area of potential damage could be decreased by reducing the maximum allowed side lengths, but such an approach would also reduce the capacity of the PV system.

An alternative approach could be the introduction of fire breaks below the PV array. The maximum allowed area of flame spread could be limited by reducing the interconnected area of the roofing membrane from one surface to several smaller areas. It is assumed that such reduction could be accomplished by introducing fire breaks blocking and absorbing the radiative heat transfer from the deflected flames. The blockage material should consist of a non-combustible material such as thin metal sheets or a layer of pebbles.

Blockage of the deflected flames below the PV modules would be another way to reduce the radiative heat transfer towards the upper surface of the roof and thus reduce the likelihood of self-sustained flame spread. The blockage could be done by the introduction of thin vertical metal curtains installed between the modules. The curtains should be installed from the upper side of the module and eventually attached to the clamps used to fasten the PV module to the mounting system, and it is not deemed necessary that the length of the curtains is equivalent to the gap height.

Finally, a mechanical solution could be designed where the gap height or inclination of the PV modules is modified when the mechanism is activated. It is assumed that an activation mechanism similar to the glass bulb of a sprinkler head could be used to activate the mechanism.

If possible, the suggested methods should be tested through medium- or large-scale experiments.

6.3.5 Repetition and improvement of experiments

Because all of the experiments conducted as part of the PhD project were conducted with novel experimental set-ups, there is room for improvement and repetition of experimental campaigns.

For both the flame spread studies on PMMA and the roof construction mock-up, analysis of the combustion products via oxygen calorimetry should be a top priority as that might enable a correlation between the gap height, the heat release rate, and the critical heat flux of the material on the lower surface of the enclosure. As such, the critical gap height for a specific roofing membrane could be determined for a worst-case scenario in terms of the initial heat release rate.

For the experimental series conducted with set-ups A and B, it was seen that the sample width affected the outcome of the experiments. Wider PMMA samples caused faster flame spread rates and lower critical gap heights as the samples were ignited along the entire width of the samples. In the experiments with inclined PV modules above the roof mock-up, the restricted width of the mock-up limited the flame spread length as the inclination caused an increasing local gap height at the location of the upstream propagating flame front. As such, it is recommended that future work increase the width of the roof construction mock-up to permit some degree of two-dimensional flame spread. However, such experiments will require an extraction hood with a significant capacity.

In addition, the introduction of flow meters in the experiments with the roof construction mock-up and horizontal PV modules would enable quantification of the flow and thus verification of the assumed increased velocity of the air entrained into the fire causing a slower flame spread rate.

6.3.6 Computational Fluid Dynamics modelling

Finally, it is suggested that future experiments are used to validate findings from computational fluid dynamics (CFD) modelling. Similar to the experiments conducted with set-ups A and B, a simple initial model should be developed, after which the complexity can be increased gradually.

The development of such a method could enable a CFD-based study of the aforementioned methods to compartmentalize either the roof construction or the PV system. In addition, a detailed model might be able to determine a critical gap height and inclination for combinations of PV modules and roof constructions. It is concluded that fuel load is minimal for PV modules with fluoropolymer backsheets such as Tedlar or Kynar. Thus, it is necessary to develop a test method to examine the products installed on the lower surface of the semi-enclosure. One of the failure criteria of the developed test method should be self-sustained flame spread within a semi-enclosure. The minimum gap height not causing self-sustained flame spread within the semi-enclosure could be a variable used to categorize the tested membranes for safe use at gap heights above a specified height.

Bibliography

[1] J. S. Kristensen and G. Jomaas, “Experimental Study of the Fire Behaviour on Flat Roof Constructions with Multiple Photovoltaic (PV) Panels,” *Fire Technology*, vol. 54, no. 6, pp. 1807–1828, 2018. [Online]. Available: https://doi.org/10.1007/s10694-018-0772-5

[2] J. S. Kristensen, “Photovoltaic installations on warehouse buildings - an experimental study of the propagation of fire,” *MSc thesis | The Technical University of Denmark (DTU) | Supervisor: Grunde Jomaas*, 2016.

[3] N. A. F. Mohd Nizam Ong, M. A. Sadiq, M. S. Md Said, G. Jomaas, M. Z. Mohd Tohir, and J. S. Kristensen, “Fault tree analysis of fires on rooftops with photovoltaic systems,” *Journal of Building Engineering*, vol. 46, no. November 2021, p. 103752, 2021. [Online]. Available: https://doi.org/10.1016/j.jobe.2021.103752

[4] F. B. M. Faudzi, “Flame Propagation Between Flat Roofing and Photovoltaic Installations,” *MSc thesis | International Master of Science in Fire Safety Engineering | The University of Edinburgh | Supervisor: Grunde Jomaas [Date accessed: 15/12/2022]*, 2019. [Online]. Available: https://static1.squarespace.com/static/5cdbcb5a7a1fbd56ceb62430/t/5e675b9c4e508a20d35f4d03/1583831985758/Thesis+Farah+Edinburgh.pdf

[5] B. Jacobs, “An investigation into the fire dynamics on flat roofs retrofitted with photovoltaic installations,” *MEng thesis | The University of Edinburgh | Supervisor: Grunde Jomaas*, 2020.

[6] J. S. Kristensen, F. B. M. Faudzi, and G. Jomaas, “Experimental study of flame spread underneath photovoltaic (PV) modules,” *Fire Safety Journal*, vol. 120, no. January 2020, p. 103027, 2021. [Online]. Available: https://doi.org/10.1016/j.firesaf.2020.103027

[7] J. S. Kristensen, B. Jacobs, and G. Jomaas, “Experimental Study of the Fire Dynamics in a Semi-enclosure Formed by Photovoltaic (PV) Installations on Flat Roof Constructions,” *Fire Technology*, 2022. [Online]. Available: https://doi.org/10.1007/s10694-022-01228-z

[8] M.-C. Hong, “A Study of the Required Spacing for Preventing Fire Spread Between Photovoltaic Arrays on Flat Roofs,” *MSc thesis | International Master of Science in Fire Safety Engineering | The University of Edinburgh | Supervisor: Grunde Jomaas [Date accessed: 15/12/2022]*, 2018. [Online]. Available: https://static1.squarespace.com/static/5cdbcb5a7a1fbd56ceb62430/t/5e6776624e508a20d3620da4/1583838836415/Ming-Cian+Hong+FINAL.pdf

[9] J. G. Quintiere, “Fire Spread on Surfaces and Through Solid Media,” in *Fundamentals of Fire Phenomena*. John Wiley & Sons, Ltd, 2006, ch. 8.

[10] BayWa r.e., “Mounting system novotegra 2020 | 2021,” 2021. [Online]. Available: https://solar-distribution.baywa-re.lu/fileadmin/Solar_Distribution_Benelux/08_Kataloge/2020_EN_Montagesystemkatalog_kompirmiert.pdf

[11] A. Guterres, “Secretary-General ’ s remarks to Global Climate Action High-Level Event - as delivered, November 11th 2021,” 2021. [Online]. Available: https://www.un.org/sg/en/node/260603

[12] OECD, “OECD Environmental Outlook to 2050 The Consequences of Inaction,” OECD Publishing, Tech. Rep., 2012. [Online]. Available: https://doi.org/10.1787/9789264122246-en

[13] European Commission, “The European Green Deal,” 2019. [Online]. Available: http://eur-lex.europa.eu/resource.html?uri=cellar:208111e4-414e-4da5-94c1-852f1c74f351.0004.02/DOC_1&format=PDF

[14] International Energy Agency (IEA), “Renewables 2020 Analysis and forecast to 2025,” 2020. [Online]. Available: https://iea.blob.core.windows.net/assets/1a24f1fe-c971-4c25-964a-57d0f31eb97b/Renewables_2020-PDF.pdf

[15] Ingka Group, “Ingka Investments makes EUR 340 million investment in nine solar PV park projects in Europe as part of its commitment towards a renewable energy future,” 2022. [Online]. Available: https://www.ingka.com/news/ingka-investments-makes-eur-340-million-investment-in-nine-solar-pv-park-projects-in-europe-as-part-of-its-commitment-towards-a-renewable-energy-future/

[16] European Commission, “EU Solar Energy Strategy,” *COMMUNICATION FROM THE COMMISSION TO THE EUROPEAN PARLIAMENT, THE COUNCIL, THE EUROPEAN ECONOMIC AND SOCIAL COMMITTEE AND THE COMMITTEE OF THE REGIONS, [Accessed: 05-05-2022]*, vol. 1, no. 69, pp. 5–24, 2022. [Online]. Available: https://eur-lex.europa.eu/resource.html?uri=cellar:516a902d-d7a0-11ec-a95f-01aa75ed71a1.0001.02/DOC_1&format=PDF

[17] D. Lincot, “The new paradigm of photovoltaics: From powering satellites to powering humanity,” *Comptes Rendus Physique*, vol. 18, no. 7-8, pp. 381–390, 2017. [Online]. Available: http://dx.doi.org/10.1016/j.crhy.2017.09.003

[18] A. Goetzberger and V. Hoffman, *Photovoltaic Energy generation*, 2005.

[19] NASA Space Science Data Coordinated Archive, “Vanguard 1,” 2000. [Online]. Available: https://nssdc.gsfc.nasa.gov/nmc/spacecraft/display.action?id=1958-002B

[20] N. M. Haegel, R. Margolis, T. Buonassisi, D. Feldman, A. Froitzheim, R. Garabedian, M. Green, S. Glunz, H. M. Henning, B. Holder, I. Kaizuka, B. Kroposki, K. Matsubara, S. Niki, K. Sakurai, R. A. Schindler, W. Tumas, E. R. Weber, G. Wilson, M. Woodhouse, and S. Kurtz, "Terawatt-scale photovoltaics: Trajectories and challenges," *Science*, vol. 356, no. 6334, pp. 141–143, 2017.

[21] N. M. Haegel, H. Atwater Jr, T. Barnes, C. Breyer, Y.-m. Chiang, S. D. Wolf, B. Dimmler, D. Feldman, J. C. Goldschmidt, D. Hochschild, R. Inzunza, I. Kaizuka, B. Kroposki, S. Kurtz, S. Leu, R. Margolis, K. Matsubara, A. Metz, W. K. Metzger, M. Morjaria, S. Niki, S. Nowak, I. M. Peters, S. Philipps, T. Reindl, A. Richter, D. Rose, K. Sakurai, M. Shikano, W. Sinke, R. Sinton, B. J. Stanbery, M. Topic, W. Tumas, Y. Ueda, J. V. D. Lagemaat, P. Verlinden, M. Vetter, E. Warren, M. Werner, M. Yamaguchi, and A. W. Bett, "Terawatt-scale photovoltaics: Transform global energy," *Science*, vol. 364, no. 6443, pp. 836–838, 2019. [Online]. Available: https://science.sciencemag.org/content/364/6443/836/tab-pdf

[22] G. Masson and A. Detollenaere, "Snapshot of Global PV Markets 2021," pp. 1–16, 2021. [Online]. Available: https://iea-pvps.org/wp-content/uploads/2021/04/IEA_PVPS_Snapshot_2021-V3.pdf

[23] G. Masson and I. Kaizuka, *Trends in Photovoltaic Applications 2020*. International Energy Agency - Photovoltaic Power Systems Programme | IEA-PVPS, 2020. [Online]. Available: https://iea-pvps.org/wp-content/uploads/2020/11/IEA_PVPS_Trends_Report_2020-1.pdf

[24] International Renewable Energy Agency (IRENA), "Data & Statistics." [Online]. Available: https://www.irena.org/statistics

[25] A. Al-Akori, "PV Systems for Rural Health Facilities in Developing Areas | Report IEA-PVPS T9-15: 2014," Berlin, pp. 1–56, 2014. [Online]. Available: https://www.researchgate.net/publication/273762878

[26] M. Safi, "India's huge solar ambitions could push coal further into shade," 2018. [Online]. Available: https://www.theguardian.com/world/2018/jun/30/indias-huge-solar-ambitions-could-push-coal-further-into-shade

[27] C.F. Møller Archtects, "Copenhagen International School," pp. 2013–2014, 2014. [Online]. Available: https://www.cfmoller.com/p/Copenhagen-International-School-Nordhavn-i2956.html

[28] IKAROS SOLAR, "IKEA Zwolle Reference," 2014. [Online]. Available: https://www.ikaros-solar.eu/content/references?id=81

[29] A. Voiland, “Longyangxia Dam Solar Park,” 2017. [Online]. Available: https://earthobservatory.nasa.gov/images/89668/longyangxia-dam-solar-park

[30] United News of India, “World ’ s largest solar project starts feeding electricity into national grid,” 2016. [Online]. Available: http://www.uniindia.com/world-s-largest-solar-project-starts-feeding-electricity-into-national-grid/business-economy/news/517726.html

[31] M. Victoria, N. Haegel, I. M. Peters, R. Sinton, A. Jäger-Waldau, C. del Cañizo, C. Breyer, M. Stocks, A. Blakers, I. Kaizuka, K. Komoto, and A. Smets, “Solar photovoltaics is ready to power a sustainable future,” *Joule*, vol. 5, no. 5, pp. 1041–1056, 2021.

[32] European Committee for Electrotechnical Standardization, “EN 50583-1:2016 Photovoltaics in buildings – Part 1 : BIPV modules,” *CENELEC*, 2016.

[33] P. Macé, David Larsson, and Jessica Benson, “Inventory on Existing Business Models , Opportunities and Issues for BIPV,” Tech. Rep., 2018. [Online]. Available: https://iea-pvps.org/wp-content/uploads/2020/02/Inventory_on_Existing_Business_Models_Opportunities_and_Issues_for_BIPV_by_Task_15.pdf

[34] Solar Energy Industries Association, “Solar Means Business 2019,” 2020. [Online]. Available: https://www.seia.org/sites/default/files/2020-10/SEIA-SMB-2019-FINAL_0.pdf

[35] G. Masson and I. Kaizuka, *Trends in photovoltaic applications 2019*. IEA | International Energy Agency, 2019. [Online]. Available: https://iea-pvps.org/wp-content/uploads/2020/02/5319-iea-pvps-report-2019-08-lr.pdf

[36] ——, “Trends in photovoltaic applications 2021,” IEA-PVPS | Inetrnational Energy Azgency - Photovoltaic Power Systems Programme, Tech. Rep., 2021. [Online]. Available: https://iea-pvps.org/wp-content/uploads/2022/01/IEA-PVPS-Trends-report-2021-1.pdf

[37] C. M. Whitaker, T. U. Townsend, A. Razon, R. M. Hudson, and X. Vallvé, “PV Systems,” in *Handbook of Photovoltaic Science and Engineering*, 2nd ed., A. Luque, Ed. John Wiley & Sons, Ltd, 2011, ch. 19, pp. 841–895.

[38] M. K. Alam, F. H. Khan, J. Johnson, and J. Flicker, “PV faults: Overview, modeling, prevention and detection techniques,” *2013 IEEE 14th Work. Control Model. Power Electron. COMPEL 2013*, 2013.

[39] V. Babrauskas, “Ignition Sources,” in *Ignition Handbook*. Issaquah, WA 98027: Fire Science Publishers, 2014, ch. 11, pp. 497–590. [Online]. Available: http://www.springerlink.com/openurl.asp?id=doi:10.1023/B:FIRE.0000026981.83829.a5

[40] D. Drysdale, “Ignition: The Initiation of Flaming Combustion,” in *An Introd. to Fire Dyn.* Chichester, UK: John Wiley & Sons, Ltd, 7 2011, ch. 6, pp. 225–275. [Online]. Available: http://doi.wiley.com/10.1002/9781119975465.ch6

[41] A. Sepanski, F. Reil, W. Vaassen, E. Janknecht, U. Hupach, N. Bogdanski, B. van Heeckeren, H. Schmidt, G. Bopp, H. Laukamp, R. Grab, S. Philipp, H. Thiem, J. Huber, R. Haselhun, H. Häberlin, A. Krutzke, B. Neu, A. Richter, B. Bansemer, and M. Halfmann, "Leitfaden: Bewertung des Brandrisikos in Photovoltaik-Anlagen und Erstellung von Sicherheitskonzepten zur Risikominimierung," *[Date accessed: 29-05-2022]*, pp. 1–308, 2015. [Online]. Available: http://www.pv-brandsicherheit.de/fileadmin/downloads_fe/Leitfaden_Brandrisiko_in_PV-Anlagen_V01.pdf

[42] Annett Sepanski, F. Reil, W. Vaaßen, E. Janknecht, U. Hupach;, N. Bogdanski, B. v. Heeckeren, H. Schmidt, G. Bopp, H. Laukamp, R. Grab, S. Philipp, H. Thiem, J. Huber, and R. Haselhuhn, "Assessing Fire Risks in Photovoltaic Systems and Developing Safety Concepts for Risk Minimization," vol. 2018, no. July 2015, 2018. [Online]. Available: https://www.energy.gov/sites/default/files/2018/10/f56/PVFireSafetyFireGuideline_Translation_V0420180614_FINAL.pdf

[43] P. Cancelliere, G. Manzini, and M. Mazzaro, "Conference presentation: A review of the photovoltaic module and panel fire tests," Naples, 2017. [Online]. Available: https://www.researchgate.net/publication/317648224_A_REVIEW_OF_THE_PHOTOVOLTAIC_MODULE_AND_PANEL_FIRE_TESTS

[44] L. Fiorentini, L. Marmo, E. Danzi, and V. Puccia, "FIRES IN PHOTOVOLTAIC SYSTEMS : LESSONS LEARNED IN ITALY," *SFPE Emerg. Trends enewsletter Issue 99, [Date Accessed:: 19-10-2016]*, 2015. [Online]. Available: http://www.sfpe.org/?page=FPE_ET_Issue_99

[45] T. O'Leary and D. M. Whaley, "Solar panel fire season is all year round and it's getting more intense in Australia," *The Conversation, [Date Accessed: 29-05-2022]*, 2021. [Online]. Available: https://theconversation.com/solar-panel-fire-season-is-all-year-round-and-its-getting-more-intense-in-australia-150751

[46] J. Weaver, "There are – data missing – solar power fires per year," 2019. [Online]. Available: https://www.pv-magazine.com/2019/08/23/there-are-data-missing-solar-power-fires-per-year/

[47] B. Meacham and M. Mcnamee, "Fire Safety Challenges of ' Green ' Buildings and Attributes," *[Date Accessed: 20-07-2021]*, 2020. [Online]. Available: https://www.nfpa.org/News-and-Research/Data-research-and-tools/Building-and-Life-Safety/Fire-Safety-Challenges-of-Green-Buildings

[48] M. Leene and R. van den Dikkenberg, "Vooronderzoek depositie bij branden met zonnepanelen," 2020. [Online]. Available: https://www.ifv.nl/kennisplein/Documents/20201208-IFV-Vooronderzoek-depositie-branden-zonnepanelen.pdf

[49] L. Kolodny, “Tesla solar panels caught fire at Amazon warehouse in 2018,” 2019. [Online]. Available: https://www.cnbc.com/2019/08/23/tesla-solar-panels-caught-fire-at-amazon-warehouse-in-2018-report.html

[50] A. Galaviz, “Amazon Fresno warehouse three-alarm fire burns solar panels , stops work,” 2020. [Online]. Available: https://www.fresnobee.com/news/local/article242015301.html

[51] T. Sylvia, “Amazon warehouse fire linked to solar installation,” 2021. [Online]. Available: https://www.pv-magazine.com/2021/06/11/amazon-warehouse-fire-linked-to-solar-installation/

[52] CBS San Francisco - Associated Press, “Fire Causes Partial Roof Collapse At Apple ’ s Giant Data Center In Arizona,” p. 2015, 2015. [Online]. Available: https://www.cbsnews.com/sanfrancisco/news/fire-causes-partial-roof-collapse-at-apples-giant-data-center-in-arizona/

[53] Daily Herald report, “Roof fire at Schaumburg IKEA causes brief evacuation,” 2020. [Online]. Available: https://www.dailyherald.com/apps/pbcs.dll/article?avis=da&date=20201124&category=news&lopenr=201129602&ref=ar

[54] CBS Chicargo, “IKEA Roof Catches Fire,” 2018. [Online]. Available: https://www.cbsnews.com/chicago/news/891896-ikea-roof-solar-panel-fire/

[55] N. Groom and N. Balu, “Walmart sues Tesla for negligence after repeated solar system fires,” 2019. [Online]. Available: https://www.reuters.com/article/us-walmart-tesla-solar-lawsuit/walmart-sues-tesla-for-negligence-after-repeated-solar-system-fires-idUSKCN1VA26B

[56] A. Bera and A. Sarkar, “Factbox : Walmart and Tesla fought in private long before solar lawsuit,” 2019. [Online]. Available: https://www.reuters.com/article/us-walmart-tesla-solar-lawsuit-factbox-idUSKCN1VC1EH?utm_campaign=trueAnthem%3A+Trending+Content&utm_content=5d5ea25d57819f000168f76d&utm_medium=trueAnthem&utm_source=twitter

[57] F. Lambert, “Tesla is getting sued by Walmart who wants them to remove 240 solar systems after fires,” 2019. [Online]. Available: https://electrek.co/2019/08/20/tesla-walmart-remove-solar-systems-fires/

[58] J. Stempel, “Tesla settles with Walmart over solar panel installations, fires,” *REUTERS, [Date Accessed:: 29-05-2022]*, pp. 6–7, 2019. [Online]. Available: https://www.reuters.com/article/us-walmart-tesla-solar-lawsuit-idUSKBN1XF240

[59] ITV, "Drone shows moment solar panel fire takes hold at We The Curious in," *[Date Accessed:: 29-05-2022]*, 2022. [Online]. Available: https://www.itv.com/news/westcountry/2022-04-11/drone-shows-moment-solar-panel-fire-takes-hold-at-we-the-curious-in-bristol?fbclid=IwAR3tkL5gkI-dvtU3ZtLRTCE8lxGo-X3JRwou9GrBHCQxsDFJq92U_FoWK5c

[60] A. Sennott, "3-alarm fire damages roof , solar panels at Newburyport printing company," pp. 2–4, 2022. [Online]. Available: https://www.bostonglobe.com/2022/02/12/metro/3-alarm-fire-damages-roof-solar-panels-newburyport-printing-company/

[61] R. Stølen, R. F. Mikalsen, and J. P. Stensaas, *RISE-rapport 2018:31 Solcelleteknologi og brannsikkerhet*, 2018. [Online]. Available: https://dibk.no/globalassets/publikasjoner_og_rapporter22/solcelleteknologi-og-brannsikkerhet_rise_fire_researcg_2018

[62] European Committee for Electrotechnical Standardization, "EN IEC 61730-1:2018 Photovoltaic (PV) module safety qualification - Part 1: Requirements for construction," Brussels, 2018.

[63] ——, "EN IEC 61730-2:2018 Photovoltaic (PV) module safety qualification - Part 2: Requirements for testeng," 2018.

[64] Underwiters Laboratories, "UL/ANSI 1703 Flat-Plate Photovoltaic Modules and Panels," 2018. [Online]. Available: https://standardscatalog.ul.com/standards/en/standard_1703_3

[65] Underwriters Laboratories, "UL 61730," 2018.

[66] European Committee for Standardization, "EN ISO 11925-2:2020 Reaction to fire tests – Ignitability of products subjected to direct impingement of flame – Part 2 : Single-flame source test," *CEN*, 2020.

[67] ——, "EN 13501-5:2016 Fire classification of construction products and building elements - Part 5: Classification using data from external fire exposure to roofs tests," *CEN*, 2016.

[68] Underwriters Laboratories, "ANSI/UL 790 Standard for Standard Test Methods for Fire Tests of Roof Coverings," 2018. [Online]. Available: https://standardscatalog.ul.com/standards/en/standard_790_8

[69] European Committee for Electrotechnical Standardization, "EN 50583-2:2016 Photovoltaics in buildings – Part 2 : BIPV systems," *CENELEC*, 2016.

[70] European Committee for Standardization, "EN 13501-1:2016 Fire classification of construction products and building elements – Part 1: Classification using data from reaction to fire tests," *CEN*, 2016.

[71] ——, “CEN/TS 1187: 2012 Test methods for external fire exposure to roofs,” *CEN*, 2012.

[72] ——, “EN 13501-2:2016 Fire classification of construction products and building elements - Part 2: Classification of construction products and from fire resistance tests , excluding ventilation services,” *CEN*, 2016.

[73] ——, “EN ISO 13823:2020 Reaction to fire tests for building products – Building products excluding floorings exposed to the thermal attack by a single burning item,” *CEN*, 2020.

[74] D. Drysdale, “Steady Burning of Liquids and Solids,” in *An Introduction to Fire Dynamics*. Chichester, UK: John Wiley & Sons, Ltd, 7 2011, no. Chapter 5, ch. 5, pp. 181–223. [Online]. Available: http://doi.wiley.com/10.1002/9781119975465.ch5

[75] European Committee for Electrotechnical Standardization, “TR 50670:2016 External fire exposure to roofs in combination with photovoltaic (PV) arrays - Test method(s),” *CENELEC*, 2016.

[76] Centre Scientifique et Techique du Batiment | CSTB, “Justification des produits photovoltaïques installés en toiture vis-à-vis du feu extérieur Protocole d ’ essai,” Tech. Rep., 2012.

[77] Underwriters Laboratories, “ANSI/UL 2703-2021, Standard for Mounting Systems, Mounting Devices, Clamping/Retention Devices, and Ground Lugs for Use with Flat-Plate Photovoltaic Modules and Panels,” 2021.

[78] S. Plester, C. Coonick, and D. Crowder, “Fire and Solar PV Systems – Investigations and Evidence,” Tech. Rep. 2.5, 2017. [Online]. Available: https://assets.publishing.service.gov.uk/government/uploads/system/uploads/attachment_data/file/630639/fire-solar-pv-systems-investigations-evidence.pdf

[79] A. Chiaramonte, A. Smith, and Z. Hood, “Fire Safety of Solar Photovoltaic Systems in Australia,” *[Date accessed: 29-05-2022]*, 2016. [Online]. Available: http://wp.wpi.edu/melbourne/projects/projects-by-term/2016-2/fire-safety-of-solar-photovoltaic-systems-in-australia/

[80] C. Gmbh, F. Reil, M. Halfmann, J. Bulk, and C. Trettin, “Untersuchungen zum Verhalten von Photovoltaik-Modulen bei externen Brandeinwirkungen, sowohl bei additiven als auch integrierten Systemen, mit der Zielsetzung einer harmonisierten europäischen normativen Prüf- und Beurteilungsmethode,” 2014. [Online]. Available: https://doi.org/10.2314/GBV:848482131

[81] M. K. Alam, F. Khan, J. Johnson, and J. Flicker, “A Comprehensive Review of Catastrophic Faults in PV Arrays: Types, Detection, and Mitigation Techniques,” *IEEE Journal of Photovoltaics*, vol. 5, no. 3, pp. 982–997, 2015.

[82] S.-q. Chen, G.-j. Yang, W. Gao, and M.-f. Guo, "Ladder Network With String Voltage and Current Measures," vol. 11, no. 1, pp. 219–231, 2021.

[83] N. G. Dhere and N. S. Shiradkar, "Fire hazard and other safety concerns of photovoltaic systems," *J. Photonics Energy*, vol. 2, no. 1, p. 22006, 2012. [Online]. Available: http://photonicsforenergy.spiedigitallibrary.org/article.aspx?doi=10.1117/1.JPE.2.022006

[84] M. C. Falvo and S. Capparella, "Safety issues in PV systems: Design choices for a secure fault detection and for preventing fire risk," *Case Stud. Fire Saf.*, vol. 3, pp. 1–16, 2015. [Online]. Available: http://dx.doi.org/10.1016/j.csfs.2014.11.002

[85] A. Mellit, G. M. Tina, and S. A. Kalogirou, "Fault detection and diagnosis methods for photovoltaic systems: A review," *Renewable and Sustainable Energy Reviews*, vol. 91, no. February, pp. 1–17, 2018. [Online]. Available: https://doi.org/10.1016/j.rser.2018.03.062

[86] S. Lu, B. T. Phung, and D. Zhang, "A comprehensive review on DC arc faults and their diagnosis methods in photovoltaic systems," *Renewable and Sustainable Energy Reviews*, vol. 89, no. October 2017, pp. 88–98, 2018. [Online]. Available: https://doi.org/10.1016/j.rser.2018.03.010

[87] J. K. Hastings, M. A. Juds, C. J. Luebke, and B. Pahl, "A study of ignition time for materials exposed to DC arcing in PV systems," *Conference Record of the IEEE Photovoltaic Specialists Conference*, pp. 003 724–003 729, 2011.

[88] M. Herz, G. Friesen, U. Jahn, M. Köntgens, S. Lindig, and D. Moser, *Quantification of Technical Risks in PV Power Systems 2021, IEA-PVPS T13-23:2021*. International Energy Agency - Photovoltaic Power Systems Programme | IEA-PVPS, 2021. [Online]. Available: https://iea-pvps.org/wp-content/uploads/2021/11/Report-IEA\T1\textendashPVPS-T13-23_2021-Quantification-of-Technical-Risks-in-PV-Power-Systems_final.pdf

[89] F. Reil, A. Sepanski, W. Herrmann, J. Althaus, W. Vaaßen, and H. Schmidt, "Qualification of Arcing Risks in PV Modules," in *38th IEEE Photovoltaic Specialists Conference*, Austin, TX, 2011, pp. 727–730. [Online]. Available: https://ieeexplore-ieee-org.proxy.findit.dtu.dk/document/6317709

[90] J. H. Wohlgemuth and S. R. Kurtz, "How can we make PV modules safer?" in *Conf. Rec. IEEE Photovolt. Spec. Conf.*, no. June, 2012, pp. 3162–3165.

[91] M. Köntges, S. Kurtz, C. E. Packard, U. Jahn, K. Berger, K. Kato, T. Friesen, H. Liu, and M. Van Iseghem, *Review of Failures of Photovoltaic Modules*, 2014.

[92] P. Cancelliere, "PV electrical plants fire risk assessment and mitigation according to the Italian national fire services guidelines," *Fire and Materials*, vol. 40, no. 2016, pp. 354–367, 2014. [Online]. Available: https://doi.org/10.1002/fam.2290

[93] C. C. Grant, “Fire Fighter Safety and Emergency Response for Solar Power Systems,” Tech. Rep. May, 2010.

[94] Z. Wu, Y. Hu, J. X. Wen, F. Zhou, and X. Ye, “A Review for Solar Panel Fire Accident Prevention in Large-Scale PV Applications,” pp. 132 466–132 480, 2020.

[95] FM Global, “FM Global Property Loss Prevention Data Sheets 1-15 | Roof Mounted Solar Photovoltaic Panels,” pp. 1–28, 2021. [Online]. Available: https://www.fmglobal.com/research-and-resources/fm-global-data-sheets

[96] L. v. Ballmoos, “Künstliche Alterung von PV- Kreuzverbindungen in der Klimakammer und Materialanalyse mittels REM | BSc. thesis,” 2015.

[97] R. Ramsdal, “Brannsjef mener solceller kompliserte Asko-brannen. Det er sol-gründer rivende uenig i,” 2017. [Online]. Available: https://www.tu.no/artikler/brannsjef-mener-solceller-kompliserte-asko-brannen-det-er-sol-grunder-rivende-uenig-i/382843

[98] H. W. Emmons, “Fire in the Forest,” *Fire Research Abstracts and Reviews*, vol. 5, pp. 163–178, 1963. [Online]. Available: http://www.nap.edu/catalog/18854

[99] L. Sherwood, B. Backstorm, D. Sloan, C. Flueckiger, B. Brooks, and A. Rosenthal, “Fire Classification Rating Testing of Stand-Off Mounted Photovoltaic Modules and Systems,” no. August, 2013. [Online]. Available: http://www.solarabcs.org/about/publications/reports/flammability-testing/pdfs/solarabcs-36-2013-1.pdf

[100] B. Backstrom and M. Tabaddor, “Effect of Rack Mounted Photovoltaic Modules on the Fire Classification Rating of Roofing Assemblies,” UL - Underwriters Laboratories Inc., Tech. Rep., 2010. [Online]. Available: http://www.solarabcs.org/current-issues/docs/UL_Report_PV_Roof_Flammability_Experiments_11-30-10.pdf

[101] ——, “Effect of Rack Mounted Photovoltaic Modules on the Flammability of Roofing Assemblies – Demonstration of Mitigation Concepts,” UL - Underwriters Laboratories In./, Tech. Rep., 2010. [Online]. Available: http://www.solarabcs.org/current-issues/docs/UL_Report_PV_and_Roof_Flammability_Mitigation_2-10-10.pdf

[102] B. Backstrom and D. Sloan, “Characterization of Photovoltaic Materials – Critical Flux for Ignition / Propagation Phase 3,” UL - Underwriters Laboratories Inc., Northbrook, IL, USA, Tech. Rep., 2012. [Online]. Available: http://www.solarabcs.org/current-issues/docs/UL_Report_Critical_Flux_Experiments_1-16-12.pdf

[103] ——, “Report of Experiments of Minimum Gap and Flashing for Rack Mounted Photovoltaic Modules Phase 4,” UL - Underwriters Laboratories Inc., Tech. Rep., 2012. [Online]. Available: http://www.solarabcs.org/current-issues/docs/UL_Report_Gap_and_Flashing_Exps_3-29-12.pdf

[104] ——, "Validation of 42" PV Module Setback on Low Slope Roof Experiments Project 7," UL - Underwriters Laboratories Inc., Tech. Rep., 2012. [Online]. Available: http://www.solarabcs.org/current-issues/docs/Validation_of_42-PV_Module_Setback_on_Low_Slope_Roof_Experiments.pdf

[105] ——, "Considerations of Module Position on Roof Deck During Spread of Flame Tests Phase 5," UL - Underwriters Laboratories Inc., Tech. Rep., 2012. [Online]. Available: http://www.solarabcs.org/current-issues/docs/UL_Report_Module_Reposition_Experiments_7-24-12.pdf

[106] ——, "Effect of Rack Mounted Photovoltaic Modules on the Fire Classification Rating of Roofing Assemblies Phase 2," UL - Underwriters Laboratories Inc., Tech. Rep., 2012.

[107] B. Backstrom, "Validation of Roof Configuration 2 Experiments Project 9," 2013. [Online]. Available: http://www.solarabcs.org/current-issues/docs/Validation_of_Roof_Configuration_2_Experiments.pdf

[108] J. S. Kristensen, B. Merci, and G. Jomaas, "Fire-induced reradiation underneath photovoltaic arrays on flat roofs," *Fire and Materials*, vol. 42, no. 3, pp. 316–323, 2018.

[109] M.-C. Despinasse and S. Krueger, "First developments of a new test to evaluate the fire behavior of photovoltaic modules on roofs," *Fire Safety Journal*, vol. 71, pp. 49–57, 2015. [Online]. Available: http://linkinghub.elsevier.com/retrieve/pii/S0379711214001623

[110] J. R. Peeters, D. Altamirano, W. Dewulf, and J. R. Duflou, "Forecasting the composition of emerging waste streams with sensitivity analysis: A case study for photovoltaic (PV) panels in Flanders," *Resources, Conservation and Recycling*, vol. 120, pp. 14–26, 2017. [Online]. Available: http://dx.doi.org/10.1016/j.resconrec.2017.01.001

[111] A. Tewarson, F. Chu, and F. Jiang, "Combustion Of Halogenated Polymers," *Fire Safety Science*, vol. 4, pp. 563–574, 1994.

[112] H. Y. Yang, X. D. Zhou, L. Z. Yang, and T. L. Zhang, "Experimental studies on the flammability and fire hazards of photovoltaic modules," *Materials*, vol. 8, no. 7, pp. 4210–4225, 2015.

[113] X. Ju, X. Zhou, F. Peng, Z. Wu, D. Lai, Y. Hu, and L. Yang, "Correlation analysis of heat flux and fire behaviour and hazards of polycrystalline silicon photovoltaic panels," *IOP Conf. Ser. Mater. Sci. Eng.*, vol. 201, no. 1, 2017.

[114] X. Ju, X. Zhou, J. Gong, K. Zhao, Y. Peng, C. Zhang, X. Ren, and L. Yang, "Impact of flat roof – integrated solar photovoltaic installation mode on building fire safety," *Fire and Materials*, vol. 42, pp. 936–948, 2019. [Online]. Available: https://doi.org/10.1002/fam.2755

[115] F. Tang, Y. Zhu, L. Chen, X. Sun, M. McNamee, P. Van Hees, and L. Hu, "Experimental study and analysis of radiation heat fluxes received by a floor beneath an inclined ceiling," *Fire and Materials*, vol. 45, no. 2, pp. 205–214, 2021.

[116] D. Drysdale, "Diffusion Flames and Fire Plumes," in *An Introduction to Fire Dynamics 3rd edition*, 2011, ch. 4, pp. 121–179. [Online]. Available: http://doi.wiley.com/10.1002/9781119975465.ch4

[117] B. Brooks, "The ground-fault protection blind spot: A safety concern for larger photovoltaic systems in the United States," *Sol. Am. Board Codes Stand.*, p. 18, 2012.

[118] Y. Hasemi, "Surface Flame Spread," in *SFPE Handbook of Fire Protection Engineering, Fifth Edition*, M. J. Hurley, D. Gottuk, J. R. Hall, K. Harada, E. Kuligowski, M. Puchovsky, J. Torero, J. M. Watts, and C. Wieczorek, Eds., 2016, ch. 23, pp. 705–723.

[119] D. Drysdale, "Spread of Flame," in *An Introduction to Fire Dynamics - Third Edition*. Chichester, UK: John Wiley & Sons, Ltd, 7 2011, ch. 7, pp. 277–315. [Online]. Available: http://doi.wiley.com/10.1002/9781119975465.ch7

[120] J. Torero, "Flaming Ignition of Solid Fuels," in *SFPE Handbook of Fire Protection Engineering, Fifth Edition*, 5th ed., M. J. Hurley, D. Gottuk, J. R. Hall, K. Harada, E. Kuligowski, M. Puchovsky, J. Torero, J. M. Watts, and C. Wieczorek, Eds., 2016, ch. 21, pp. 633–661.

[121] D. Drysdale, "Fire Science and Combustion," in *An Introd. to Fire Dyn.* Chichester, UK: John Wiley & Sons, Ltd, 7 2011, ch. 1, pp. 1–34. [Online]. Available: http://doi.wiley.com/10.1002/9781119975465.ch1

[122] F. P. Incropera, D. P. DeWitt, T. L. Bergman, and A. S. Lavine, "Introduction," in *Foundations of Heat Transfer INternational Student version*, sixth edit ed. John Wiley & Sons, Inc, 2013, ch. 1.

[123] F. A. Williams, "Mechanisms of Fire Spread," *Symposium (Internatio nal) on Combustion*, vol. 16, no. 1, pp. 1281–1294, 1977.

[124] Editor-in-Chief: G. Rein, *Newsletter No 31*, G. Rein, Ed. IAFSS, 2011, vol. 31. [Online]. Available: https://iafss.org/wp-content/uploads/IAFSS-Newsletter-31-August-2011.pdf

[125] T. Hirano, S. E. Noreikis, and T. E. Waterman, "Measured velocity and temperature profiles near flames spreading over a thin combustible solid," *Combustion and Flame*, vol. 23, no. 1, pp. 83–96, 1974.

[126] D. Drysdale, "Spontaneous Ignition within Solids and Smouldering Combustion," in *An Introduction to Fire Dynamics*, 3rd ed. Chichester, UK: John Wiley & Sons, Ltd, 7 2011, no. 1939, ch. 8, pp. 317–348. [Online]. Available: http://doi.wiley.com/10.1002/9781119975465.ch8

[127] M. J. Gollner, X. Huang, J. Cobian, A. S. Rangwala, and F. A. Williams, “Experimental study of upward flame spread of an inclined fuel surface,” *Proceedings of the Combustion Institute*, vol. 34, no. 2, pp. 2531–2538, 2013. [Online]. Available: http://dx.doi.org/10.1016/j.proci.2012.06.063

[128] J. L. Torero, “The building envelope: failing to understand complexity in tall building design,” in *Rethinking Building Skins: Transformative Technologies and Research Trajectories*, 2021, ch. 13, pp. 341–357.

[129] H. Ingason, “Two dimensional rack storage,” *4th International Symposium of Fire Safety Science*, pp. 1209–1220, 1994. [Online]. Available: https://publications.iafss.org/publications/fss/4/1209/view/fss_4-1209.pdf

[130] J. L. De Ris and L. Orloff, “Flame heat transfer between parallel panels,” *Fire Safety Science*, pp. 999–1010, 2005.

[131] K. Livkiss, S. Svensson, B. Husted, and P. van Hees, “Flame Heights and Heat Transfer in Façade System Ventilation Cavities,” *Fire Technology*, vol. 54, no. 3, pp. 689–713, 2018. [Online]. Available: https://doi.org/10.1007/s10694-018-0706-2

[132] J. E. Mendez, D. Lange, J. P. Hidalgo, and M. S. McLaggan, “Effect of cavity parameters on the fire dynamics of ventilated façades,” *Fire Safety Journal*, vol. 133, no. April, p. 103671, 2022. [Online]. Available: https://doi.org/10.1016/j.firesaf.2022.103671

[133] A. C. Fernandez-pello and T. Hirano, “Controlling Mechanisms of Flame Spread,” *Fire Science and Technology*, vol. 1, pp. 17–54, 1982. [Online]. Available: https://doi.org/10.3210/fst.2.17

[134] L. Jiang, C. H. Miller, M. J. Gollner, and J. H. Sun, “Sample width and thickness effects on horizontal flame spread over a thin PMMA surface,” *Proceedings of the Combustion Institute*, vol. 36, no. 2, pp. 2987–2994, 2017. [Online]. Available: http://dx.doi.org/10.1016/j.proci.2016.06.157

[135] O. Korobeinichev, M. Gonchikzhapov, A. Tereshchenko, I. Gerasimov, A. Shmakov, A. Paletsky, and A. Karpov, “An experimental study of horizontal flame spread over PMMA surface in still air,” *Combustion and Flame*, vol. 188, pp. 388–398, 2018. [Online]. Available: https://doi.org/10.1016/j.combustflame.2017.10.008

[136] G. Boyer, “Fully coupled CFD simulation of the pyrolysis of non-charring polymers: A predictive approach,” *Fire Saf. J.*, vol. 91, no. xxxx, pp. 208–217, 2017. [Online]. Available: http://dx.doi.org/10.1016/j.firesaf.2017.03.070

[137] W. D. Drotning and E. P. Roth, “Effects of moisture on the thermal expansion of poly(methylmethacrylate),” *Journal of Materials Science*, vol. 24, no. 9, pp. 3137–3140, 1989.

[138] Nordisk Plast, “Data Sheet: Nordisk PLast PLEXIGLAS XT-GS,” pp. 1–7, 2020. [Online]. Available: https://www.nordiskplast.dk/downloads

[139] I. Pope, J. P. Hidalgo, R. M. Hadden, and J. L. Torero, “A simplified correction method for thermocouple disturbance errors in solids,” *International Journal of Thermal Sciences*, vol. 172, no. October 2021, 2022.

[140] “The Britannica Dictionary, date accessed: 16/10/2022.” [Online]. Available: https://www.britannica.com/dictionary/cavity

[141] C. Tien, K. Lee, A. Stretton, and C. Lautenberger, “Radiation Heat Transfer,” in *SFPE Handbook of Fire Protection Engineering, Fifth Edition*, 5th ed., M. J. Hurley, D. Gottuk, J. R. Hall, K. Harada, E. Kuligowski, M. Puchovsky, J. Torero, J. M. Watts, and C. Wieczorek, Eds., 2016, pp. 1–3493.

[142] D. A. Crowl and J. F. Louvar, “Chemical Process Safety - Fundamentals with Applications,” *ISBN: 978-1-13-278283-8*, 2011.

[143] C. Coonick, “Fire and Solar PV Systems-Investigations and Evidence,” *bre National Solar Centre [Accessed: 01-06-2022]*, vol. 44, no. 2.9, p. 61, 2018. [Online]. Available: https://assets.publishing.service.gov.uk/government/uploads/system/uploads/attachment_data/file/786882/Fires_and_solar_PV_systems-Investigations_Evidence_Issue_2.9.pdf

[144] K. Kinsey and M. Ahrens, “NFIRS Incident Types Why aren ’ t they telling a clearer story ?” NFPA Research, Tech. Rep. January, 2016. [Online]. Available: https://www.nfpa.org/-/media/Files/News-and-Research/Fire-statistics-and-reports/Emergency-responders/osNFIRSIncidentType.ashx?la=en

[145] L. Fiorentini and L. Marmo, *Principles of Forensic Engineering Applied to Industrial Accidents*.

[146] M. Maisch, “CER reports significant decline in potentially unsafe PV systems,” *PV-magazine, [Accessed: 01-06-2022]*, 2020. [Online]. Available: https://www.pv-magazine-australia.com/2020/06/24/cer-reports-significant-decline-in-potentially-unsafe-pv-systems/

[147] Australian Renewable Energy Agency, “Solar energy,” *Australian Goverment [Accessed: 01-06-2022]*, 2020. [Online]. Available: https://arena.gov.au/renewable-energy/solar/

[148] G. Holmes, R. Hay, E. Davies, J. Hill, J. Barrett, D. Style, E. Vause, K. Brown, A. Gault, and C. Stark, “UK housing: Fit for the future?” *Committee on Climate Change [Accessed: 01-06-2022]*, no. February, p. 135, 2019. [Online]. Available: https://www.theccc.org.uk/wp-content/uploads/2019/02/UK-housing-Fit-for-the-future-CCC-2019.pdf

[149] Statista, “Number of solar PV energy generating sites in the United Kingdom (UK) Number of sites generating electricity from solar photovoltaic in the United Kingdom (UK) from 2007 to 2020,” 2022. [Online]. Available: https://www.statista.com/statistics/418830/number-of-solar-photovoltaic-installations-uk/

[150] K. Hertz, “SS3 - Steel structures Worked examples.pdf.”

[151] L. Zhou, A. C. Fernandez-Pello, and R. Cheng, “Flame spread in an opposed turbulent flow,” *Combust. Flame*, vol. 81, no. 1, pp. 40–49, 7 1990. [Online]. Available: https://doi.org/10.1016/0010-2180(90)90068-3

[152] L. Zhou and A. Fernandez-Pello, “Concurrent turbulent flame spread,” vol. 23, no. Symposium (International) on combustion / The Combustion Institute, pp. 1709–1714, 1990. [Online]. Available: https://doi.org/10.1016/S0082-0784(06)80446-7

[153] Aremco Products Incorporated, “Technical Bulletin A5-S2: HIGH TEMPERATURE HIGH EMISSIVITY COATINGS,” pp. 1–2, 2018. [Online]. Available: https://www.aremco.com/wp-content/uploads/2018/05/A05_S2_18_Emissivity.pdf

[154] SolarWorld AG, “Data sheet: Sunmodule Pro-Series. SW 250 POLY,” pp. 3–4. [Online]. Available: https://www.solarypsi.org/repository/documents/HA_House/sunmodule-solar-panel-pro-series-250-poly-33mm-frame-ds.pdf

[155] Suntech Power, “Data sheet: Suntech STP280 - 24/Vd 280,” pp. 1–2, 2011. [Online]. Available: http://www.thaipowertech.com/images/introw_1320224700/Suntech280W.pdf

[156] GCL System Integration Technology Co. Ltd, “Data sheet: GCL-P6/60H275.” [Online]. Available: https://www.gclsi.com/uploads/5ba3833b/EN-P660.pdf

[157] AU Optronics Corporation, “Data sheet: BenQ Solar SunForte PM096B00.” [Online]. Available: https://www.europe-solarstore.com/download/benq/BenQ_Sunforte_PM096B00_datasheet.pdf

[158] Axitec Solar, “Data sheet: AXIPlus SE AC-250P/156-60S.” [Online]. Available: https://es-media-prod.s3.amazonaws.com/media/components/panels/spec-sheets/AXIplusSE_9sCPC84.pdf

[159] Rudolf Grauer AG, “Swiss Boy Lab Jacks •.” [Online]. Available: http://grauer.ch/en/index.php?page=laborhebebuehnen&layout=produkte

[160] ScandiBoard, “ScandiBoard 850 Material safety data sheet Material safety data sheet,” pp. 1–8, 2012. [Online]. Available: http://www.scandisupply.com/Files/Filer/EU/MSDSFF8502012-06-26.pdfhttp://www.scandisupply.com/Files/Filer/EU/MSDSFF8502012-06-26.pdf

[161] S. McAllister and M. Finney, “Effect of Crib Dimensions on Burning Rate,” *Seven Int. Semin. Fire Explos. Hazards ISFEH7*, vol. 7, no. April, pp. 1–10, 2013. [Online]. Available: https://www.fs.fed.us/rm/pubs_other/rmrs_2013_mcallister_s001.pdf

[162] Y. Hasemi, S. Yokobayashi, T. Wakamatsu, and A. V. Ptchelintsev, “Firesafety of Building Components Exposed to a Localized Fire - Scope and Experiments on Ceiling/Beam System Exposed to a Localized Fire,” in *ASIAFLAM*. Hong Kong: InterScience Communications, 1995, pp. 351 – 361.

[163] B. Y. Lattimer, “Heat Transfer from Fires to Surfaces,” in *SFPE Handbook of Fire Protection Engineering, Fifth Edition*, M. J. Hurley, D. Gottuk, J. R. Hall, K. Harada, E. Kuligowski, M. Puchovsky, J. Torero, J. M. Watts, and C. Wieczorek, Eds., 2016, ch. 25, pp. 745–798.

[164] British Board of Agrément, “BBA Certificate: Bauder single ply PVC roof waterproofing membranes,” pp. 1–13, 2019. [Online]. Available: https://www.bauder.co.uk/getmedia/ab9cafc7-47f1-40db-8217-e8e0681e29a8/Thermofol-BBA-Cerificate.pdf

[165] ROCKWOOL A/S, “ROCKWOOL Stålunderlag Data sheet,” 2020. [Online]. Available: https://cdn01.rockwool.dk/siteassets/o2-rockwool/dokumentation-og-certifikater/dokumentation/andet/datablade/staalunderlag.pdf?f=20200225035353

[166] Kingspan Insulation Ltd, “UK Declaration of Performance: Kingspan Thermaroof TR26,” 2016. [Online]. Available: https://ks-kentico-prod-cdn-endpoint.azureedge.net/kingspan-live/kingspangreatbritain/media/general-use/kingspan-thermaroof-tr26-declaration-of-performance-1000-1001-ukdop-en-gb.pdf?ext=.pdf

[167] Plastform Ltd, “Plastopor EPS 70.” [Online]. Available: http://plastform.hr/eng/fasadni-stiropor-eps-70.php

[168] F. P. Incropera and D. P. DeWitt, *Fundamentals of Heat and Mass Transfer*, 5th ed. John Wiley & Sons, 2002.

[169] D. P. Bentz and K. R. Prasad, “NISTIR 7401 Thermal Performance of Fire Resistive Materials I . Characterization with Respect to Thermal Performance Models,” National Institute of Standards and Technology - NIST, Gaithersburg, Tech. Rep., 2007. [Online]. Available: https://concrete.nist.gov/~bentz/nistir7401.pdf

[170] S. McAllister and M. Finney, “The Effect of Wind on Burning Rate of Wood Cribs,” *Fire Technology*, vol. 52, no. 4, pp. 1035–1050, 2016.

[171] M. L. Janssens, “Measuring Rate of Heat Release by Oxygen Consumption,” *Fire Technol.*, vol. 27, no. 3, pp. 234–249, 1991. [Online]. Available: https://doi.org/10.1007/BF01038449

[172] British Standard ISO, "BS ISO: 5660-1:2015 Reaction-to-fire tests — Heat release, smoke production and mass loss rate, Part 1: Heat release rate (cone calorimeter method)," Tech. Rep., 2015.

[173] J. R. Howell and M. P. Meng, "Supplementary material for: Radiative transfer configuration factor catalog : A listing of relations for common geometries," *Journal of Quantitative Spectroscopy and Radiative Transfer*, vol. 112, no. 5, p. appendix, 2011. [Online]. Available: https://doi.org/10.1016/j.jqsrt.2010.10.002

[174] D. Drysdale, "Heat Transfer," in *An Introduction to Fire Dynamics*. Chichester, UK: John Wiley & Sons, Ltd, 7 2011, ch. 2, pp. 35–82. [Online]. Available: http://dx.doi.org/10.1002/9781119975465.ch2http://doi.wiley.com/10.1002/9781119975465.ch2

[175] J. de Ris, "Fire radiation—a review," *Symposium (International) on Combustion*, 1979. [Online]. Available: http://www.sciencedirect.com/science/article/pii/S0082078479800971

[176] R. A. Bradstock and T. D. Auld, "Soil Temperatures During Experimental Bushfires in Relation to Fire Intensity: Consequences for Legume Germination and Fire Management in South-Eastern Australia," *The Journal of Applied Ecology*, vol. 32, no. 1, p. 76, 1995.

[177] J. E. Keeley, "Fire intensity, fire severity and burn severity: A brief review and suggested usage," *International Journal of Wildland Fire*, vol. 18, no. 1, pp. 116–126, 2009.

[178] G. M. Byram, "Combustion of Forest Fuels," in *Forest Fire Control and Use*, K. P. Davis, Ed., 1959, vol. 42, no. 3, ch. 3, pp. 61–89.

[179] P. Leppänen and M. Malaska, "Experimental Study on the Smouldering Combustion of Mineral Wool Insulation in Chimney Penetrations," *Fire Technology*, vol. 55, no. 6, pp. 2171–2194, 2019.

[180] S. R. Ray, A. C. Fernandez-Pello, and I. Glassman, "A Study of the Heat Transfer Mechanisms in Horizontal Flame Propagation," *Journal of Heat Transfer*, vol. 102, no. 2, p. 357, 1980.

[181] F. Tang, P. Hu, and J. X. Wen, "Flame evolution and radiation hazards of rectangular fires between two parallel walls," *Proceedings of the Combustion Institute*, vol. 000, pp. 1–11, 2022. [Online]. Available: https://doi.org/10.1016/j.proci.2022.09.035

[182] E. Ruiz-Reina, M. Sidrach-de Cardona, and M. Piliougine, "Technical Papers and Presentations Heat Transfer and Working Temperature Field of a Photovoltaic Panel under Realistic Environmental Conditions," 2014, pp. 7–8. [Online]. Available: https://www.comsol.com/paper/heat-transfer-and-working-temperature-field-of-a-photovoltaic-panel-under-realis-18983

[183] Bauder Limited, “Product Data Sheet: Bauder Thermofol U15 FR Membrane,” 2021. [Online]. Available: https://www.bauder.co.uk/getmedia/5f449e55-e498-4949-b9ac-b5866b46971d/Bauder-Thermofol-U15-Membrane-Product-Data-Sheet_1.pdf

[184] SIKA, “Product Data Sheet: Sikaplan ® S-20,” pp. 2–5, 2020. [Online]. Available: https://deu.sika.com/content/dam/dms/deaddconst01/x/sikaplan_s-20.pdf

Appendix A

Additional figures of experimental set-up

A.1 Laboratory jacks

One or two laboratory jacks were installed below the aluminium frames of set-ups A and B. The lab jacks, each with a maximum capacity of 40 kg, were the model SwissBoy 115 manufactured by Rudolf Grauer AG. The top plate was slightly modified as seen from figure A.1b

(a) Side view of laboratory jack with base plate.

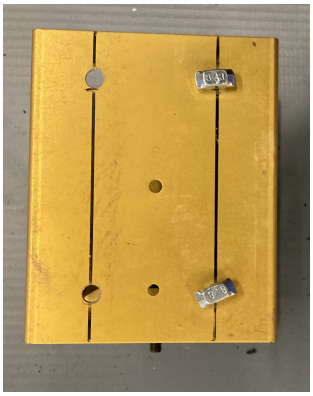

(b) Top view of modified laboratory jack. Two T-bolts installed at the right side.

Figure A.1: Side and top view of laboratory jack used for gap height adjustment. The holes drilled along the black lines are a modification of the original product [159].

A.2 Set-up A - additional figures

An aluminium bracket was designed to enable flexible installation of the heat flux gauge in all experiments. Two elongated holes enabled attachment to the aluminium profiles by the use of a standard t-bolt, whereas four holes were drilled in the top flange of the bracket as seen in figure A.2. The diameter of the large hole was slightly larger than the ø25 mm of the Huksuflux SBG01 HFG, whereas tree threaded bores made it possible to fasten the HFG. As such, the HFG could be installed from bellow or on top of the bracket as used in the specific setup.

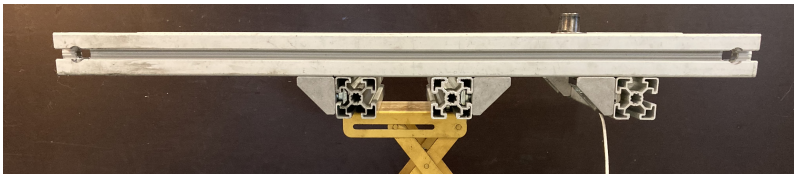

(a) Side view of the aluminium support installed on laboratory jack (section 3.3.2).

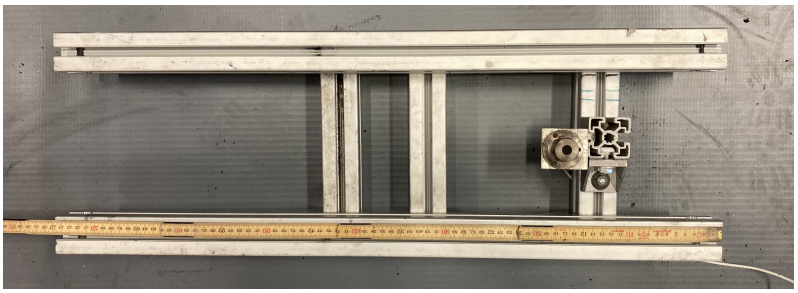

(b) Top view. Note: mirrored image for consistency.

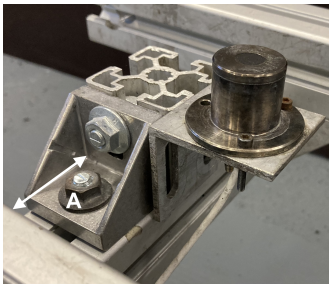

(c) Bolt A enable movement perpendicular to the direction of flame spread.

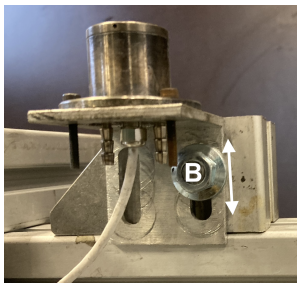

(d) Bolt B enable vertical adjustment.

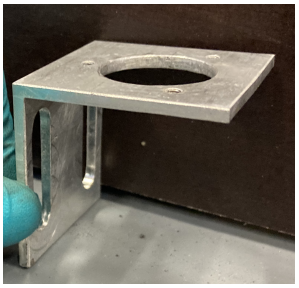

(e) Bracket used for installation of HFG.

Figure A.2: Detailed images of the aluminium support and installation of the heat flux gauge.

An image of the eight thermocouples installed through the calcium silicate board to enable embedding into the PMMA is found i Figure A.3a. One of the quartz discs used for protection of the heat flux gauge, in combination with the metal ring used for elevation of the disc, can be found in Figure A.3b.

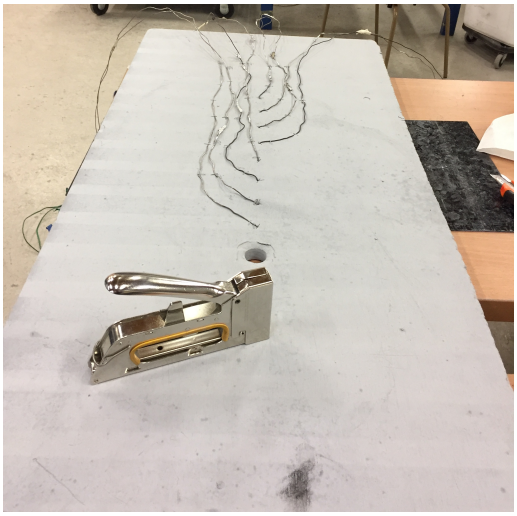

(a) Underside of the calcium silicate board (CSB). From top: i) Eight thermocouples fastened to the CSB, ii) ø26 mm hole used to install the heat flux gauge through, iii) Stapler.

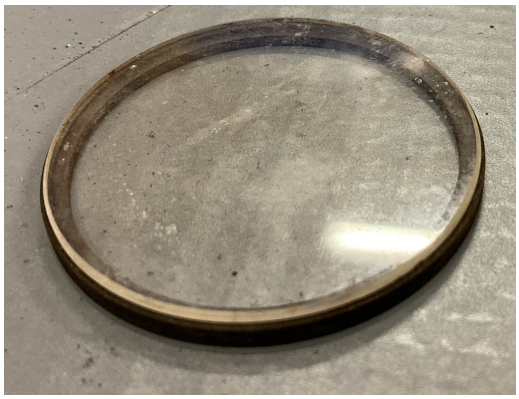

(b) ø50 mm metal ring and a quartz disc.

Figure A.3: Installation process of thermocouples and quartz disc used for protection of heat flux gauge.

A.3 Time dependent raw data for Figure 4.10

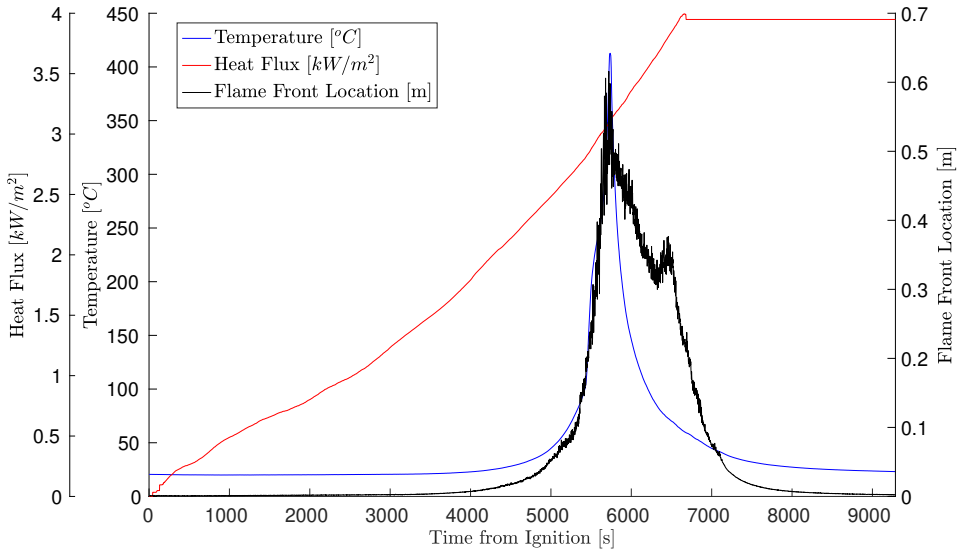

Figure A.4: Raw data from experiment A8. The data is the basis for the flame front dependent plot of PMMA temperature and heat flux in figure 4.10 (see Section 4.3). Note that the heat flux was measured 55 cm from the point of ignition, whereas the temperature was measured 50 cm from the point of ignition in accordance with Figure A.2b in Section 3.4.

Appendix B

Material data sheets

B.1 Calcium silicate board

The product FireFree ScandiBoard 850 from ScandiSupply. Data sheet on next page. [160].

FireFree ScandiBoard 850

FireFree ScandiBoard 850 is a lightweight calcium silicate board, which is tested after EN ISO 1716:2002, EN ISO 1182:2010, DIN 4102-1 and approved after the European standard EN 13501-1:2007 as non-combustible.

FireFree ScandiBoard 850 has been tested for quartz and asbestos content by The National Institute of Occupational Health, Denmark. No content of quartz or asbestos has been detected.

FireFree ScandiBoard 850 is available in thicknesses from 22 - 100 mm and can be processed to the dimension needed for a specific construction from a maximum size of 2.440x 1.220 mm. FireFree ScandiBoard 850 can be sanded on both sides on request.

Standard sizes
Length x width in mm
1.220 x 1.000
2.040 x 1.220
2.440 x 1.220
Special sizes are made to order.
And sanding on request.

Tolerances

	Trimmed	Sanded
Length/width	± 2.5 mm	± 2.5 mm
Thickness	± 1.5 mm	± 0.5 mm

Storage
The boards will be packed on pallets. Place the pallets on a smooth and dry spot and protect them against the weather.

Product profile
FireFree ScandiBoard 850 is characterized by:
• Non-combustibility
• Extremely lightweight
• Good mechanical characteristics
• Frost resistant
• Low moisture expansion and contraction
• Good thermal resistance
• Rot resistant
• Environmentally friendly
• Easy to machine and work with

Max. service temp. 1000 °C

Bulk density, dry 250 kg/m³

pH value 10,3

Compressive strength
(EN 1094-5: 1995) 2.8 MPa

Modulus of rupture
(EN 993-6: 1995) 1.7 MPa

Coefficient of reversible thermal expansion (BS 1902: section 5.3: 1990) @ 20°C-750°C (68°F-1382°F) $5.5x10^{-6}$ m/(mK)

Coefficient of moisture expansion
(DTI rep.) @ 23°C 50%RH to 23°C 10%RH, $4.0x10^{-3}$mm/(m%RH)

Coefficient of moisture contraction
(DTI rep.) @ 23°C 50%RH to 23°C 100%RH, 0 mm/(m%RH)

Sound reduction index

Thickness 19 mm	25 dB
Thickness 38 mm	28 dB
Thickness 60 mm	30 dB

Thermal conductivity

@ 20°C	0.06 W/(m×K)
@ 200°C	0.08 W/(m×K)
@ 400°C	0.10 W/(m×K)
@ 600°C	0.12 W/(m×K)

Chemical analysis, typical

Silica SiO2	45%
Calcium oxide CaO	45%
Loss on ignition 1025°C (1877°F) LOI	8%

Water content 2.5%

Colour Grey

Non-combustibility tests:
EN ISO 1716:2002, EN ISO 1182:2010, DIN 4102-1 and classified after the European standard EN 13501-1:2007 as non-combustible.

B.2 PIR insulation

The product Kingspan Therma TR26 was used as PIR insulation through all experiments in the thesis. The product was delivered by Kingspan ltd. and the data sheet can be found on next page [166].

UK Declaration of Performance

Thermaroof® TR26

1000.UKDoP.TR26.003

1001.UKDoP.TR26.003

Unique identification code of the product-type:	**Thermaroof ® TR26**
Intended use/es:	**Thermal insulation for buildings**
Manufacturer:	**Kingspan Insulation Ltd, Herefordshire HR6 9LA,UK**
System/s of AVCP:	**System 4 (Reaction to fire), System 3 (Other Properties)**
Designated technical specification:	**BS-EN 13165:2012+A2:2016**
UK Assessment body/ies:	**University of Salford: 1145,, B.I.T.S: 1334**

Essential characteristics		**Performance**
Thermal resistance	Thermal resistance R_D ((m².K)/W)	d_N 20mm 0.95 d_N 30mm 1.35 d_N 40mm 1.80 d_N 50mm 2.25 d_N 60mm 2.70 d_N 70mm 3.15 d_N 80mm 3.60 d_N 90mm 4.05 d_N 100mm 4.50 d_N 120mm 5.45 d_N 130mm 5.90 d_N 140mm 6.35 d_N 150mm 6.80 d_N 160mm 7.25
	Thermal conductivity λ_D (W/(m.K))	d_N 20mm d_N 160mm 0.022
	Thickness tolerance	T2
Reaction to fire	Reaction to fire	F
Durability of reaction to fire against heat, weathering, ageing / degradation	Durability of the reaction to fire of the product as placed on the market	NPD
	Durability of thermal resistance and thermal conductivity against ageing/ degradation	NPD
Durability of Thermal Resistance against heat, weathering, ageing / degradation	Thermal resistance R_D ((m².K)/W) Thermal conductivity λD (W/(m.K))	Thermal resistance as table above 0.022
	Durability characteristics	NPD
	Dimensional stability under specified temperature and humidity condition	DS(70,90)3 DS(-20,-)1
	Deformation under specified compressive load and temperature conditions	NPD

UK Declaration of Performance

	Determination of the aged values of thermal resistance and thermal conductivity	λD 0,022 W/m·K
Compressive strength	Compressive stress or compressive strength	CS(10\Y)150
Tensile / Flexural strength	Tensile strength perpendicular to faces	TR40
Durability of compressive strength against ageing / degradation	Compressive creep	NPD
Water permeability	Short term water absorption	NPD
	Long term water absorption	NPD
	Flatness after one sided wetting	NPD
Water vapour permeability	Water vapour transmission	NPD
Acoustic absorption index	Sound absorption	NPD
Continuous Glowing Combustion	Glowing Combustion	NPD
Release of dangerous substances to the indoor environment	Release of dangerous substances	NPD
NPD: No Performance Determined		

EU Regulation 305/2011, as retained in UK law, and as amended by SI no. 465/2019 (the Construction Products (Amendment etc.) (EU Exit) Regulations 2019) and SI no. 1359/2020 (the Construction Products (Amendment etc.) (EU Exit) Regulations 2020.)

Signed for and on behalf of the manufacturer by:

……
Ralph Mannion
Managing Director
Pembridge &Selby ,England, UK
Date signed: 18/01/2022
Issue Number: 003

KI\GB\UKDoP\TR26\003\Jan22a

B.3 Mineral wool

The product Sttålunderlag Energy manufactured by ROCKWOOL for the Danish market was used as mineral wool through all experiments in the thesis. The product was delivered by ROCKWOOL International and the data sheet can be found on teh next page. From personal correspondence with the company.

Stålunderlag Energy

ROCKWOOL Stålunderlag Energy anvendes til udvendig isolering af flade tage, og er en stiv og halvhård plade fremstillet af ubrændbar, fugt- og vandafvisende stenuld. Pladen er opbygget efter "dual density" princippet, dvs. den øverste del af pladen har en højere densitet hvilket medfører en forbedret trædefasthed.

Anvendelse

ROCKWOOL Stålunderlag Energy anvendes til udvendig isolering af flade tage som det nederste lag i en flerlagsisolering primært på underlag af ståltrapez. Stålunderlag Energy skal fastgøres mekanisk.

Montagevejledning

ROCKWOOL flerlagsisolering skal altid mekanisk fastgøres. Regler for dimensionering, antal af skruer og beslag iht. beslagleverandørens anvisning samt anvisning fra ROCKWOOL A/S.

Særlige oplysninger

Stålunderlag Energy er optaget/registreret i databasen for byggeprodukter, som kan anvendes/indgå i Svanemærket byggeri.

Emballering

ROCKWOOL StålUnderlag Energy leveres på miljøpaller afdækket med plastomvikling. Pallestørrelse mm. : 2000 x 1200 Pallehøjde mm. : ca. 1350 Pallevægt: ca. 285-320 kg

Kvalitetssikring

ROCKWOOL A/S har et kvalitetsstyringssystem, som er certificeret efter DS/EN ISO 9001. ROCKWOOL A/S er medlem af VIF (Dansk forening af fabrikanter af varmeisoleringsmaterialer).

ROCKWOOL produkter er CE-certificerede. ROCKWOOL A/S er tilsluttet byggeleveranceklausulen for leverancer til byggeri i Danmark.

ROCKWOOL Byggeprodukter er løbende under udvikling, og produkternes tekniske specifikationer er angivet med forbehold for ændringer.

Tekniske egenskaber

Varmeledningsevne (EN 12667)	λ_D (W/m·K)	0,036
Reaktion på brand (EN 13501-1)	Euroklasse	A2
Røgudvikling (EN 13823)	s (klasse)	s1

Brændende smådråber/partikler (EN 13823)	d (klasse)	d0
Tykkelsestolerance (EN 823)	T (klasse)	T4
Varmekapacitet (EN 10456)	c_p (J/kg·K)	1030
Korttidsvandabsorption (EN 1609)	WS (≤ 1,0 kg/m²)	WS
Vanddamptransmission (EN 12086)		MU1
Punktstyrke (EN 12430)	PL(5) (N (5mm))	PL(5)300
Kompressionsstyrke (EN 826)	CS(Y) (kPa)	CS(10)30

Dimensionstabilitet (EN 1604)	DS	DS (70,90)
Mekaniskeegenkaber		ROCKWOOL Stålunderlag Energy tåler ikke gangtrafik. Ved udlægning af en flerlagsløsning skal færdslen foregå på underlaget eller på ROCKWOOL Hardrock Energy / ROCKWOOL TF-Plade

Godkendelser

Produktstandard	EN 13162:2012+A1:2015
DoP-nummer	DOP-000243
CE-certifikatnummer	1073-CPR-137
Notificeret certificeringsorgan	{ "en": "Danish Technological Institute Dancert A/S (1073)", "da-DK": "Danish Technological Institute Dancert A/S (1073)" }
KEYMARK certifikatnummer	004-SDG-5-137

Sortiment

Artikel nr.	DB nr.	Densitet (ca.) (ρ ≈)	Længde	Bredde	Tykkelse	R_D	Salgsenhed	Emballering
		kg/m³	mm	mm	mm	m²·K/W		
87112	5959601	117	2000	600	50	1,35	Palle	Miljøpalle
79989	5130843	113	2000	600	60	1,65	Palle	Miljøpalle
87110	1622565	101	2000	600	80	2,20	Palle	Miljøpalle

B.4 Polymethyl methacrylate (PMMA)

All PMMA used in the experiments were 2 mm thick opaque sheets ordered from *Nordisk Plast*. The product name was: *Plexiglas XT black 9N870 SH-film*, which is equivalent to the column named *Plexiglas®XT OAOOO:OAO7O* [138].

PLEXIGLAS®

Solid sheet, block, multi-skin sheet, corrugated sheet, tube and rod

Typical property values (at 23°C and 50% relative humidity)

Mechanical properties	PLEXIGLAS® GS 0F00; 0Z09	PLEXIGLAS® XT 0A000; 0A070	PLEXIGLAS® Resist 45; 65; 75; 100	Unit	Test standard
Density ρ	1.19	1.19	1.19	g/cm³	ISO 1183
Impact strength a_{cU} (Charpy)	15	15	45; 65; 75; no break	kJ/m²	ISO 179/1fu
Notched impact strength a_{iN} (Izod)	1.6	1.6	2,5; 4,5; 6,0; 6,5	kJ/m²	ISO 180/1 A
Notched impact strength a_{cN} (Charpy)	-	-	3,5; 6,5; 7,5; 8,0	kJ/m²	ISO 179/1eA
Tensile strength σ_M				MPa	ISO 527-2/1B/5
– 40 °C	110	100	-		
23 °C	80	72	60; 50; 45; 40		
70 °C	40	35	-		
Elongation at break ε_B	5.5	4.5	-	%	ISO 527-2/1B/5
Nominal elongation at break ε_{tB}	-	-	10; 15; 20; 25	%	ISO 527-2/1B/50
Flexural strength σ_{bB} Standard test specimen (80 x 10 x 4 mm³)	115	105	95; 85; 77; 69	MPa	ISO 178
Compressive yield stress σ_{dF}	110	103	-	103	ISO 604
Max. safety stress $\sigma_{max.}$ (up to 40 °C)	5–10	5–10	5–10	MPa	-
Modulus of elasticity E_t (short-term value)	3300	3300	2700; 2200; 2000; 1800	MPa	ISO 527-2/1B/1
Min. cold bending radius	330 x thickness	330 x thickness	270 x thickness; 210 x thickness; 180 x thickness; 150 x thickness	-	-
Dynamic shear modulus G at approx. 10 Hz	1700	1700	-	MPa	ISO 537
Indentation hardness $H_{961/30}$	175	175	145; 130; 120; 100	MPa	ISO 2039-1
Abrasion resistance in Taber abrader test (100 rev.; 5.4 N; CS-10F)	20 –30	20 –30	20 –30; 30 –40; 30 –40; 30 –40	% Haze	ISO 9352
Coefficient of friction μ				-	-
plastic / plastic	0.8	0.8	-		
plastic / steel	0.5	0.5	-		
steel / plastic	0.45	0.45	-		
Poisson's ratio μ_b (dilatation speed of 5% per min; up to 2% dilatation; at 23 °C)	0.37	0.37	0.41; 0.42. 0.41; 0.43	-	ISO 527-1
Resistance to puck impact from thickness	-	-	-; from 5mm; -; -	-	Similar to DIN 18 032. Part 3

Nordisk Plast A/S • Virkevangen 80, Assentoft • DK-8960 Randers SØ • Tlf. +45 86 48 48 11
CVR 44065118 • salg@nordiskplast.dk • www.nordiskplast.dk

PLEXIGLAS®

Solid sheet, block, multi-skin sheet, corrugated sheet, tube and rod

Thermal properties					
	PLEXIGLAS® GS 0F00; 0Z09	PLEXIGLAS® XT 0A000; 0A070	PLEXIGLAS® Resist 45; 65; 75; 100	Unit	Test standard
Coefficient of linear thermal expansion α for 0 – 50 °C	$7 \cdot 10^{-5}$ (= 0,07)	$7 \cdot 10^{-5}$ (= 0,07)	$7 \cdot 10^{-5}$; $8 \cdot 10^{-5}$; $9 \cdot 10^{-5}$; $11 \cdot 10^{-5}$ (0,07; 0,08; 0,09; 0,11)	1/K (mm/m °C)	DIN 53752-A
Possible expansion due to heat and moisture	5	5	5; 6; 6; 8	mm/m	-
Thermal conductivity λ	0.19	0.19	-	W/mK	DIN 52612
U-value k for thickness				W/m^2K	DIN 4701
1 mm	5.8	5.8	5.8		
3 mm	5.6	5.6	5.6		
5 mm	5.3	5.3	5.3		
10 mm	4.4	4.4	4.4		
Specific heat c	1.47	1.47	1.47	J/gK	-
Forming temperature	160 – 175	150 – 160	150 – 160; 140 – 150; 140 – 150; 140 – 150	°C	-
Max. surface temperature (IR radiator)	200	180	-	°C	-
Max. permanent service temperature	80	70	70; 70; 70; 65	°C	-
Reverse forming temperature	> 80; > 90	> 80; > 80	> 80; > 80; > 75; > 70	°C	-
Ignition temperature	425	430	-	°C	DIN 51794
Smoke gas volume	very little	very little	very little	-	DIN 4102
Smoke gas toxicity	none	none	none	-	DIN 53436
Smoke gas corrosiveness	none	none	none	-	-
Building material class	B2	B2	B2	-	DIN 4102
Combustion behavior	Class 3 E	Class 3 E	- E	- -	BS 476, Part 7 + 6 DIN EN 13501
Vicat softening temperature	115	103	102; 100; 100; 97	°C	ISO 306, Method B 50
Heat deflection temperature under load (HDT)	-	-	-	°C	ISO 75
deflection 1.8 MPa	105; 107	95	94; 93; 92; 90	-	-
deflection 0.45 MPa	113; 115	100	99; 98; 96; 93	-	-

Nordisk Plast A/S • Virkevangen 80, Assentoft • DK-8960 Randers SØ • Tlf. +45 86 48 48 11
CVR 44065118 • salg@nordiskplast.dk • www.nordiskplast.dk

B.5 Roofing membrane

Two types of PVC-based roofing membrane where used during the project.

- BAUDER Thermofol U15 FR, Thickness: 1.5 mm, Blue Gray [183].
- SIKA Sikaplan S20, Thickness: 2.0 mm, Light Gray [184].

Due to a change of the classification system during the PhD project, the certification in accordance with EN 13501-5 are not similar. Bauder Thermofol U15 FR are compliant with EN 13501-5 B_{ROOF}(t4) when tested as part of a roof system, whereas SIKA Sikaplan S20 was compliant with EN 13501-5 B_{ROOF}(t1) as a stand alone product. Furthermore, the two membranes are not compliant with the same test method, as B_{ROOF}(t4) refer til the UK test method, and B_{ROOF}(t1) refer to the test method accepted in the Germany and the Netherlands in accordance with EN 13501-5 [67]. The Critical heat fluxes, heat of combustion are found on the following pages, and the data sheets on page 202 and 204

B.5.1 Critical heat flux for both membranes

The critical heat flux of both membranes were found to be around 7 kW/m^2 as seen from figure B.1,

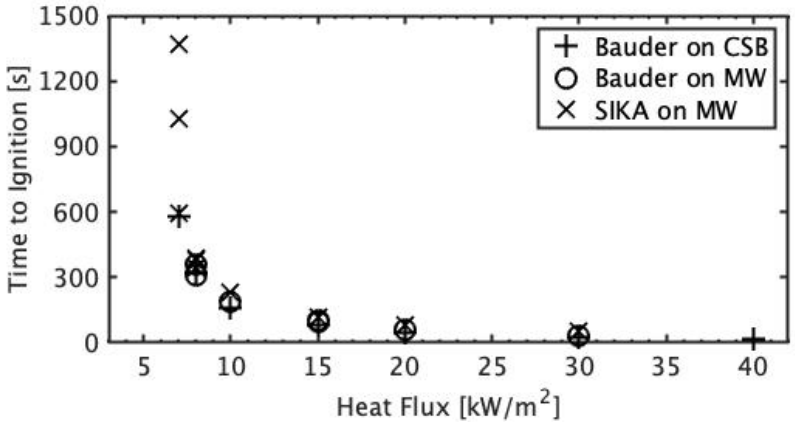

Figure B.1: Time to piloted ignition as a function of heat flux measured in the cone calorimeter. No self-sustained ignition occurred for a heat flux of respectively 6 kW/m^2 and 7 kW/m^2 when the BAUDER membrane was tested on a 22 mm thick calcium silicate board (CSB) or mineral wool (MW), whereas the outcome was inconsistent when a heat flux of 7 kW/m^2 was applied to the SIKA membrane.

B.5.2 Heat of combustion

The heat of combustion of the SIKA membrane was measured to 25.3 kJ/g by Kristensen in 2016 [2], whereas heat of combustion for the Bauder membrane was determined to 24.6 with a IKA C200 bombcalorimeter at the DTU fire laboratory as seen in table B.1.

Table B.1: Heat of combustion for the Bauder Thermofol U15 FR roofing membrane

Test	Sample mass	Heat of Combustion
#1:	1.010 g	24794 J/g
#2:	0.998 g	24464 J/g
#3:	0.898 g	24451 J/g
Average:		**24570 J/g**

Revision: 25/10/2021 – V3

PRODUCT DATA SHEET

Bauder Thermofol U15 FR Membrane

Bauder Thermofol U15 FR Membrane is a 1.5mm gauge polyester reinforced Poly Vinyl Chloride membrane (PVC). The product is highly flexible due to the incorporation of internal plasticizers during the manufacturing process. The combination of materials gives high tensile strength, good thermal stability, chemical resistance and flexibility. Primarily employed on mechanically fastened installations, although can be adhered or loose laid ballasted under certain circumstances.

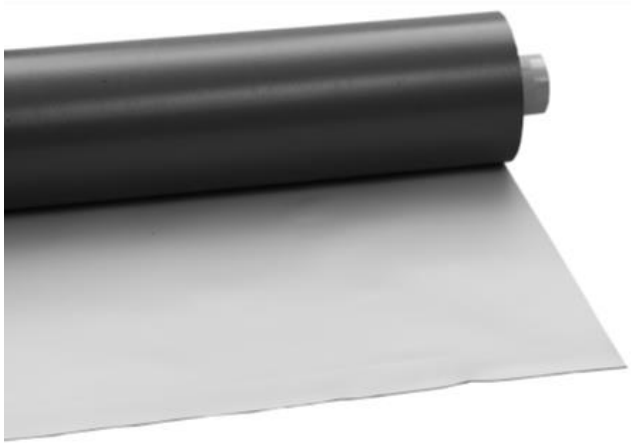

PRODUCT INFORMATION AND TECHNICAL PERFORMANCE		
Weights and Sizes	**Unit**	**Value**
Roll width	m	1.5
Roll length	m	20
Thickness	mm	1.5
Weight	kg/m²	1.80
Reinforcement		Pre-coated cross-weave polyester

SURFACE FINISHES	MEMBRANE COLOURS
Top:	Light Grey – RAL 7035 U15
	Blue Grey – RAL 7031 U15
	Anthracite – RAL 7016 U15
Bottom:	Dark Grey

UNITED KINGDOM
Bauder Ltd
70 Landseer Road, Ipswich, Suffolk IP3 0DH
T: +44 (0)1473 257671 E: info@bauder.co.uk
bauder.co.uk

IRELAND
Bauder Ltd
O'Duffy Centre, Carrickmacross, Co. Monaghan
T: +353 (0)42 9692 333 E: info@bauder.ie
bauder.ie

Revision: 25/10/2021 – V3

PRODUCT DATA SHEET

PRODUCT INFORMATION AND TECHNICAL PERFORMANCE

Characteristics		Test method	Unit	Value
External fire performance*		EN 13501-5		No performance declared
Reaction to fire		EN 13501-1		Class E according to EN 13501-1
Watertightness method B		EN 13956 : 2012 EN 13967 : 2012		Passed
Tensile force	md		N/mm	≥ 1000/50
	cd		N/mm	≥ 1000/50
Elongation at maximum tensile force	md		%	≥ 19
	cd		%	≥ 19
Root Resistance				FLL Fulfilled
Resistance to impact	Hard surface		mm	> 400
	Soft surface		mm	> 700
Resistance to static loading	Hard surface		kg	≥ 20
	Soft surface		kg	≥ 20
Tear resistance			N	> 200
Joint peel resistance			N/mm	≥ 200/50
Joint shear resistance			N/mm	≥ 600/50
Durability			h	> 1000 - Passed
Foldability			°C	≤-30
Dangerous substances				No performance declared

* Determination of external fire performance is a system test, which can be influenced by system components, which are not produced or sold by Bauder Limited, thus performance for each product cannot be given.

CERTIFICATION AND ENVIRONMENTAL INFORMATION

BBA Certificate	BBA Fire Rating – Test results indicate the product to be designated as being Un-Restricted 06/4354
FM Certificate	Assembly 229709 (other assemblies available)
Environmental Product Declaration (EPD)	EPD -BAU-20130188-IBCC0DE
International Standards Organisation (ISO)	ISO 9001:2015 Quality Management Certificates EN1271 (UK) and 70499/03-15_e (Germany). ISO 14001:2015 Environmental Management Certificates A10552 (UK) and 70499/03-15_d (Germany). ISO 50001: 2011 Energy Management Certificate 70499/03-15_c
BRE Green Guide generic product rating	A+

INSTALLATION GUIDANCE

Refer to the Thermofol Single Ply Installation Guide

UNITED KINGDOM
Bauder Ltd
70 Landseer Road, Ipswich, Suffolk IP3 0DH
T: +44 (0)1473 257671 E: info@bauder.co.uk
bauder.co.uk

IRELAND
Bauder Ltd
O'Duffy Centre, Carrickmacross, Co. Monaghan
T: +353 (0)42 9692 333 E: info@bauder.ie
bauder.ie

BUILDING TRUST

PRODUKTDATENBLATT

Sikaplan® S-20

Kunststoffabdichtungsbahn zur Detailausbildung

BESCHREIBUNG

Sikaplan® S-20 (Dicke 2 mm) ist eine homogene Kunststoffabdichtungsbahn, basierend auf Polyvinylchlorid (PVC).
DE/E1 PVC-P-NB-2,0

ANWENDUNG

- Detailausbildungen
- Stoßbänder bei Verbundblechen

PRODUKTMERKMALE/ VORTEILE

- Hervorragende Beständigkeit gegen Witterungseinflüsse (UV- Strahlung)
- Hohe Widerstandsfähigkeit gegen mechanische Einwirkung
- Hohe Reißfestigkeit und Reißdehnung
- Hervorragende Kälteflexibilität
- Recycelbar

PRÜFZEUGNISSE

- Kunststoffbahn für Dachabdichtungen gemäß DIN EN 13956, anerkannt von der Zertifizierungsstelle 1213-CPD-4125 und versehen mit dem CE-Zeichen
- DIN SPEC 20000-201
- DIN 18531-2
- Verhalten bei Brandeinwirkung gemäß DIN EN 13501-1, Klasse E
- Geprüft gegen äußere Brandeinwirkung gemäß DIN EN 1187-1: 2001
- Widerstand gegen Flugfeuer und strahlende Wärme gemäß DIN 4102-7 (für von Sika geprüfte Dachaufbauten)

PRODUKTINFORMATIONEN

Lieferform

Rollen sind mit einer gelben PE-Folie einzeln verpackt.
Verpackungseinheit: siehe aktuelle Preis- und Sortimentsübersicht.

Rollenlänge:	15,00 m
Rollenbreite:	1,1 m
Rollengewicht:	41,8 kg

Aussehen/Farbton

Oberfläche:	glatt
Farben:	
Oberseite:	hellgrau (ähnlich RAL 7047)
Rückseite:	dunkelgrau

(Sonderfarben auf Anfrage)

Lagerfähigkeit

In ungeöffneter und unbeschädigter Originalverpackung behält das Produkt seine Eigenschaften.

Lagerbedingungen

Rollen in horizontaler Position auf Paletten lagern. Vor direkter Sonneneinstrahlung, Regen und Schnee schützen. Paletten während des Transports

	oder der Lagerung nicht stapeln.	
Produktdeklaration		(DIN EN 13956 / DIN SPEC 20000-201)
Sichtbare Mängel	keine sichtbaren Mängel	(DIN EN 1850-2)
Länge	15,00 (-0 / +5 %) m	(DIN EN 1848-2)
Breite	1,10 (-0,5 / +1 %) m	(DIN EN 1848-2)
Effektive Dicke	2,00 (-5 / +10 %) mm	(DIN EN 1849-2)
Geradheit	≤ 30 mm	(DIN EN 1848-2)
Planlage	≤ 10 mm	(DIN EN 1848-2)
Flächengewicht	2,50 (-5 / +10 %) kg/m²	(DIN EN 1849-2)

TECHNISCHE INFORMATIONEN

Widerstand gegen Hagelschlag	starre Unterlage flexible Unterlage	≥ 20 m/s ≥ 36 m/s	(DIN EN 13583)
Widerstand gegen stoßartige Belastung	starre Unterlage flexible Unterlage	≥ 600 mm (Methode A) ≥ 900 mm (Methode B)	(DIN EN 12691)
Reißfestigkeit	längs (Mr)* quer (QMr)* *Mr = Maschinenrichtung *QMr = Quer zur Maschinenrichtung	≥ 12 N/mm² ≥ 12 N/mm²	(DIN EN 12311-2)
Reißdehnung	längs (Mr)* quer (QMr)* *Mr = Maschinenrichtung *QMr = Quer zur Maschinenrichtung	≥ 250 % ≥ 250 %	(DIN EN 12311-2)
Dimensionsstabilität	längs (Mr)* quer (QMr)* *Mr = Maschinenrichtung *QMr = Quer zur Maschinenrichtung	≤ 2,0 % ≤ 2,0 %	(DIN EN 1107-2)
Weiterreißwiderstand	längs (Mr)* quer (QMr)* *Mr = Maschinenrichtung *QMr = Quer zur Maschinenrichtung	≥ 100 N ≥ 100 N	(DIN EN 12310-2)
Schälwiderstand der Fügenaht	≥ 300 N/50 mm		(DIN EN 12316-2)
Scherwiderstand der Fügenaht	≥ 500 N/50 mm		(DIN EN 12317-2)
Verhalten beim Falzen bei tiefen Temperaturen	≤ -25 °C		(DIN EN 495-5)
Brandverhalten	Klasse E		(DIN EN ISO 11925-2) (Klassifizierung gemäß DIN EN 13501-1)
Auswirkung von flüssigen Chemikalien inklusive Wasser	auf Anfrage		(DIN EN 1847)
Beanspruchung durch Feuer von außen	Teile 1 bis 4 (für von Sika geprüfte Dachaufbauten) B_{ROOF} (t1) < 20º, > 20º Widerstandsfähigkeit gegen Flugfeuer und strahlende Wärme (für von Sika geprüfte Dachaufbauten)		(DIN EN 1187) (DIN EN 13501-5)

	Erfüllt für Dachneigung ≤ 20º, ≥ 20º	(DIN 4102-7)
UV-Einwirkung	bestanden (> 5.000 h) Klasse 0	(DIN EN 1297) (DIN SPEC 20000-201 / DIN EN 1297)
Wasserdampfdurchlässigkeit	μ = 20.000	(DIN EN 1931)
Wasserdichtheit	bestanden 400 kPa/72h	(DIN EN 1928) (DIN SPEC 20000-201)

SYSTEMINFORMATIONEN

Verträglichkeit	Nicht verträglich in direktem Kontakt mit Kunststoffen aus anderen Werkstoffgruppen, Dämmstoffen z.B. EPS. Nicht verträglich mit Teer, Bitumen, öl- und lösemittelhaltigen Medien.

ANWENDUNGSINFORMATIONEN

Lufttemperatur	-5 °C min. / +60 °C max. bei Heißluftschweißen +5 °C min. / +60 °C max. bei Kaltschweißen
Untergrundtemperatur	-10 °C min. / +60 °C max. bei Heißluftschweißen +5 °C min. / +60 °C max. bei Kaltschweißen

VERARBEITUNGSANWEISUNG

Der Einbau der Dachabdichtung sollte von Sika® Roofing geschulten Verarbeitern ausgeführt werden.

VERARBEITUNG

Nicht zur Verlegung in der Fläche geeignet.

WEITERE HINWEISE

Der Einsatz von Sikaplan® S-20 ist auf geographische Regionen mit einer minimalen monatlichen Durchschnittstemperatur von -10 °C begrenzt. Die dauerhafte Umgebungstemperatur während der Nutzung ist auf +50 °C beschränkt.

MESSWERTE

Alle technischen Daten, Maße und Angaben in diesem Datenblatt beruhen auf Labortests. Tatsächlich gemessene Daten können in der Praxis aufgrund von Umständen außerhalb unseres Einflussbereiches abweichen.

LÄNDERSPEZIFISCHE DATEN

Die Angaben in diesem Produktdatenblatt sind gültig für das von der Sika Deutschland GmbH ausgelieferte Produkt. Bitte beachten Sie, dass Angaben in anderen Ländern davon abweichen können. Beachten Sie das im Ausland gültige Produktdatenblatt.

ÖKOLOGIE, GESUNDHEITS- UND ARBEITSSCHUTZ

VERORDNUNG (EG) NR. 1907/2006 - REACH

Dieses Produkt ist ein Erzeugnis nach Artikel 3 der Verordnung (EG) Nr. 1907/2006 (REACH). Es enthält keine Stoffe, die bei üblicher Anwendung aus dem Erzeugnis freigesetzt werden. Ein Sicherheitsdatenblatt nach Artikel 31 der gleichen Verordnung ist nicht erforderlich, um dieses Produkt auf den Markt zu bringen, zu transportieren oder es anzuwenden. Für die sichere Nutzung befolgen Sie die Anweisungen im Produktdatenblatt. Nach unserem derzeitigen Kenntnisstand enthält dieses Produkt keine SVHC (besonders besorgniserregende Stoffe) in Anhang XIV der REACH-Verordnung oder auf der von der Europäischen Chemikalien-Agentur ECHA veröffentlichten Kandidatenliste in Konzentrationen über 0.1 % (w/w).

RECHTLICHE HINWEISE

Die vorstehenden Angaben, insbesondere die Vorschläge für Verarbeitung und Verwendung unserer Produkte, beruhen auf unseren Kenntnissen und Erfahrungen im Normalfall, vorausgesetzt die Produkte wurden sachgerecht gelagert und entsprechend der Vorgaben unserer jeweiligen Produktdatenblätter angewandt. Wegen der unterschiedlichen Materialien, Untergründen und abweichenden Arbeitsbedingungen kann eine Gewährleistung eines Arbeitsergebnisses oder eine Haftung, aus welchem Rechtsverhältnis auch immer, weder aus diesen Hinweisen, noch aus einer mündlichen Beratung begründet werden, es sei denn, dass uns insoweit Vorsatz oder grobe Fahrlässigkeit zur Last fällt. Hierbei hat der Anwender nachzuweisen, dass er schriftlich alle Informationen und Kenntnisse, die zur sachgemäßen und erfolgversprechenden Beurteilung durch Sika erforderlich sind, rechtzeitig und vollständig an Sika übermittelt hat. Der Anwender hat die Produkte auf ihre Eignung für den vorgesehenen Anwendungszweck eigenverantwortlich zu prüfen. Änderungen der Produktspezifikationen bleiben vorbehalten. Schutzrechte Dritter sind zu beachten. Im Übrigen gelten unsere jeweiligen Verkaufs-, Liefer-. und Zahlungsbedingungen, einzusehen und herunterzuladen unter www.sika.de. Es gilt das jeweils neueste Produktdatenblatt, das von uns angefordert oder im Internet unter www.sika.de heruntergeladen werden kann.

Sika Deutschland GmbH
Roofing
Kornwestheimer Strasse 103-107
70439 Stuttgart
Tel.: +49 711/8009-0
roofing@de.sika.com
www.sika.de/dachabdichtung

B.6 Black paint

The Ceramic-based, black pigmented coating for carbon and stainless steel Aremco HiE-Coat 840 MX was used to paint the stainless-steel board described in section 3.2.1 [153].

AREMCO

HIGH TEMPERATURE HIGH EMISSIVITY COATINGS

Technical Bulletin A5-S2

PRODUCT HIGHLIGHTS

Aremco's HiE-Coat™ 840-Series line of high emissivity coatings are black-body formulations designed to significantly improve the thermal efficiency of infrared heaters, furnaces, incinerators, and ovens used throughout the appliance, ceramics, chemical processing, metallurgical, and refining industries. Natural gas and oil savings in the range of 5–10% are typical using these coatings.

840-C Ceramic-based, black-pigmented coating for ceramic fiber modules, light-weight refractory board, and dense refractories to 2000 °F (1093 °C).

840-CX Ceramic-based, black-pigmented coating for ceramic fiber modules, light-weight refractory board, and dense refractories to 2400 °F (1316 °C).

840-CM Ceramic-based, black-pigmented coating for dense refractories and refractory metals to 2000 °F (1093 °C).

840-M Ceramic-based, black pigmented coating for carbon and stainless steel to 2000 °F (1093 °C).

840-MX Ceramic-based, black pigmented coating for carbon and stainless steel to 2400 °F (1316 °C).

840-MS Silicone-Ceramic, black pigmented coating for aluminum, copper, carbon and stainless steel to 1100 °F (593 °C).

High emissivity coatings absorb and re-radiate significantly more radiant and convective heat than an uncoated burner tube or refractory to a cooler load. For refractories lined systems, this reduces the amount of heat stored in the lining which results in less thermal shock and related thermal stresses, resulting in longer refractory life and reduced maintenance costs. Since less energy is absorbed by the refractory lining, faster heat-ups result, reducing cycle time and energy costs.

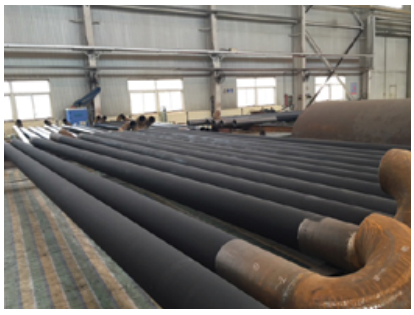

HiE-Coat™ 840-M coats gas-fired heating tubes.

HiE-Coat™ 840-C coats ceramic fiberboard infrared heater.

HiE-Coat™ 840-M coats industrial heat exchanger.

HiE-Coat™ 840-M coats gas burner component.

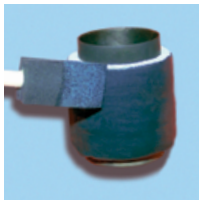

HiE-Coat™ 840-C coats exhaust pipe insulation.

Aremco Products, Inc., 707-B Executive Boulevard, Valley Cottage, NY 10989 **T** (845) 268-0039 **E** aremco@aremco.com **W** aremco.com

Rev. 4/18

HIE-COAT™ HIGH EMISSIVITY COATINGS

Product Number	840-C	840-CX[6]	840-CM	840-M	840-MX[6]	840-MS
Type			Inorganic-Ceramic			Silicone-Ceramic
Applications	Light-Weight Refractory	Light-Weight Refractory	Dense Refractory	Carbon Steel	Carbon Steel	Aluminum
	Fiber Modules	Fiber Modules	Refractory Metals	Stainless Steel	Stainless Steel	Copper
	Dense Refractory	Dense Refractory				Carbon & Stainless Steel
Color (cured)	Jet Black	Jet Black	Jet Black	Jet Black	Jet Black	Jet Black
Maximum Temperature, °F (°C)	2000 (1093)	2400 (1316)	2000 (1093)	2000 (1093)	2400 (1316)	1100 (593)
No. Components	1	1	1	1	1	1
Mix Ratio, by Weight (by Volume)	NA	NA	NA	NA	NA	NA
Viscosity, cP[1]	70–160	50–150	600–800	400–800	300–700	250–500
Specific Gravity, g/cc	1.60	1.52	1.54	1.61	1.57	1.49
Solids by Weight, %	58.5	51.5	48.0	47.3	47.3	57.1
Solids by Volume, %	27.3	20.25	19.9	22.1	22.1	42.5
WFT, mils (microns)[2]	3.66 (92.9)	4.94 (125.4)	5.03 (127.7)	4.52 (114.8)	4.52 (114.8)	2.40 (61.0)
DFT, mils (microns)[3]	1.00 (25.4)	1.00 (25.4)	1.00 (25.4)	1.0 (25.4)	1.0 (25.4)	1.00 (25.4)
Theoretical Dry Film Coverage[4] @ 1 mil, ft²/gal (m²/liter)	438 (10.8)	325 (8.0)	319 (7.8)	355 (8.7)	355 (8.7)	681 (16.7)
Curing, Min Air Set, hrs[5]	1.0–2.0	1.0–2.0	1.0	1.0	1.0	1.0
Curing, Heat Cure, °F, hrs	200, 1	200, 1	200, 0.5 + 500 / 1	200, 1 + 500 / 1	200, 1 + 500 / 1	480 / .75
Application Temperature, °F	50–90	50–90	50–90	50–90	50–90	50–120
Thinner	840-C-T	840-CX-T	840-CM-T	840-M-T	840-MX-T	PM Acetate
Flash Point, °F/°C	NA	NA	NA	NA	NA	~118 (48)
Volatiles, lbs/gal	0.0	0.0	0.0	0.0	0.0	5.3
Shelf Life, months	6	6	6	6	6	6
Storage Temperature, °F	55–85	55–85	55–85	55–85	55–85	40–90

Reference Notes

[1] Viscosity is measured using a Brookfield LV Viscometer; spindle and speed selection vary depending on the product.
[2] Estimated Wet Film Thickness (WFT).
[3] Recommended Dry Film Thickness (DFT).
[4] Actual coverage will vary depending on material losses during mixing and application.
[5] Where a value is provided for "Min Air Set", it is recommended to set the coating at room temperature for, at minimum, the specified time prior to curing.
[6] Part numbers ending in "X" are made with black pigment that does not contain any copper; copper can produce "greening" of the coating when exposed to flame impingement.

Surface Preparation Notes

All surfaces should be free of oil, grease, dirt, corrosives, oxides, paints or other foreign matter. No further preparation is required when coating ceramics, refractories or graphites. Quartz should be sandblasted whenever possible. Smooth metal surfaces should be sandblasted or etched using Aremco's Corr-Prep™ CPR2000.

Abbreviations

NA	Not Applicable	DFT	Dry Film Thickness
NR	Not Required	WFT	Wet Film Thickness

Spectral Normal Emissivity at 800 °C

HiE-Coat™ 840-C

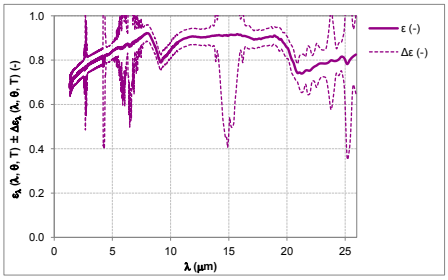

λ (μm)	2	3.5	4.7	8.3	10	12.5	17.5	20	25
ϵ_λ (λ,θ,T) (-)	0.735	0.799	0.827	0.903	0.848	0.904	0.896	0.860	0.809
Δε (-), k = 2	0.036	0.036	0.036	0.037	0.035	0.036	0.042	0.051	0.066

HiE-Coat™ 840-M

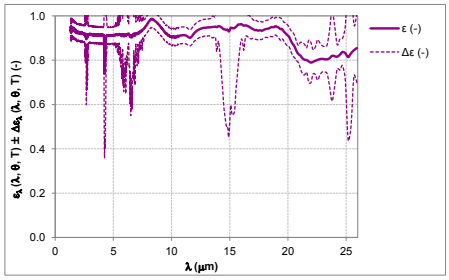

λ (μm)	2	3.5	4.7	8.3	10	12.5	17.5	20	25
ϵ_λ (λ,θ,T) (-)	0.924	0.915	0.911	0.986	0.906	0.943	0.934	0.913	0.832
Δε (-), k = 2	0.038	0.037	0.037	0.039	0.037	0.037	0.041	0.047	0.062

For more Spectral Normal Emissivity Charts, visit aremco.com/tech-notes

Refer to Price List for complete order information.